DOCTOR OF PHILOSOPHY

Structural studies to inform antimicrobial drug discovery and the basis of immunity against T6 effectors

O'Rourke, Patrick

Award date:
2013

DOCTOR OF PHILOSOPHY

Structural studies to inform antimicrobial drug discovery and the basis of immunity against T6 effectors

Patrick O'Rourke

2013

University of Dundee

A thesis submitted for the degree of Doctor of Philosophy

Structural studies to inform antimicrobial drug discovery and the basis of immunity against T6 effectors

Patrick E. F. O'Rourke

Supervisor:
Professor William N. Hunter

The Wellcome Trust Biocentre
College of Life Sciences
University of Dundee
Scotland

August 2013

CONTENTS

LIST OF FIGURES

LIST OF TABLES

Acknowledgements

All the members of the Hunter laboratory have been supportive and friendly. In particular, Dr. Thomas Eadsforth has been my post-doctoral mentor and friend throughout my investigations. Sharon Shepherd provided me with instruction and training in protein purification techniques. Dr. Paul Fyfe assisted me during my first few months in the laboratory and provided me with training in the use of the new X-ray diffraction system.

Special acknowledgement is paid here to the contribution of Dr. Justyna Kalinowska-Tłuścik whose work in optimising both expression and crystallisation of the *Pf*IspF protein I have successfully reproduced in my own work.

Thanks must go to Dr. Vincent Rao and Dr. Velupillai Srikannathasan for sharing with me their unprocessed diffraction data on the Type VI secretion system proteins, Rap1a and Rap2a. Thanks also go to Dr. David Robinson who helped me perform bio-layer interferometry experiments; and to Dr. Mark Agacan for advice on the use of the in-house X-ray generators.

I acknowledge the assistance of all those involved in providing lab-services including wash-up, autoclave and media support.

I am grateful to the Biotechnology and Biological Sciences Research Council and to Pfizer, Inc. for awarding a BBSRC-CASE scholarship in support of my work with Prof. Hunter. I also gratefully acknowledge access to the excellent facilities at the synchrotron sources Diamond Light Source in Oxfordshire and the European Synchrotron Radiation Facility in Grenoble.

I would like to thank my supervisor Prof. Bill Hunter for his warm encouragement, excellent advice and support.

I am especially pleased to acknowledge the kind support of my parents and friends during the course of my PhD studies.

Patrick O'Rourke.

DECLARATION

I hereby declare that the following thesis is based on the result of investigations conducted by myself, and that this thesis is of my own composition. This thesis has not, in whole or in part, been previously presented for a higher degree. Work other than my own is clearly indicated in the text by reference to the relevant researchers or publication.

Patrick E. F. O'Rourke

The work presented in this thesis is the work of the candidate P. O'Rourke. Conditions of the relevant Ordinance and Regulations have been fulfilled.

Prof. W. N. Hunter.

SUMMARY

Work presented in this thesis is in two parts.

Part one: The X-ray crystal structures of potential antimicrobial drug targets.

The protein **IspF** (2*C*-methyl-D-erythritol-2,4-cyclodiphosphate synthase, EC: 4.6.1.12) from two pathogens (*Burkholderia cenocepacia* and *Plasmodium falciparum*) has been investigated. IspF is an enzyme of isoprenoid-precursor biosynthesis and is considered to be a potential drug target. The results of structural and fragment-screening efforts presented here inform early stage drug discovery efforts.

The structure of the **PabC** protein (4-amino-4-deoxychorismate lyase, EC: 4.1.3.38) from the Gram-negative pathogen *Pseudomonas aeruginosa* was also determined. PabC is involved in the production of *para*-aminobenzoic acid on the path to folate. Comparisons with previously solved PabC structures identified a spatially conserved tyrosine residue in the active site and suggest that a re-evaluation of a published mechanism is warranted.

Part two: Immunity proteins in the Gram-negative Type VI secretion system

The X-ray crystal structures of the proteins **Rap1a** and **Rap2a** from *Serratia marcescens*, inhibitors of the peptidoglycan amidase toxins secreted by some Gram-negative bacteria employing the Type VI secretion pathway, were determined by molecular replacement and analysed.

Part one:

Chapter 1: Introduces isoprenoid-precursor biosynthesis and its importance as a potential source of novel drug targets for infectious diseases. The structure of IspF from the methyl-*D*-erythritol phosphate (MEP) pathway was sought, in complex with ligands, to inform early-stage drug discovery efforts. The PabC protein is introduced. The significance of *para*-aminobenzoic acid for bacterial folate biosynthesis and the history of anti-folate drug discovery are discussed. Some general background information is provided describing the processes of fragment based screening and structure-based drug discovery.

Chapter 2: Details of materials used and experimental procedures are given.

Chapter 3: (Results and Discussion - IspF structures) High resolution structures of IspF from the pathogens *B. cenocepacia* and *P. falciparum* are presented. The crystal structures of *Bc*IspF with cytidine derivatives were determined by molecular replacement methods, refined and analysed. The active site contained two molecules of cytidine monophosphate (CMP) and a structure was subsequently re-determined from a crystal grown in the presence of a lower CMP concentration. A structure of *Bc*IspF with citrate, a buffer component, bound at the active site is also reported. Despite several concerted attempts, no co-crystal structures could be obtained with novel ligands. The structure of *Pf*IspF is described bound to cytidine diphosphate (CDP). This reproduced earlier studies on this protein in the Hunter lab by Dr. Kalinowska-Tłuścik, demonstrating a robust protocol for production of *Pf*IspF crystals. Additionally, *holo*-crystals of *Pf*IspF without any cytidine derivatives present were obtained and the structure determined. A chemical fragment screen was performed against biotinylated *Bc*IspF and the *E. coli* IspF orthologue employing the bio-layer interferometry technique (BLI). Fragments identified are described.

Chapter 4: *Pa*PabC structure
The structure of PabC, an essential enzyme from *P. aeruginosa*, is described. This structure demonstrates the presence of a structurally conserved tyrosine residue in the active site that had been overlooked in previous studies.

Part two:
Chapter 5: Introduces the Type VI secretion system (T6SS) of Gram-negative bacteria and describes the structural determination of two proteins from *Serratia marcescens*, Rap1a and Rap2a, that confer immunity against certain peptidoglycan amidase effectors of the T6SS.

Chapter 6: The structures of Rap1a and Rap2a are described and compared to previously reported immunity proteins from different bacteria. Rap1a is shown to adopt a unique fold for an immunity protein, similar to that of other periplasmic proteins.

Abbreviations

S.I. units are used throughout with the exception of Å representing 10^{-10} m; and temperatures values, which are given in degrees Celsius (°C).

ASA	Accessible surface area
ATP	Adenosine-5'-triphosphate
BAP	Biotin acceptor peptide
Bis-Tris	2-[Bis(2-hydroxyethyl)amino]-2--(hydroxymethyl)propane-1,3-diol
BLI	Biolayer interferometry
Cα	Carbon-alpha of an amino acid
CDP	Cytidine 5'-diphosphate
CHES	*N*-cyclohexyl-2-aminoethanesulfonic acid
CMP	Cytidine 5'-monophosphate
CoA	Coenzyme A
DDU	Drug Discovery Unit
DHFR	Dihydrofolate reductase (EC: 1.5.1.3)
DHPS	Dihydropteroate synthase (EC: 2.5.1.15)
DMAPP	Dimethylallyl pyrophosphate
DMSO	Dimethyl sulfoxide
DOXP	1-deoxy-*D*-xylulose 5-phosphate
DSF	Differential scanning fluorimetry
DXR	1-deoxy-*D*-xylulose 5-phosphate reductoisomerase (EC: 1.1.1.267)
DXS	1-deoxy-*D*-xylulose 5-phosphate synthase (EC: 2.2.1.7)
EC	Enzyme Commission number
EDTA	(Ethylenediamine)tetra-acetic acid
ESI-MS	Electrospray ionisation mass spectrometry
ESRF	European Synchrotron Radiation Facility
FPLC	Fast protein liquid chromatography
FPP	Farnesyl pyrophosphate
GPP	Geranyl pyrophosphate
GTP	Guanosine-5'-triphosphate
HEPES	4-(2-hydroxyethyl)piperazine-1--ethanesulfonic acid
His-tag	Hexahistidine protein purification tag
HMBPP	(*E*)-4-hydroxy-3-methyl-but-2-enyl pyrophosphate
HMG-CoA	3-hydroxy-3-methylglutaryl-CoA
HPLC	High-performance liquid chromatography

IDI	IPP-isomerase (EC: 5.3.3.2)
IPP	Isopentenyl pyrophosphate
IPTG	Isopropyl β-*D*-1-thiogalactopyranoside
IspD	2-*C*-methyl-*D*-erythritol 4-phosphate cytidylyltransferase (EC: 2.7.7.60)
IspE	4-diphosphocytidyl-2*C*-methyl-*D*-erythritol kinase (EC: 2.7.1.148)
IspF	2-*C*-methyl-*D*-erythritol-2,4-cyclodiphosphate synthase (EC: 4.6.1.12)
IspG	HMBPP synthase (EC: 1.17.7.1)
IspH	HMBPP reductase (EC: 1.17.1.2)
LB media	Luria-Bertani (lysogeny broth) media
mA_2pm	*meso*-diaminopimelate
MALDI-TOF MS	Matrix-assisted laser desorption/ionisation time-of-flight mass spectrometry
MEcPP	2-*C*-methyl-*D*-erythritol 2,4-cyclodiphosphate
MEP	Methyl-*D*-erythritol phosphate
MES	2-(*N*-morpholino)ethanesulfonic acid
NADPH	Nicotinamide adenine dinucleotide phosphate
NCS	Non-crystallographic symmetry
NMR	Nuclear magnetic resonance spectroscopy
OD_{600}	Optical density at 600 nm
PABA	*para*-aminobenzoic acid
PabC	4-amino-4-deoxychorismate lyase (EC: 4.1.3.38)
PAGE	Polyacrylamide gel electrophoresis
PCR	Polymerase chain reaction
PDB	Protein Data Bank
PEG	Polyethylene glycol
PLP	Pyridoxal 5'-phosphate
PP_i	Pyrophosphate
PVDF	Polyvinylidene difluoride
R^2	Coefficient-of-determination value
Rap	Resistance associated protein
RMSD	Root-mean-square deviation
RT-PCR	Real-time polymerase chain reaction
SDS	Sodium dodecyl sulfate
SPR	Surface plasmon resonance spectroscopy
Ssp	Small secreted protein
T6SS	Type VI secretion system
T6 effectors	Effector proteins of the Type VI secretion system
TEV	Tobacco Etch Virus protease
TLC	Thin layer chromatography
Tris	Tris(hydroxymethyl)aminomethane
v/v	Volume per volume
w/v	Weight per volume

Publications

The work presented in this thesis has resulted in two publications.

O'Rourke PEF, Eadsforth TC, Fyfe PK, Shepherd SM and Hunter WN (2011) *Pseudomonas aeruginosa* 4-amino-4-deoxychorismate lyase: spatial conservation of an active site tyrosine and classification of two types of enzyme. ***PLoS One*, 6 (9):e24158**

Srikannathasan V, English G, Bui NK, Trunk K, O'Rourke PEF, Rao VA, Vollmer W, Coulthurst SJ and Hunter WN (2013) Structural basis for Type VI secreted peptidoglycan DL-endopeptidase function, specificity and neutralization in *Serratia marcescens*. ***Acta Cryst. D*, 69: 2468-2482**

PART ONE

THE X-RAY CRYSTAL STRUCTURES OF POTENTIAL ANTIMICROBIAL DRUG TARGETS

CHAPTER 1

INTRODUCTION

Introduction

1.1 Structure-based drug discovery and fragment screening

Modern drug discovery is often a long and costly process. Target-based approaches to antimicrobial drug discovery involve careful selection of proteins demonstrated or predicted to be essential. Crystallographic structural information about the target proteins, especially when structures in complex with ligands are available, can provide valuable information at the early stages of drug discovery; informing target assessment, rationalising structure-activity relationships between ligands and suggesting sites for potential improvements to the lead compounds (Hunter, 2009; Moynie *et al.*, 2013; Verlinde & Hol, 1994; Whittle & Blundell, 1994). In addition, high-quality structures can provide a template for virtual screening efforts (Mpamhanga *et al.*, 2009). The structure-based discovery of drugs in clinical use targeting human immunodeficiency virus (Kempf *et al.*, 1995; Wlodawer & Erickson, 1993), influenza virus (von Itzstein *et al.*, 1993) and kinases involved in cancer development (Bollag *et al.*, 2010; Noble *et al.*, 2004; Tsai *et al.*, 2008) are examples that illustrate the efficacy of this approach (Figure 1.1).

Identifying ligands for target proteins during drug discovery can be challenging, as both high affinity and selective interactions are sought. Libraries of chemical compounds with mass typically less than 300 Da, called 'fragments', can be screened in an attempt to identify starting points for such ligands (Congreve *et al.*, 2008; Scott *et al.*, 2012). Structural studies complement this approach as once the relative binding location and orientation of fragments is elucidated, medicinal chemistry can often provide suggestions to link, fuse or otherwise elaborate on these starting points. Such elaborated ligands often have much higher binding affinities than the original fragments, offering an attractive route to lead compounds; particularly for proteins

where either no or only a limited number of ligands are known (de Kloe *et al.*, 2009). Alternatively, fragments can be screened by attempting to co-crystallise with the target protein or by soaking into preformed crystals and determining the structure of complexes by high-throughput crystallography (Hartshorn *et al.*, 2005). Owing to the relatively small size and typically weak affinity of fragments, ranging from µM to mM, sensitive biophysical assays, such as surface plasmon resonance (SPR) or nuclear magnetic resonance spectroscopy (NMR), are usually required for screening (Navratilova & Hopkins, 2010; Shuker *et al.*, 1996).

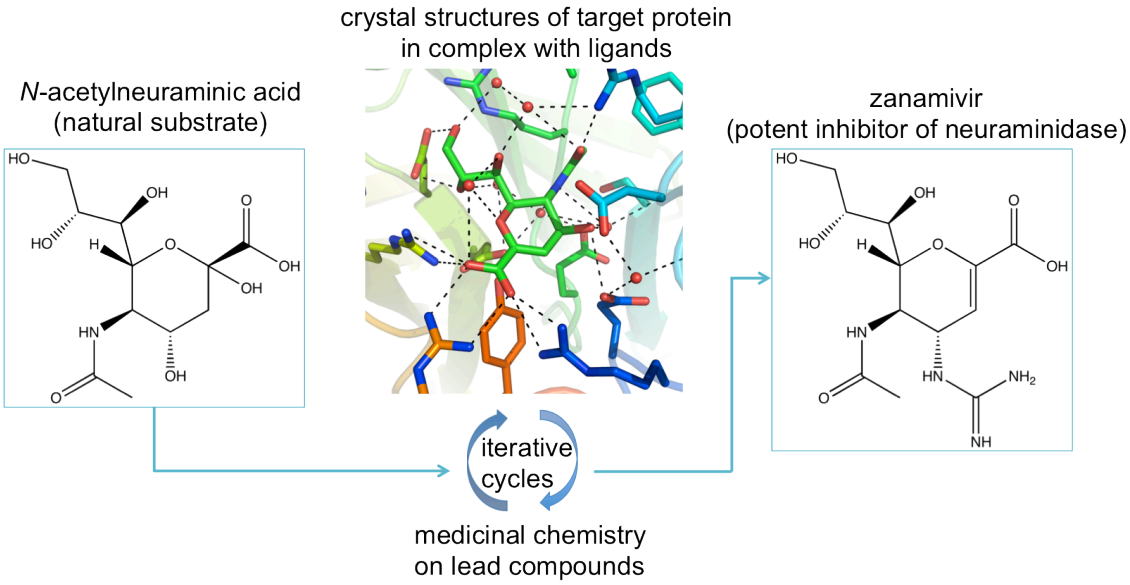

Figure 1.1 An illustrative example of rational drug design informed by X-ray structural studies. The development of zanamivir, a potent neuraminidase inhibitor for the treatment of influenza, is represented in schematic form. Structural determination of the target protein in complex with ligands and lead compounds suggested routes for elaboration of the lead compounds by medicinal chemistry. Iterative cycles of chemistry and structural determination support each other during the drug discovery process, leading to the identification of successively more potent compounds. In this example the crystal structure of the target revealved the presence of two glutamate residues adjacent to the lead compound. Addition of a guanidino group (present in the final inhibitor, zanamivir) to promote interaction with these glutamates increased potency. (Smith *et al*., 2001; von Itzstein *et al.*, 1993)

In the studies presented in this thesis, the structures of essential proteins from several human pathogens were determined. *Pseudomonas aeruginosa* and *Burkholderia cenocepacia* are Gram-negative bacteria, implicated in hospital-acquired infections of immuno-compromised patients, and *Plasmodium falciparum* is a protozoan parasite - the causative agent of cerebral malaria.

1.2.1 The role of isoprenoids in microbial cells

Isoprenoids, also known as terpenoids, are a large and structurally diverse class of natural products. All isoprenoids derive from the five-carbon universal precursors isopentenyl pyrophosphate (IPP) and dimethylallyl pyrophosphate (DMAPP), isomeric building blocks bearing an unsaturated carbon-carbon double bond that can be linked to together to form longer chains known as prenyl groups, such as geranyl- (C10), farnesyl- (C15) and geranylgeranyl (C20) pyrophosphate (Figure 1.2). The attachment of prenyl groups to proteins is a common protein post-translational modification that results in anchoring to lipid membranes. More complex isoprenoid structures, including membrane components such as cholesterol in eukaryotes and hopanoids in bacteria can be formed by cyclisation and further chemical modifications. Certain compounds bearing isoprenoid-derived side chains, such as menaquinone and ubiquinone, are essential to respiratory redox chains for energy generation in cells, where they function as membrane associated mobile electron carriers. Long-chain membrane associated isoprenoid compounds are employed as scaffolds during the assembly of glycan structures. In eukaryotes dolichol pyrophosphate fulfills this role in *N*-glycosylation, and for many bacteria undecaprenyl pyrophosphate functions in the synthesis of peptidoglycan precursors during assembly of the cell wall (Bouhss *et al.*, 2008; Ershov, 2007).

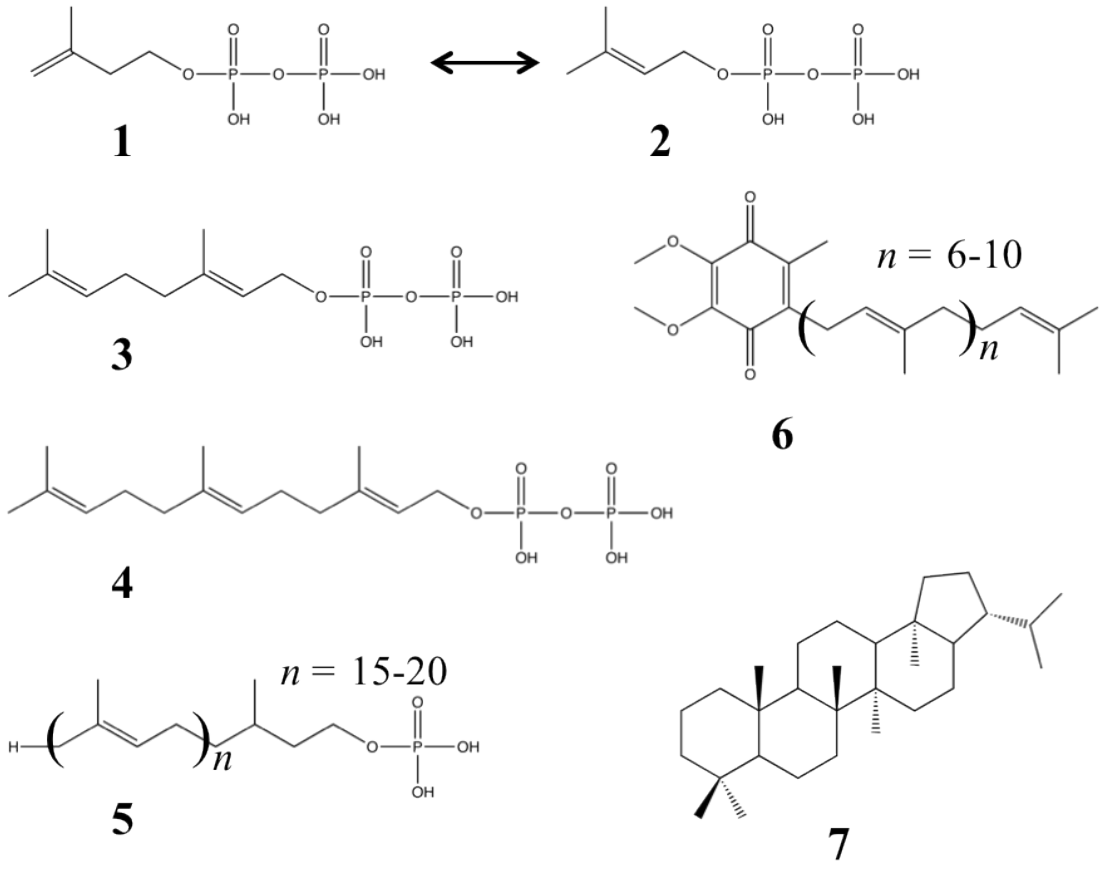

Figure 1.2 Isoprenoid compounds. The chemical structures of selected isoprenoid compounds are shown. **1**: isopentenyl pyrophosphate (IPP). **2**: dimethylallyl pyrophosphate (DMAPP). **3**: geranyl pyrophosphate (GPP). **4**: farnesyl pyrophosphate (FPP). **5**: dolichol phosphate. **6**: ubiquinone. **7**: hopane. A double-headed arrow has been drawn to indicate that the isoprenoid-precursors, **1** and **2**, are isomers. (Adapted from Ershov, 2007)

1.2.2 The methyl-*D*-erythritol phosphate (MEP) pathway of isoprenoid-precursor biosynthesis

Two biosynthetic pathways have been discovered for the production of the universal isoprenoid-precursor molecules IPP and DMAPP. The mevalonate pathway, which was discovered first (Bloch, 1964), starts with the condensation of two molecules of acetyl-CoA to form acetoacetyl-CoA. This is followed by conversion to 3-hydroxy-3-methylglutaryl-CoA (HMG-CoA), which is in turn converted to mevalonic acid; an intermediate metabolite from which the pathway derives its name, by the action of the NADPH-dependent enzyme HMG-CoA reductase (EC: 1.1.1.34). Mevalonic acid is subsequently phosphorylated twice and decarboxylated to form IPP. IPP and DMAPP

are interconverted by Mg^{2+} dependent IPP-isomerase (IDI) enzymes (EC: 5.3.3.2). HMG-CoA reductase is known to be a key regulatory enzyme on the mevalonate pathway (Brown & Goldstein, 1980). Inhibitors of this enzyme such as the statin drugs, for example lovastatin (Alberts *et al.*, 1980), are in clinical use for the treatment of hypercholesterolaemia (Figure 1.3).

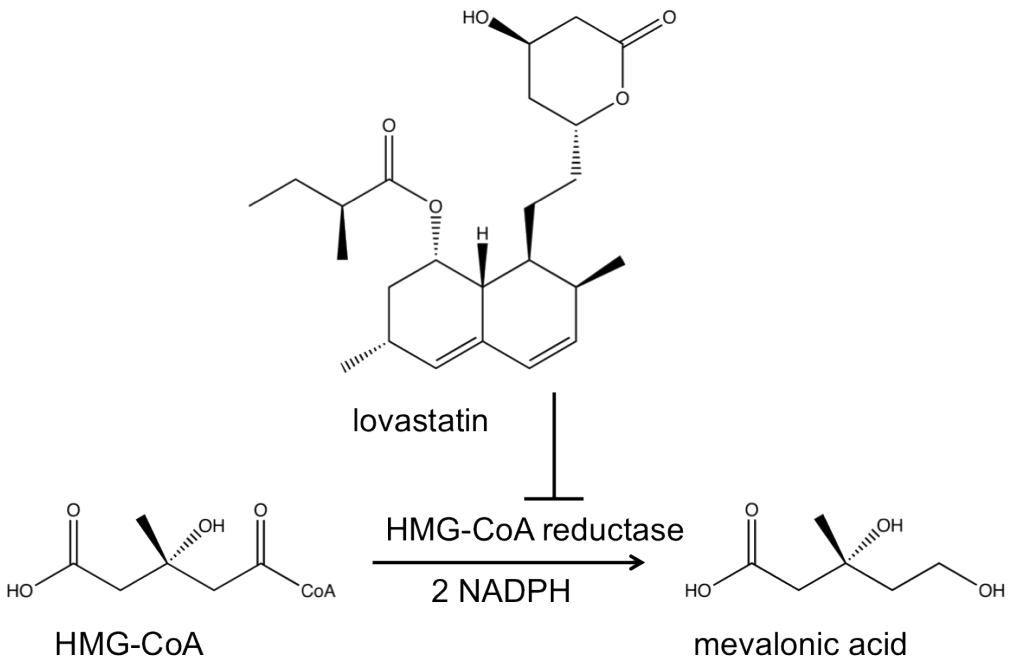

Figure 1.3 Lovastatin inhibits HMG-CoA reductase, a key regulatory enzyme on the mevalonate pathway of isoprenoid-precursor biosynthesis.

In 1993, Rohmer *et al.*, provided evidence for the existence of a novel, non-mevalonate pathway for isoprenoid-precursor biosynthesis (Figure 1.4). Incorporation of ^{13}C isotopes into isoprenoid species including hopanoids and ubiquinone was monitored by NMR using labelled test-substrates in several bacteria. The labelling pattern was distinct from that established for the mevalonate pathway, and was consistent with the formation of IPP *via* a novel pathway starting from pyruvate and a triose phosphate, later shown to be glyceraldehyde-3-phosphate (Rohmer *et al.*, 1996). This contention was tested and confirmed by investigating the isotope labelling pattern

observed in isoprenoids in the eukaryotic green-alga *Scenedesmus obliquus* following a similar procedure (Schwender *et al.*, 1996). Isoprenoid-precursor biosynthesis in plants was re-investigated in light of the work on green-algae (Lichtenthaler *et al.*, 1997). In that study, isoprenoids extracted from the cytoplasm, sitosterol and stigmasterol, were derived from the classical mevalonate pathway; whereas isoprenoids found exclusively in chloroplasts, phytol, β-carotene, lutein and the isoprenoid side chain of plastoquinone-9, exhibited the novel labelling pattern observed previously in bacteria (Rohmer *et al.*, 1993) and algae (Schwender *et al.*, 1996). This suggested that in higher plants the mevalonate pathway operates in the cytoplasm and the non-mevalonate pathway operates in the chloroplasts (Lichtenthaler *et al.*, 1997; reviewed in Lichtenthaler, 1999).

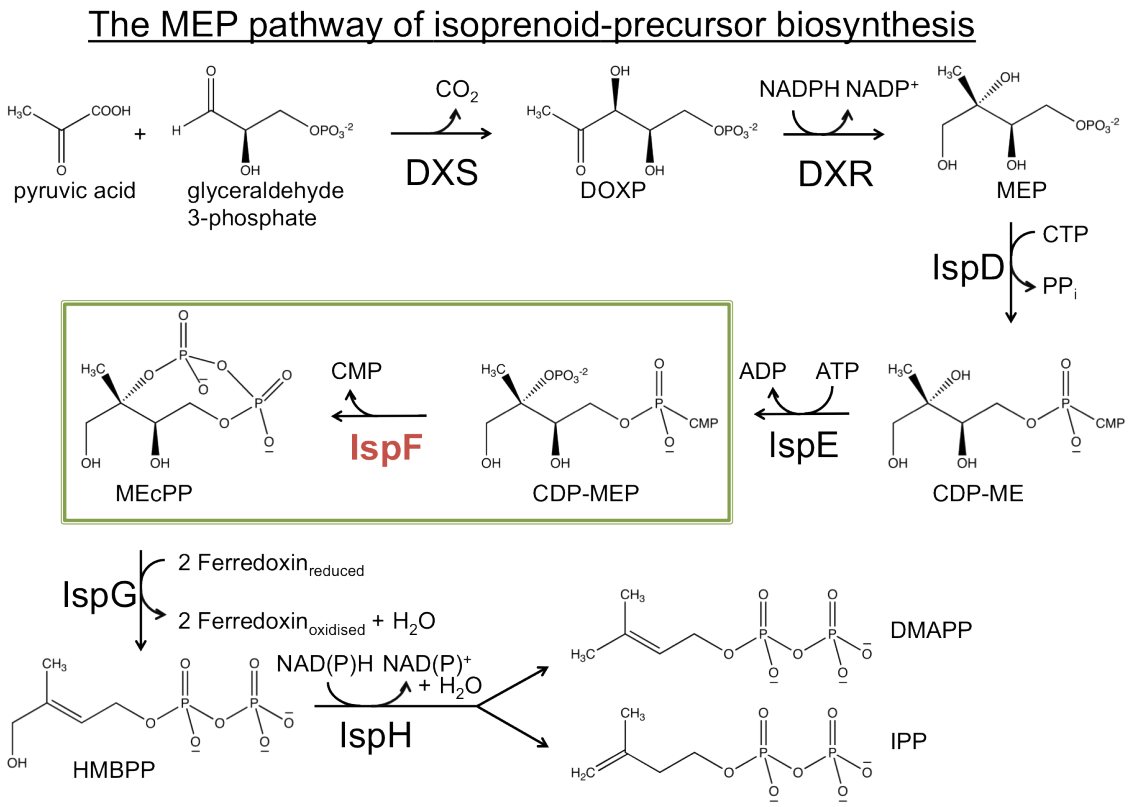

Figure 1.4 The MEP pathway for isoprenoid-precursor biosynthesis. The universal precursors for isoprenoid biosynthesis, IPP and DMAPP, are formed *via* the MEP pathway. IspF, the fifth enzyme on this pathway, is the subject of studies reported in this thesis.

The non-mevalonate pathway was subsequently re-named the 1-deoxy-D-xylulose-5-phosphate (DOXP) pathway, when it was demonstrated that DOXP is the first metabolite on this pathway downstream of pyruvate and glyceraldehyde-5-phosphate, and the enzyme responsible for its synthesis (DOXP synthase, DXS, EC: 2.2.1.7) was characterised (Sprenger *et al.*, 1997). Since DOXP is also required for the synthesis of thiamine and pyridoxol, the non-mevalonate pathway in now referred to as the 2*C*-methyl-D-erythritol-4-phosphate (MEP) pathway, named after the first committed metabolite on the pathway to IPP/DMAPP. DOXP is converted to MEP by the enzyme DOXP reductoisomerase (DXR, EC: 1.1.1.267; Takahasi *et al.*, 1998). DXR was shown to require NADPH and divalent cations for activity (Takahasi *et al.*, 1998). Fosmidomycin (Figure 1.5), a low-molecular weight natural product, inhibits DXR (Section 1.2.3). Radiolabelled MEP was prepared (Rohdich *et al.*, 1999) and, following incubation with *E. coli* cell extracts, thin layer chromatography (TLC) and NMR analyses showed that an enzyme activity transferred a cytidine 5'-phosphate moiety to the phosphate group of MEP, to form 4-diphosphocytidyl-2-*C*-methylerythritol. A database search for cytidylyltransferases turned up the N-terminal domain of the *acs1* gene from *Haemophilius influenzae*, the enzyme product of which forms CDP-ribitol (Follens *et al*., 1999). A bioinformatic analysis led to the identification of the gene *ygbP*, encoding 2-*C*-methyl-*D*-erythritol 4-phosphate cytidylyltransferase (IspD, EC: 2.7.7.60). Enzyme assays demonstrated that IspD indeed has MEP-cytidyltransferase activity; and when the cytidylated product (CDP-ME) was incubated with chromoplasts of *Capsicum annuum* it became incorporated into plant isoprenoids (Rohdich *et al.*, 1999). Comparative genomic bioinfomatics identified a gene (*ychB*) that followed the same distribution as other genes involved in the MEP pathway. The protein encoded by *ychB,* known as IspE (EC: 2.7.1.148), was shown by TLC and NMR analyses to transfer a phosphate group from ATP to the 2-

hydroxy group of CDP-ME. The product (CDP-MEP) was incorporated into the plant isoprenoids, phytoene and β-carotene (Lüttgen *et al.*, 2000). Previous work (Rohdich *et al*., 1999) had demonstrated the existence of gene fusions between *ygbP* and another gene, *ygbB*. In 2000, Herz *et al*., sought to demonstrate that the YgbB protein, later re-named IspF, was involved in the MEP pathway. IspF from *E. coli* was recombinantly expressed, and purified protein was incubated with ^{13}C-labelled CDP-MEP *in vitro* and demonstrated by TLC and NMR to catalyze the production of 2*C*-methyl-D-erythritol 2,4-cyclodiphosphate (MEcPP), releasing cytidine 5'-monophosphate (CMP). This reaction was shown to require Mg^{2+} or Mn^{2+} ions. MEcPP was incorporated into carotenoids (Herz *et al.*, 2000). Thus, IspF displays 2*C*-methyl-D-erythritol-2,4-cyclodiphosphate synthase (EC: 4.6.1.12) activity (Section 1.2.5). MEcPP is converted to (*E*)-4-hydroxy-3-methyl-but-2-enyl pyrophosphate (HMBPP) by the iron-sulfur cluster dependent enzyme, HMBPP synthase (IspG, EC: 1.17.7.1), introducing the carbon-carbon double bond characteristic of isoprenoids (Kollas *et al.*, 2002). The last step on the MEP pathway is performed by HMBPP reductase (IspH, EC: 1.17.1.2), another iron-sulfur cluster dependent enzyme, which produces both IPP and DMAPP from HMBPP (Altincicek *et al.*, 2002; Rodhich *et al.*, 2002; Wolff *et al.*, 2003). While many organisms possess IDI enzymes that interconvert IPP and DMAPP, IDI may be dispensable since IspH produces both precursors (Rodhich *et al.*, 2002) and genes encoding IDI are absent from the genomes of several organisms that use the MEP pathway (Cunningham *et al.*, 2000). In *E. coli* for example, the gene encoding the sole IDI enzyme is inessential (Hahn *et al.*, 1999). Structural studies have provided insight into the mechanisms of enzymes on the MEP pathway (Hunter, 2007; Zhao *et al.*, 2013).

The MEP pathway of isoprenoid-precursor biosynthesis is widely distributed in various bacteria, algae, and in the chloroplasts of higher plants. Several apicomplexan

parasites, including *Plasmodium* species responsible for malaria, contain the MEP pathway in an organelle known as an apicoplast (Section 1.2.4). Conversely, the MEP pathway is replaced with the classical mevalonate pathway in animals, fungi, archaea and the cytoplasm of plants (Rohdich *et al.*, 2001). Thus, the MEP pathway contains potential drug-target enzymes whose inhibition may provide broad-spectrum antimicrobial activity, and this is particularly attractive since this pathway is absent in humans.

1.2.3 Fosmidomycin, a known drug targeting the MEP pathway

Fosmidomycin, a phosphonic acid bearing an hydroxamate and an aldehyde (Figure 1.5), was first isolated as a natural product from *Streptomyces lavendulae* in 1980 by researchers at Fujisawa Pharamceutical Co. Ltd., Osaka, (Okuhara *et al.*, 1980a). In 1989 it was shown that fosmidomycin exerts its anti-bacterial effects by inhibiting isoprenoid biosynthesis (Shigi, 1989). Fosmidomycin inhibited the production of menaquinones and ubiquinones in growing *E. coli* and inhibited the production of carotenoids and menaquinones in *Micrococcus luteus* (Shigi, 1989). It was further noticed that the bacteria that were susceptible to fosmidomycin were unable to incorporate mevalonate, whereas those that could incorporate mevalonate were not susceptible, however the existence of the MEP pathway, or non-mevalonate pathway, was not known at the time.

Both fosmidomycin and a methylated derivative, FR-900098 (Okuhara *et al.*, 1980b), were shown to potently inhibit recombinant DXR from three different strains of *P. falciparum*, HB3, A2 and Dd2; with IC_{50} values ranging from 90 - 370 nM (Jomaa *et al.*, 1999). Mice infected with the closely-related *P. vinckei* species were cured following treatment with either compound. Fosmidomycin inhibited the growth of blood-stage *P. falciparum* with an EC_{50} value of 0.98 μM (Yeh & DeRisi, 2011). High

resolution crystal structures of DXR from *P. falciparum* in complex with fosmidomycin (1.9 Å), FR-900098 (1.9 Å) and inhibitor-free (2.2 Å) were solved by Umeda *et al.* in 2011. Clear electron density was observed for fosmidomycin and FR-900098 in the active site. The hydroxamate group of the inhibitors binds to the active site magnesium cation, with the oxygen atoms in *cis*-configuration.

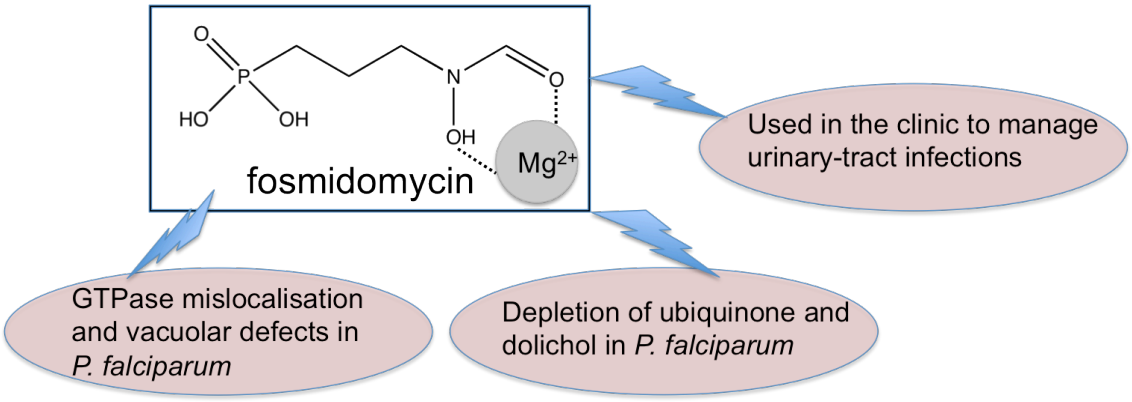

Figure 1.5 Chemical structure of fosmidomycin. **Fosmidomycin, a phosphonic acid bearing an hydroxamate and aldehyde group, is a natural product with anti-microbial properties. Fosmidomycin inhibits DXR on the MEP pathway, binding to the active site Mg^{2+}. Fosmidomycin has been used clinically to manage urinary tract infections; and is now under investigation as a potential anti-malarial drug. (Cassera *et al.*, 2004; Howe *et al.*, 2012; Lell *et al.* 2003; Umeda *et al.*, 2011)**

An open-label, uncontrolled trial evaluated fosmidomycin for the treatment of acute uncomplicated *P. falciparum* malaria in subjects aged 18-50 in Gabon and Thailand (Lell *et al.*, 2003). The drug was shown to be a safe and effective anti-malarial, exhibiting rapid parasite and fever clearance - within 44 hours. However, a high number of recrudescent infections were observed following treatment cessation, particularly in Thailand and the authors of the study cautioned against its use as a monotherapy. A follow-up study evaluated the efficacy of a combination treatment of fosmidomycin with clindamycin in children aged 7-14 in Gabon (Borrmann *et al.*, 2004). In contrast to the previous trial, combination therapy with clindamycin resulted in complete parasite elimination and absence of clinical signs of infection, provided treatment lasted more than three days on a 12 hour dosing schedule. Fosmidomycin is

thus an example of an effective anti-malarial and its use in clinical trials chemically validates the MEP pathway as a source of targets for drug discovery (Rohdich *et al.* 2005; Hunter, 2011).

1.2.4 Targeting the MEP pathway in *P. falciparum*

P. falciparum contains an organelle known as an apicoplast which resembles a cyanobacterium and is thought to have arisen from an ancestral secondary endosymbiosis with an alga (Ralph *et al.*, 2004). In 1999, Jomaa *et al*., reported that DXR localises to the apicoplast in *P. falciparum*. Indeed, all MEP pathway enzymes in *P. falciparum* bear an apicoplast localisation sequence (Ralph *et al.*, 2004) and chemical disruption of apicoplast replication results in parasites that are IPP auxotrophs (Yeh & DeRisi, 2011). The presence of an active MEP pathway in all intra-erythrocytic stages has been experimentally confirmed, and treatment with fosmidomycin depletes intermediates downstream of DXR as well as ubiquinone and dolichol compounds (Cassera *et al.*, 2004). Treatment with fosmidomycin also leads to a loss of protein prenylation, causing various small GTPases such as Rab5 to mislocalise which results in defects in both vesicular trafficking and the integrity of vacuolar membranes (Howe *et al.*, 2013). In 2012 No *et al.* published an example of successful targeting of an isoprenoid-utilising protein downstream of the MEP pathway. A library of bisphosphonates was screened against the intraerythrocytic form of *P. falciparum* and lipophilic derivatives of the drugs risedronate and zoledronate were identified as leads. X-ray crystal structures of the likely target, geranylgeranyl diphosphate synthase (EC: 2.5.1.29), were determined from the *P. vivax* orthologue in complex with these compounds. Such inhibitors suppressed parasitaemia in a murine model infected with *P. chabaudi* (No *et al.*, 2012). *P. falciparum* also synthesises carotenoids that have a likely role in anti-oxidant defense, and inhibition of synthesis by norflurazon suppresses parasite growth in a dose-dependent manner (Tonhosolo *et al.*, 2009). The prospect of developing novel antimalarial agents that exploit the MEP pathway dependence of *P.*

falciparum, following the example of fosmidomycin, is particularly attractive (Hunter, 2011; van der Meer & Hirsch, 2012).

1.2.5 IspF – Known structures, catalytic mechanism and essentiality

The structure of IspF is known from twelve different species in addition to the two disclosed in this thesis, and thus the overall fold is well established. IspF forms a homotrimer and active sites are located at interfaces between adjacent subunits. Subunits form a fluted β-prism consisting of four β-stands that are oriented approximately parallel to the three-fold axis of symmetry that runs through the center of the molecule; flanked by three α-helices (Kemp *et al.*, 2002). A hydrophobic cavity is present along the axis in most species, but is absent in the IspF from *Thermus thermophilus* (*Tt*IspF, Kishida *et al.*, 2003). The genes encoding IspF and IspD are fused in numerous organisms, an unusual arrangement since these enzymes catalyse non-consecutive steps of the MEP pathway; IspE must first phosphorylate the product of IspD to form the substrate for IspF. Bifunctional IspD-IspF from *Campylobacter jejuni* has been biochemically characterised (Gabrielsen *et al.*, 2004a) and the crystal structure has been determined (Gabrielsen *et al.*, 2004b). The overall structure of IspF is unchanged in the fusion protein. Although IspE associates with the IspD-IspF protein in solution (Gabrielsen *et al.*, 2004b), no rate-enhancement is observed upon complexation (Lherbet *et al.*, 2006), and thus the physiological significance of such an association remains to be clarified.

In 2002, structural studies were published on IspF from *E. coli* (*Ec*IspF) by three groups (Kemp *et al.*, Richard *et al.,* Steinbacher *et al.*, 2002) that provided insight into the catalytic mechanism (Table 1.1). A metal, identified as Zn^{2+} (Kemp *et al.*, 2002), binds at the active site coordinated by the side chains of two histidines and an aspartate. IspF catalyses the production of MEcPP by facilitating an intramolecular nucleophilic

attack on the substrate, CDP-MEP, bridging β-phosphate by the 2-phosphate (Figure 1.6). Zn^{2+} aligns and polarises the β-phosphate for nucleophilic attack and is indispensible for catalysis. The cytidine portion of the substrate is held in a rigid binding pocket, whereas the predominantly apolar binding pocket for the methylerythritol phosphate portion is more flexible.

Table 1.1 IspF proteins of known structure

Organism name	Representative Protein Data Bank (PDB) code
Arabidopsis thaliana	**2PMP (Calisto *et al*., 2007)**
***Burkholderia cenocepacia* (this thesis)**	**4C8G (O'Rourke *et al*., 2013; to be published)**
Burkholderia pseudomallei	**3IEQ (Begley *et al*., 2011)**
***Campylobacter jejuni* (bifunctional IspDF)**	**1W55 (Gabrielsen *et al*., 2004b)**
Escherichia coli	**1U3L (Steinbacher *et al*., 2002)**
Francisella tularensis	**3RE2 (No associated publication)**
Haemophilus influenzae	**1JN1 (Lehmann *et al*., 2002)**
Mycobacterium smegmatis	**2UZH (Buetow *et al*., 2007)**
***Plasmodium falciparum* (this thesis)**	**4C81 (O'Rourke *et al*., 2013; to be published)**
Plasmodium vivax	**3B6N (No associated publication)**
Salmonella enterica serovar Typhimurium	**3GHZ (No associated publication)**
Shewanella oneidensis	**1T0A (Ni *et al*., 2004)**
Thermus thermophilus	**1IV2 (Kishida *et al*., 2003)**
Yersinia pestis	**3FPI (No associated publication)**

In *Ec*IspF structures Mg^{2+}, positioned by Glu135, fixes the α- and β-phosphate groups of the CDP moiety (Kemp *et al.*, 2002; Steinbacher *et al.*, 2002). Mg^{2+} is essential for catalysis (Herz *et al.*, 2000) and is thought to stabilise the negative charge on the α-phosphate of the CMP leaving group and may help stabilise the transition state complex. The α-phosphate is further positioned by Thr133. Residues in proximity to

the Zn^{2+} site conserved in sequence and structure are expected to contribute to catalysis; these include His34 and Ser35 which form a phosphate binding site for the attacking 2-phosphate group (Steinbacher *et al.*, 2002). Additionally, the His34 side chain positions a loop of ten residues, Pro62 - Ala71, that surround the methylerythritol phosphate moiety. The 2*C* methyl group makes a favourable hydrophobic contact with highly conserved Ile57 in a structure of *Ec*IspF in complex with CDP-ME, which is a substrate analogue lacking the attacking phosphate. Orientation of the methyl-D-erythritol moiety is achieved by hydrogen bonds from the 3-hydroxy group to main chain carbonyl groups of Phe61 and Ile57 and the product, MEcPP, binds to His34, Ser35, Ile57, Phe61 and Asp63 (Steinbacher *et al.*, 2002). In *Tt*IspF a lysine side chain, Lys132, binds to the bridging β-phosphate further polarising the substrate, however this interaction is not conserved in *Ec*IspF, but is replaced by a water positioned by Thr132. Some of the interactions described here are presented in the corresponding results section (Chapter 3, Figure 3.3 and 3.4).

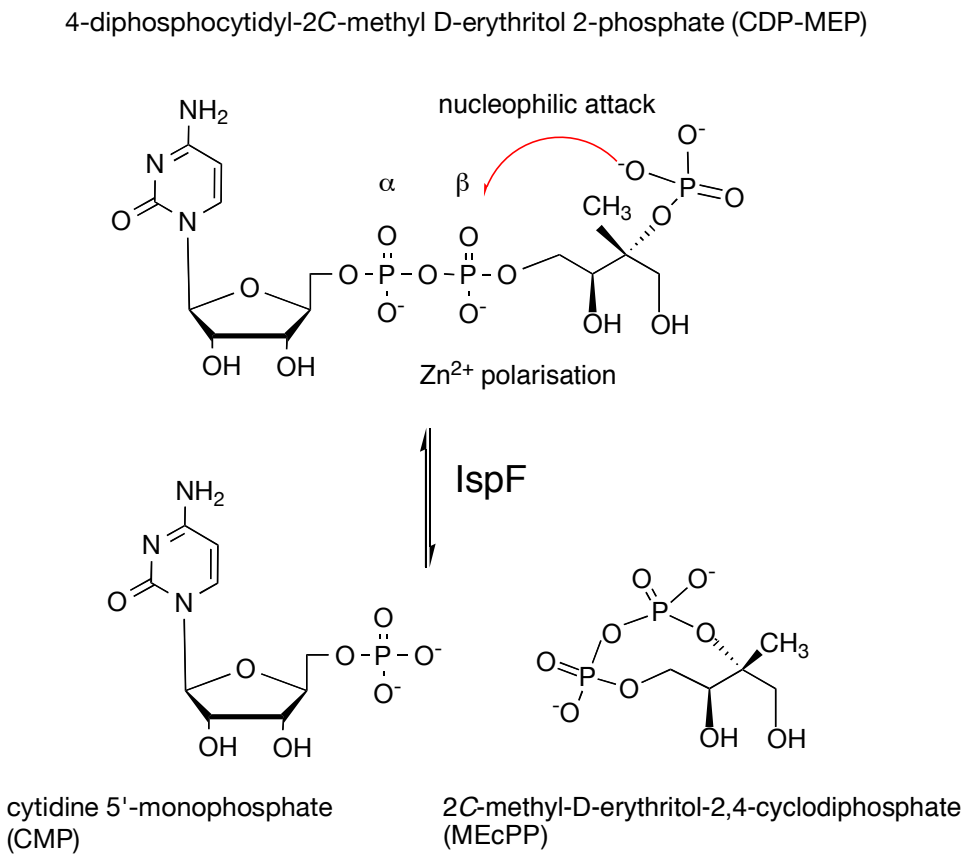

Figure 1.6 Reaction catalysed by IspF. IspF catalyses the production of 2*C*-methyl-D-erythritol-2,4-cyclodiphosphate (MEcPP) from 4-diphosphocytidyl-2*C*-methyl-D-erythritol-2-phosphate (CDP-MEP), with the loss of cytidine 5'-monophosphate (CMP). Curly-arrows indicate the flow of electrons. This reaction is an example of electrophilic catlysis, with Zn^{2+} acting as a Lewis acid.

The essentiality of IspF for growth and survival of *E. coli* has been established (Campbell & Brown, 2002; Campos *et al.*, 2001; Freiberg *et al.*, 2001; Sauret-Güeto *et al.*, 2003). Deletion of the *ispF* gene, formerly referred to as *ygbB*, does not support growth and is fatal (Freiberg *et al.*, 2001). When IspF expression was impaired by deletion of *ispF* and replacement with a copy at a distant and conditionally expressed locus, thereby depleting isoprenoid-precursors, *E. coli* exhibited an aberrant filamentous phenotype indicative of disrupted peptidoglycan synthesis (Section 1.2.1). Additionally, heightened sensitivity to the cidal effect of fosmidomycin and various inhibitors of cell wall biosynthesis was observed (Campbell & Brown, 2002). The essentiality of IspF has been demonstrated in other organisms including, *Bacillus subtilis* (Campbell & Brown, 2002) and *Mycobacterium tuberculosis* (Buetow *et al.*, 2007).

1.3.1 *para*-Aminobenzoic acid biosynthesis

para-Aminobenzoic acid (also known as 4-aminobenzoic acid, PABA) is synthesised by many microogranisms and plants since it is required to form folate (Figure 1.7). Folate, also known as vitamin B_9, is a generic name for a family of structurally related compounds; essential cofactors in several enzymes. Folates typically function as single carbon unit donors in catalysed reactions (Reviewed, for example, by Benkovic, 1980; Gisondi *et al.*, 2007; Lucock, 2000). Folate is required for the formation of thymidylate and methionine and as such is essential for nucleic acid synthesis, cell growth and division. Unlike plants and most microorganisms, humans do not synthesise their own folate and so it must be obtained in the diet. Folate deficiency can have several injurious effects including certain forms of anaemia and, during pregnancy, it is associated with a range of complications and adverse outcomes including a higher risk of neural tube defects in children (Kirke *et al.*, 1993; Lucock, 2000; Varela-Moreiras *et al.*, 2009).

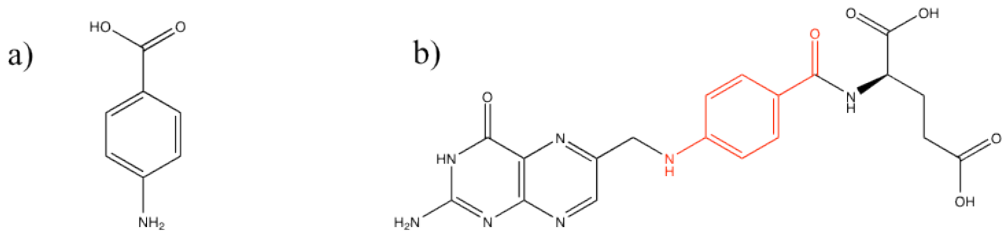

Figure 1.7 Chemical structure of a) *para*-aminobenzoic acid (PABA). b) folic acid (mono-L-glutamyl), also known as vitamin B_9. The *para*-aminobenzoic acid derived moiety, highlighted in red, links a pterin moiety to L-glutamic acid.

The enzyme dihydropteroate synthase (DHPS, EC: 2.5.1.15) links PABA to a GTP-derived pterin moiety, 7,8-dihydro-6-hydroxymethylpterin-pyrophosphate. The product of this reaction, 7,8-dihydropteroate, is subsequently glutamylated and reduced

to form the intracellular pool of available folate (Lucock, 2000; Richey and Brown, 1969). Thus, a PABA-derived moiety has a structural role in the folate molecule (Figure 1.7). In *E. coli* and many other bacteria, PABA is synthesised in two steps starting from chorismate (Nichols *et al.*, 1989). The first step produces 4-amino-4-deoxychorismate (Anderson *et al.*, 1991) by transferring ammonia, derived from glutamine, to chorismate. This reaction is performed by aminodeoxychorismate synthase (EC: 2.6.1.85), a heterodimer of proteins encoded by the *pabA* and *pabB* genes (Parsons *et al.*, 2002). 4-amino-4-deoxychorismate is then converted to PABA with the loss of pyruvic acid (Figure 1.10). 4-amino-4-deoxychorismate lyase (PabC, EC: 4.1.3.38), a pyridoxyl 5′-phosphate (PLP) - dependent enzyme (Figure 1.8), catalyzes this second step (Green & Nichols, 1991; Nichols *et al.*, 1989). In the Gram-positive bacterium *Bacillus subtilis* a third chemical step is required for PABA biosynthesis. Chorismate is first converted to 2-amino-2-deoxyisochorismate before production of 4-amino-4-deoxychorismate, which is then converted to PABA and pyruvate by PabC (Schadt *et al.*, 2009).

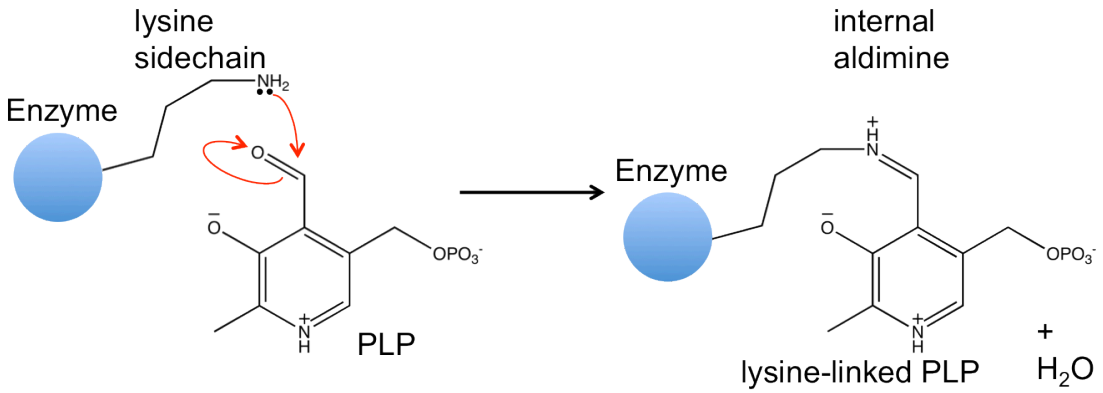

Figure 1.8 PLP forms a covalent link with the amino group of lysine sidechains.
The ε-amino group of a lysine sidechain, typically in the enzyme active-site acts as a nucleophile, attacking PLP to form an enzyme-PLP adduct (Schiff base); with water as a leaving group. This lysine-linked PLP is referred to as the internal aldimine form. Curly arrows indicate the flow of electrons.

1.3.2 Anti-folate drug discovery and sulphonamides as antimicrobial agents

Since PABA is required for folate production and by extension a range of physiological processes in many microorganisms, PABA biosynthesis presents itself as a potential target for antimicrobial drug development. Targeting PABA biosynthesis directly has been chemically validated as a viable approach to identifying antimicrobial compounds, as exemplified by the natural products *atrop*-abyssomicin C (Keller *et al.*, 2007; Riedlinger *et al.*, 2004) and rubreserine (Camara *et al.*, 2012) that both inhibit aminodeoxychorismate synthase and show potent activity. In 2004, Bulloch *et al.* demonstrated the mechanism though which the known anti-bacterial agent (6*S*)-6-fluoroshikimate targets PABA biosynthesis; it is converted to 2-fluorochorismate *in vivo* by chorismate synthase (EC: 4.2.3.5), which proceeds to irreversibly inhibit aminodeoxychorismate synthase.

Several anti-infective medicines in both current clinical use and historically have achieved their salutary effect through inhibition of folate metabolism in microbes. A large number of sulphonamide drugs were discovered during the 1930s, starting with prontosil - shown to be a pro-drug of the active agent, sulfanilamide (Domagk, 1947). Sulphonamide antimicrobials inhibit DHPS, thereby depleting folate levels (Brown, 1962; Woods, 1940). This is due to their structural similarity to the PABA molecule (Figure 1.9). Prior to the introduction of penicillin, 'sulfa drugs' and their derivatives were highly sucessful; for example the sulfone drug dapsone was widely used to treat leprosy (Barr, 2010; Shepard, 1969).

Dihydrofolate reductase (DHFR, EC: 1.5.1.3) is another enzyme of folate metabolism that has been targeted for therapeutic benefit. Several DHFR inhibitors, such as trimethoprim and pyrimethamine are used clinically to manage a range of conditions including urinary tract infections, bacterial pneumonia and protozoal

infections. Indeed, DHFR inhibitors are often given in combination with sulphonamide drugs for synergistic effect (Bushby & Hitchings, 1968; Masters *et al.*, 2003); well-established drug combinations include co-trimoxazole (a combination of trimethoprim with sulfamethoxazole) and pyrimethamine with sulfadiazine or sulfadoxine (World Health Organization, List of Essential Medicines, 2011).

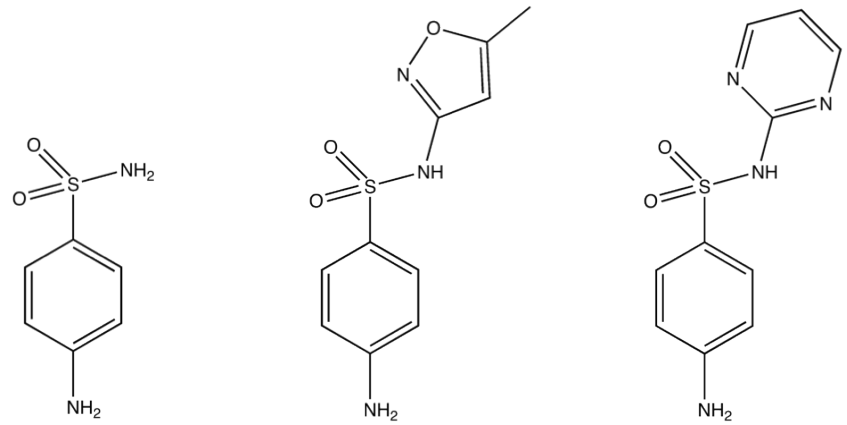

Figure 1.9 Chemical structures of sulphonamide antimicrobials that inhibit folate biosynthesis.

Structural studies of the enzymes involved in PABA and folate metabolism can provide significant insight into the mechanism of the reaction catalysed (Nakai *et al.*, 2000, Parsons *et al.*, 2002, Schnell *et al.*, 2004), the molecular nature of drug-resistance (Vanichtanankul *et al.*, 2011; Yun *et al.*, 2012) and can guide early-stage drug discovery initiatives (Chhabra *et al.*, 2012; Eadsforth *et al.*, 2012; Morgan *et al*., 2011).

1.3.3 PabC

4-Amino-4-deoxychorismate lyase, encoded by the *pabC* gene, catalyzes the formation of PABA from 4-amino-4-deoxychorismate (Figure1.10) as part of the biosynthetic route to folate (Green & Nichols, 1991; Ye *et al.*, 1990).

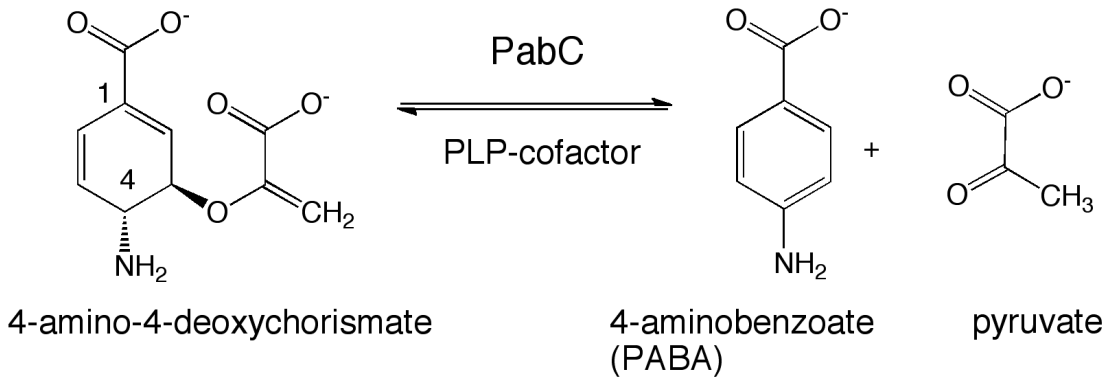

Figure 1.10 PabC catalyzes the conversion of 4-amino-4-deoxychorismate to PABA and pyruvate.

Inhibitors of microbial PabC would reduce PABA levels and so deplete the supply of folic acid available to the microorganism. Provided that the microbe cannot obtain sufficient PABA or folate from the cellular environment or by other means these cells would be expected to cease growth and die. This is what is observed in *pabC* knockouts in *E. coli* (Green *et al.*, 1992), *Pseudomonas aeruginosa* (Hoang *et al.*, 1998) and *Acinetobacter baylyi* (de Berardinis *et al.*, 2008). Combining novel PabC inhibitors with sulphonamides or with other anti-folates such as the dihydrofolate reductase inhibitor trimethoprim, could produce a synergistic antimicrobial effect. New inhibitors of PabC would allow such a hypothesis to be tested.

X-ray crystal structures of PabC from *E. coli* (PDB code: 1ETO; Nakai *et al.*, 2000), *Thermus thermophilus* (2ZGI; Padmanabhan *et al.*, 2009) and *Legionella pneumophila* (3LUL) have been determined. PabC displays a similar overall fold to branched-chain amino acid transferases and D-amino acid transferases (Eliot & Kirsch, 2004; Jhee *et al.*, 2000; Nakai *et al.*, 2000). These aminotransferases have been investigated to identify potential inhibitors in support of research for treatments of neurodegenerative disease (Castell *et al.*, 2010; Hu *et al.*, 2006; Lepore *et al.*, 2010; Soper & Manning, 1981). Moreover, since PLP-dependent enzymes provide opportunities for the design of mechanism-based suicide inhibitors (Eliot & Kirsch, 2004) this enzyme family appears an attractive one from the perspective of structure and mechanism-based drug discovery. For example, the anti-trypanosomal medicine

eflornithine (α-difluoromethylornithine) used in the treatment of African sleeping sickness is a suicide inhibitor of the PLP-dependant enzyme ornithine decarboxylase (EC: 4.1.1.17), forming an adduct with the active site cofactor (Grishin *et al.*, 1999).

The absence of the PabC enzyme in humans and its essentiality in various microbes suggests that its inhibition offers the possibility of new therapies targeting a range of microbial infections and structural studies provide useful data to assess the potential of this protein for such early stage drug discovery (Hunter, 2009; O'Rourke *et al.*, 2011).

1.4 Biophysical screening techniques

Bio-layer interferometry (BLI) is an optical technique that can be used to perform label-free fragment screening against an immobilised protein target. The sensors used in the assay are fiber optic tips with a streptavidin-coated protein binding surface and protein target can be biotinylated to facilitate binding to the sensor (Figure 1.11). Following protein loading and capture by the streptavidin surface, the sensors are immersed in wells containing analytes, typically chemical fragments and control compounds, and a binding response is recorded in real-time. A sensor records the interference pattern produced by white light reflected from two layers in the sensor, an internal reference layer and the protein binding surface, or 'bio-layer'. Binding of ligand to the bio-layer increases the optical thickness and shifts the interference pattern, resulting in an apparent shift in wavelength of the reflected light (Wartchow *et al.*, 2011).

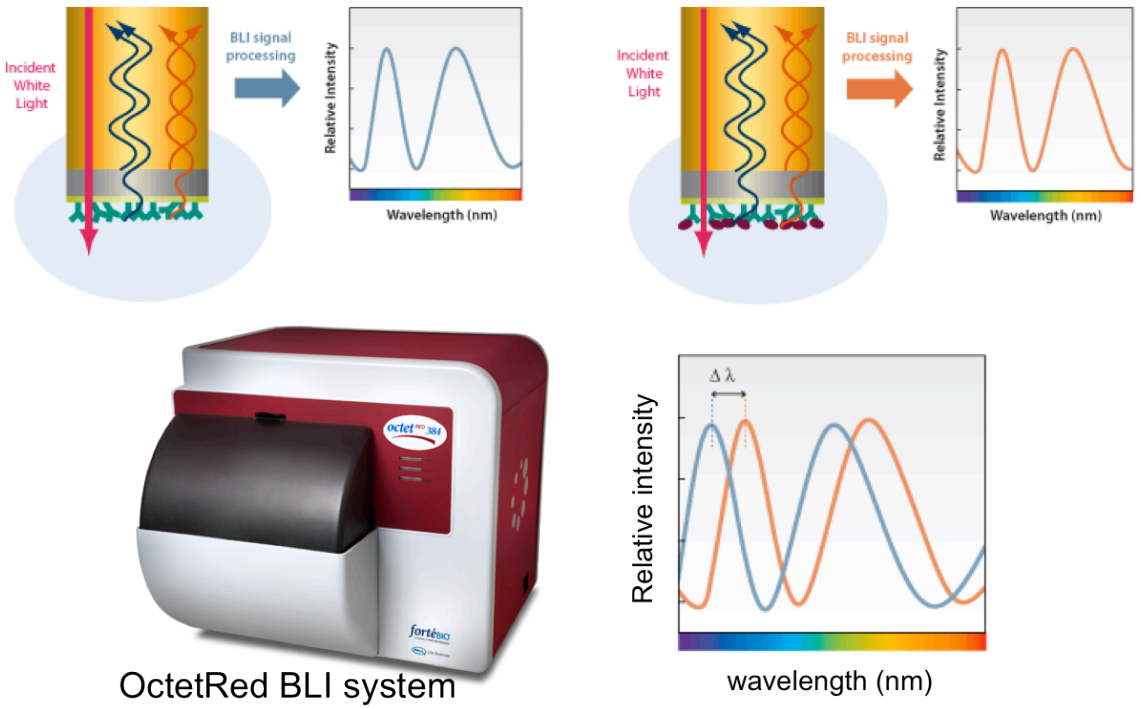

Figure 1.11 Principles of BLI. A protein target is immobilised on the biolayer and subjected to incident white light. An optical interference pattern is recorded from light returning from the biolayer and compared to that returning from an internal reference layer. An increase in mass at the biolayer, due to the binding of a chemical fragment for example, will increase the optical thickness, shifting the interference pattern, which results in an apparent shift in wavelength (Δλ) of the reflected light (Wartchow *et al*., 2011). The OctetRed BLI system is shown inset.
Images taken from the ForteBio website: http://www.fortebio.com/bli_technology.html

In differential scanning fluorimetry (DSF), protein unfolding in response to increasing temperature can be measured by monitoring the fluorescence signal of a dye with an affinity for hydrophobic residues (Pantoliano *et al.*, 2001). The dye will be excluded from the hydrophobic interior of the protein and will not fluoresce until the protein exposes hydrophobic residues as it unfolds. The assay is typically performed using an RT-PCR machine to incrementally raise the temperature. Melt curves can be fit to the fluorescence data and the temperature corresponding to the transition mid-point (T_m) during unfolding can be calculated. The stabilisation of a protein by ligand or buffer can be inferred from a positive shift in T_m (Ericsson *et al.*, 2006; Niesen *et al.*, 2007). Screening of buffers using differential scanning fluorimetery can also identify conditions to pursue or avoid during crystallisation (Ericsson *et al.*, 2006; Reinhard *et al.*, 2013).

Both of these methods were used in these studies; buffer screening with differential scanning fluorimetry (Section 2.1.4) and screening of fragment libraries with BLI (Section 2.1.5).

1.5 Aims - Part one

This study sought to determine the crystal structures of potential drug targets from human pathogens to inform early stage drug discovery. Studies of recombinant IspF, an essential enzyme on the MEP pathway; from *B. cenocepacia* and *P. falciparum* were pursued. Fragment screening was carried out to identify novel ligands. The suitability of the enzyme from these organisms as a platform for ligand co-crystallisation studies was assessed. Additionally, the structure of PabC from *P. aeruginosa*, an essential enzyme required for the synthesis of PABA, was determined to provide insight into catalytic mechanism and to facilitate studies of this enzyme in antimicrobial drug discovery.

CHAPTER 2

MATERIALS AND METHODS

Materials and methods

2.1.1 Reagents, bacterial strains, growth media and equipment

All chemical reagents used were of the highest possible purity available and were sourced from VWR and Sigma-Aldrich unless otherwise stated. *E. coli* strains were sourced from Life Technologies, Promega and Stratagene. PCR amplifications of DNA were performed using a programmable thermal cycler (GeneAmp 2700, Applied Biosystems). Oligonucleotide primers for PCR were sourced from Life Technologies. DNA ligase and restriction enzymes were sourced from Fermentas, New England Biolabs and Promega. All sodium dodecyl sulfate-polyacrylamide gel electrophoresis (SDS-PAGE) was performed using NuPAGE Bis-Tris pre-cast gels sourced from Life Technologies.

Plasmid preparations and DNA gel-extractions were performed using Qiagen kits (QIAprep spin miniprep, QIAquick gel extraction). DNA electrophoresis was performed in gels prepared to contain 10% w/v agarose (VWR) and 0.0002% w/v ethidium bromide (10 mg mL^{-1} stock, Electran, VWR BDH Prolabo). DNA sequencing was performed by DNA Sequencing & Services (University of Dundee) using Applied Biosystems Big-Dye Ver 3.1 chemistry on an Applied Biosystems model 3730 automated capillary DNA sequencer. All LB bacterial growth media used in these studies were prepared and autoclaved by the Media Services staff (University of Dundee). Shake-flask bacterial culture was performed using either an incubation shaker (Multitron, Infors-HT) or a room temperature orbital shaker (KS501 Digital, IKA). Both electrospray ionisation mass spectrometry (ESI-MS), and matrix-assisted laser desorption/ionisation - time-of-flight mass spectrometry (MALDI-TOF MS) were performed by the Proteomics and Mass Spectrometry Facility (FingerPrints, University of Dundee). In particular, MALDI-TOF MS analyses were performed by Samantha Kosto on an AB Sciex Voyager DE-STR system using a sinapinic acid matrix. Samples

for MALDI-TOF MS were diluted in de-ionised water and loaded onto the matrix in a concentration range between 2-5 pmol.

Table 2.1 List of key details for the proteins reported in this thesis (Part 1)

	*Bc*IspF	*Pf*IspF	*Pa*PabC
UniProt code	**B4EC22**	**P62368**	**Q9HZN6**
Enzyme nomenclature	**2*C*-methyl-D-erythritol 2,4-cyclodiphosphate synthase**	**2*C*-methyl-D-erythritol 2,4-cyclodiphosphate synthase**	**4-amino-4-deoxychorismate lyase**
E.C. number	**4.6.1.12**	**4.6.1.12**	**4.1.3.38**
Source organism	***Burkholderia cenocepacia*, strain J2315**	***Plasmodium falciparum*, isolate 3D7**	***Pseudomonas aeruginosa*, strain PAO1**
Number of amino acids	**182**	**184**	**292**
Molecular mass (Da)	**19328.8**	**20545.5**	**32291.9**
Theoretical isoelectric point	**6.4**	**9.0**	**6.0**
Theoretical extinction coefficent (ε)	**5960 (Bradford assay was used to estimate concentration)**	**11920**	**33710**
PDB codes	**4C8G (CMP complex), 4C8E (2 x CMP complex), 4C8I (citrate complex)**	**4C81 (CDP complex), 4C82 (*holo*-structure)**	**2Y4R (PLP complex)**

2.1.2 Gene cloning and plasmid preparation

The genes encoding the proteins described in this thesis were amplified from genomic DNA by PCR (Table 2.2), with the exception of *Ec*IspF which was provided by Dr. Thomas Eadsforth and *Pf*IspF which was purchased as a synthetic gene (below). PCR products were blunt-end ligated into a TOPO cloning vector (Life Technologies), then ligated into an expression vector, pET15b-TEV, that encoded the protein-of-interest bearing an N-terminal hexahistidine purification tag (His-tag) linked *via* a tobacco-etch virus (TEV) protease cleavage site.

Table 2.2 Oligonucleotide primers for PCR

*Bc*IspF Forward Reverse	 5'- CAT ATG GAC TTC AGA ATC GGA CAA GG -3' 5'- GGA CCT CAG CCG CCC TGC TTC ACC -3'	 Strain J2315
*Pa*PabC Forward Reverse	 5'- CAT ATG CTG GAC TGG GTC GAC -3' 5'- GGA TCC TCA GAA ATC CAG GTC G -3'	 Strain PAO1

The gene encoding IspF from *P. falciparum* isolate 3D7, GenBank accession number: XP_001349603, was synthesised (Genscript, Boston) with codons optimised for recombinant expression in *E. coli*. *NdeI* and *BamHI* restriction sites were included at the 5' and 3' ends of the gene. The sequence encoding residues 1-59, a predicted apicoplast targeting sequence, was excluded and the codon for Cys60 was replaced with one for serine. The synthetic gene was provided by Dr. Scott Cameron in a pUC57 shuttle vector and was subcloned into the pET15b-TEV vector.

The genes encoding *Bc*IspF and *Ec*IspF were also ligated into a pET15b-TEV vector that had been further modified to append an N-terminal biotin acceptor peptide to the protein in addition to the protease-cleavable His-tag. These vectors were used in the production of biotinylated IspF proteins for fragment screening.

2.1.3 Protein production

Recombinant production was performed in *E. coli* BL-21 (DE3) Gold for all proteins. Strains were transformed with expression plasmids by heat-shock. Transformants were selected following outgrowth at 37 °C, on LB agar plates supplemented with the antibiotics chloramphenicol and/or carbenicillin. 1 L shake-flask cultures were grown in LB at 37 °C and monitored by UV spectrophotometry (BioPhotometer, Eppendorf). When the optical density at 600 nm (OD_{600}) reached 0.6, expression was induced with

0.1 mM IPTG - with the exception of *Ec*IspF, which was induced at an OD_{600} of 1.0. Culturing was continued for a further 16 hours at 18 °C, or 22 °C in the case of *Bc*IspF, before cells were harvested.

2.1.4 Differential scanning fluorimetry and buffer screening

All assays reported here were performed in 96-well plates (Thermo-Fast, Thermo Scientific) on a Stratagene-Mx30005P RT-PCR machine. SYPRO Orange (Life Technologies) was used as the fluorescent dye. Buffer screening was carried out for all proteins reported here; with the exception of the IspF samples, which were found to give either irreproducible (*Pf*IspF) or uninterpretable (*Bc*IspF) responses during assessment.

2.1.5 Fragment screening by bio-layer interferometry

A fragment screen using the Drug Discovery Unit (DDU, University of Dundee) fragment library was performed by BLI (Octet Red system, ForteBio) on two enzymes; *Bc*IspF and *Ec*IspF. *Bc*IspF was screened first against the original fragment set (652 commercially available compounds). *Ec*IspF was screened later against a revised version of the fragment library that had been changed to remove non-specific binders and to add novel fragments with different scaffolds (Table 2.3; Dr. David Robinson, personal communication).

Table 2.3 BLI fragment screen assay conditions

Biotinylated-*Bc*IspF	**Original DDU fragment library** (652 fragments at 200 μM in 100% DMSO)	Buffer: 20 mM NaCl, 100 μM $MgCl_2$, 100 μg $ZnCl_2$, 20 mM Tris-HCl, pH 7.5
Biotinylated-*Ec*IspF	**Revised DDU fragment library** (658 fragments at 200 μM in 100% DMSO)	Buffer: 50 mM NaCl, 100 μM $MgCl_2$, 100 μM $ZnCl_2$, 50 mM Tris-HCl, pH 7.7

Both *Bc*IspF and *Ec*IspF were loaded onto biosensors (SuperStreptavidin, ForteBio) at 1 μM and screened at 25 °C, alongside double-referenced biosensors (one set referenced with assay buffer, and one set with blocked streptavidin). Known IspF ligands, CMP and CDP, were used as positive controls. Fragment screens were conducted after immobilising target proteins for ten minutes, blocking unoccupied binding sites with the biotin analogue biocytin at 10 μg mL^{-1} for one minute, followed by surface washing and equilibration of the biosensors in assay buffer for five minutes. Coefficient-of-determination (R^2) values were calculated for sensorgram fitting curves and used as a measure of reliablity throughout the screens.

2.1.6 Screening for crystallisation conditions

An automated liquid-handling system (Phoenix, Art Robbins) was used in screening for crystallisation conditions in combination with commercially available screens (JCSG-*plus*, Molecular Dimensions; $AmSO_4$ suite, PEGs suite, Classics suite, Qiagen). All samples were filtered through a 0.1 μm PVDF filter (Ultrafree, Millipore) immediately prior to screening. The protein samples were dispensed (100 nL drops) into 96-well sitting-drop plates (MRC-2, Molecular Dimensions). Reservoirs were dispensed in a 1:1 or 1:2 ratio with the protein sample (100 nL protein + 100 nL reservoir, or, 100 nL

protein + 200 nL reservoir). Plates were then sealed and stored at room temperature in a benchtop protein crystal drop imager (Minstrel DT system, Rigaku).

Crystallisation plates were inspected at regular intervals for up to one month. Productive conditions identified in initial screens were optimised by scaling-up to larger volumes (1-2 µl) in hanging-drop vapour diffusion trays (24-well Linbro plates, Hampton Research). The crystallisation landscape around identified conditions was investigated by varying the concentrations of various reservoir components and/or the protein concentration, pH and temperature (20 °C or 4 °C).

2.2.1 Purification of *Pf*IspF

Cells were harvested by centrifugation at 3000 *g* for 30 minutes at 18 °C and re-suspended in 100 mM KCl, 100 mM L-arginine, 50 mM CHES, pH 9.5 (buffer A). DNAseI and a protease inhibitor tablet (EDTA-free, Roche) were added prior to cell lysis by passage through a French pressure cell. The cell lysate was clarified by ultracentrifugation at 40000 *g* for 30 minutes at 18 °C (Avanti centrifuge, Beckmann) and supernatant was syringe-filtered through a pre-filter followed by a 0.2 µm filter (Sartorius).

*Pf*IspF precipitates during purification at temperatures below 18 °C (Dr. Kalinowska-Tłuścik, personal communication). Therefore all procedures described were performed at room temperature unless otherwise stated. The cell lysate was loaded onto a nickel ion affinity chromatography column (5 mL HisTrap HP, GE Healthcare) with the assistance of an FPLC system (Äkta Explorer, GE Healthcare). A linear concentration gradient of imidazole, from 0 - 1M, was applied to elute *Pf*IspF (which eluted at 200 mM imidazole). Protein sample was then dialysed against fresh buffer A. The purification tag (His-tag) was cleaved with His-tagged TEV protease at 20 °C for 16 hours. The protease-treated sample was re-applied to a nickel ion affinity

chromatography column, which eluted the cleaved protein while removing the TEV protease and remaining uncleaved *Pf*IspF. Fractions were analysed by SDS-PAGE and those containing *Pf*IspF were pooled. The protein was further purified on a size-exclusion chromatography column (Superdex 200 26/60, GE Healthcare) equilibrated with buffer A. This column had previously been calibrated (by Sharon Shepherd) with molecular weight standards; thyroglobulin (670 kDa), γ-globulin (158 kDa), ovalbumin (44 kDa), myoglobin (17 kDa), and vitamin B_{12} (1.35 kDa); (Bio-Rad). The high level of *Pf*IspF purity was confirmed by SDS-PAGE and MALDI-TOF MS. The sample was concentrated to 6 mg mL^{-1} using a centrifugal filter (Vivaspin 20, Sartorius) to provide a stock solution for crystallisation. Protein concentration was estimated spectrophotometrically; a theoretical extinction coefficient, ε: 11920 M^{-1} cm^{-1} at 280 nm, was calculated by the *ProtParam* server (Gasteiger *et al.,* 2005).

2.2.2 Purification of *Bc*IspF

*Bc*IspF was purified in the manner described for *Pf*IspF, except that buffer B (100 mM NaCl, 100 mM Tris-HCl, pH 7.5) was used throughout the process and the His-tag was not cleaved off the protein. Further, the marked temperature sensitivity observed for *Pf*IspF was not seen for *Bc*IspF and samples were kept either on ice or at 4 °C throughout.

2.2.3 Purification of biotinylated *Bc*IspF and *Ec*IspF for BLI

Cultures containing *Bc*IspF were harvested by centrifugation and re-suspended in buffer D (150 mM NaCl, 50 mM Tris-HCl, pH 8.0). To this was added one protease inhibitor tablet (EDTA-free, Roche) and DNAse I. The re-suspended cells were lysed and the high-speed supernatant was recovered as described for *Pf*IspF. The supernatant was syringe-filtered and loaded on to a nickel ion affinity chromatography column. The

protein was eluted from the column with a linear gradient of imidazole. Protein sample was dialysed into fresh buffer D then treated with TEV protease (16 hours at 4 °C). A sample was taken for MALDI-TOF MS before and after treatment with protease.

Protease-treated protein was passed through a second nickel ion affinity chromatography column and protein cleaved from its purification tag, was collected in the flow-through. This cleaved protein was dialysed into biotinylatyion buffer (10 mM Tris-HCl, 200 mM KCl, 5 mM $MgCl_2$). Following dialysis, the protein was prepared for biotinylation by being diluted to <10 μM in biotinylation buffer. D-biotin was added to a final concentration of 100 μM, and the biotinylation reaction was started with the addition of 500 μM ATP and 1 μM of the biotin ligase, BirA (His-tagged, provided by Dr. Vincent Rao). The reaction was carried out for four hours at 20 °C. The protein eluted in the flow-through of a third nickel ion affinity chromatography column, removing the BirA enzyme. Biotinylated-*Bc*IspF was concentrated and exchanged into a buffer for size-exclusion chromatography (20 mM NaCl, 20 mM Tris-HCl, pH 7.5) by centrifugal filtration, to remove residual biotin and ATP. Sample was loaded on to a size-exclusion chromatography column (Superdex 200 26/60, GE Healthcare). The peak was collected and a sample was sent for MALDI-TOF MS analysis. Protein, diluted to 5 mg mL^{-1} in size-exclusion chromatography buffer and supplemented with 10% glycerol, was flash-cooled in liquid nitrogen and stored at -80 °C for later use on the Octet Red BLI system. *Ec*IspF was purified and biotinylated as described above for *Bc*IspF, except that the buffer condition used throughout purification was different (50 mM NaCl, 50 mM Tris-HCl, pH 7.7), and that the His-tag was kept.

2.2.4 Purification of *Pa*PabC

*Pa*PabC was purified in the manner described for *Pf*IspF, except that a different buffer was used throughout the process (500 mM NaCl, 100 mM HEPES, pH 7.5) and that the His-tag was kept. Samples were kept either on ice or at 4 °C throughout. Sample purity and mass were confirmed by electrospray ionisation mass spectrometry.

2.3.1 Crystallisation of *Pf*IspF in complex with CDP

A stock solution of *Pf*IspF was prepared at 6 mg mL^{-1} in buffer A supplemented with 2 mM $MgCl_2$. CDP disodium salt was added to a final concentration of 2 mM. Crystals were obtained by mixing protein (2 μl) with reservoir solution (2 μl) at 20 °C. The reservoir solution consisted of 1.8-2.5 M $(NH_4)_2SO_4$, 5 mM $ZnCl_2$ and 100 mM Bis-Tris, pH 5.5. Prisms (0.15 x 0.15 x 0.15 mm) appeared within 2-4 days. Crystals were cryo-protected with a saturated sucrose solution and data were collected at the European Synchrotron Radiation Facility (ESRF, Grenoble).

2.3.2 Crystallisation of *holo-Pf*IspF

*Pf*IspF was prepared as before except that fosmidomycin, an hydroxamate compound (Figure 1.5), was added to the protein sample (20 mM) prior to crystallisation. Crystals of similar morphology were obtained as described above and a dataset was collected under a gaseous nitrogen cryostream at −173 °C on an in-house rotating-anode X-ray source (MicroMax 007 HF, Rigaku) with an image plate detector (RAXIS IV^{++}).

Despite the presence of fosmidomycin, a putative ligand, no interpretable electron density was observed in the resulting maps (Results, Chapter 3), producing a *holo-Pf*IspF structure.

2.3.3 Crystallisation of *Bc*IspF in complex with CMP

*Bc*IspF was prepared at 5 mg mL^{-1} in buffer B supplemented with 2 mM $MgCl_2$, to which was added CMP disodium salt to a final concentration of 20 mM. A second sample was prepared at 10 mg mL^{-1} in buffer C (100 mM NaCl, 2 mM $MgCl_2$, 100 mM sodium formate, pH 5.0) to which CMP was also added (2 mM final concentration).

The *Bc*IspF sample in buffer B was crystallised by mixing (2 µL) with reservoir (2 µL) containing 25% w/v PEG 3350, 2.2 M $(NH_4)_2SO_4$, 0.1 M sodium formate, pH 5.0, and 1% v/v dioxane. Orthorhombic blocks reached maximum size within ten days. A crystal of approximate dimensions 0.15 x 0.10 x 0.10 mm was used for data collection. Buffer B supplemented with 20% v/v glycerol was used as a cryoprotectant.

The second *Bc*IspF sample, in buffer C, was crystallised by mixing (2 µL) with reservoir (4 µL) containing 5% w/v PEG 1000, 33% v/v ethanol, 0.1 M Na_2HPO_4, pH 4.0, and 2% v/v dioxane. Prisms grew within six days. A crystal of approximate dimensions 0.25 x 0.10 x 0.10 mm was used for data collection. A mixture of buffer C with reservoir (1:2), replacing PEG 1000 with PEG 4000 at 25% w/v, was used as a cryoprotectant.

2.3.4 Crystallisation of *Bc*IspF in complex with citrate

*Bc*IspF at 10mg mL^{-1} in buffer C without $MgCl_2$ present was crystallised by mixing (1.5 µL) with reservoir (3 µL) containing 5% w/v PEG 1000, 36% v/v ethanol, 0.1 M Na_2HPO_4 and 0.1 M citric acid, pH 4.2. Prisms grew within 4 days, belonging to a different crystal form. A crystal of approximate dimensions 0.4 x 0.10 x 0.10 mm was used for data collection. A mixture of sample buffer with reservoir (1:2), replacing PEG 1000 with PEG 4000 at 25% w/v, was used as a cryoprotectant. Datasets for

*Bc*IspF crystals were collected on the in-house X-ray system as described for *Pf*IspF (Section 2.3.2).

2.3.5 Crystallisation of *Pa*PabC

To *Pa*PabC at 33 mg mL^{-1} in sample buffer (100 mM HEPES, 500 mM NaCl pH 7.5), PLP and PABA were added (final concentration: 0.1 mM and 10 mM respectively). PLP increased the thermal stability of *Pa*PabC in a dose-dependent manner; the optimum concentration was determined by DSF. *Pa*PabC was crystallised by mixing sample (1 μL) with reservoir (1 μL) containing 10% w/v PEG 400, 1.8 M $(NH_4)_2SO_4$ and 100 mM MES, pH 6.5. Clumps of pale yellow, orthorhombic blocks grew over one week. Mother liquor supplemented with 25% v/v glycerol was used as a cryo-protectant. A crystal fragment (0.3 × 0.2 × 0.1 mm) was flash-cooled in liquid nitrogen and sent for data collection at a synchrotron-radiation source (ESRF).

2.4 Data processing, structure solution and refinement

Data were indexed and integrated using either *MOSFLM* (Leslie, 2006; Battye *et al*., 2011) or *XDS* (Kabsch, 2010) and scaled using *SCALA* (Evans, 2006) with 5% of data kept for R_{free} calculations. All structures were solved by molecular replacement. Search models for molecular replacement used coordinates from orthologues in *E. coli* (PDB code: 1GX1; ~33% identity, Kemp *et al*., 2002) and *B. pseudomallei* (PDB code: 3F0G; 63%, Begley *et al.*, 2011) for *Pf*IspF and *Bc*IspF respectively, edited to remove all non-protein atoms. The search model for *Pa*PabC was prepared by generating a poly-alanine model of the *E. coli* PabC structure (35% identity, Nakai *et al.*, 2000) in *CHAINSAW* (Stein, 2008). Molecular replacement calculations were performed using

either *PHASER* (McCoy *et al.*, 2007; Collaborative Computational Project, Number 4, 1994) or *MOLREP* (Vagin and Teplyakov, 1997).

Refinements were performed in *REFMAC5* (Murshudov *et al.*, 2011) and models were inspected and manipulated in *COOT* (Emsley *et al.*, 2010). Strict non-crystallographic symmetry (NCS) restraints were employed in the early stages of refinement and then removed towards the end. Greater weighting was given to geometric parameters than default values during refinement of medium resolution structures of *Bc*IspF. The validation tools in *COOT* and the *MolProbity* server (Chen *et al.*, 2010) were used to assess model geometry. Comparisons with structures in the PDB were performed using the *DALI* server (Holm & Rosenström, 2010). *AREAIMOL* (Collaborative Computational Project, Number 4, 1994) and the *Protein Interfaces, Surfaces & Assemblies* server, (Krissinel & Henrick, 2007) were used to calculate surface and interface areas. Figures of proteins were prepared using *PyMOL* molecular graphics software (DeLano, 2002).

CHAPTER 3

IspF; STRUCTURAL ANALYSIS and FRAGMENT SCREENING

3.1 *Pf*IspF and *Bc*IspF results

3.1.1 Structure of IspF

Structures were determined of *Bc*IspF in complex with either CMP or citrate, and of *Pf*IspF in complex with CDP, as well as a *holo-Pf*IspF structure (where *holo-* refers to the protein in complex with the Zn^{2+} cofactor, without any other ligands present in the active site). All structures are at a resolution of 2.0 Å or better. Crystallographic statistics are presented in Tables 3.1 and 3.2. Sequence alignments and structural overlays of IspF from *P. falciparum*, *B. cenocepacia*, *B. pseudomallei* and *E. coli* were inspected to inform on conservation of residues and interactions, and an alignment of *Bc*IspF with *Pf*IspF is shown in Figure 3.1.

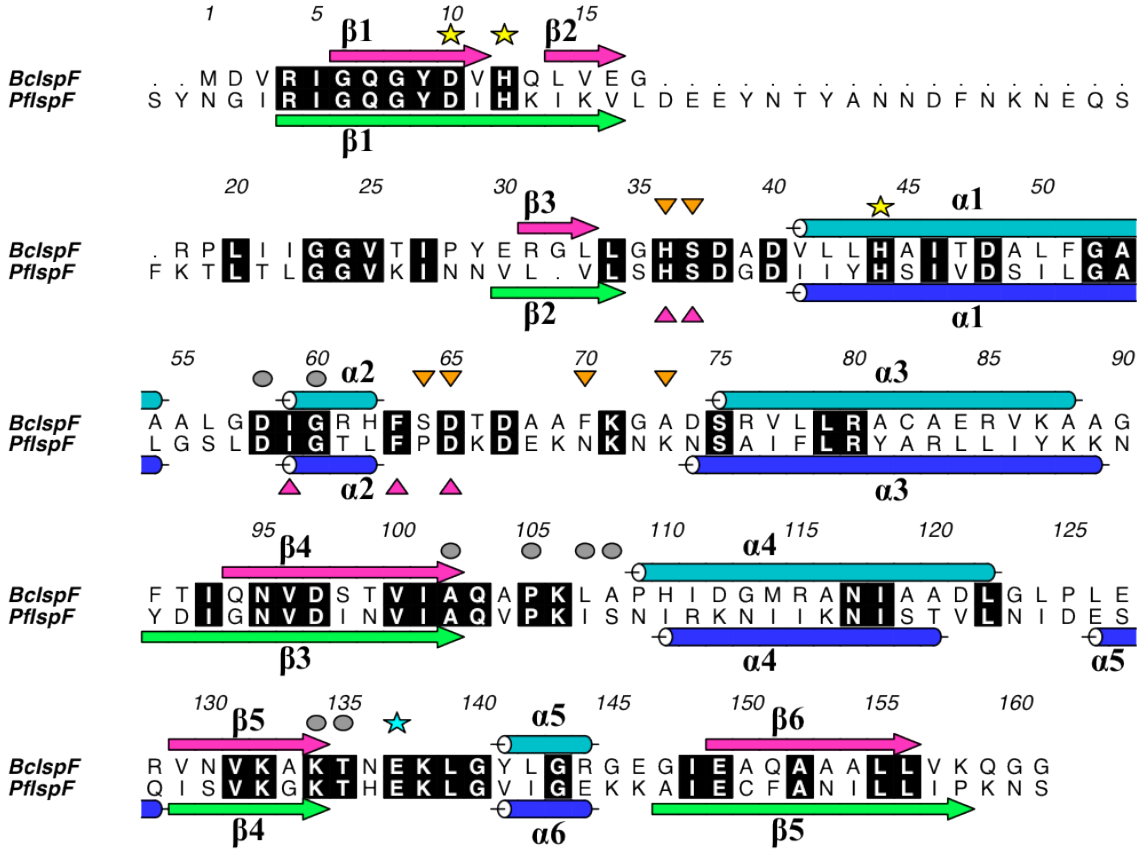

Figure 3.1 Sequence alignment of *Bc*IspF and *Pf*IspF. The alignment has been annotated with elements of secondary structure. Only the *Bc*IspF sequence has been numbered. Strictly conserved residues between the two species are highlighted in black. Residues that bind Zn^{2+} are marked with a yellow star, those that bind at position 1 with a grey disk and those at position 2 with an orange triangle. Residues that bind MEcPP in *Ec*IspF (Steinbacher *et al.*, 2002) are marked with a magenta triangle. A conserved glutamate that binds either Mg^{2+} or Mn^{2+} in *Ec*IspF structures is highlighted with a blue star. This figure was prepared using *ALINE* (Bond & Schüttelkopf, 2009).

The calculated masses of monomeric *Bc*IspF and *Pf*IspF are 19.3 kDa and 20.5 kDa respectively. IspF forms a homotrimer, both in the crystal structures and in solution; size-exclusion chromatography returns an estimate of 57 kDa for each. IspF from both species adopts the established fold reported from other organisms; a core region containing four β-strands, flanked by α-helices (Section 1.2.5, Figure 3.2). The accessible surface area (ASA) of an IspF subunit averages out as approximately 8130 $Å^2$ for *Bc*IspF and 8680 $Å^2$ for *Pf*IspF; for comparsion the value for *Ec*IspF is 7900 $Å^2$.

A search for structurally-related proteins in the PDB using the *DALI* server (Holm & Rosenström, 2010) showed that *Pf*IspF aligns 143 residues with an RMSD of 0.8 Å, and 151 residues with an RMSD of 1.2 Å with IspF from *P. vivax* and *A. thaliana* respectively. *Bc*IspF aligns 151 residues with an RMSD of 0.4 Å to IspF from *B. pseudomallei*. In *Bc*IspF structures the asymmetric unit consists of three subunits, chain A, B, C; related by a three-fold non-crystallographic axis of symmetry. NCS is high with least squares overlays of Cα positions in the range 0.2 - 0.3 Å; nonetheless some differences are present and these are described below. One subunit is present in the asymmetric unit of *Pf*IspF and the trimer is generated by the symmetry operations (-x+y, -x, z) and (y, y-x, z). A least squares superimposition of Cα positions from both *Pf*IspF structures matches all 156 residues with an RMSD of 0.3 Å. Since there are no pronounced differences between the CDP bound and *holo*- *Pf*IspF structures, only the former is discussed. In 2007, a *holo*-structure of IspF to a resolution of 2.3 Å from *P. vivax*, a closely related species to *P. falciparum*, was deposited with the PDB without an associated publication (code: 3B6N). Although Zn^{2+} has been modelled at the active site, a water molecule most likely occupies the metal binding site instead, or the site is only partially occupied, since the corresponding *B*-value is 2.6 times greater than the average *B*-value of the protein atoms and the side chain of one of the two histidines that

coordinate the metal in other structures is in an unsuitable orientation. In contrast, in *Pf*IspF the *B*-value for Zn^{2+} is within 30% of the average *B*. Further, *Pf*IspF provides a higher resolution structure from a *Plasmodium* species.

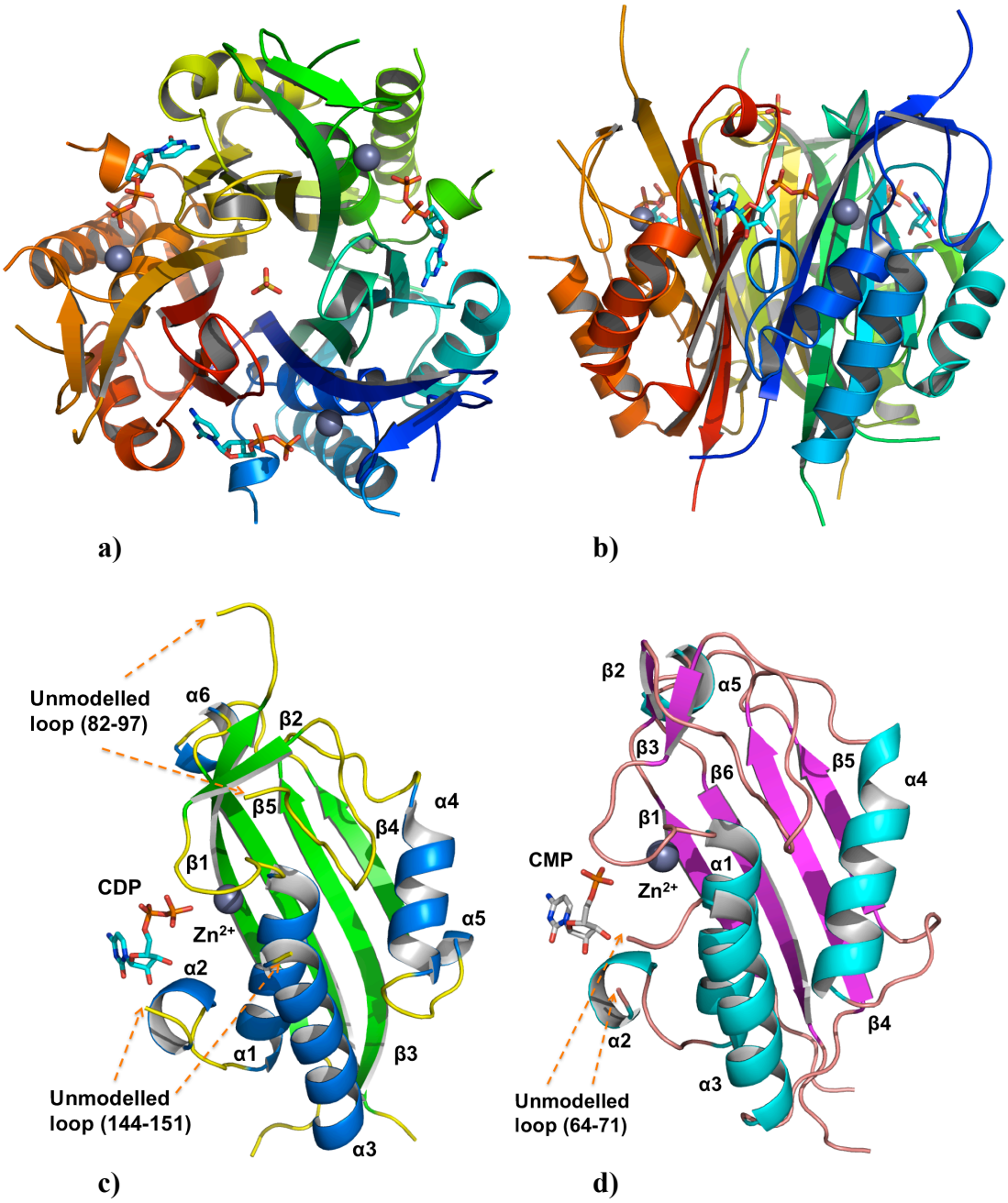

Figure 3.2 Overall structure of IspF. IspF forms a homotrimer. **a)** Axial view. **b)** Side view. The figure has been drawn using the coordinates for *Pf*IspF in complex with CDP; a trimer has been generated from symmetry-related subunits. Subunits (displayed as ribbons) are coloured blue, orange and green respectively. Zn^{2+} cations are displayed as grey spheres, sulfate and CDP are displayed as sticks.). The secondary structure of *Pf*IspF and *Bc*IspF subunits is shown in **c)** and **d)** respectively, similarly orientated. The location of unmodelled loops is highlighted with arrows.

Electron density is absent for a loop between α2 and α3 that covers the active site in both *Pf*IspF structures and the *Bc*IspF complex with a single CMP in the active

site, spanning Asp144 - Asn151 and Phe63 - Ala73 respectively. In contrast, these loop residues could be modelled in the *Bc*IspF structure where two molecules of CMP are present. The loop residues have elevated *B*-factors, 2.4 times greater than the average *B*-value for the entire the protein. The same loop could only be modelled for chain A in the *Bc*IspF-citrate complex. These observations are consistent with the inference that the loop that covers the active site is flexible (Kemp *et al.*, 2002; Steinbacher *et al.*, 2002). Such flexibility has been speculated to have a role in catalysis (Lehmann *et al.*, 2002). *Pf*IspF contains a 19 residue sequence at the N-terminus, Lys76 - Glu94, that does not align with sequences from other organisms (Figure 3.1). Residues Tyr82 - Phe97, which overlap with this region, are unmodelled in *Pf*IspF because corresponding electron density is absent. The highly conserved His115 and Ser116 that are located on a six residue loop above the Zn^{2+} binding site (Figure 3.1) are also flexible and have elevated *B*-factors in all structures except in one chain of a *Bc*IspF-CMP structure where they are unmodelled.

The active site is located in a cleft formed by adjacent subunits (Section 1.2.5). Zn^{2+}, which plays a functional role in catalysis is present in all structures and coordinated by the side chains of Asp10, His12 and His44 in *Bc*IspF. In *Ec*IspF a highly conserved glutamate, Glu135, helps coordinate either a Mg^{2+} or Mn^{2+} together with the bridging phosphates of the substrate or CDP (Kemp *et al.*, 2002; Steinbacher *et al.*, 2002). However, no metal is seen at this site in any structure reported here.

A hydrophobic cavity is present at the trimeric core of IspF. In *Bc*IspF the cavity is lined by the side chains of Tyr9, Val11, Ile101 and Tyr141, and the floor of the cavity is formed by a ring of hydrophobic residues; Val3 and Leu155 from all three subunits. In *Pf*IspF the side chains of Phe230 form the floor of the cavity. Anions such as sulfate, phosphate or pyrophosphate bind at the entrance to this cavity in several IspF structures, for example phosphate is observed in IspF from *Arabidopsis thaliana* (PDB

code: 2PMP; Calisto *et al.*, 2007). In the structure of *Bc*IspF crystallised with $(NH_4)_2SO_4$ as a precipitant, a sulfate is coordinated by Arg144. In *Pf*IspF, a sulfate at a similar site is coordinated by the main chain amides of Val220 from all three subunits. In structures of *Bc*IspF in which Na_2HPO_4 was the precipitant, Tyr141 amide groups bind a phosphate in a similar fashion. Isoprenoid-species such as geranyl- or farnesyl-pyrophosphate have been observed in the cavity that is present in IspF structures from other species, and a possible role in feedback regulation has been suggested (Kemp *et al.*, 2005; Ni *et al.*, 2004; Sgraja *et al.*, 2005). A molecule of di(hydroxyethyl)ether; a likely decomposition product or impurity of PEG 3350 used in crystallisation, occupies the cavity in one of the *Bc*IspF structures (Table 3.2), possibly mimicking a prenyl chain. A solvated Mg^{2+} is present further down the cavity in one of the *Bc*IspF structures, forming interactions similar to IspF from *B. pseudomallei* (Begley *et al.*, 2011). A shell of water molecules surround Mg^{2+} in an octahedral coordination geometry. These waters are bound by Glu149, and waters in the second shell bind to the hydroxyl groups of Tyr9 and Tyr141. A Mg^{2+} at a similar position is coordinated directly by the side chains of the conserved Glu149 from all three subunits in IspF from *Salmonella enterica* serovar Typhimurium (PDB code: 3GHZ) and *E. coli* (Ramsden *et al.*, 2009).

Table 3.1 Crystallographic statistics for *Pf*IspF

Structure	***Pf*IspF - CDP complex**	***holo* - *Pf*IspF**
Space group	*H*3	*H*3
Unit cell dimensions *a, b, c* (Å)	84.9, 84.9, 101.0	84.2, 84.2, 102.5
Resolution range[a] (Å)	41.63-1.60 (1.69-1.60)	29.71-2.00 (2.11-2.00)
No. reflections	181781 (16968)	41802 (5780)
Unique reflections	35607 (5194)	18068 (2622)
Completeness (%)	99.4 (99.3)	98.6 (97.0)
R_{merge}[b] (%)	9.3 (42.0)	9.4 (48.2)
Multiplicity	5.1 (3.3)	2.3 (2.2)
$< I/\sigma(I) >$	11.1 (2.6)	5.3 (2.0)
Wilson *B* ($Å^2$)	24.4	32.0
R_{work}[c]/R_{free}[d] (%)	14.4, 16.5	19.4, 22.6
Number of residues / waters / ligands	156 residues, 85 waters, 1 CDP, 2 Zn^{2+}, 3 Cl^-, 1 SO_4^{2-}	156 residues, 94 waters, 2 Zn^{2+}, 1 SO_4^{2-}
RMSD bond lengths (Å) / bond angles[e] (°)	0.005 1.000	0.019 2.087
Mean *B*-factors ($Å^2$) Main chain, side chain Waters Ligands	 25.1, 33.8 35.2 31.5 (CDP) 35.8 (Zn^{2+}, Cl^-, SO_4^{2-})	 34.2, 39.5 47.8 44.5 (Zn^{2+}, SO_4^{2-})
Ramachandran plot Favoured regions (%) Allowed regions (%) Outliers	 98.6 0.7 1 outlier: Asp79	 95.3 4.0 1 outlier: Asp79

[a.] Values in parentheses refer to the highest resolution shell. [b.] $R_{merge} = \sum_{hkl}\sum_i |I_i(hkl) - \langle I(hkl)\rangle| / \sum_{hkl}\sum_i I_i(hkl)$; where $I_i(hkl)$ is the intensity of the *i*th measurement of reflection *hkl* and $\langle I(hkl)\rangle$ is the mean value of $I_i(hkl)$ for all *i* measurements. [c.] $R_{work} = \sum_{hkl}||F_o|-|F_c|| / \sum|F_o|$, where F_o is the observed structure factor and F_c is the calculated structure factor. [d.] R_{free} is the same as R_{work} except calculated with a subset, 5%, of data that are excluded from the refinement calculations. [e.] (Engh & Huber, 1991). These considerations apply to all tables of crystallographic statistics presented in this thesis.

Table 3.2 Crystallographic statistics for *Bc*IspF

Structure	***Bc*IspF - 1 x CMP complex**	***Bc*IspF - 2 x CMP complex**	***Bc*IspF - citrate complex**
Space group	*C*2	*C*2	*C*2
Unit cell dimensions *a, b, c* (Å), β	97.2, 88.6, 72.4, 103.9°	97.9, 89.3, 73.0, 104.2°	131.7, 52.5, 72.1, 94.6°
Resolution range (Å)	29.84-2.00 (2.10-2.00)	19.32-1.90 (2.00-1.90)	40.90-2.00 (2.10-2.00)
No. reflections	98451 (13335)	164120 (24760)	119715 (15957)
Unique reflections	38409 (5579)	47918 (6972)	33460 (4696)
Completeness (%)	96.0 (95.4)	99.9 (100.0)	99.4 (96.1)
R_{merge} (%)	11.0 (32.2)	13.8 (32.3)	3.2 (7.8)
Multiplicity	2.6 (2.4)	3.4 (3.6)	3.6 (3.4)
$< I/\sigma(I)>$	5.9 (2.7)	6.2 (3.1)	23.9 (12.8)
Wilson *B* ($Å^2$)	16.5	16.3	18.7
R_{work}/R_{free} (%)	23.7, 28.0	20.4, 25.1	15.6, 19.8
Number of residues / waters / ligands	458 residues, 173 waters, 3 CMP, 3 Zn^{2+}, 1 Mg^{2+}, 1 PO_4^{3-}	483 residues, 420 waters, 6 CMP, 3 Zn^{2+}, 1 SO_4^{2-}, 1 di(hydroxyethyl)ether	460 residue, 320 waters, 3 citrate, 3 Zn^{2+}, 1 PO_4^{3-}
RMSD bond lengths (Å) / bond angles (º)	0.020 2.198	0.011 1.526	0.020 2.101
Mean *B*-factors ($Å^2$) Main chain, side chain Waters Ligands	 13.6, 15.3 16.5 15.1 (CMP) 24.8 (Zn^{2+}, Mg^{2+}, PO_4^{3-})	 18.7, 20.4 29.9 18.2 (CMP, # 1) 28.7 (CMP, # 2) 25.0 (other ligands)	 16.2, 20.1 26.7 34.4 (citrate) 26.1 (Zn^{2+}, PO_4^{3-})
Ramachandran plot Favoured regions (%) Allowed regions (%) Outliers	 96.9 2.2 4 outliers: Ser37A/C, Tyr29B, Gly17C	 97.8 2.2 No outliers	 97.7 2.3 No outliers

3.1.2 Complexes with CMP and CDP

Residues from both subunits that form the active site position cytidine nucleotides though hydrogen bonding (Figures 3.1 and 3.3). In *Bc*IspF, carbonyl groups from Ala102 and *cis*-Pro105 bind to the N4 base amine, and the amide groups of Leu107 and Ala108 bind to the N3 and O2 atoms of the cytosine respectively. Ribose hydroxyl O2' is held by Asp58 from the adjacent subunit. Gly60 amide, also from the adjacent subunit, binds the O3' hydroxyl, however this interaction is not conserved in *Pf*IspF. Thr135 amide and side chain hydroxyl bind to an oxygen on the α-phosphate.

Lys134NZ binds the CMP α-phosphate and may play a role in catalysis by helping to position the transition-state intermediate or, in conjunction with Zn^{2+}, align the substrate for nucleophilic attack; but this interaction is not observed in *Pf*IspF. This interaction in *Bc*IspF is reminiscent of that previously reported for the active site Lys132 in *Tt*IspF (Kishida *et al.*, 2003), and an overlay (not shown) confirms this, except that in *Tt*IspF Lys132NZ binds the β-phosphate. Lys106 side chain is situated above the cytosine and provides van der Waals contacts.

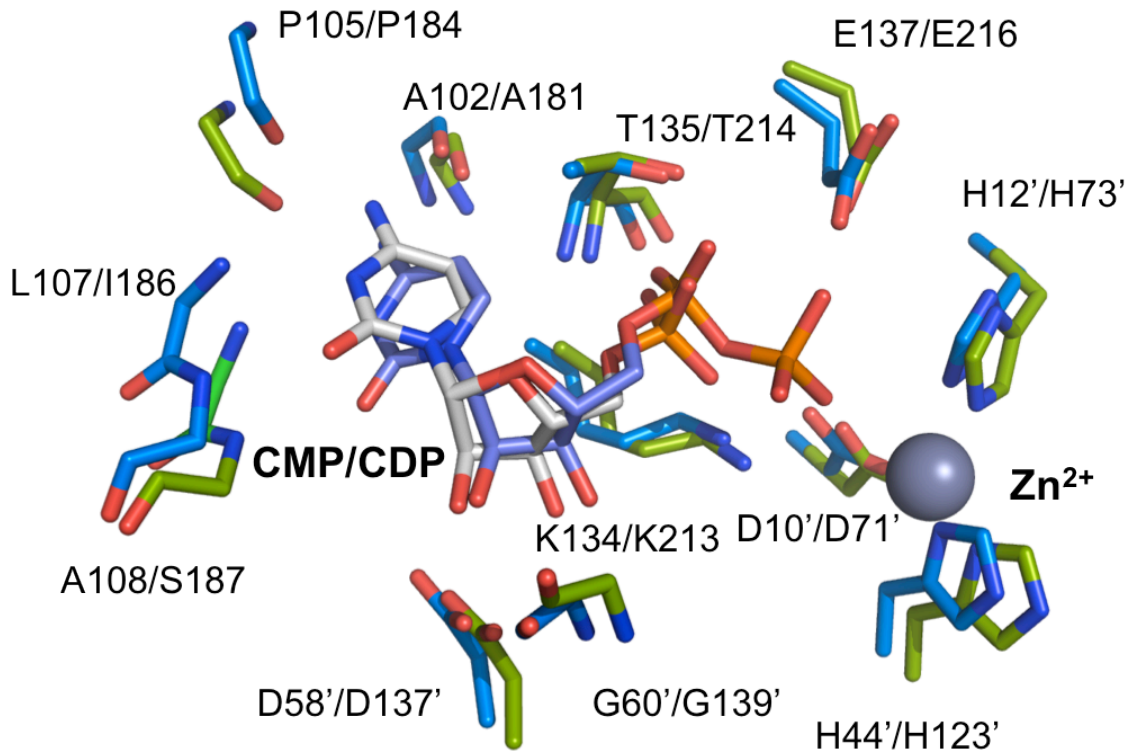

Figure 3.3 Superimpostion of position 1 residues in *Bc*IspF and *Pf*IspF. Structurally conserved residues that bind CMP or CDP at position 1 in IspF are displayed as sticks. Sequence numbers for *Bc*IspF are followed by those for *Pf*IspF; and residues contributed from the adjacent subunit are marked with a prime ('). *Bc*IspF and *Pf*IspF are coloured cyan and green respectively. Interactions are detailed in the text.

Unexpectedly, a second molecule of CMP was observed in the active site in a structure of *Bc*IspF co-crystallised in the presence of 10 mM ligand (Section 2.3.3). The previously described cytidine-binding site is referred as position 1, and this new site as position 2 (Figure 3.4). Residues that bind CMP at position 2 (CMP #2) are from the same subunit that binds the active site Zn^{2+}. The CMP #2 phosphate associates directly with the active site Zn^{2+}. Ser64 carbonyl binds cytosine O2 thorough a water

molecule. Phe70 and Ala73 carbonyl groups position a water molecule that binds cytosine N3. Ala73 carbonyl also binds directly to cytosine N4, together with Ser37 side chain OG. Asp65 binds to ribose O2'. His36 main chain amide and carbonyl position waters that each bind to the phosphate. Overlay with the *Ec*IspF-product complex shows that CMP #2 binds in the same location as MEcPP (Figure 3.5; Steinbacher *et al.*, 2002). Additionally, citrate may mimic the MEcPP product, or transition state since it binds directly, and indirectly through solvent, to residues conserved with *Ec*IspF that are known to bind MEcPP (Section 3.1.3). Residues that bind MEcPP are conserved in *Pf*IspF as His115, Ser116, Ile138, Phe142 and Asp144 (Figures 3.1 and 3.5).

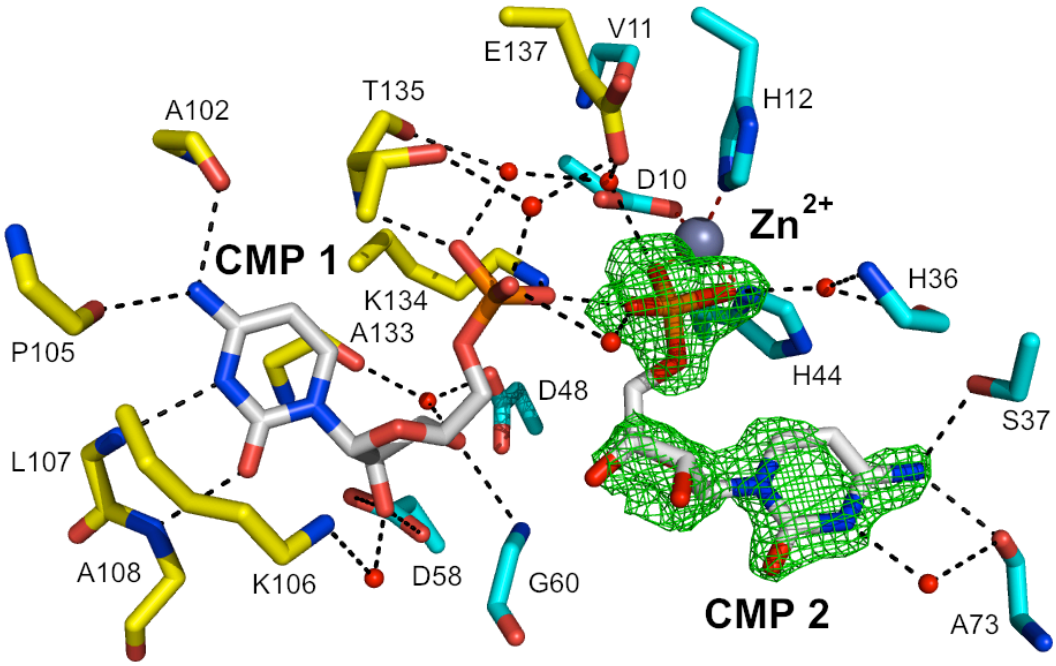

Figure 3.4 CMP binding interactions at the enzyme active site in *Bc*IspF. Interactions between *Bc*IspF and CMP, and the coordination of Zn^{2+} are highlighted with black and red dashed lines respectively. The established nucleotide binding site is labelled CMP "1"; the novel CMP-binding site is labelled CMP "2". Solvent molecules are depicted as red spheres. There are some minor differences in the residues involved in binding interactions with CMP #2 in active sites related by NCS (not shown). Adjacent subunits are coloured yellow and cyan respectively. Electron density is displayed as green chicken-wire corresponding to an $|F_o\text{-}F_c|$ map (omit map) for CMP #2 contoured at 2.5 σ.

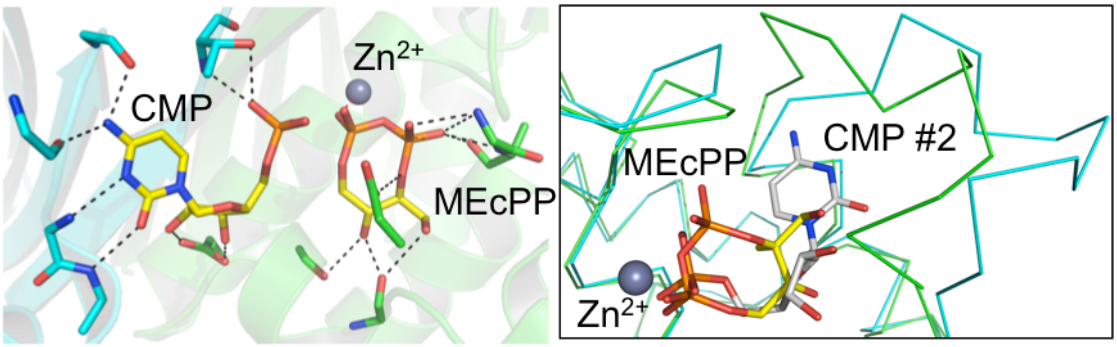

a) Product binding site in *Ec*IspF **b)** Overlay of MEcPP and CMP #2

Figure 3.5 CMP #2 occupies the same site as MEcPP. a) The binding interactions between *Ec*IspF (PDB code: 1JY8) and the reaction products CMP and MEcPP. Relevant residues are discussed in the text and marked in Figure 3.1. **b)** An overlay of *Ec*IspF product complex and *Bc*IspF. CMP #2 binds in a similar site as MEcPP and also associates with Zn^{2+}. Further, the loop surrounding the ligands (*Ec*IspF: Phe61-Ser73; *Bc*IspF: Phe63-Ser75) adopts a strikingly different conformation.

3.1.3 *Bc*IspF-citrate complex

Attempts to produce *holo-Bc*IspF crystals for ligand soaking experiments identified conditions with citrate in the crystallisation reservoir (Section 2.3.4). However *holo-Bc*IspF crystals had not been formed, instead electron density consistent with citrate was present, blocking the three active sites. Citrate was well defined in one site and modelled at full-occupancy, but poorly defined in the remaining two sites. The well-defined citrate binds to the active site Zn^{2+} *via* both a carboxylate and hydroxyl. In contrast, citrate is present at lower occupancy, 0.75, in the remaining sites and adopts a different pose, with only a carboxylate binding to Zn^{2+}. The carboxylates of the well-defined citrate also interact with the main chain amides of His36 and Ser37, and side chains of Asp65 and Lys134 (Figure 3.6). An additional solvent mediated interaction is formed with the side chain of Glu137 (not shown). This well resolved citrate helped to order the loop covering the active site in this subunit and an overlay (not shown) demonstrated that these residues adopt the conformation observed in the *Ec*IspF-MEcPP complex (Steinbacher *et al.*, 2002).

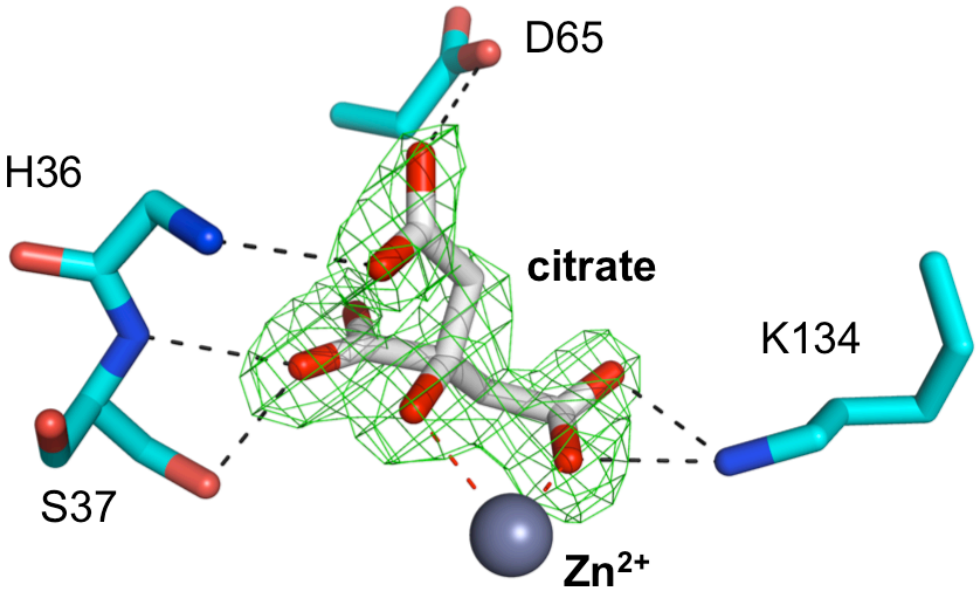

Figure 3.6 Citrate binding to Zn^{2+} in *Bc*IspF. A well resolved citrate binds to Zn^{2+} and makes interactions in the active site through carboxyl groups. An omit map is displayed for citrate in green chicken wire contoured at 3σ. Residues are shown as sticks and a grey sphere represents Zn^{2+}. Interactions are marked with dashed lines. Solvent mediated interactions are not shown.

3.1.4 Co-crystallisation with potential ligands

Crystallisation of *Pf*IspF and *Bc*IspF in the presence of fosmidomycin, benzohydroxamic acid, acetohydroxamic acid or pyrithione was attempted. A dataset was collected to resolution of 2.0 Å from a crystal of *Bc*IspF that formed in the presence of 10 mM pyrithione. The structure demonstrated that pyrithione leaches Zn^{2+} from the active site (not shown) and once both Zn^{2+} and pyrithione were known to be absent the structure was not refined further. Crystals of *Bc*IspF were prepared in the presence of both 2 mM CMP and stoichiometric amounts (0.5 μM) of pyrithione. Nine such crystals were screened for diffraction quality and a data set was collected from one to a resolution of 2.1 Å and refined (R_{work} 20.8%, R_{free} 24.6%). Electron density was present for both CMP and Zn^{2+}, however no pyrithione was visible in the resulting maps. Similarly, structures of IspF determined in the presence the other compounds, showed no density for the putative ligands and were not subsequently refined.

A fragment screen against *Bc*IspF, described in Section 3.3.1., identified six compounds that gave a reliable binding response. Co-crystallisation and ligand soaking

experiments were performed with three of the fragments identified (fragments **a**-**c**, Figure 3.8). When fragments were present at 1 mM, crystals were only observed to form in the presence of 1 mM CMP. Higher concentrations of fragments resulted in precipitation; fragment **c** undergoing phase-separation. A crystal of *Bc*IspF that formed in the presence of 1 mM CMP and 1 mM of fragment **a** was collected and the structure determined (not shown). Electron density maps indicated that CMP was present but no density for fragment **a** was identifiable. Another dataset was collected from a crystal that had been co-crystallised with 1 mM CMP present and subsequently soaked for three hours with a cocktail of fragments **a**-**c**. Fragments were dissolved in DMSO and reached a final concentration of 5 mM in the crystallisation drop. In this crystal structure also, CMP was present but no ligand density was identified. Longer soaking times resulted in crystal damage or poor diffraction.

3.2 Structural studies on IspF - Conclusions

The structures of IspF from two pathogens have been determined, demonstrating similarity to known structures from other species. These proteins have been assessed for suitability as platforms for structure-based drug discovery. However, since numerous attempts to obtain the structure of protein-ligand complexes failed, it is concluded that neither *Bc*IspF nor *Pf*IspF are promising candidates for such studies; at least using the crystallisation conditions reported here, all of which are at high ionic strength. Future studies may employ *Ec*IspF or *Bp*IspF, for which successful co-crystallisation with small molecule ligands have been reported (Crane *et al.*, 2006; Ramsden *et al.*, 2009; Begley *et al.*, 2011), in concert with efforts to co-crystallise with the fragments identified in this thesis (Section 3.3). As observed previously, the cytidine-binding pocket is rigid in both structures, whereas the pocket that binds the methylerythritol-phosphate portion of the substrate is relatively flexible.

The unexpected observation of a second molecule of CMP in the active site of *Bc*IspF, as well as the presence of citrate in a related structure may inform on ligand design. Novel ligands addressing the MEcPP pocket could conceivably be designed to recapitulate the binding interactions observed for CMP #2, although loop flexibility and the requirement to select out a single conformation from an ensemble may introduce unfavourable entropic costs to binding (Zürcher & Diederich, 2008). Potential ligands could be generated, for example, by extending out from a core cyclohexa-1,5-dien-1-amine fragment, replacing the water molecules in Figure 3.4 that bind to Ala73, Phe70 and Ser64 with hydrogen bonding groups, and strengthening the interaction with Asp65 by replacing the ribose O2' hydroxyl with a positively charged group such as a primary amine. A screen of six generic Zn^{2+}-binding compounds identified L-tryptophan hydroxamate as one of the compounds with the highest affinity for IspF known to date (K_d: 2 μM), suggesting that addition of a hydroxamate group may anchor ligands in the active site (Ramsden *et al.*, 2009). Additionally, any compounds targeting position 2 that might be developed could be linked with CMP analogues that target position 1 to produce compounds that may block both sites, mimicking the substrate or transition state.

3.3 IspF fragment screening

3.3.1 *Bc*IspF screening results

Dissociation constant values (K_d) recorded for CMP and CDP were 18 µM and 3.7 µM respectively using the BLI technique (Figure 3.7). These measurements provided a positive control for the fragment screen.

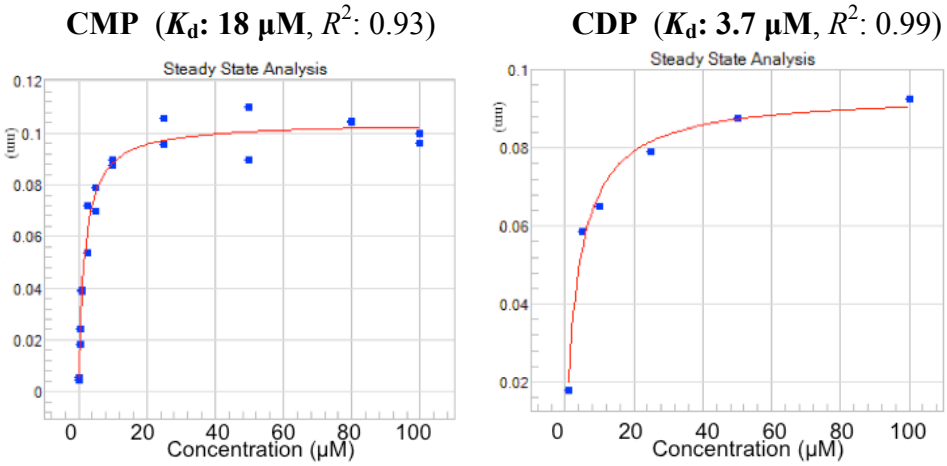

Figure 3.7 Measuring the binding affinities of cytidine nucleotides for *Bc*IspF. The response of *Bc*IspF to CMP and CDP was recorded by BLI, acting as a positive control for fragment screening (CMP was measured in duplicate). The dose-dependent binding curves were generated using statistically smoothed data derived from the raw sensorgram traces with interpolation. K_d values were calculated using this smoothed data. R^2-values indicate the goodness-of-fit and reliability of the data.

Seven compounds (**a-g**) were identified in the screen against *Bc*IspF (Figure 3.8). One of the fragments (**g**) is now considered to be a non-specific binder since it has been flagged in several unrelated screens (Dr. David Robinson). Fragments **a-c** were selected for purchase. However co-crystal structures with *Bc*IspF could not be determined despite several efforts (Section 3.1.4).

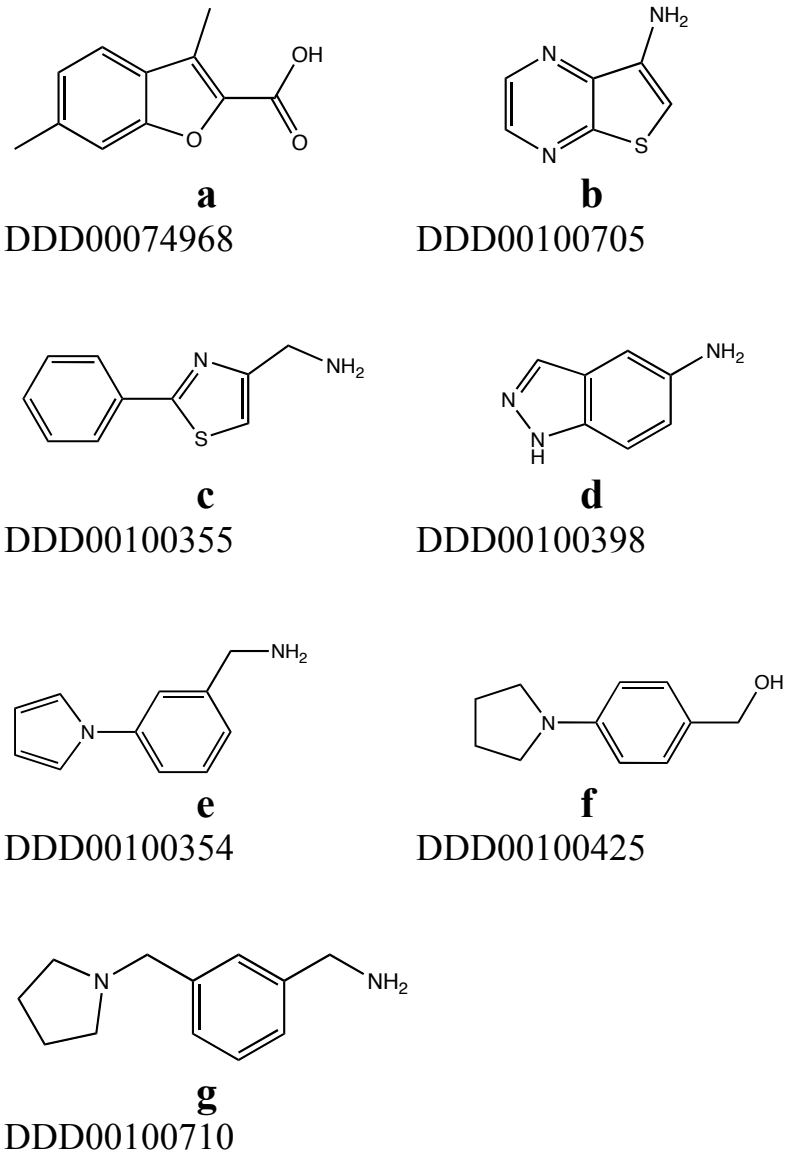

Figure 3.8 Fragments identified in the screen against *Bc*IspF. The chemical structures and identification codes of seven compounds (**a**-**g**) that were identified as potential IspF binders are shown.

3.3.2 *Ec*IspF screening results

CMP gave a positive control signal (K_d: 40 μM, R^2: 0.96). In 2009, Ramsden *et al.* reported a K_d value of 900 μM, however experimental differences complicate direct comparison. The previously reported K_d value was arrived at using an SPR assay with *Ec*IspF bound to sensors *via* amine-coupling. Additionally, a different buffer was used; 2 mM MgCl, 50 mM Na_2HPO_4, pH 7 (Ramsden *et al.*, 2009). Nonetheless, the R^2 value reported in the current study provides reliability. The content of the DDU fragment library changed between the screen on *Bc*IspF and subsequently on *Ec*IspF (Section 2.1.5). 31 compounds from the revised library were identified that gave a double-referenced binding response to *Ec*IspF, corresponding to 4.7 % of all the compounds in the fragment library. 28 of these fragments were taken forward to generate dose-response curves (Figure 3.9). The three excluded compounds, DDD00100335, DDD00100377 and DDD00100546, were not considered reliable since they produced the large binding responses characteristic of non-specific aggregation. Consideration of the reliability and goodness-of-fit statistical scores, including R^2-values as well as direct inspection of the raw sensorgrams produced for each of the 28 fragments allowed the identification of the most reliable hits (Figure 3.10). These fragments have K_d values ranging from approximately 30 - 700 μM.

a)

BLI Sensorgram for *Ec*IspF dose-dependent response to fragment j

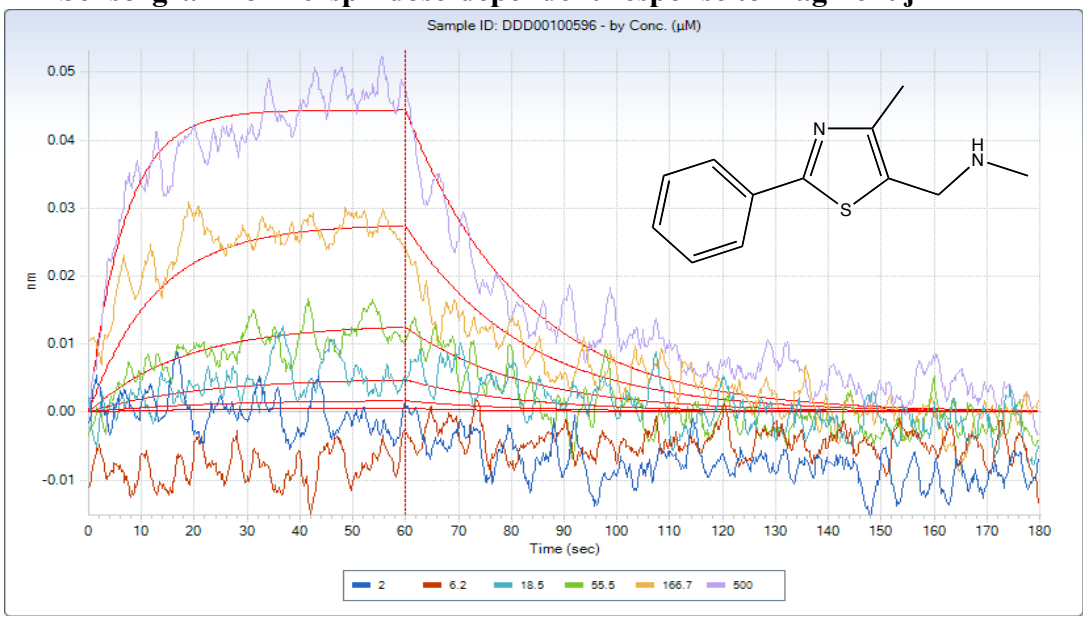

b)

Dose-dependent binding curve for j generated from sensorgram

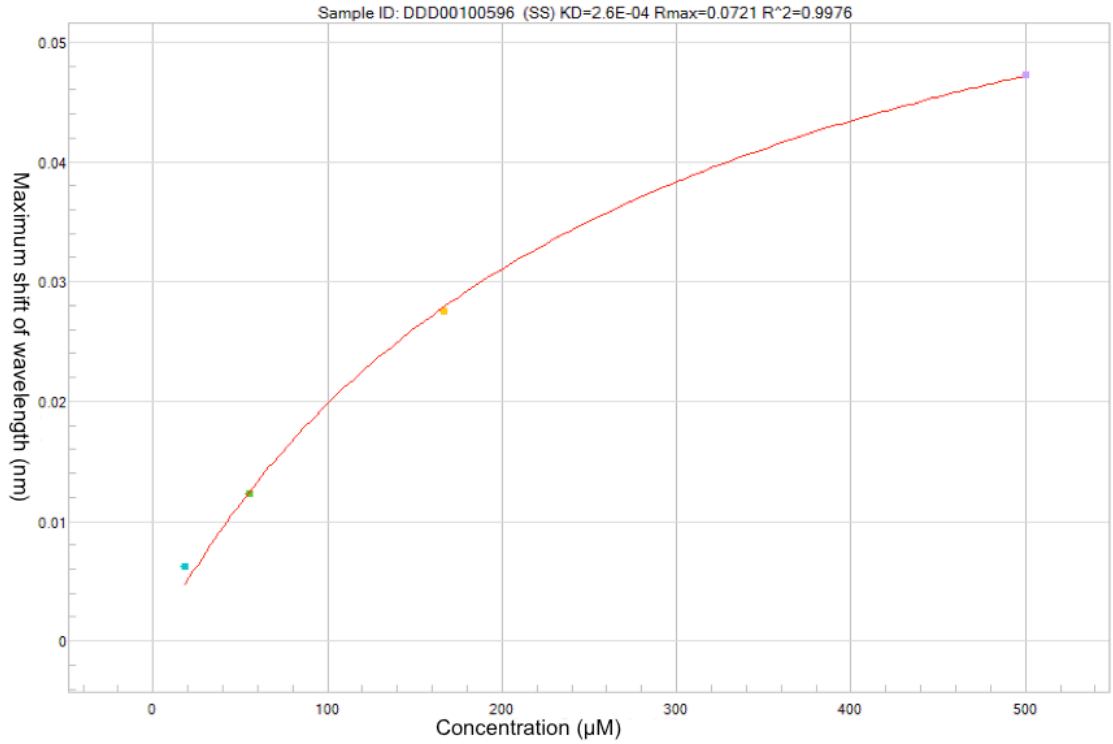

Figure 3.9 An example of BLI data from fragment screening of *Ec*IspF. **a)** The binding response to the fragment (inset) is shown. Vertical displacement represents binding response in nm at increasing concentrations (2, 6.2, 18.5, 55.5, 166.7 & 500 µM). **b)** A dose-dependent binding curve generated for the fragment using statistically smoothed data derived from the raw sensorgram traces with interpolation. The maximum shift in wavelength (after 60 seconds) is plotted for each concentration. Readings from the two lowest concentration points were discarded owing to weak and noisy signal. K_d values were calculated using this smoothed data.

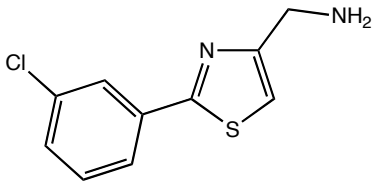

h

DDD00100744, R^2: 0.78

K_d: 30 µM

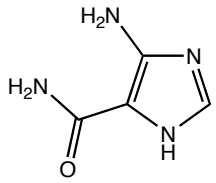

i

DDD00100759, R^2: 0.96

K_d: 670 µM

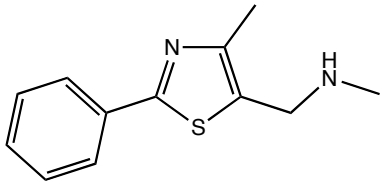

j

DDD00100596, R^2: 0.86

K_d: 200 µM

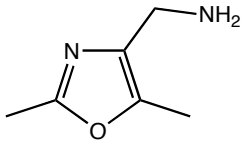

k

DDD00100638, R^2: 0.95

K_d: 500 µM

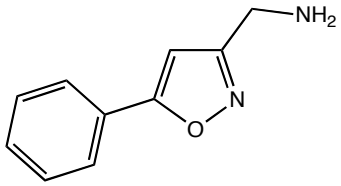

l

DDD00100615, R^2: 0.80

K_d: 380 µM

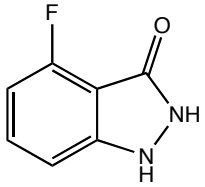

m

DDD00060900, R^2: 0.79

K_d: 720 µM

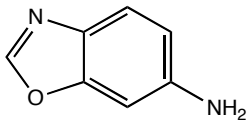

n

DDD00100669, R^2: 0.93

K_d: 100 µM

Figure 3.10 Fragments identified in the screen against *Ec*IspF. The chemical structures of the compounds (**h**-**n**) identified in the screen against *Ec*IspF with the highest reliability scores and best quality sensorgrams are shown. In addition to the compounds displayed, fragment **e** (Figure 3.8) was re-identified in this screen (K_d: 75 µM, R^2: 0.82). K_d values have been calculated from a global fit of the BLI sensorgram data and R^2-values represent the reliability of the fit.

3.3.3 IspF fragment screening - Discussion

A total of 13 unique chemical fragments were identified that gave reliable binding responses in the two BLI fragment screens reported here. Of the fragments identified for *Bc*IspF from the original DDU fragment library, only fragment **c** and fragment **e** (Figure 3.8) were present in the revised library that was screened against *Ec*IspF. Fragment **e**, was re-identified in the later screen against *Ec*IspF. Curiously, while fragment **c** was not re-identified in the later screen, fragment **h** (Figure 3.10) differs from fragment **c** by a single chlorine atom.

Computational docking and modelling of the identified fragments was considered unsuitable owing to their small size, limited number of hydrogen bonding groups and the relatively large, open active site of IspF. For example, *Ec*IspF has an active site volume of 1530 $Å^3$, according to the CASTp volume calculation server set to a probe radius of 1.4 Å (Dundas *et al.*, 2006).

Six of the fragments contain either a thiazole or an oxazole (fragment **c** in Figure 3.8; fragments **h, j, k, l** and **n** in Figure 3.10). Thiazole-bearing fragments have been reported to bind IspF previously (Begley *et al*., 2011). Such a fragment was observed to bind in a pocket outside the active site in a co-crystal structure with IspF from the related *Burkholderia* species, *B. pseudomallei* (Begley *et al*., 2011). In that crystal structure an arginine residue, Arg69, forms a cation-π interaction with the thiazole ring, however Arg69 is not conserved in *Bc*IspF and *Ec*IspF - replaced by Ala69 and Ala67 respectively. The thiazole- and oxazole-bearing fragments reported here may bind to the active site Zn^{2+} cation. Most of the fragments identified contain metal binding groups, planar groups and can make hydrophobic contacts, similar to CDP-MEP, the substrate of IspF.

In fragment screening it is considered good practice to validate initial hits by counter-screening with a complementary biophysical technique (Scott *et al.*, 2012). Assessment and counter-screening of fragment hits using either isothermal titration calorimetry or NMR, accompanied by attempts at co-crystallisation with *Ec*IspF for structural determination would be ideal, but this has not been pursued due to time-constraints. Future work could build from the results of the initial fragment screens reported here.

A convenient enzyme kinetics assay for IspF is unavailable; however unambiguous demonstration of enzyme activity and determination of inhibition constants will require such an assay. Fluorescent IspF substrate-analogues have been designed, which may facilitate a fluorescence-displacement approach (Crane *et al*., 2006). Alternatively, Narayanasamy *et al*. described a novel IspF kinetics assay in 2010; which involves coupling CMP release to four enzymes (nucleotide monophosphate kinase, pyruvate kinase, pyruvate oxidase and horseradish peroxidase); which alter the emission wavelength of a fluorescent dye. Future work could also direct effort to developing a simpler kinetics assay (Narayanasamy *et al*., 2010).

CHAPTER 4

*Pa*PabC; STRUCTURAL ANALYSIS

4.1 *Pa*PabC - Overall structure

A single species, ~50 kDa, commensurate with a *Pa*PabC homodimer was observed during size-exclusion chromatography. A dimer was also observed in the X-ray crystal structure. Two polypeptide chains, labelled A and B, constitute the asymmetric unit (Figure 4.1), and crystallographic statistics are presented in Table 4.1.

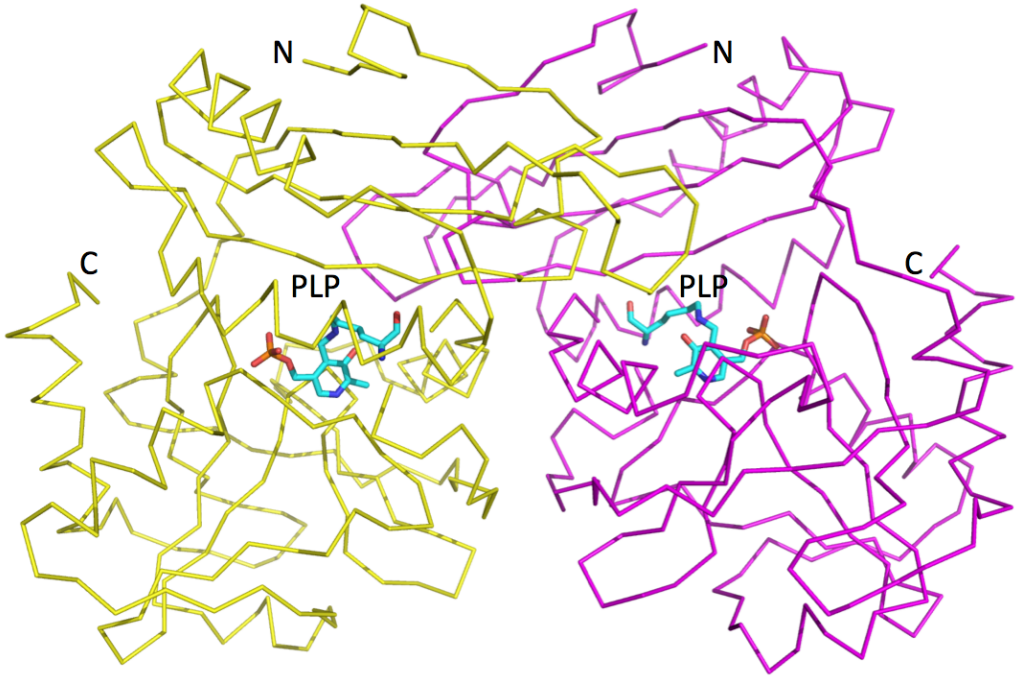

Figure 4.1 The *Pa*PabC dimer. Each subunit is depicted as a Cα trace (yellow and magenta) with PLP shown as a stick model. The N- and C- terminal residue positions are labelled.

The subunits display a high degree of NCS, with an RMSD of 0.4 Å following least squares fitting of 270 Cα positions. It is therefore only necessary to detail one subunit and one active site. The subunit is constructed from two domains (Figure 4.2). The N-terminal domain (domain I) is smaller than the C-terminal domain (domain II). Domain I comprises residues 1–107, which contains three α-helices, α1-α3, and a four-stranded anti-parallel β-sheet in order β1-β4-β3-β2. Domain II comprises residues 112–271 that form five α-helices, α4–α8, one short two-stranded parallel β-sheet, β5–β6, and one short two-stranded anti-parallel β-sheet, β7–β8. Residues 108–111 link the two domains. The PLP cofactor is covalently bound to Lys140 in domain II and the active site is found in a cleft formed between the two domains (Figures 4.1, 4.2, 4.3).

Table 4.1 Crystallographic statistics for *Pa*PabC

PDB code	**2Y4R**
Space group	$P2_12_12_1$
Unit cell dimensions *a, b, c* (Å)	 40.8, 66.8, 202.7
Resolution range (Å)	30.00 - 1.75 (1.84 - 1.75)
No. reflections	209336 (26399)
Unique reflections	56255 (8090)
Completeness (%)	98.9 (98.5)
R_{merge}	7.8 (45.1)
Multiplicity	3.7 (3.3)
$< I/\sigma(I)>$	10.7 (2.5)
Wilson *B* ($Å^2$)	18.4
R_{work}/R_{free}	16.7, 21.5
Number of residues / waters / ligands	538 residues, 474 waters, 2 PLP, 3 Cl^-, 2 SO_4^{2-}, 2 glycerol, 3 di(hydroxyethyl)ether, 5 tetraethylene glycol, 3 1,2-ethanediol
RMSD bond lengths (Å) / bond angles (º)	0.025 2.100
Mean *B*-factors ($Å^2$) Main chain, side chain Waters Ligands	 Chain A: 15.1, 18.2 Chain B: 18.5, 20.7 30.8 (PLP) Chain A: 15.8, Chain B: 21.5 36.3 (other ligands)
Ramachandran plot Favoured regions (%) Allowed regions (%) Outliers	 93.7 5.7 3 outliers: Arg90A & B, Leu89B

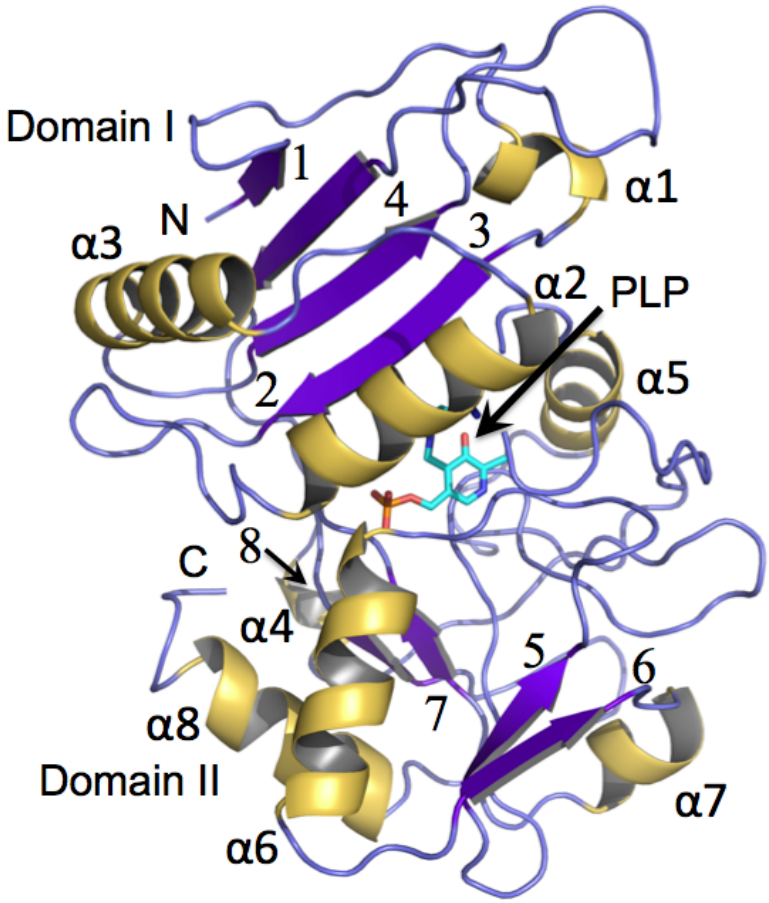

Figure 4.2 Ribbon diagram of the *Pa*PabC monomer. Secondary structural elements have been numbered and the position of PLP is indicated. β-strands are shown in purple, α-helix in yellow.

Sixty residues from each subunit, provided by both domains, contribute to dimer formation. These residues participate in around 30 hydrogen-bonding associations and eight salt bridge interactions to stabilise the quaternary structure. Most of the residues that contribute to the dimer interface are found in two patches; residues Ala10 - Gly25 centred on α1 and residues Arg127 - Ala152 centered on α5. The approximate dimensions of the dimer are 80 × 40 × 40 Å and this displays a solvent accessible surface area of approximately 21000 Å^2. The contact area between the two subunits covers approximately 2050 Å^2, about 15% of the surface of a subunit. These values are similar to those observed for other PabC proteins; for example the interface of the *E. coli* protein (Nakai *et al.*, 2000) covers an area of 2130 Å^2.

The structures of PabC from three organisms, *E. coli*, *L. pneumophila* and *T. thermophilus*, display a high degree of structural conservation with *Pa*PabC. Least

squares fitting of the Cα positions of single subunits results in RMSD values between 1.3 - 2.0 Å, with a coverage in the range of 81 - 92% of the structures. The sequence identity shared with *Pa*PabC, falls in the range 26 - 35%.

4.2 PLP cofactor binding site and interactions

The active site of *Pa*PabC is positioned between the two domains of the monomer close to the dimer interface (Figure 4.1). Here, the PLP cofactor is covalently linked to Lys140 and oriented by interactions with key residues, a selection of which are depicted in Figure 4.3. The PLP phosphate accepts hydrogen bonds donated by a cluster of main chain amide groups from Val200, Met201 and Ser237, and the side chain of Arg46. The side chain of Arg46 is positioned by interactions with the side chain of Glu28, which in turn accepts a hydrogen bond from His43 ND1. Two well ordered water molecules mediate hydrogen bonding networks linking the phosphate group to Asn178 OD1 and Arg202 N on one side, and the main chain O and N groups of Thr29 on the other. The cofactor ring is sandwiched between Val197 and the main chain of a tripeptide segment comprising Val175-Phe176-Ser177. A hydrogen bond between Asn236 ND2 and the carbonyl of Phe176, in conjunction with bonds formed between the amide groups and side chain of Glu161, determine the conformation of the tripeptide that forms a tight turn between β9 and β10 covering part of the cofactor. The PLP methyl group makes van der Waals interactions with Gln147 CG and is positioned 3.2 Å distant from the carbonyl oxygen of Val175. The geometry of this latter contact is compatible with the presence of a C-H•••O hydrogen bond (Leonard *et al.*, 1995). The side chain of Gln147 is held in place by a hydrogen bond with Arg144 NE. Bonds formed with the carbonyl groups of Leu139 and His141 position the side chain of Arg144. There are also three water molecules, which form a network of hydrogen bonds linking the side chain of Arg144 to other sections of the enzyme (not shown). In

addition the positive dipole from α6 - the closest residue on this helix is Gly199 - provides an attractive force to interact with the PLP phosphate. The side chain of Glu173 displays a degree of conformational freedom with two rotamers being observed. One rotamer places the side chain to accept a hydrogen bond donated from PLP N1 (Figure 4.3). The alternative rotamer places the carboxylate at a distance of 3.7 Å from N1. Tyr92 from the partner subunit forms a hydrogen bond to PLP O3. The cofactor is also likely to posses an intra-molecular hydrogen bond involving O3 and NZ of Lys140. The side chain of Phe27, Val197 and aliphatic components of Arg46 and Arg144 surround the side chain of Lys140 (not shown).

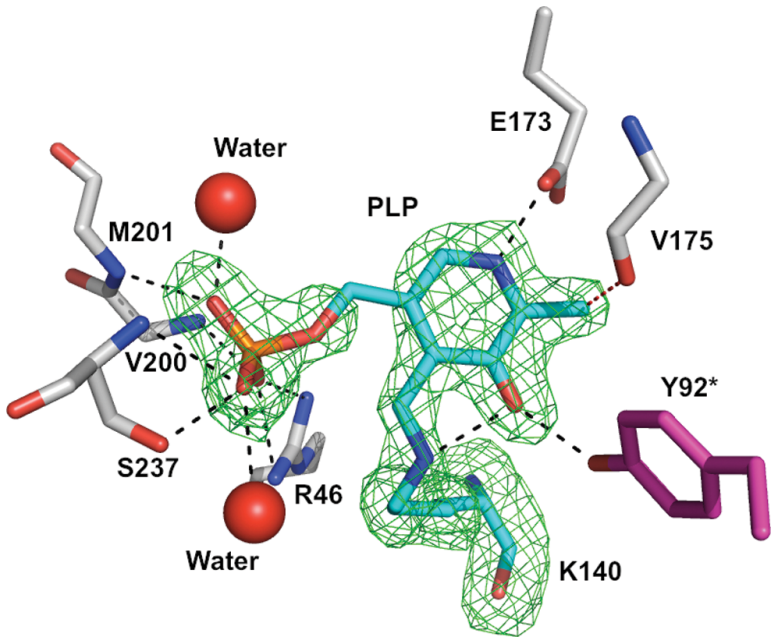

Figure 4.3 Omit map for PLP and Lys140 from subunit A of *Pa*PabC. $|(F_o)-(F_c)|$ difference density contoured at 3 σ (green chicken wire). Selected hydrogen bonding associations between the protein, two water molecules (red spheres) and PLP are depicted as dashed lines. An asterisk marks Tyr92 contributed from subunit B. The side chain of Glu173 displays two rotamers with only one shown.

No structures of PabC-ternary complexes have yet been published to inform on aspects of substrate recognition and enzyme activity. It was considered important to attempt structural determination of *Pa*PabC in complex with a number of compounds including PABA, pyruvate, phenylpyruvate, thiomersal and sulfanilamide. For example, the structure reported here was crystallised in the presence of 10 mM PABA. However, no electron density compatible with binding of any such ligand in the

substrate-binding pocket has been identified. Therefore, the position of PLP and Lys140 NZ, together with the conservation of amino acid sequence and structures was judged to give an indication of where substrate binds; as well as which residues are important for substrate recognition and catalytic function. Consideration of an amino acid sequence alignment and structural overlay of *Pa*PabC with three other structures in the PDB proved particularly informative (Discussion) when combined with molecular modelling and docking of the covalent intermediate formed during catalysis.

4.3 *Pa*PabC active site – Comparision with orthologues

Overlays of *Pa*PabC with the structures of three orthologues were generated, together with sequence alignments, for comparison of active site residues. The contributions of 24 residues within 5 Å of PLP to binding the cofactor (Section 4.2) and organising the active site are summarised in Figure 4.4. Seven of these residues are strictly conserved in PabC from *P. aeruginosa*, *E. coli*, *L. pneumophila* and *T. thermophilus* (Phe27, Thr29, His43, Arg46, Gly199, Lys140 and Arg202 in *Pa*PabC). With one exception these residues contribute to the active site using the chemical properties of their side chains. The exception is Gly199 where any alteration on Cα would result in a steric clash with the phosphate group of PLP. Another seven residues contribute to the active site primarily through the hydrogen bonding capacity of the main chain (Val175, Phe176, Ser177, Leu139, His141, Val200 and Met201). Phe176 is not conserved in any of the three other sequences but the remainders are conserved in at least one other orthologue. Ser237 interacts with the PLP phosphate using main chain and side chain groups. This residue is only different in the *E. coli* sequence where it is replaced by an alanine and an additional water molecule binds nearby helping to satisfy hydrogen-bonding capacity. A similar observation is made when considering *Pa*PabC Asn236. This residue is conserved in *Ec*PabC and *Lp*PabC but is changed to glycine in *Tt*PabC

where a water molecule is observed to replace the side chain. Asn178 is strictly conserved in *Ec*PabC and *Lp*PabC but changed to serine in *Tt*PabC. The side chain here helps to form one side of the cofactor-binding site. Val197 is conserved in *Ec*PabC and conservatively substituted as leucine in the other two sequences. The residue at this position in the active site forms van der Waals interactions with the cofactor. In *Pa*PabC Arg144 NE donates hydrogen bonds to Gln147 OE1 and the carbonyl of His141; interactions that help to create one side of the cofactor-binding site and to fix the position of Val197. These residues and the interactions they form are conserved in *Ec*PabC but not in *Lp*PabC or *Tt*PabC. Sequence and structure alignments indicate that *Pa*PabC Arg144 is replaced by tyrosine in both *Lp*PabC and *Tt*PabC, and *Pa*PabC Gln147 replaced by an alanine in *Lp*PabC and a tyrosine in *Tt*PabC (Discussion).

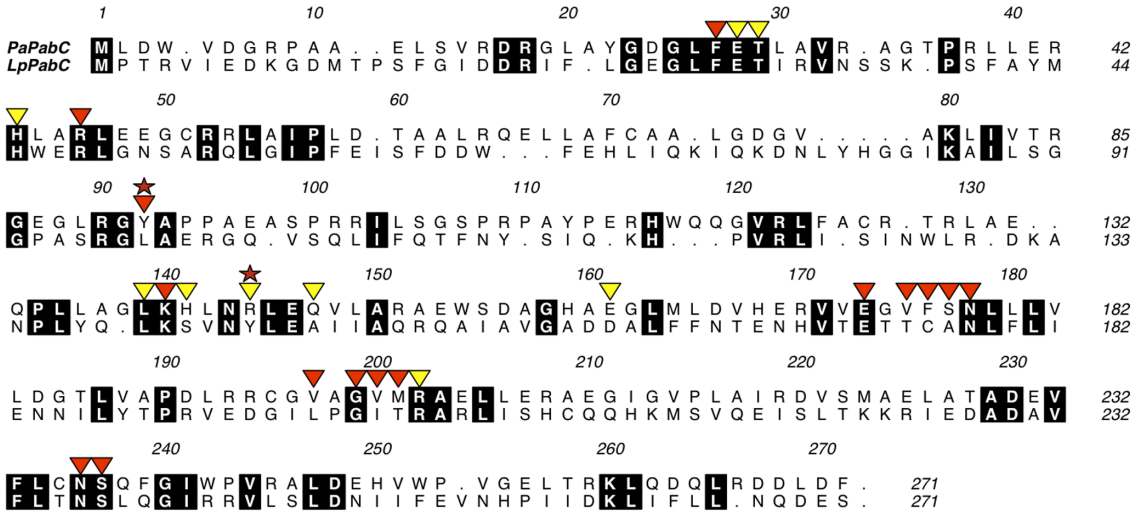

Figure 4.4 Alignment of *Pa*PabC and *Lp*PabC. Residues encased in black are strictly conserved. Red stars indicate the tyrosine residues at position I (*Pa*PabC Y92), and position II (*Lp*PabC Y144). Triangles mark residues that are discussed in the text. Red triangles identify Lys140 and residues that interact directly with the Lys140-PLP adduct; yellow triangles mark residues that contribute to the organisation of the active site or that participate in solvent mediated interactions between the protein and the cofactor.

There are three glutamates among the 24 residues discussed above (Glu28, Glu161 and Glu173). Glu28 helps to position Arg46 to bind the cofactor phosphate. Both residues are strictly conserved in *Lp*PabC. A conservative substitution of the glutamate to threonine occurs in both *Ec*Pabc and *Tt*PabC, and the interactions to support the binding of arginine to the cofactor are preserved. Glu161 helps to configure

a tripeptide segment to cover part of the cofactor (not shown) and this feature is conserved since a glutamate is present in the other structures (an aspartate occupies this position in *Lp*PabC). The carboxylate side chain of Glu173 can interact directly with the cofactor by accepting a hydrogen bond donated from N1. In a similar fashion to what is observed for Glu161, such interactions occur in the orthologues with the residue either strictly conserved, or as in *Tt*PabC, replaced by aspartate.

4.4 *Pa*PabC - Discussion

A catalytic mechanism, based on previous studies of PLP-dependent enzymes, was proposed for PabC prior to any structural data being available (Green *et al.*, 1992). Following structure determination of *Ec*PabC, a model of substrate binding was prepared to inform an assessment of the mechanism (Nakai *et al.*, 2000). The contribution of PLP was considered the same, that is, following covalent linkage the enzyme-cofactor adduct undergoes a nucleophilic attack by the substrate amino group to produce an external aldimine. PLP, which contains a conjugated electronic structure linked to the pyridine-ring nitrogen N1, acts as an electron sink; weaking the bond between the α-proton and C4 of the substrate (Figure 1.10). The PLP-substrate species then undergoes α-proton elimination, to the ε-amino group of a lysine to yield a quinonoid intermediate. In *Ec*PabC Lys159 forms the covalent link to the cofactor and is likely responsible for α-proton abstraction. Nakai *et al.*, further suggested that Thr28 of *Ec*PabC supplies a proton, converting the methylene group of the substrate to a methyl group as pyruvate is released. PABA is released and the Schiff-base form of the enzyme is recovered as PLP reacts with Lys159 (Figure 4.5).

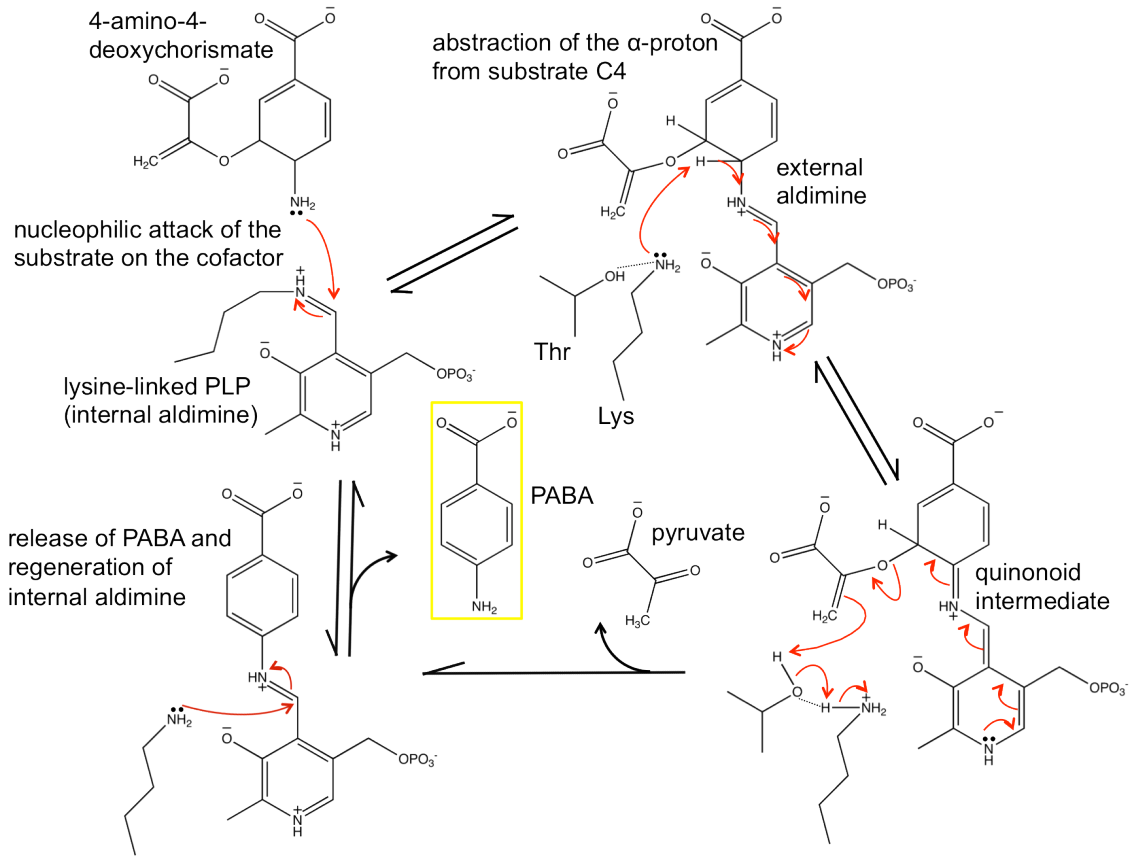

Figure 4.5 Proposed catalytic mechanism of PabC. Curly arrows indicate the flow of electrons. The amino group of the substrate, 4-amino-4-deoxychorismate, attacks the Schiff-base to form an external aldimine. The displaced lysine is proposed to abstract the α-proton from the substrate at C4, producing a quinonoid intermediate. Aromatisation of the substrate ring leads to the loss of pyruvate. Concomitant with the loss of pyruvate a suitably placed threonine is proposed to act as a proton donor to facilitate conversion of methylene to methyl. Regeneration of the internal aldimine following nucleophilic attack of lysine displaces PABA (highlighted in a yellow box).
(Mechanism described in Nakai *et al.*, 2000)

Three residues described as contributing to the mechanism of action in *Ec*PabC, Thr28, Lys97 and Lys159 (Nakai *et al.*, 2000), are strictly conserved in *Pa*PabC as Thr29, Lys80 and Lys140. They are also conserved in *Lp*PabC and *Tt*PabC with the conservative change of Lys80 to arginine in the thermophilic orthologue (Figure 4.4). Lys140 of *Pa*PabC is suitably placed to support α-proton abstraction and although Thr29 may engage in the proposed proton shuffling with both the olefin moiety of the substrate and Lys80, an alternative residue (Tyr90) might fulfil this role. Tyr90 may have been overlooked because Nakai *et al.*, had access to only a single structure of PabC. Alignments based on sequences alone would not identify a tyrosine that is conserved in the three-dimensional structure.

In *Ec*PabC and *Pa*PabC tyrosine hydroxyl groups (Tyr109 and Tyr92 respectively), from the partner subunit, donate a hydrogen bond to PLP O3 (Figures 4.3, 4.5) in an interaction that influences the electronic structure of the cofactor (Nakai *et al.*, 2000). The sequence alignment of PabC orthologues suggests a degree of variation in the identity of the amino acid that occupies the position of this tyrosine (Figure 4.4). In contrast, the structural overlays are striking since they clearly identify a spatially conserved tyrosine in relation to the cofactor (Figure 4.6). In *Ec*PabC and *Pa*PabC, Tyr109 and Tyr92 respectively, are contributed from the partner subunit (position I). However, in *Lp*PabC and *Tt*PabC, Tyr144 and Tyr130 respectively, are contributed from the same subunit (position II).

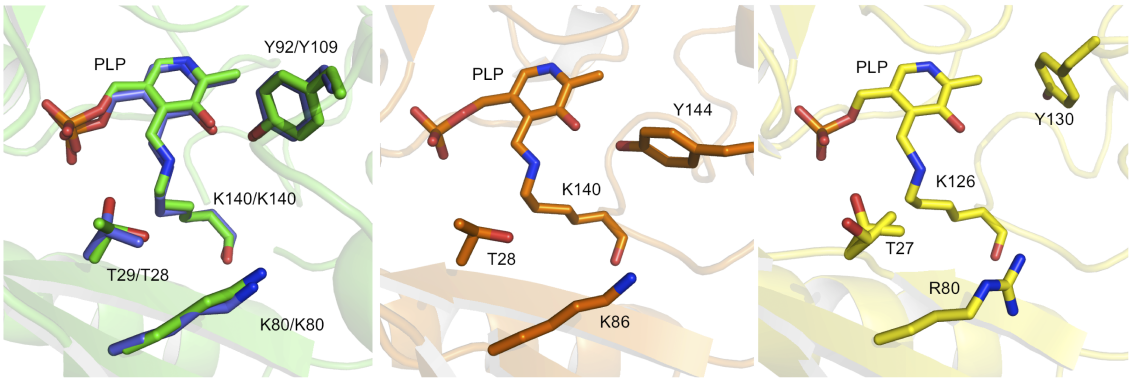

a) **b)** **c)**

Figure 4.6 Structural conservation of tyrosine in the PabC active site. PLP is shown in the same manner as Figure 4.3. **a)** A structural overlay of *Pa*PabC (green C atoms) and *Ec*PabC (blue C atoms). Here, Tyr92 and Tyr109, which represent position I, are contributed from the partner subunit. **b)** *Lp*PabC. **c)** *Tt*PabC. Thr27 displays two rotamers. In the *Lp*PabC and *Tt*PabC structures, Tyr144 and Tyr130 respectively represent position II and belong to the same subunit that forms the PLP-binding site.

A conservative group of 129 putative PabC sequences were retrieved from the UniProt database, aligned using *MUSCLE* (Edgar, 2004) and then inspected following pairwise alignment with *Pa*PabC. This was done to investigate the distribution of tyrosine at these two positions (I & II); seeking to address the hypothesis that if tyrosine is present at position I then it is likely absent from position II and *vice versa*. This hypothesis holds true for 125 out of the 129 sequences. Two sequences, which share less than 30% sequence identity, have a tyrosine at both positions. Analyses of the sequences suggests that PabC can be classified into two groups depending on whether

this active site tyrosine is provided by the same subunit which primarily forms the active site or from a partner subunit.

The high degree of conservation of an active site tyrosine in three-dimensional structures of PabC suggests a functional role. One possibility is that this residue could act as a proton donor for the conversion of methylene to methyl that completes the reaction. Such a conversion would have little influence on the cleavage of the C-O bond of the substrate since the driving force for that reaction would be production of an aromatic six-carbon ring system. A model of the catalytic intermediate (4-amino-4-deoxychorismate linked to PLP, Figures 4.5, 4.7) was specifically prepared to investigate the potential role of this active site tyrosine and to re-evaluate the olefin conversion process that completes the reaction (calculations were performed by Dr. Thomas Eadsforth).

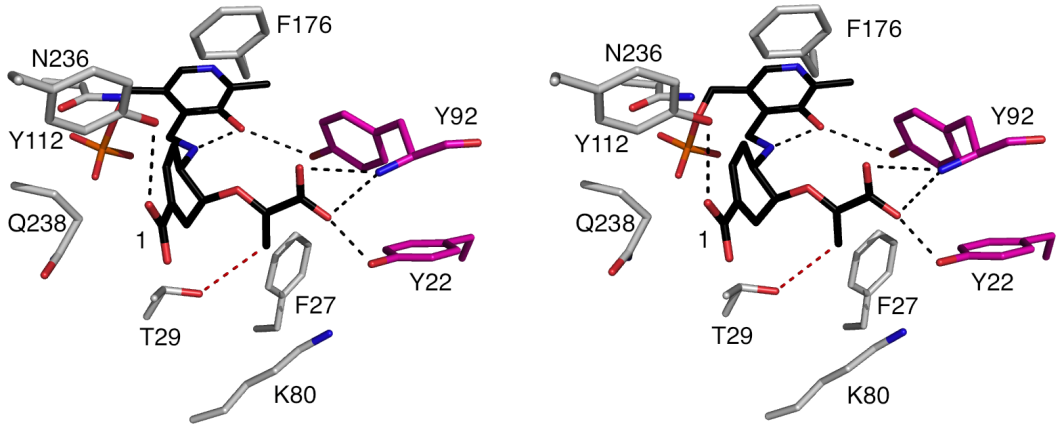

Figure 4.7 A stereoview of the catalytic intermediate docked into the active site of *Pa*PabC. Protein components are coloured as in Figure 4.3. The C atoms of the modelled intermediate (1) are in black. Black dashed lines represent potential hydrogen bonding interactions, with a separation of 3.5 Å or less, and the red dashed line between Thr29 OG1 and the sp^2 hybridised C indicates the proximity of functional groups likely involved in catalysis.

The model was prepared using the *PRODRG* server (Schüttelkopf & van Aalten, 2004) and placed in the active site with *COOT* using the position of PLP as a guide. Docking in the active site was performed using *ICM pro* (MolSoft L.L.C.) with the centre of the ligand-binding site defined by a cavity that contained the residues within 5

Å of the ligand. The top ten docking poses, as scored by *ICM pro* gave similar orientations in the active site and one was selected for display.

The model suggests that Tyr112 donates a hydrogen bond to the C1 carboxylate while, with contributions from the partner subunit, the main chain amide of Tyr92 and hydroxyl group of Tyr22 donate hydrogen bonds to the other carboxylate of the intermediate (Figure 4.7). Tyr92 contributes to the positioning and electronic structure of the cofactor by virtue of the hydrogen bond involving the hydroxyl group with the PLP carbonyl (Figure 4.3). For example, it has been suggested that a tyrosine at a similar position in the PLP-depedent enzyme aspartate aminotransferase affects the pK_a of the Schiff base; and this has been investigated by generating Tyr-Phe mutants (Goldberg *et al*., 1991; Inoue *et al.*, 1991). The bulk of the tyrosine side chain serves to create a hydrophobic wall on one side of the active site. Although placed to interact with the catalytic intermediate this residue does not appear to be involved in donating a proton to convert methylene to methyl (Figure 4.7). Rather, Thr29, as first postulated by Nakai *et al.*, appears to fulfil such a role with the hydroxyl group placed about 3.5 Å from the olefin (Figure 4.7). Lys80 NZ is around 4.3 Å distant from the sp^2 hybridised C and it is possible that an alternative rotamer could bring this functional group into proximity; providing a proton itself or activating the Thr29 hydroxyl for proton donation. Thr29 is strictly conserved in 123 out of the 129 PabC sequences and conservatively substituted by serine in another five sequences.

To further investigate the structure-activity relationship of PabC, and to assess the potential of this enzyme as a target for structure-based drug discovery will require the powerful combination of steady-state kinetic analysis with site-directed mutagenesis studies, alongside screening of chemical libraries. In particular, the construction of Tyr92-Phe, Thr29-Ala, Lys80-Met and Glu173-Gln mutants will permit assessment of the contribution of these residues to catalysis (Goldberg *et al*., 1991; Inoue *et al.*, 1991).

Following production of the substrate from commercially available chorismate and glutamine by recombinant PabA-PabB, the kinetics of PabC can be assayed by determining the production of PABA upon addition of the enzyme. This would involve taking aliquots at various time-points, incubating in 1 M HCl to inactivate the enzymes, and then quantifying PABA concentrations using HPLC (He *et al*., 2004; and references therein). UV-visible spectroscopy could be performed in parallel to gain insight into the electronic structure of the PLP cofactor (Fasella, 1967). Substrate-analogues containing Michael acceptors or halogens could also be considered during inhibitor design and testing, since these may potentially form covalent adducts with the cofactor (Eliot & Kirsch, 2004). It will be imperative to extend from this work and to elucidate a means whereby structural data on enzyme-ligand complexes can be obtained.

PART TWO

IMMUNITY PROTEINS IN THE GRAM-NEGATIVE TYPE VI SECRETION SYSTEM

CHAPTER 5

Rap1a and Rap2a -

INTRODUCTION AND METHODS

Introduction

Preamble: Dr. Vincent Rao and Dr. Velupillai Srikannathasan performed the purification, crystallisation and X-ray data collection of Rap1a and Rap2a respectively. My contribution to this project involved the processing of datasets, determining the structures by molecular replacement and analysing the results. This work, performed as part of a team, has been accepted for publication and this thesis draws on this source extensively. The relevant publication is referred to throughout as (Srikannathasan *et al*., 2013).

5.1 Type VI secretion systems (T6SS)

Specialised secretion systems are key to bacterial fitness, survival and pathogenesis. They contribute a myriad of roles in the processes that influence growth, colonisation, attack and defense as bacteria interact with each other and with eukaryotic organisms (Filloux, 2011; Gerlach & Hensel, 2007). The recently identified Type VI secretion system (T6SS), present in about 25% of Gram-negative bacteria for which genome sequences are available (Boyer *et al.,* 2009; Pukatzki *et al*., 2006), can be used to target bacterial and eukaryotic cells, and is thus important for both inter-bacterial competition and pathogenesis (Burtnick *et al.*, 2011; de Pace *et al*., 2010; Jani & Cotter, 2010). Anti-bacterial T6SSs mediate efficient killing of competitors by direct injection of toxic, antagonistic effector proteins into target cells (Hood *et al*., 2010; MacIntyre *et al*., 2010; Murdoch *et al*., 2011; Schwarz *et al*., 2010).

T6SS gene clusters encode the core components of a secretion machine capable of membrane perforation (Table 5.1). This is a multi-protein needle-like assembly (Figure 5.1) -resembling the contractile tail of a bacteriophage - that delivers effectors across three envelope layers in a single step (Basler *et al.*, 2012; Bönemann *et al.*, 2010; Cascales & Cambillau, 2012; Silverman *et al*., 2012). The clusters also encode accessory and post-translational regulatory components. Some T6SS-secreted effector proteins are also encoded within these large gene clusters. In the case of anti-bacterial

T6SSs, effectors are always encoded adjacent to specific, cognate immunity proteins. Immunity proteins bear appropriate signals to direct their localisation to the compartment in which the toxic effectors act; for example, a Sec-signal sequence guides localisation to the periplasm. The provision of a cognate immunity protein provides protection against attack from sister cells (Coulthurst, 2013).

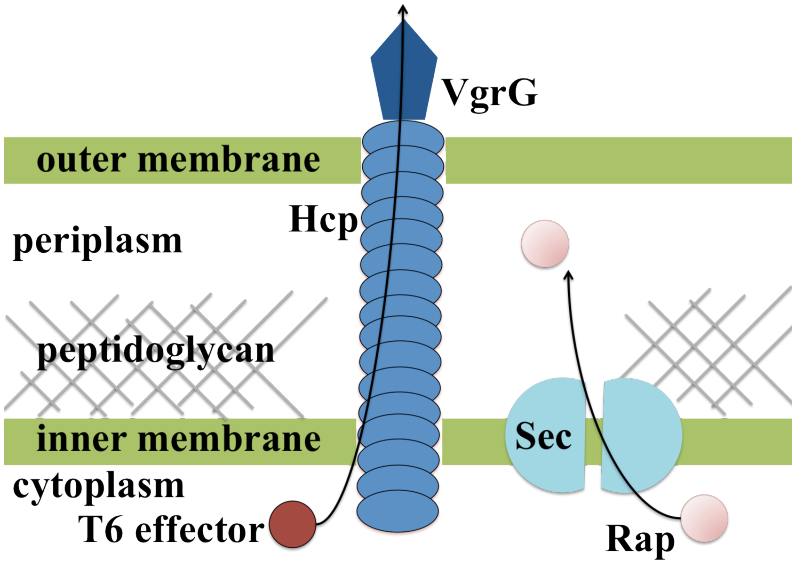

Figure 5.1 Schematic model of the Type VI secretion apparatus. The components of the T6SS assemble to form a cell-puncturing needle that resembles an inverted bacteriophage tail. Hcp protein forms a membrane-spanning tube with an internal diameter of ~40 Å (Mougous *et al*., 2006), and VgrG protein punctures membranes of target cells. Inner and outer membranes are shown as green rectangles, and a grey palisade represents the peptidoglycan layer. Certain immunity proteins such as Rap, shown as a light pink disk, localise to the periplasm *via* the Sec transporter, coloured cyan. Effector proteins of the T6SS (T6 effectors, red disk), such as the peptidoglycan amidase Ssp1 are thought to be secreted into target cells by transit through the Hcp tube.

Different catalytic activities are associated with T6SS effectors. These include actin cross-linking and ADP-ribosylation that disrupt the cytoskeleton of mammalian and amoebal cells (Pukatzki *et al*., 2007; Rosales-Reyes *et al*., 2012; Suarez *et al*., 2010), and phospholipases that degrade phosphatidylethanolamine, the major component of the bacterial membrane (Russell *et al.,* 2013). The best-characterised effectors are peptidoglycan hydrolases, which exhibit potent anti-bacterial activity (Russell *et al.,* 2012; Russell *et al*., 2011). These enzymes degrade peptidoglycan, the

heteropolymer that occupies the periplasmic space imparting mechanical strength to the cell wall and helping to maintain the shape of Gram-negative bacteria.

Table 5.1 Components of the T6SS apparatus
(Cascales and Cambillau, 2012; and references therein)

Components of the T6SS	Localisation of component	Homologous proteins
TssA	cytosol (putative)	n/a
TssB	associates with outer membrane	bacteriophage sheath
TssC	associates with outer membrane	bacteriophage sheath
TssD/Hcp	forms a hexameric ring, secretion tube	bacteriophage tail gp19
TssE	not known	bacteriophage wedge gp25
TssF	not known	n/a
TssG	not known	n/a
TssH/ClpV	cytosol, AAA^+ ATPase	Hsp100/Clp AAA^+ ATPase
TssI/VgrG	forms trimers, cell puncturing device	bacteriophage tail spike gp27-gp5
TssJ/SciN	outer membrane lipoprotein	transthyretin
TssK	cytosol (putative)	n/a
TssL	inner membrane	T4bSS IcmH/DotU protein
TssM	inner membrane	T4bSS IcmF protein

Peptidoglycan hydrolases constitute a large enzyme family, which displays a rich diversity in terms of structure, mechanism and specificity (Vollmer *et al*., 2008). There are enzymes specific for every glycosidic and amide bond in peptidoglycan. Such diversity is exploited to regulate bacterial cell growth, division and daughter cell separation, and of particular interest here, to provide bactericidal properties that can be exploited in niche competition. Several classes of peptidoglycan hydrolase have been identified as T6SS effector proteins. These are termed Tse proteins. Tse3 of *P. aeruginosa* is a muramidase, cleaving the glycan backbone (Russell *et al*., 2011), and the C-terminal domain of *Vibrio cholerae* VgrG-3, a component at the tip of the secretion apparatus (Figure 5.1), is suggested to have lysozyme-like muramidase activity (Brooks *et al*., 2013). A diverse group of T6SS-secreted peptidoglycan amidases, which cleave the peptide cross-links, has been described (Russell *et al*., 2012). Within this superfamily, four distantly-related families with distinct cleavage specificities were defined. Family 1 ('Tae1'), which includes Tse1 of *P. aeruginosa*,

hydrolyse peptide crosslinks at the γ-D-glutamyl-*meso*-diaminopimelate DL-bond; representatives of Families 2 and 3 ('Tae2' and 'Tae3') hydrolyse DD-crosslinks between D-*m*A_2pm (*meso*-diaminopimelate) and D-alanine, and a representative of Family 4, Tae4 from *Salmonella enterica* serovar Typhimurium, also hydrolyses the γ-D-glutamyl- *m*A_2pm DL-bond. Structures of Tse1 from *P. aeruginosa,* and Tae4 from *S.* Typhimurium and *Enterobacter cloacae* (Benz *et al*., 2012; Chou *et al*., 2012; Ding *et al*., 2012; Zhang *et al*., 2013) place these T6-secreted effectors in the NlpC/P60 family of endopeptidases, amidases and acyltransferases; named after the New lipoprotein C from *Escherichia coli* and a 60 kDa extracellular protein from *Listeria monocytogenes* (Anantharaman & Aravind, 2003). The opportunistic pathogen *Serratia marcescens* has recently been shown to utilise T6-dependent secretion of two Family 4 amidases, Ssp1 and Ssp2, to mediate anti-bacterial activity (English *et al*., 2012).

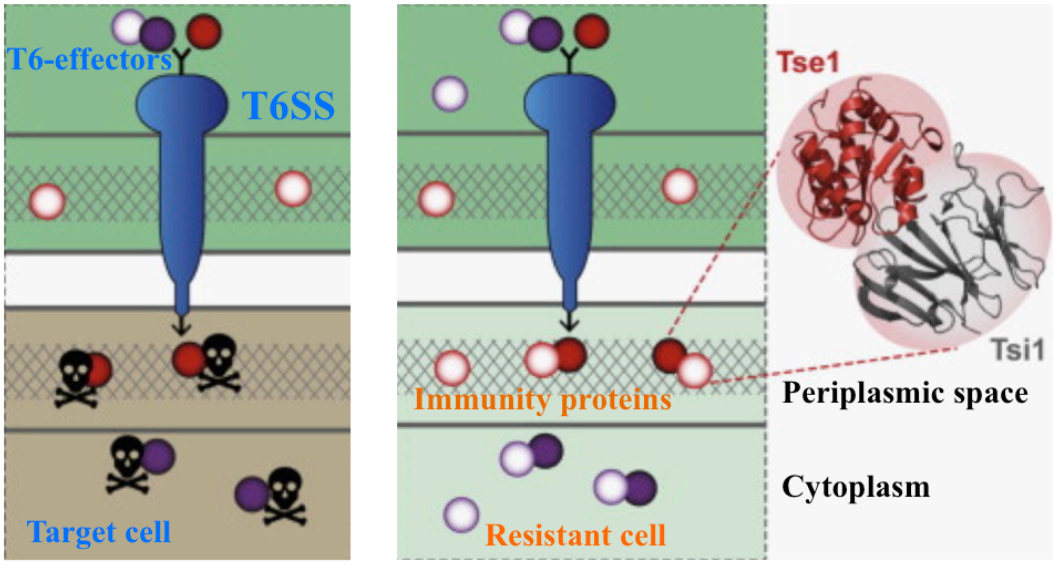

Figure 5.2 The T6SS delivers toxic effectors to target cells. A schematic close-up is depicted of two adjacent bacteria during an attack by one (dark green) using the T6SS. **a)** T6 effectors are translocated from the attacking bacterium into a susceptible target cell, inflicting damage in the periplasmic space or in the cytoplasm. **b)** A resistant cell, such as a sibling of the attacking strain, neutralises T6 effectors through the action of specific immunity proteins. In the example shown, the peptidoglycan amidase 'Tse1' is bound and inhibited by the immunity protein 'Tsi1' (crystal structures inset; Ding *et al.*, 2012). This figure has been adapted with permission from Coulthurst, 2013.

Table 5.2 List of key details for the proteins reported in this thesis (Part 2)

	Rap1a	Rap2a
Source organism	***Serratia marcescens*, strain Db10**	
Number of residues	**101 (mature protein)**	**100 (mature protein)**
Signal sequence omitted	**Yes; 26 residues at N-terminus**	**Yes; 24 residues at N-terminus**
Molecular mass (Da)	**11486.0**	**11106.4**
Theoretical isoelectric point	**6.2**	**5.1**
PDB codes	**3ZFI (1.98 Å resolution)**	**3ZIB (1.90 Å resolution)**
Position of disulfide bonds	**Cys78-Cys122**	**Cys42-Cys102**

Bacteria that secrete potent peptidoglycan hydrolase effectors, using the T6SS to attack competitors, could generate a deleterious effect on their own population. To cope with this potential for 'friendly fire' damage, such bacteria also possess cognate immunity or resistance proteins located in the periplasm (Figure 5.2). These immunity proteins bind their cognate effectors with low nanomolar affinity to neutralise them in a highly specific manner, (English *et al*., 2012). Four distinct families of putative immunity proteins are associated with four Tae amidase families (Tai1-Tai4; Russell *et al*., 2012). In *S. marcescens,* the resistance associated proteins, Rap1a and Rap2a, neutralise Ssp1 and Ssp2, respectively (English *et al.,* 2012). The crystal structures of Rap1a and Rap2a are reported in this thesis (Table 5.2). Rap1a and Rap2a have only marginal sequence identity and are scarcely alignable. Additionally two other Rap proteins, Rap1b and Rap2b are, together with Ssp1 and Ssp2, encoded in the same locus within the T6SS gene cluster. Structures of Rap1b and Rap2b have revealed a novel α-helix fold and dimeric assembly (English *et al*., 2012), which was later observed in the Tai4 protein from *E. cloacae* (*Ec*Tai4) and *S.* Typhimurium (*S*TTai4, Zhang *et al.,* 2013). This fold is a template for some T6SS immunity proteins, called Tsi proteins, but not all. For example, analysis of the Tse1-Tsi1 effector-immunity protein combination found in *P. aeruginosa* revealed Tsi1 as an all-β protein (Benz *et al*., 2012;

Ding *et al*., 2012; Shang *et al*., 2012), whereas Tsi2 in the same organism, the immunity protein associated with the cytoplasmic effector Tse2, has a helical fold distinct again (Li *et al*., 2012). That effector immunity defense systems based on distinct folds have evolved is perhaps to be expected, given the strong evolutionary pressure applied by multifarious secreted effectors. Indeed such pressure may even have contributed to the acquisition of effector-immunity pairs encoded outside of T6SS operons - for example all three Tse/Tsi pairs of *P. aeruginosa*.

5.2 Aims - Part two

Structures of Rap1a and Rap2a from *S. marcescens* were sought to gain insight into their fold and function, and to allow comparison with immunity proteins of known structure.

Methods

5.3 Rap1a and Rap2a - Crystallisation, molecular replacement and analysis

Rap1a was dialysed against 150 mM sodium chloride, 25 mM Tris-HCl, pH 7.5, prior to crystallisation trials. The sitting drop vapor diffusion method was used with 0.2 μL drops in a 1:1 ratio of protein at 9 mg mL^{-1} with reservoir at 20 °C. A slender orthorhombic crystal of Rap1a, approximate dimensions 150 x 35 x 35 μm, grew within one month using a reservoir of 25% PEG 3350 and 100 mM Bis-Tris, pH 5.5. Monoclinic blocks of Rap2a were grown by combining protein at a concentration of 13.5 mg mL^{-1} in 100 mM sodium phosphate, pH 6.4, with a reservoir of 25% PEG 1000 and 0.1 M MES, pH 6.5. These crystals attained a maximum dimension of 200 μm within five days. Crystals were soaked briefly in mother liquor adjusted to contain 20 % (v/v) glycerol as a cryo-protectant prior to being flash-cooled in liquid nitrogen then used for diffraction experiments.

Datasets for Rap1a and Rap2a were collected at Diamond Light Source, indexed and integrated in *iMOSFLM* (Battye *et al*., 2011) and scaled with *SCALA* (Evans, 2006). The structures were solved by molecular replacement in *PHASER* (McCoy *et al.*, 2007). The starting model for Rap1a was taken from the structure of an Ssp1-Rap1a complex that had been solved by Dr. Velupillai Srikannathasan (PDB code: 4BI8; Srikannathasan *et al.*, 2013); while that for Rap2a was a poly-alanine model prepared from the structure of the related Rap protein, Rap2b (PDB code: 4B6I; English *et al.*, 2012). All non-protein atoms were removed from the models and initial *B*-factors were adjusted to match the Wilson *B*-values obtained during scaling. Following successful molecular replacement the models were subject to several rounds of rigid-body refinement followed by real-space refinement in *REFMAC5* (Murshudov *et al.*, 2011),

interspersed with inspection of the electron density maps and model improvement in *COOT* (Emsley *et al.*, 2010). Strict NCS restraints and van der Waals contact distance restraints were applied from the start of refinement. NCS restraints were dropped at a late stage in the refinement following addition of water molecules to the models. Side chains with more than one conformation visible in the density maps were modelled as rotamers with partial occupancies. Model quality was validated using the *MolProbity* server (Chen *et al.*, 2010) and the validation tools found in *COOT*. Coordinates and structure factors for Rap1a and Rap2a have been deposited with the PDB, under codes 3ZFI and 3ZIB respectively.

CHAPTER 6

Rap1a and Rap2a –

RESULTS AND DISCUSSION

6.1 Structure of Rap1a

The structure of Rap1a was determined to 1.98 Å resolution and the amino acid sequence and assigned secondary structure is depicted in Figure 6.1. Crystallographic statistics are presented in Table 6.1.

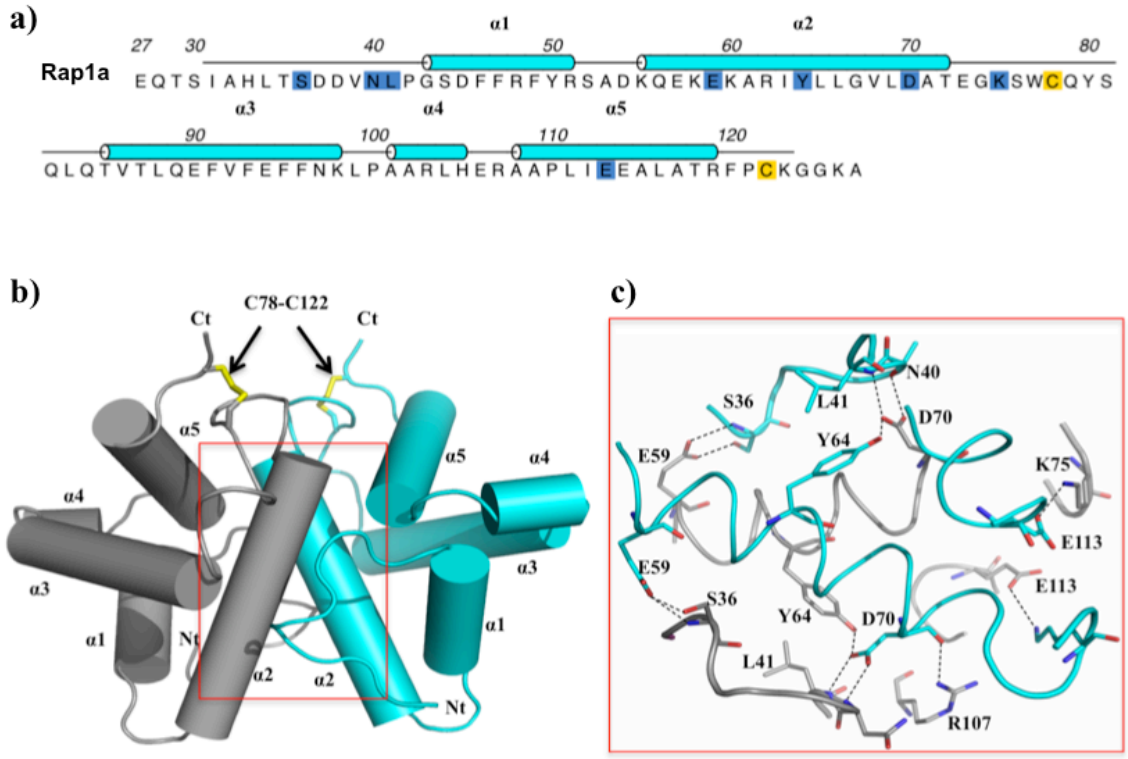

Figure 6.1 Overall structure of Rap1a. **a)** The sequence of mature Rap1a. The 26-residue N-terminal signal sequence is not shown. The assigned α-helical secondary structure is shown and numbered. Residues involved in disulfide bond formation are coloured in yellow and those that contribute to the dimer interface are encased in blue. **b)** Cartoon representation of the Rap1a dimer with labelled helices, Nt and Ct mark the N and C-terminal positions. The disulfides formed between Cys78 and Cys122 are shown as yellow sticks. **c)** Residues and hydrogen bonds (dashed lines) at the dimer interface. C atoms are grey and cyan to distinguish the subunits.

The Rap1a subunit displays a compact globular structure constructed from five α-helices that assemble to form the highly stable, symmetric dimer that constitutes the asymmetric unit (Figure 6.1). This is consistent with the size-exclusion chromatography data, which identified that only a dimer was observed in solution (not shown). The NCS is highly conserved with an RMSD for a least squares overlay of 96 Cα positions of 0.6 Å. A disulfide bond is formed between Cys78 on the α2-α3 loop and Cys122 at the C-terminal region. This interaction appears crucial to stabilising the

subunit fold since it helps position α2, α3 and α5 close to each other and these segments of secondary structure provide the side chains that form the hydrophobic core of the subunit. During initial recombinant expression tests it was noted that soluble protein was produced only in *E. coli* Rosetta-gami (DE3) cells; a strain that promotes the formation of disulfide bonds in the cytoplasm and so mimics what might occur in the oxidative environment of the periplasm. This suggests the covalent bond is necessary for correct folding to occur, and for stability of the Rap1a fold and dimeric quaternary structure.

Table 6.1 Crystallographic statistics for Rap1a and Rap2a

Structure / PDB code	**Rap1a / 3ZFI**	**Rap2a / 3ZIB**
Space group	$C222_1$	$P2_1$
Unit cell dimensions *a, b, c* (Å)	82.7, 93.0, 51.3	39.7, 81.4, 58.5 β 91.5°
Resolution range (Å)	46.50-1.98 (2.09-1.98)	40.67-1.90 (2.00-1.90)
No. reflections	63106 (8849)	214423 (31351)
Unique reflections	14089 (2003)	29067 (4190)
Completeness (%)	99.9 (100.0)	99.4 (98.9)
R_{merge}	6.6 (48.6)	9.7 (51.6)
Multiplicity	4.5 (4.4)	7.4 (7.5)
$< I/\sigma(I) >$	13.4 (2.7)	15.3 (4.0)
Wilson *B* ($Å^2$)	31.5	21.7
R_{work}/R_{free}	19.2, 23.4	18.3, 23.4
Number of residues / waters	185, 57	377, 137
RMSD bond lengths (Å) / bond angles (º)	0.018 1.925	0.019 1.745
Mean *B*-factors ($Å^2$) Main chain, side chain Waters	 Chain A 34.3, 40.9 Chain B 35.2, 40.0 38.4	 Chain A 19.7, 23.7 Chain B 23.0, 28.3 Chain C 22.4, 27.5 Chain D 18.9, 24.0 30.6
Ramachandran plot Favoured regions (%) Allowed regions (%) Outliers	 97.0 3.0 No outliers	 99.0 1.0 No outliers

Interactions involving residues on α2 make the major contribution to dimer formation. Each subunit contributes a surface area of 1130 $Å^2$ to the dimer interface, which is 20 % of the solvent accessible surface area (ASA, 5700 $Å^2$) of a subunit. Such a percentage of surface area is indicative of a stable association. Nine residues from each subunit form a network of hydrogen bonds using both main chain and side chain functional groups (Ser36, Asn40, Leu41, Glu59, Tyr64, Asp70, Lys75, Arg107 and Glu113; Figure 6.1). There are also indirect hydrogen bonding interactions *via* well-ordered water molecules that link a number of side chains and main chains (not shown). Hydrophobic interactions that contribute to the stability of the dimer mainly involve the aliphatic side chains of Val39, Ile63, Leu66, Val68 and Ala71 but also Tyr80 (not shown).

Overlays were attempted with the structures of known immunity proteins, including Rap2a (Section 6.2), Rap1b, Rap2b from *S. marcescens* (English *et al.*, 2012), and the Tai4 proteins (Zhang *et al.*, 2013), however these proteins were all dissimilar from Rap1a. Thus Rap1a adopts a unique fold for an immunity protein. A search using the *DALI* server identified two proteins, YmgD and HdeA from *E. coli*, with some degree of structural similarity to Rap1a. Both are acidic, α-helical periplasmic proteins, and overlays in *COOT* and *PyMOL* show that almost all secondary structural elements match. YmgD and HdeA contain 89 and 90 amino acids respectively, discounting residues in periplasmic localisation sequences - for comparison, mature Rap1a contains 101 residues.

YmgD (UniProt: P0AB46) shares 13% sequence identity with Rap1a and is a functionally uncharacterised homodimeric protein that becomes up regulated in response to alkaline-stress (pH > 8.0, Maurer *et al.*, 2005). The structure has been determined by NMR (PDB codes: 2LRV and 2LRM, Wang *et al.*, unpublished) and aligns 81 Cα positions to Rap1a with an RMSD of 3.4 Å (Figure 6.2).

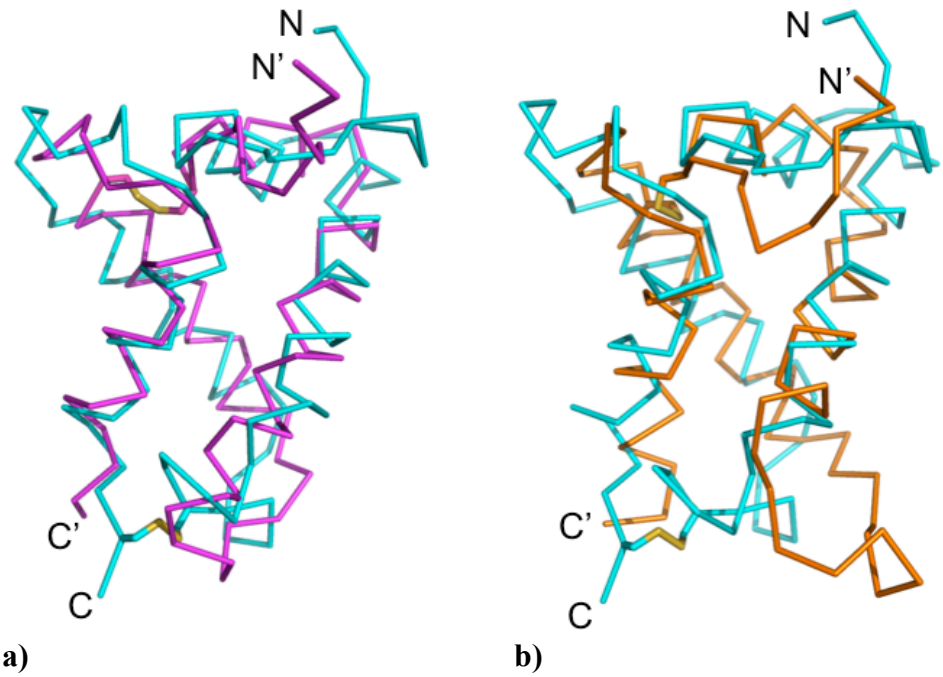

Figure 6.2 Superimposition of YmgD and HdeA on Rap1a. **a)** Superimposition of YmgD on Rap1a. Rap1a is coloured cyan and YmgD is coloured magenta. **b)** Superimposition of HdeA on Rap1a. HdeA is coloured orange. Disulfides are displayed as sticks in yellow, protein backbones are displayed as Cα traces.

HdeA (UniProt: P0AES9), which has marginal sequence identity with Rap1a (~5%), is a periplasmic acid-stress chaperone. HdeA forms a well-ordered, inactive homodimer at neutral pH, but under acidic conditions (pH < 3) it dissociates into partially unfolded monomers and binds to other periplasmic proteins; acting as a chaperone that prevents aggregation (Foit *et al.*, 2013; Hong *et al.*, 2005). The crystal structure has been determined by two different groups (PDB codes: 1DJ8, Gajiwala & Burley, 2000; and 1BG8, Yang *et al.*, 1998) and aligns 72 Cα positions with Rap1a, with an RMSD of 2.9 Å (Figure 6.2). Disulfide bonds are present at a similar position in both YmgD (Cys36-87) and HdeA (Cys39-87), but different from that in Rap1a (Cys78-122). Such similarity between Rap1a and these periplasmic chaperones suggests the possibility of an evolutionary link from a common ancestor.

In the structure of the Ssp1-Rap1a complex (Srikannathasan *et al.*, 2013) there are two molecules in the asymmetric unit, one Ssp1 and one Rap1a, and a crystallographic two-fold axis generates a heterotetramer (Figure 6.3). The overall

dimensions of this assembly are approximately 90 x 50 x 50 Å. The solvent accessible surface area of Ssp1 is 5840 Å^2, and about 16% of this is occluded when the complex with Rap1a is formed (Srikannathasan *et al.*, 2013).

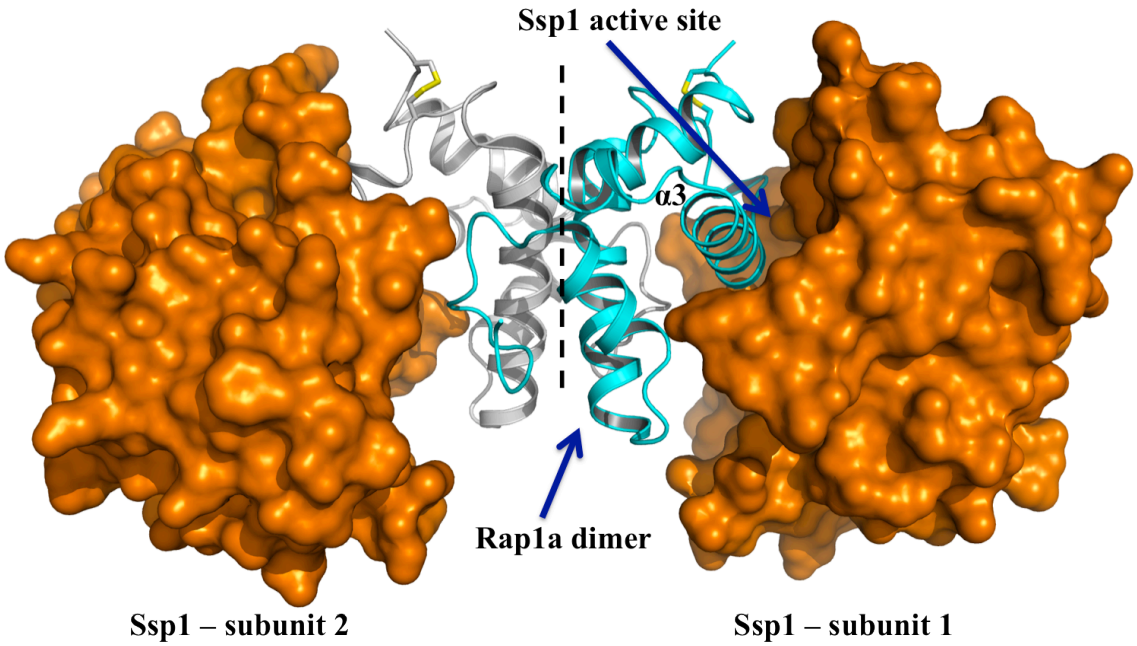

Figure 6.3 The heterotetrameric Ssp1-Rap1a complex. Ssp1 is shown as van der Waals surface in orange, and the Rap1a subunits as grey and cyan ribbons. A dashed line running through the centre of the figure indicates the position of the crystallographic axis of symmetry. Disulfide bonds in Rap1a are displayed as yellows sticks. An arrow indicates the location of the active site in Ssp1 subunit 1. Rap1a sterically blocks the Ssp1 active site; Rap1a α3 is highlighted. This figure has been adapted from Srikannathasan *et al.*, 2013.

Both α3 and the α3-α4 loop of Rap1a are directly positioned to block the Ssp1 active site (Figure 6.3). Gln84 of Rap1a forms a hydrogen bond with Nδ of the catalytic Ssp1 His133 and is a clear marker of the steric block provided by the immunity protein. An overlay (not shown) of the two Rap1a structures, alone and in complex with Ssp1, gives an RMSD of 0.4 Å for 94 Cα atoms indicating that the overall structure is highly similar with no major conformational differences. Therefore, Rap1a is a pre-formed binding partner for Ssp1 under the right redox state. However, there is a localised effect following complex formation. In Rap1a, the segment linking α2 and α3, residues 74 to 84 shows high average *B*-factors, 76.4 Å^2, compared to the overall average *B*-factor,

31.5 Å^2, and relatively diffuse electron density. This region contributes to Ssp1-Rap1a complex formation and becomes well ordered with an average *B*-factor of 15.6 Å^2 compared to the overall *B*-factor of 22.6 Å^2 for the Rap1a component of the complex (Srikannathasan e*t al.*, 2013).

6.2 Structure of Rap2a

Rap2a, like Rap1a, is predicted to be localised in the periplasm and could only be produced in soluble recombinant form using the *E. coli* Rosetta-gami (DE3) strain. It is also a stable dimer in solution as shown by size-exclusion chromatography (English *et al*., 2012). The structure was determined at 1.9 Å resolution with four molecules in the asymmetric unit arranged as two dimers (Table 6.1). These four molecules, subunits A:B and C:D, are similar overall with RMSD values between superimposed Cα atoms ranging from 0.6 Å - 0.7 Å. Minor deviations from NCS are present in a five-residue loop between α2 and α3, Gly67-Leu71, and indicate some conformational freedom in that part of the molecule. The ASA of a Rap2a subunit averages out at approximately 6110 Å^2. Each dimer covers an area that is approximately 20 % of the ASA.

The Rap2a subunit displays a compact globular structure of five α-helices with an extended loop linking α3 to α4 (Figure 6.4). A disulfide bond between Cys42 and Cys102 links α1 with α4 and interactions from these elements of secondary structure help to create the helical bundle fold and in particular to align α2. Together α1, α2, the α2-α3 loop and α4 form the dimer interface, giving rise to a two-fold NCS axis, and here a combination of hydrogen bonding, salt bridge and van der Waals interactions serve to stabilise the association (not shown). Main chain hydrogen-bonding contributions come from the amides of Ser48, Ala49, Met97, Thr98 and Met99 on both chains. Side chain contributions come from the hydroxyl groups of Tyr28 and Tyr47,

and carboxylates of Glu51, Asp55 and Asp104. There are in addition several solvent mediated contacts that serve to link functional groups on partner subunits (not shown). The side chains of Leu39, Ile43, Tyr47, Val52, Met99 and Ile103 are involved in van der Waals interactions with the partner subunit to stabilise the dimer.

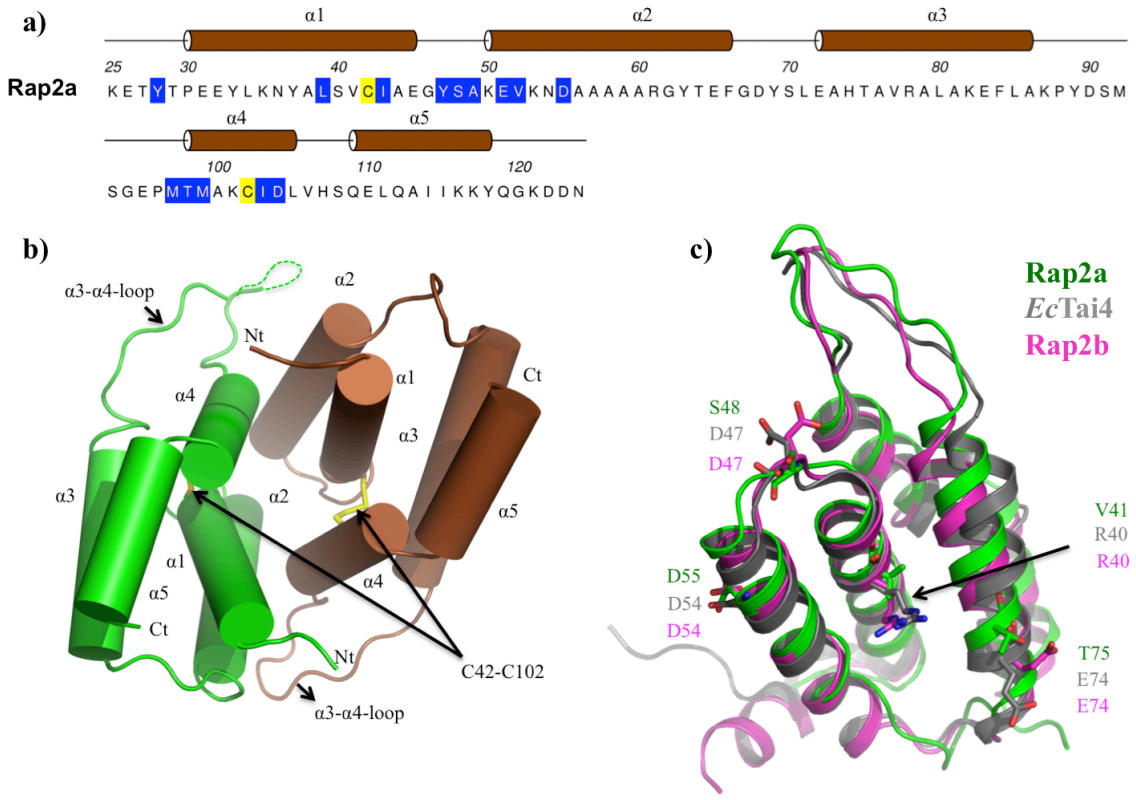

Figure 6.4 Overall structure of Rap2a. a) The amino acid sequence with assigned secondary structure and helices numbered. Residues involved in disulfide bond formation are coloured in yellow and residues involved in subunit-subunit interactions are encased in blue. **b)** Cartoon representation of the Rap1a dimer with subunits coloured brown and green. The disulfides, N and C termini are labelled. **c)** Cartoon representation of Rap2b (magenta; English *et al*., 2012) and *Ec*Tai4 (grey; Zhang *et al.*, 2013) superimposed on Rap2a (green). Selected residues are displayed as sticks. In *Ec*Tai4, Asp54 and Asp47 contribute to the hydrogen-bonding network at the dimer interface and are absolutely conserved in Rap2b, while in Rap2a Asp47 is replaced by Ser48. *Ec*Tai4 Arg40 and Glu74, conserved in Rap2b, have a major role in binding with the T6 effector *Ec*Tae4 (Zhang *et al.*, 2013) - these residues are replaced by Val41 and Thr75 in Rap2a.

Despite a low level of sequence conservation, the structural similarities of five T6SS immunity proteins (Rap1b, Rap2a, Rap2b, *Ec*Tai4 and *S*TTai4) indicate an orthologous sub-set. This structurally defined set is consistent with the designation of a 'Tai4' family of immunity proteins cognate to Tae4 effectors (Russell *et al*., 2012). Pairwise comparisons indicate a range of sequence identities from 18 to 38%, and

matching between 90 and 92 Cα positions gives an RMSD range of 1.2 to 1.7 Å, indicative of a close structural similarity (Table 6.2). Such similarity is exemplified by superimposition of Rap2a, Rap2b and *Ec*Tai4 (Figure 6.4). Strikingly, the extended or protruding loop structure is structurally conserved between these species, despite high variability in the amino acid sequence (English *et al*., 2012; Zhang *et al*., 2013). Parts of the *Ec*Tai4 subunit involved in interaction with an effector, identified by Val41 and Thr75 of Rap2a, are also well conserved in terms of three-dimensional structure (Figure 6.4).

Table 6.2 Structural similarity of Rap2a to known Tai4-family proteins.

Structure (PDB code)	*S*TTai4 (4HFF)	Rap2b (4B6I)	*Ec*Tai4 (4HFK)	Rap1b (4AX2)
% sequence identity to Rap2a	38	23	18	21
No. Cα / RMSD (Å)	92 1.3	92 1.2	90 1.6	91 1.7

This sub-set of immunity proteins also displays similar dimer structures and the Cys42 - Cys102 disulfide bond in Rap2a is conserved in the other two *S. marcescens* proteins, Rap1b and Rab2b, highlighting the importance of this covalent interaction to the creation of the subunit fold and stable quaternary structure. In the structure of *Ec*Tai4 and *S*TTai4 there are conserved cysteines that match to the disulfide forming residues in the Rap proteins however they are in a reduced form. In *S*TTai4 for example the Cys48 SG Cys108 SG distance is 3.6 Å and the electron density unambiguously defines reduced cysteine residues. This difference in the redox states may simply reflect distinct experimental conditions.

6.3 Structural basis of immunity to T6 effectors - Conclusions

Rap2a has a similar fold to that seen previously for the Tai4 family of immunity proteins including Rap1b, Rap2b, *Ec*Tai4 and *S*TTai4. In contrast, Rap1a adopts a novel fold for an immunity protein. These two structurally distinct families of Tai4 immunity proteins are built upon similar underlying principles; namely stable, dimeric small α-helical bundles. *S. marcescens* Rap1a and Rap2a appear to rely on the formation of disulfide linkages for folding and activity. Intriguingly, the unexpected structural similarity of Rap1a to the periplasmic chaperones HdeA and YmgD permits speculation that these proteins share a common evolutionary ancestor.

The Type VI associated endopeptidase effectors are highly basic proteins as exemplified by Ssp1 and Ssp2, with predicted pI values of 9.1 and 9.3 respectively. The immunity proteins are acidic; the pI values for the four Rap proteins fall in the range 5.1 to 6.3 after omitting the signal peptides. Such complementarity of charge contributes to the high affinity interactions that support complex formation, despite distinctive structures and variation in sequence, and may generate long-range electrostatic attraction to assist correct binding.

CHAPTER 7

REFERENCES

References

Alberts AW, Chen J, Kuron G, Hunt V, Huff J, Hoffman C, Rothrock J, Lopez M, Joshua H, Harriss E, Patchett A, Monaghan R, Currie S, Stapley E, Albers-Schonberg G, Hensens O, Hirshfield J, Hoogsteen K, Liesch J and Springer J (1980) Mevinolin: A highly potent competitive inhibitor of hydroxymethylglutaryl-coenzyme A reductase and a cholesterol-lowering agent. Proc. Natl. Acad. Sci. 77: 3957-3961

Altincicek B, Duin EC, Reichenberg A, Hedderich R, Kollas AK, Hintz M, Wagner S, Wiesner J, Beck E and Jomaa H (2002) LytB protein catalyses the terminal step of the 2-*C*-methyl-D-erythritol-4-phosphate pathway of isoprenoid biosynthesis. FEBS Lett. 532: 437-440

Anantharaman V and Aravind L (2003) Evolutionary history, structural features and biochemical diversity of the NlpC/P60 superfamily of enzymes. Genome Biol. 4: R11

Anderson KS, Kati WM, Ye Q, Liu J, Walsh CT, Benesi AJ and Johnson KA (1991) Isolation and structure elucidation of the 4-amino-4-deoxychorismate intermediate in the PABA enzymatic pathway. J. Am. Chem. Soc. 113: 3198-3200

Barr J (2010) A short history of dapsone, or an alternative model of drug development. J. Hist. Med. Allied Sci. 66: 425-467

Basler M, Pilhofer M, Henderson GP, Jensen GJ and Mekalanos JJ (2012) Type VI secretion requires a dynamic contractile phage tail-like structure. Nature 483: 182-186

Battye TGG, Kontogiannis L, Johnson O, Powell HR and Leslie AGW (2011) *iMOSFLM*: a new graphical interface for diffraction-image processing with *MOSFLM*. Acta Cryst. D 67: 271-281

Begley DW, Hartley RC, Davies DR, Edwards TE, Leonard JT, Abendroth J, Burris CA, Bhandari J, Myler PJ, Staker BL and Stewart LJ (2011) Leveraging structure determination with fragment screening for infectious disease drug targets: MECP synthase from *Burkholderia pseudomallei*. J. Struct. Funct. Genomics 12: 63-76

Benkovic SJ (1980) On the mechanism of action of folate- and biopterin-requiring enzymes. Annu. Rev. Biochem. 49: 227-251

Benz J, Sendlmeier C, Barends TR and Meinhart A (2012) Structural insights into the effector-immunity system Tse1/Tsi1 from *Pseudomonas aeruginosa*. PLoS One 7: e40453

Bloch KE (1964) The biological synthesis of cholesterol. Nobel lecture. (http://www.nobelprize.org/nobel_prizes/medicine/laureates/1964/bloch-lecture.pdf)

Bollag G, Hirth P, Tsai J, Zhang J, Ibrahim PN, Cho H, Spevak W, Zhang C, Zhang Y, Habets G, Burton EA, Wong B, Tsang G, West BL, Powell B, Shellooe R, Marimuthu A, Nguyen H, Zhang KY, Artis DR, Schlessinger J, Su F, Higgins B, Iyer R, D'Anderea K, Koehler A, Stumm M, Lin PS, Lee RJ, Grippo J, Puzanov I, Kim KB, Ribas A, McArthur GA, Sosman JA, Chapman PB, Flaherty KT, Xu X, Nathanson KL and

Nolop K (2010) Clinical efficacy of a RAF inhibitor needs broad target blockade in *BRAF*-mutant melanoma. Nature 467: 596-599

Bond CS and Schüttelkopf AW (2009) *ALINE*: A WYSIWYG protein-sequence alignment editor for publication-quality alignments. Acta Cryst. D 65: 510-512

Bönemann G, Pietrosiuk A and Mogk A (2010) Tubules and donuts: a type VI secretion story. Mol. Microbiol. 76: 815-821

Borrmann S, Issifou S, Esser G, Adegnika AA, Ramharter M, Matsiegui P, Oyakhirome S, Mawili-Mboumba DP, Missinou MA, Kun JFJ, Jomaa H and Kremsner PG (2004) Fosmidomycin-clindamycin for the treatment of *Plasmodium falciparum* malaria. J. Infect. Dis. 190: 1534-1540

Boyer F, Fichant G, Berthod J, Vandenbrouck Y and Attree I (2009) Dissecting the bacterial type VI secretion system by a genome wide *in silico* analysis: what can be learned from available microbial genomic resources? BMC Genomics 10: 104

Brooks TM, Unterweger D, Bachmann V, Kostiuk B and Pukatzki S (2013) Lytic activity of the *Vibrio cholerae* type VI secretion toxin VgrG-3 is inhibited by the antitoxin TsaB. J. Biol. Chem. 288: 7618-7625

Brown GM (1962) The biosynthesis of folic acid. II. Inhibition by sulfonamides. J. Biol. Chem. 237: 536-540

Brown MS and Goldstein JL (1980) Multivalent feedback regulation of HMG CoA reductase, a control mechanism coordinating isoprenoid synthesis and cell growth. J. Lipid. Res. 21: 505-517

Bouhss A, Trunkfield AE, Bugg TDH and Mengin-Lecreulx D (2008) The biosynthesis of peptidoglycan lipid-linked intermediates. FEMS Microbiol. Rev. 32: 208-233

Buetow L, Brown AC, Parish T and Hunter WN (2007) The structure of *Mycobacteria* 2*C*-methyl-D-erythritol-2,4-cyclodiphosphate synthase, an essential enzyme, provides a platform for drug discovery. BMC Struct. Biol. 7: 68

Bulloch EMM, Jones MA, Parker EJ, Osborne AP, Stephens E, Davies GM, Coggins JR and Abell C (2004) Identification of 4-amino-4-deoxychorismate synthase as the molecular target for the antimicrobial action of (6*S*)-6-fluoroshikimate. J. Am. Chem. Soc. 126: 9912-9913

Burtnick MN, Brett PJ, Harding SV, Ngugi SA, Ribot WJ, Chantratita N, Scorpio A, Milne TS, Dean RE, Fritz DL, Peacock SJ, Prior JL, Atkins TP and Deshazer D (2011) The cluster 1 type VI secretion system is a major virulence determinant in *Burkholderia pseudomallei*. Infect Immun. 79: 1512-1525

Bushby SR and Hitchings GH (1968) Trimethoprim, a sulphonamide potentiator. Br. J. Pharmacol. Chemother. 33: 72-90

Calisto BM, Perez-Gil J, Bergua M, Querol-Audi J, Fita I and Imperial S (2007) Biosynthesis of isoprenoids in plants: structure of the 2C-methyl-D-erithrytol 2,4-

cyclodiphosphate synthase from *Arabidopsis thaliana.* Comparison with the bacterial enzymes. Protein Sci. 16: 2082-2088

Camara D, Bisanz C, Barette C, Van Daele J, Human E, Barnard B, Van der Straeten D, Stove CP, Lambert WE, Douce R, Maréchal E, Birkholtz LM, Cesbron-Delauw MF, Dumas R and Rébeillé F (2012) Inhibition of *p*-aminobenzoate and folate syntheses in plants and apicomplexan parasites by natural product rubreserine. J. Biol. Chem. 287: 22367-22376

Campbell TL and Brown ED (2002) Characterization of the depletion of 2-*C*-methyl-D-erythritol-2,4-cyclodiphosphate synthase in *Escherichia coli* and *Bacillus subtilis*. J. Bacteriol. 184: 5609-5618

Campos N, Rodríguez-Concepción M, Sauret-Güeto S, Gallego F, Lois L and Boronat A (2001) *Escherichia coli* engineered to synthesize isopentenyl diphosphate and dimethylallyl diphosphate from mevalonate: a novel system for the genetic analysis of the 2-*C*-methyl-D-erythritol 4-phosphate pathway for isoprenoid biosynthesis. Biochem. J. 353: 59-67

Cascales E and Cambillau C (2012) Structural biology of type VI secretion systems. Philos. Trans. R. Soc. Lond. B 367: 1102-1111

Cassera MB, Gozzo FC, D'Alexandri FL, Merino EF, del Portillo HA, Peres VJ, Almeida IC, Eberlin MN, Wunderlich G, Wiesner J, Jomaa H, Kimura EA and Katzin AM (2004) The methylerythritol phosphate pathway is functionally active in all intraerythrocytic stages of *Plasmodium falciparum*. J. Biol. Chem. 279: 51749-51759

Castell A, Mille C and Unge T (2010) Structural analysis of mycobacterial branched-chain aminotransferase: implications for inhibitor design. Acta Cryst. D 66: 549-557

Chen VB, Arendall WB, Headd JJ, Keedy DA, Immormino RM, Kapral GJ, Murray LW, Richardson JS and Richardson DC (2010) *MolProbity*: all-atom structure validation for macromolecular crystallography. Acta Cryst. D 66: 12-21

Chhabra S, Dolezal O, Collins BM, Newman J, Simpson JS, Macreadie IG, Fernley R, Peat TS and Swarbrick JD (2012) Structure of *S. aureus* HPPK and the discovery of a new substrate site inhibitor. PLoS One 7: e29444

Chou S, Bui NK, Russell AB, Lexa KW, Gardiner TE, LeRoux M, Vollmer W and Mougous JD (2012) Structure of a peptidoglycan amidase effector targeted to Gram-negative bacteria by the type VI secretion system. Cell Rep. 1: 656-664

Collaborative Computational Project, Number 4 (1994) The CCP4 suite: Programs for protein crystallography. Acta Cryst. D 50: 760-763

Coulthurst SJ (2013) The Type VI secretion system - a widespread and versatile cell targeting system. Res. Microbiol. 164: 640-654

Congreve M, Chessari G, Tisi D and Woodhead AJ (2008) Recent developments in fragment-based drug discovery. J. Med. Chem. 51: 3661-3680

Crane CM, Kaiser J, Ramsden NL, Lauw S, Rohdich F, Eisenreich W, Hunter WN,

Bacher A and Diederich F (2006) Fluorescent inhibitors for IspF, an enzyme in the non-mevalonate pathway for isoprenoid biosynthesis and a potential target for antimalarial therapy. Angew. Chem. Int. Ed. 45: 1069-1074

Cunningham FX, Lafon TP and Gantt E (2000) Evidence of a role for LytB in the nonmevalonate pathway of isoprenoid biosynthesis. J. Bacteriol. 182: 5841-5848

de Berardinis V, Vallenet D, Castelli V, Besnard M, Pinet A, Cruaud C, Samair S, Lechaplais C, Gyapay G, Richez C, Durot M, Kreimeyer A, Le Fèvre F, Schächter V, Pezo V, Döring V, Scarpelli C, Médigue C, Cohen GN, Marlière P, Salanoubat M and Weissenbach J (2008) A complete collection of single-gene deletion mutants of *Acinetobacter baylyi* ADP1. Mol. Syst. Biol. 4: Epub Article 174

de Kloe GE, Bailey D, Leurs R and de Esch IJP (2009) Transforming fragments into candidates: small becomes big in medicinal chemistry. Drug Discov. Today 14: 630-646

DeLano WL (2002) The PyMOL Molecular Graphics System. Schrödinger, LLC.

de Pace F, Nakazato G, Pacheco A, de Paiva JB, Sperandio V and da Silveira WD (2010) The type VI secretion system plays a role in type 1 fimbria expression and pathogenesis of an avian pathogenic *Escherichia coli* strain. Infect. Immun. 78: 4990-4999

Ding J, Wang W, Feng H, Zhang Y and Wang DC (2012) Structural insights into the *Pseudomonas aeruginosa* type VI virulence effector Tse1 bacteriolysis and self-protection mechanisms. J. Biol. Chem. 287: 26911-26920

Domagk G (1947) Further progress in chemotherapy of bacterial infections. Nobel lecture. (http://www.nobelprize.org/nobel_prizes/medicine/laureates/1939/domagk-lecture.pdf)

Dundas J, Ouyang Z, Tseng J, Binkowski A, Turpaz Y and Liang J (2006) CASTp: computed atlas of surface topography of proteins with structural and topographical mapping of functionally annotated residues. Nucl. Acid Res. 34: 116-118

Eadsforth TC, Gardiner M, Maluf FV, McElroy S, James D, Frearson J, Gray D and Hunter WN. (2012) Assessment of *Pseudomonas aeruginosa* N^5,N^{10}-methylenetetrahydrofolate dehydrogenase - cyclohydrolase as a potential antibacterial drug target. PLoS One 7: e35973

Edgar RC (2004) MUSCLE: multiple sequence alignment with high accuracy and high throughput. Nucleic Acids Res. 32: 1792-1797

Eliot AC and Kirsch JF (2004) Pyridoxal phosphate enzymes: Mechanistic, structural, and evolutionary considerations. Annu. Rev. Biochem. 73: 383-415

Emsley P, Lohkamp B, Scott WG and Cowtan K (2010) Features and development of *Coot*. Acta Cryst. D 66: 486-501

Engh RA & Huber R (1991) Accurate bond and angle parameters for X-ray protein structure refinement. Acta Cryst. A 47: 392-400

English G, Trunk K, Rao VA, Srikannathasan V, Hunter WN and Coulthurst SJ (2012) New secreted toxins and immunity proteins encoded within the Type VI secretion system gene cluster of *Serratia marcescens*. Mol. Microbiol. 86: 921-936

Ericsson UB, Hallberg BM, DeTitta GT, Dekker N and Nordlund P (2006) Thermofluor-based high-throughput stability optimization of proteins for structural studies. Anal. Biochem. 357: 289-298

Ershov Y V (2007) 2-C-Methylerythritol phosphate pathway of isoprenoid biosynthesis as a target in identifying of new antibiotics, herbicides, and immunomodulators: A review. Appl. Biochem. Microbiol. 43:133-157 (English translation from Russian, Pleiades Publishing, 2007)

Evans P (2006) Scaling and assessment of data quality. Acta Cryst. D 62: 72-82

Fasella P (1967) Pyridoxal phosphate. Annu. Rev. Biochem. 36: 185-210

Filloux A (2011) Protein secretion systems in *Pseudomonas aeruginosa*: An essay on diversity, evolution and function. Front. Microbiol. 2:155

Freiberg C, Wieland B, Spaltmann F, Ehlert K, Brotz H and Labischinski H (2001) Identification of novel essential *Escherichia coli* genes conserved among pathogenic bacteria. J. Mol. Microbiol. Biotechnol. 3: 483-489

Foit L, George JS, Zhang BW, Brooks CL and Bardwell JC (2013) Chaperone activation by unfolding. Proc. Natl. Acad. Sci. 110: 1254-1262

Follens A, Veiga-da-Cunha M, Merckx R, van Schaftingen E and van Eldere J (1999) *asc1* of *Haemophilus influenza* type a capsulation locus region II encodes a bifunctional ribulose 5-phosphate reductase-CDP-ribitol pyrophosphorylase. J. Bacteriol. 181: 2001-2007

Gabrielsen M, Rohdich F, Eisenreich W, Gräwert T, Hecht S, Bacher A and Hunter WN (2004a) Biosynthesis of isoprenoids. A bifunctional IspDF enzyme from *Campylobacter jejuni*. Eur. J. Biochem. 271: 3028-3035

Gabrielsen M, Bond CS, Hallyburton I, Hecht S, Bacher A, Eisenreich W, Rohdich F and Hunter WN (2004b) Hexameric assembly of the bifunctional methylerythritol 2,4-cyclodiphosphate synthase and protein-protein associations in the deoxy-xylulose-dependent pathway of isoprenoid precursor biosynthesis. J. Biol. Chem. 279: 52753-52761

Gajiwala KS and Burley SK (2000) HDEA, a periplasmic protein that supports acid resistance in pathogenic enteric bacteria. J. Mol. Biol. 295: 605-612

Gasteiger E, Hoogland C, Gattiker A, Duvand S, Wilkins MR, Appel RD and Bairoch A (2005) Protein identification and analysis tools on the ExPASy server. The Proteomics Protocols Handbook, Humana Press, pp. 571-607

Gerlach RG and Hensel M (2007) Protein secretion systems and adhesins: the molecular armory of Gram-negative pathogens. Int. J. Med. Microbiol. 297: 401-415

Gisondi P, Fantuzzi F, Malerba M and Girolomoni G (2007) Folic acid in general medicine and dermatology. J. Dermatolog. Treat. 18: 138-146

Goldberg JM, Swanson RV, Goodman HS and Kirsch JF (1991) The tyrosine-225 to phenylalanine mutation of *Escherichia coli* aspartate aminotransferase results in an alkaline transition in the spectrophotometeric and kinetic pK_a values and reduced values of both k_{cat} and K_m. Biochemistry 30: 305-312

Green JM and Nichols BP (1991) *p*-Aminobenzoate biosynthesis in *Escherichia coli*. Purification of aminodeoxychorismate lyase and cloning of *pabC*. J. Biol. Chem. 266: 12971-12975

Green JM, Merkel WK and Nichols BP (1992) Charaterization and sequence of *Escherichia coli pabC*, the gene encoding aminodeoxychorismate lyase, a pyridoxal phosphate-containg enzyme. J. Bacteriol. 174: 5317-5323

Grishin NV, Osterman AL, Brooks HB, Phillips MA and Goldsmith EJ (1999) X-ray structure of ornithine decarboxylase from *Trypanosoma brucei*: The native structure and the structure in complex with α-difluoromethylornithine. Biochemistry 38: 15174-15184

Hahn FM, Hurlburt AP and Poulter CD (1999) *Escherichia coli* open reading frame 696 is *idi*, a nonessential gene encoding isopentenyl diphosphate isomerase. J. Bacteriol. 181: 4499-4504

Hartshorn MJ, Murray CW, Cleasby A, Frederickson M, Tickle IJ and Jhoti H (2005) Fragment-based lead discovery using X-ray crystallography. J. Med. Chem. 48: 403-413

He Z, Stigers Lavoie KD, Bartlett PA and Toney MD (2004) Conservation of mechanism in three chorismate-utilizing enzyme. J. Am. Chem. Soc. 126: 2378-2385

Herz S, Wungsintaweekul J, Schuhr CA, Hecht S, Lüttgen H, Sagner S, Fellermeier M, Eisenreich W, Zenk MH, Bacher A and Rohdich F (2000) Biosynthesis of terpenoids: YgbB protein converts 4-diphosphocytidyl-2*C*-methyl-D-erythritol 2-phosphate to 2*C*-methyl-D-erythritol 2,4-cyclodiphosphate. Proc. Natl. Acad. Sci. 97: 2486-2490

Hoang TT, Karkhoff-Schweizer RR, Kutchma AJ and Schweizer HP (1998) A broad-host-range Flp-FRT recombination system for site-specific excision of chromosomally-located DNA sequences: applications for isolation of unmarked *Pseudomonas aeruginosa* mutants. Gene 212: 77-86

Holm L and Rosenström P (2010) Dali server: conservation mapping in 3D. Nucleic Acids Res. 38: W545-549

Hong W, Jiao W, Hu J, Zhang J, Liu C, Fu X, Shen D, Xia B and Chang Z (2005) Periplasmic protein HdeA exhibts chaperone-like activity exclusively within stomach pH range by transforming into disordered conformation. J. Biol. Chem. 280: 27029-27034

Hood RD, Singh P, Hsu F, Güvener T, Carl Ma, Trinidad RR, Silverman JM, Ohlson BB, Hicks KG, Plemel RL, Li M, Schwarz S, Wang WY, Merz AJ, Goodlett DR and Mougous JD (2010) A type VI secretion system of *Pseudomonas aeruginosa* targets a toxin to bacteria. Cell Host Microbe 7: 25-37

Howe R, Kelly M, Jimah J, Hodge D and Odom AR (2013) Isoprenoid biosynthesis inhibition disrupts Rab5 localization and food vacuolar integrity in *Plasmodium falciparum*. Eukaryot. Cell 12: 215-223

Hu L, Boxer PA, Kesten SR, Lei HJ, Wustrow DJ, Moreland DW, Zhang L, Ahn K, Ryder TR, Liu X, Rubin JR, Fahnoe K, Carroll RT, Dutta S, Fahnoe DC, Probert AW, Roof RL, Rafferty MF, Kostlan CR, Scholten JD, Hood M, Ren X, Schielke GP, Su T, Taylor CP, Mistry A, McConnell P, Hasemann C and Ohren J (2006) The design and synthesis of human branched-chain amino acid aminotransferase inhibitors for treatment of neurodegenerative diseases. Bioorg. Med. Chem. Lett. 16: 2337-2340

Hunter WN (2007) The non-mevalonate pathway of isoprenoid precursor biosynthesis. J. Biol. Chem. 282: 21573-21577

Hunter WN (2009) Structure-based ligand design and the promise held for antiprotozoan drug discovery. J. Biol. Chem. 284: 11749-11753

Hunter WN (2011) Isoprenoid precursor biosynthesis offers potential targets for drug discovery against diseases caused by apicomplexan parasites. Curr. Top. Med. Chem. 11: 2048-2059

Inoue K, Kuramitsu S, Okamoto A, Hirotsu K, Higuchi T, Morino Y and Kagamiyama H (1991) Tyr225 in aspartate aminotransferase: contribution of the hydrogen bond between Tyr225 and coenzyme to the catalytic reaction. J. Biochem. 109: 570-576

Jani AJ and Cotter PA (2010) Type VI secretion: not just for pathogenesis anymore. Cell Host Microbe 8: 2-6

Jhee KH, Yoshimura T, Miles EW, Takeda S, Miyahara I, Hirotsu K, Soda K, Kawata Y and Esaki N (2000) Stereochemistry of the transamination reaction catalyzed by aminodeoxychorismate lyase from *Escherichia coli*: close relationship between fold type and stereochemistry. J. Biochem. 128: 679-686

Jomaa H, Wiesner J, Sanderbrand S, Altincicek B, Wiedemeyer C, Hintz M, Türbachova I, Eberl M, Zeidler J, Lichtenthaler HK, Soldati D and Beck E (1999) Inhibitors of the nonmevalonate pathway of isoprenoid biosynthesis as antimalarial drugs. Science 285: 1573-1576

Kabsch W (2010) *XDS*. Acta Cryst. D. 66: 125-132

Keller S, Schadt HS, Ortel I and Süssmuth RD (2007) Action of *atrop*-abyssomicin C as an inhibitor of 4-amino 4-deoxychorismate synthase PabB. Angew. Chem. Int. Ed. 46: 8284-8286

Kemp LE, Bond CS and Hunter WN (2002) Structure of 2*C*-methyl-D-erythritol 2,4-cyclodiphosphate synthase: an essential enzyme for isoprenoid biosynthesis and target for antimicrobial drug development. Proc. Natl. Acad. Sci. 99: 6591-6596

Kemp LE, Alphey MS, Bond CS, Ferguson MA, Hecht S, Bacher A, Eisenreich W, Rohdich F and Hunter WN (2005) The identification of isoprenoids that bind in the intersubunit cavity of *Escherichia coli* 2*C*-methyl-D-erythritol-2,4-cyclodiphosphate synthase by complementary biophysical methods. Acta Cryst D 61: 45-52

Kempf DJ, Marsh KC, Denissen JF, McDonald E, Vasvanonda S, Flentge CA, Green BE, Fino L, Park CH, Kong X, Wideburg NE, Saldivar A, Ruiz L, Kati WM, Sham HL, Robins T, Stewart KD, Hsu A, Platiner JJ, Leonard JM and Norbeck DW. (1995) ABT-538 is a potent inhibitor of human immunodeficiency virus protease and has high oral bioavailability in humans. Proc. Natl. Acad. Sci. 92: 2484-2488

Kirke PN, Molloy AM, Daly LE, Burke H, Weir DG and Scott JM (1993) Maternal plasma folate and vitamin B12 are independent risk factors for neural tube defects. Q. J. Med. 86: 703-708

Kishida H, Wada T, Unzai S, Kuzuyama T, Takagi M, Terada T, Shirouzu M, Yokoyama S, Tame JRH and Park S (2003) Structure and catalytic mechanism of 2-*C*-methyl-D-erythritol 2,4-cyclodiphosphate (MECDP) synthase, an enzyme in the non-mevalonate pathway of isoprenoid synthesis. Acta Cryst. D 59: 23-31

Kollas AK, Duin EC, Eberl M, Altincicek B, Hintz M, Reichenberg A, Henschker D, Henne A, Steinbrecher I, Ostrovsky DN, Hedderich R, Beck E, Jomaa H and Wiesner J (2002) Functional characterization of GcpE, an essential enzyme of the non-mevalonate pathway of isoprenoid biosynthesis. FEBS Lett. 532: 432-436

Krissinel E and Henrick K (2007) Inference of macromolecular assemblies from crystalline state. J. Mol. Biol. 372: 774-797

Lehmann C, Lim K, Toedt J, Krajewski W, Howard A, Eisenstein E and Herzberg O (2002) Structure of 2*C*-methyl-D-erythrol-2,4-cyclodiphosphate synthase from *Haemophilus influenzae*: Activation by conformational transition. Proteins 49: 135-138

Lell B, Ruangweerayut R, Wiesner J, Missinou MA, Schindler A, Baranek T, Hintz M, Hutchinson D, Jomaa H and Kremsner PG (2003) Fosmidomycin, a novel chemotherapeutic agent for malaria. Antimicrob. Agents Chemother. 42: 735-738

Leonard GA, McAuley-Hecht K, Brown T and Hunter WN (1995) Do C-H•••O hydrogen bonds contribute to the stability of nucleic acid base pairs? Acta Cryst. D 51: 136-139

Lepore BW, Liu D, Peng Y, Fu M, Yusuda C, Manning JM, Silverman RB and Ringe D (2010) Chiral discrimination among aminotransferases: inactivation by 4-amino-4,5-dihydrothiophenecarboxylic acid. Biochemistry 49: 3138-3147

Leslie AG (2006) The integration of macromolecular diffraction data. Acta Cryst. D 62: 48-57

Lherbet C, Pojer F, Richard SB, Noel JP and Poulter CD (2006) Absence of substrate channeling between the active sites in the *Agrobacterium tumefaciens* IspDF and IspE enzymes of the methyl erythritol phosphate pathway. Biochemistry 45: 3548-3553

Li M, Le Trong I, Carl MA, Larson ET, Chou S, De Leon JA, Dove SL, Stenkamp RE and Mougous JD (2012) Structural basis for type VI secretion effector recognition by a cognate immunity protein. PLoS Pathog. 8: e1002613

Lichtenthaler HK, Schwender J, Disch A and Rohmer M (1997) Biosynthesis of isoprenoids in higher plant chloroplasts proceeds via a mevalonate-independent pathway. FEBS Lett. 400: 271-274

Lichtenthaler HK (1999) The 1-deoxy-D-xylulose-5-phosphate pathway of isoprenoid biosynthesis in plants. Annu. Rev. Plant Physiol. Plant Mol. Biol. 50: 47-65

Lucock M (2000) Folic acid: nutritional biochemistry, molecular biology, and role in disease processes. Mol. Genet. Metab. 71: 121-138

Lüttgen H, Rohdich F, Herz S, Wungsintaweekul J, Hecht S, Schuhr CA, Fellermeier M, Sagner S, Zenk MH, Bacher A and Eisenreich W (2000) Biosynthesis of terpenoids: YchB protein of *Escherichia coli* phosphorylates the 2-hydroxy group of 4-diphosphocytidyl-2*C*-methyl-D-erythritol. Proc. Natl. Acad. Sci. USA 97:1062-1067

MacIntyre DL, Miyata ST, Kitaoka M and Pukatzki S (2010) The *Vibrio cholerae* type VI secretion system displays antimicrobial properties. Proc. Natl. Acad. Sci. 107: 19520-19524

Masters PA, O'Bryan TA, Zurlo J, Miller DQ and Joshi N (2003) Trimethoprim-sulfamethoxazole revisted. Arch. Intern. Med. 163: 402-410

Maurer LM, Yohannes E, Bondurant SS, Radmacher M and Slonczewski JL (2005) pH regulates genes for flagellar motility, catabolism, and oxidative stress in *Escherichia coli* K-12. J. Bacteriol. 187: 304-319

McCoy AJ, Grosse-Kunstleve RW, Adams PD, Winn MD, Storoni LC and Read RJ (2007) *Phaser* crystallographic software. J. Appl. Cryst. 40: 658-674

Morgan RE, Batot GO, Dement JM, Rao VA, Eadsforth TC and Hunter WN (2011) Crystal structures of *Burkholderia cenocepacia* dihydropteroate synthase in the apo-form and complexed with the product 7,8-dihydropteroate. BMC Struct. Biol. 11: 21

Mougous JD, Cuff ME, Raunser S, Shen A, Zhou M, Gifford CA, Goodman AL, Joachimiak G, Ordoñez CL, Lory S, Walz T, Joachimiak A and Mekalanos JJ (2006) A virulence locus of *Pseudomonas aeruginosa* encodes a protein secretion apparatus. Science 312: 1526-1530

Moynie L, Schnell R, McMahon SA, Sandalova T, Boulkerou WA, Schmidberger JW, Alphey M, Cukier C, Duthie F, Kopec J, Liu H, Jacewicz A, Hunter WN, Naismith JH and Schneider G (2013) The AEROPATH project targeting *Pseudomonas aeruginosa*: crystallographic studies for assessment of potential targets in early-stage drug discovery. Acta Cryst. F 69: 25-34

Mpamhanga CP, Spinks D, Tulloch LB, Shanks EJ, Robinson DA, Collie IT, Fairlamb AH, Wyatt PG, Frearson JA, Hunter WN, Gilbert IH and Brenk R (2009) One scaffold, three binding modes: novel and selective pteridine reductase 1 inhibitors derived from fragment hits discovered by virtual screening. J. Med. Chem. 52: 4454-4465

Murdoch SJ, Trunk K, English G, Fritsch MJ, Pourkarimi E and Coulthurst SJ (2011) The opportunistic patogen *Serratia marcescens* utilizes type VI secretion to target bacterial competitors. J. Bacteriol. 193: 6057-6069

Murshudov GN, Skubák P, Lebedev AA, Pannu NS, Steiner RA, Nicholls RA, Winn MD, Long F and Vagin AA (2011) *REFMAC*5 for the refinement of macromolecular crystal structures. Acta Cryst. D 67: 355-367

Nakai T, Mizutani H, Miyahara I, Hirotsu K, Takeda S, Jhee K, Yoshimura T and Esaki N (2000) Three-dimensional structure of 4-amino-4-deoxychorismate lyase from *Escherichia coli*. J. Biochem. 128: 29-38

Narayanasamy P, Eoh H, Brennan PJ and Crick DC (2010) Synthesis of 4-diphosphocytidyl-2-C-methyl-D-erythritol 2-phosphate and kinetic studies of *Mycobacterium tuberculosis* IspF. Chem. Biol. 17: 117-122

Navratilova I and Hopkins AL (2010) Fragment screening by surface plasmon resonance. ACS Med. Chem. Lett. 1: 44-48

Ni S, Robinson H, Marsing GC, Bussiere DE and Kennedy MA (2004) Structure of 2*C*-methyl-D-erythritol-2,4-cyclodiphosphate synthase from *Shewanella oneidensis* at 1.6 Å: identification of farnesyl pyrophosphate trapped in a hydrophobic cavity. Acta Cryst. D 60: 1949-1957

Nichols BP, Seibold AM, Doktor SZ (1989) *para*-Aminobenzoate synthesis from chorismate occurs in two steps. J. Biol. Chem. 264: 8597-8601

Niesen FH, Berglund H and Vedadi M (2007) The use of differential scanning fluorimetry to detect ligand interactions that promote protein stability. Nat. Protoc. 2: 2212-2221

No JH, de Macedo Dossin F, Zhang Y, Liu Y, Zhu W, Feng X, Yoo JA, Lee E, Wang K, Hui R, Freitas-Junior LH and Oldfield E (2012) Lipophilic analogs of zoledronate and risedronate inhibit *Plasmodium* geranylgeranyl diphosphate synthase (GGPPS) and exhibit potent antimalarial activity. Proc. Natl. Acad. Sci. 109: 4058-4063

Noble MEM, Endicott JA and Johnson LN (2004) Protein kinase inhibitors: Insights into drug design from structure. Science 303: 1800-1805

Okuhara M, Kuroda Y, Goto T, Okamoto M, Terano H, Kohsaka M, Aoki H and Imanaka H (1980a) Studies on new phosphonic acid antibiotics III. Isolation and characterization of FR-31564, FR-32863 and FR-33289. J. Antibiot. 33: 24-28

Okuhara M, Kuroda Y, Goto T, Okamoto M, Terano H, Kohsaka M, Aoki H and Imanaka H (1980b) Studies on new phosphonic acid antibiotics I. FR-900098, isolation and characterization. J. Antibiot. 33: 13-17

O'Rourke PEF, Eadsforth TC, Fyfe PK, Shepherd SM and Hunter WN (2011) *Pseudomonas aeruginosa* 4-amino-4-deoxychorismate lyase: spatial conservation of an active site tyrosine and classification of two types of enzyme. PLoS One 6: e24158

Padmanabhan B, Bessho Y, Ebihara A, Antonyuk SV, Eilis MJ, Strange RW, Kuramitsu S, Watanabe N, Hasnain SS and Yokoyama S (2009) Structure of putative 4-amino-4-deoxychorismate lyase from *Thermus thermophilus* HB8. Acta Cryst. F 65: 1234-1239

Pantoliano MW, Petrella EC, Kwasnoski JD, Lobanov VS, Myslik J, Graf E, Carver T, Asel E, Springer BA, Lane P and Salemme FR (2001) High-density miniaturized thermal shift assays as a general strategy for drug discovery. J Biomol. Screen.

Parsons JF, Jensen PY, Pachikara AS, Howard AJ, Eisenstein E and Ladner JE (2002) Structure of *Escherichia coli* aminodeoxychorismate synthase: architectural conservation and diversity in chorismate-utilizing enzymes. Biochemistry 41: 2198-2208

Pukatzki S, Ma AT, Sturtevant D, Krastins B, Sarracino D, Nelson WC, Heidelberg JF and Mekalanos JJ (2006) Identification of a conserved bacterial protein secretion system in *Vibrio cholerae* using the *Dictyostelium* host model system. 103: 1528-1533

Pukatzki S, Ma AT, Revel AT, Sturtevant D and Mekalanos JJ (2007) Type VI secretion system translocates a phage tail spike-like protein into target cells where it cross-links actin. Proc. Natl. Acad. Sci. 104: 15508-15513

Ralph SA, van Dooren GG, Waller RF, Crawford MJ, Fraunholz MJ, Foth BJ, Tonkin CJ, Roos DS and McFadden GI (2004) Metabolic maps and functions of the *Plasmodium falciparum* apicoplast. Nat. Rev. Microbiol. 2: 203-216

Ramsden NL, Buetow L, Dawson A, Kemp LA, Ulaganathan V, Brenk R, Klebe G and Hunter WN (2009) A structure-based approach to ligand discovery for 2*C*-methyl-D-erythritol-2,4-cyclodiphosphate synthase: A target for antimicrobial therapy. J. Med. Chem. 52: 2531-2542

Reinhard L, Mayerhofer H, Geerlof A, Mueller-Dieckmann J and Weiss MS (2013) Optimization of protein buffer cocktails using Thermofluor. Acta Cryst. F 69: 209-214

Richard SB, Ferrer J, Bowman ME, Lillo AM, Tetzlaff CN, Cane DE and Noel JP (2002) Structure and mechanism of 2-C-methyl-D-erythritol 2,4-cyclodiphosphate synthase. An enzyme in the mevalonate-independent isoprenoid biosynthetic pathway. J. Biol. Chem. 277: 8667-8672

Richey DP and Brown GM (1969) The biosynthesis of folic acid IX. Purificiation and properties of the enzymes required for the formation of dihydropteroic acid. J. Biol. Chem. 244: 1582-1592

Riedlinger J, Reicke A, Zähner H, Krismer B, Bull AT, Maldonado LA, Ward AC, Goodfellow M, Bister B, Bischoff D, Süssmuth RD and Fiedler HP (2004) Abyssomicins, inhibitors of the *para*-aminobenzoic acid pathway produced by the marine *Verrucosispora* strain AB-18-032. J. Antibiot. 57: 271-279

Rohdich F, Wungsintaweekul J, Fellermeier M, Sagner S, Herz S, Kis K, Eisenreich W, Bacher A and Zenk MH (1999) Cytidine 5'-triphosphate-dependent biosynthesis of isoprenoids: YgbP protein of *Escherichia coli* catalyzes the formation of 4-diphosphocytidyl-2-*C*-methylerythritol. Proc. Natl. Acad. Sci. 96: 11758-11763

Rohdich F, Kis K, Bacher A and Eisenreich W (2001) The non-mevalonate pathway of isoprenoids: genes, enzymes and intermediates. Curr. Opin. Chem. Biol. 5: 535-540

Rohdich F, Hecht S, Gärtner K, Adam P, Krieger C, Amslinger S, Arigoni D, Bacher A and Eisenreich W (2002) Studies on the nonmevalonate terpene biosynthetic pathway: Metabolic role of IspH (LytB) protein. Proc. Natl. Acad. Sci. 99: 1158-1163

Rohdich F, Bacher A and Eisenreich W (2005) Isoprenoid biosynthetic pathways as anti-infective drug targets. Biochem. Soc. Trans. 33: 785-791

Rohmer M, Knani M, Simonin P, Sutter B and Sahm H (1993) Isoprenoid biosynthesis in bacteria: a novel pathway for the early steps leading to isopentenyl diphosphate. Biochem. J. 295: 517-524

Rohmer M, Seemann M, Horbach S, Bringer-Meyer S and Sahm H (1996) Glyceraldehyde 3-phosphate and pyruvate as precursors of isoprenic units in an alternative non-mevalonate pathway for terpenoid biosynthesis. J. Am. Chem. Soc. 118: 2564-2566

Rosales-Reyes R, Skeldon AM, Aubert DF and Valvano MA (2012) The Type VI secretion system of *Burkholderia cenocepacia* affects multiple Rho family GTPases disrupting the actin cytoskeleton and the assembly of NADPH oxidase complex in macrophages. Cell Microbiol. 14: 255-273

Russell AB, Hood RD, Bui NK, LeRoux M, Vollmer W and Mougous JD (2011) Type VI secretion delivers bacteriolytic effectors to target cells. Nature 475: 343-347

Russell AB, Singh P, Brittnacher M, Bui NK, Hood RD, Carl MA, Agnello DM, Schwarz S, Goodlett DR, Vollmer W and Mougous JD (2012) A widespread bacterial type VI secretion effector superfamily identified using a heuristic approach. Cell Host Microbe 11: 538-549

Russell AB, LeRoux M, Hathazi K, Agnello DM, Ishikawa T, Wiggins PA, Wai SN and Mougous JD (2013) Diverse type VI secretion phospholipases are functionally plastic antibacterial effectors. Nature 496: 508-512

Sauret-Güeto S, Ramos-Valdivia A, Ibáñez E, Boronat A and Rodríguez-Concepción M (2003) Identification of lethal mutations in *Escherichia coli* genes encoding enzymes of the methylerythritol phosphate pathway. Biochem. Biophys. Res. Commun. 307: 408-415

Schadt HS, Schadt S, Oldach F and Süssmuth RD (2009) 2-Amino-2-deoxyisochorismate is a key intermediate in *Bacillus subtilis p*-aminobenzoic acid biosynthesis. J. Am. Chem. Soc. 10: 3481-3483

Schnell JR, Dyson HJ and Wright PE (2004) Structure, dynamics, and catalytic function of dihydrofolate reductase. Annu. Rev. Biophys. Biomol. Struct. 33: 119-140

Schüttelkopf AW and van Aalten DM (2004) *PRODRG*: a tool for high-throughput crystallography of protein-ligand complexes. Acta Cryst. D 60: 1355-1363

Yang F, Gustafson KR, Boyd MR and Wlodawer A (1998) Crystal structure of *Escherichia coli* HdeA. Nat. Struct. Biol. 5: 763-764

Schwarz S, Hood RD and Mougous JD (2010) What is type VI secretion doing in all those bugs? Trends Microbiol. 18: 531-537

Schwender J, Seemann M, Lichtenthaler HK and Rohmer M (1996) Biosynthesis of isoprenoids (carotenoids, sterols, prenyl side-chains of chlorophylls and plastoquinone) via a novel pyruvate/glyceraldehyde 3-phosphate non-mevalonate pathway in the green alga *Scenedesmus obliquus*. Biochem. J. 316: 73-80

Scott DE, Coyne AG, Hudson SA and Abell C (2012) Fragment-based approaches in drug discovery and chemical biology. Biochemistry 51: 4990-5003

Sgraja T, Kemp LE, Ramsden N and Hunter WN (2005) A double mutation of *Escherichia coli* 2*C*-methyl-D-erythritol-2,4-cyclodiphosphate synthase disrupts six hydrogen bonds with, yet fails to prevent binding of, an isoprenoid diphosphate. Acta Cryst. F 61: 625-629

Shang G, Liu X, Zhang J, Li N, Zhu C, Liu S, Yu Q, Zhao Y, Zhang H, Hu J, Cang H, Xu S and Gu L (2012) Structural insight into how *Pseudomonas aeruginosa* peptidoglycanhydrolase Tse1 and its immunity protein Tsi1 function. Biochem. J. 448: 201-211

Shepard CC (1969) Chemotherapy of leprosy. Annu. Rev. Pharmacol. 9: 37-50

Shigi Y (1989) Inhibition of bacterial isoprenoid synthesis by fosmidomycin, a phosphonic acid-containing antibiotic. J. Antimicrob. Chemother. 24: 131-145

Shuker SB, Hajduk PJ, Meadows RP and Fesik SW (1996) Discovering high-affinity ligands for proteins: SAR by NMR. Science 274: 1531-1534

Silverman JM, Brunet YR, Cascales E and Mougous JD (2012) Structure and regulation of the type VI secretion system. Annu. Rev. Microbiol. 66: 453-472

Smith BJ, Colman PM, von Itzstein M, Danylec B and Varghese JN (2001) Analysis of inhibitor binding in influenza virus neuraminidase. Protein Sci. 10: 689-696

Soper TS and Manning JM (1981) Different modes of action of inhibitors of bacterial D-amino acid transaminase. A target enzyme for the design of new antibacterial agents. J. Biol. Chem. 256: 4263-4268

Sprenger GA, Schorken U, Wiegert T, Grolle S, de Graaf AA, Taylor SV, Begley TP, Bringer-Meyer S and Sahm H (1997) Identification of a thiamin-dependent synthase in *Escherichia coli* required for the formation of the 1-deoxy-D-xylulose 5-phosphate precursor to isoprenoids, thiamin, and pyridoxol. Proc. Natl. Acad. Sci. 94: 12857-12862

Srikannathasan V, English G, Bui NK, Trunk K, O'Rourke PEF, Rao VA, Vollmer W, Coulthurst SJ and Hunter WN (2013) Structural basis for Type VI secreted peptidoglycan DL-endopeptidase function, specificity and neutralization in *Serratia marcescens*. Acta Cryst. D, 69: 2468-2482

Stein N (2008) *CHAINSAW*: a program for mutating pdb files used as templates in molecular replacement. J. Appl. Cryst. 41: 641-643

Steinbacher S, Kaiser J, Wungsintaweekul J, Hecht S, Eisenreich W, Gerhardt S, Bacher A and Rohdich F (2002) Structure of 2*C*-methyl-D-erythritol-2,4-cyclodiphosphate synthase involved in mevalonate-independent biosynthesis of isoprenoids. J. Mol. Biol. 316: 79-88

Suarez G, Sierra JC, Erova TE, Sha J, Horneman AJ and Chopra AK (2010) A type VI secretion system effector protein, VgrG1, from *Aeromonas hydrophila* that induces host cell toxicity by ADP ribosylation of actin. J. Bacteriol. 192: 155-168

Takahashi S, Kuzuyama T, Watanabe H and Seto H (1998) A 1-deoxy-D-xylulose 5-phosphate reductoisomerase catalyzing the formation of 2-*C*-methyl-D-erythritol 4-phosphate in an alternative nonmevalonate pathway for terpenoid biosynthesis. Proc. Natl. Acad. Sci. 95: 9879-9884

Tonhosolo R, D'Alexandri FL, de Rosso VV, Gazarini ML, Matsumura MY, Peres VJ, Merino EF, Carlton JM, Wunderlich G, Mercadante AZ, Kimura EA and Katzin AM (2009) Carotenoid biosynthesis in intraerythrocytic stages of *Plasmodium falciparum*. J. Biol. Chem. 284: 9974-9985

Tsai J, Lee JT, Wang W, Zhang J, Cho H, Mamo S, Bremer R, Gillette S, Kong J, Haass NK, Sproesser K, Li L, Smalley KSM, Fong D, Zhu Y, Marimuthu A, Nguyen H, Lam B, Liu J, Cheung I, Rice J, Suzuki Y, Luu C, Settachatgul C, Shellooe R, Cantwell J, Kim S, Schlessinger J, Zhang KYJ, West BL, Powell B, Habets G, Zhang C, Ibrahim PN, Hirth P, Artis DR, Herlyn M and Bollag G (2008) Discovery of a selective inhibitor of oncogenic B-Raf kinase with potent antimelanoma activity. Proc. Natl. Acad. Sci. 105: 3041-3046

Umeda T, Tanaka N, Kusakabe Y, Nakanishi, Kitade Y and Nakamura KT (2011) Molecular basis of fosmidomycin's action on the human malaria parasite *Plasmodium falciparum*. Sci. Rep. 1: Epub Article 9

Vagin A and Teplyakov A (1997) *MOLREP*: an automated program for molecular replacement. J. Appl. Cryst. 30: 1022–1025

van der Meer J and Hirsch AKH (2012) The isoprenoid-precursor dependence of *Plasmodium* spp. Nat. Prod. Rep. 29: 721-728

Vanichtanankul J, Taweechai S, Yuvaniyama J, Vilaivan T, Chitnumsub P, Kamchonwongpaisan S and Yuthavong Y (2011) Trypanosomal dihydrofolate reductase reveals natural antifolate resistance. ACS Chem. Biol. 6: 905-911

Varela-Moreiras G, Murphy MM and Scott JM (2009) Cobalamin, folic acid, and homocysteine. Nutr. Rev. 67: S69-S72

Verlinde CLMJ and Hol WGJ (1994) Structure-based drug design: progress, results and challenges. Structure 2: 577-587

Vollmer W, Joris B, Charlier P and Foster S (2008) Bacterial peptidoglycan (murein) hydrolases. FEMS Microbiol. Rev. 32: 259-286

von Itzstein M, Wu W, Kok GB, Pegg MS, Dyason JC, Jin B, Phan TV, Smythe ML, White HF, Oliver SW, Colman PM, Varghese JN, Ryan DM, Woods JM, Bethell RC, Hotham VJ, Cameron JM and Penn CR (1993) Rational design of potent sialidase-based inhibitors of influenza virus replication. Nature 363: 418-423

Wartchow CA, Podlaski F, Li S, Rowan K, Zhang X, Mark D and Huang K (2011) Biosensor-based small molecule fragment screening with biolayer interferometry. J. Comput. Aided Mol. Des. 25: 669-676

Whittle PJ and Blundell TL (1994) Protein structure-based drug design. Annu. Rev. Biophys. Biomol. Struct. 23: 349-375

Wlodawer A and Erickson JW (1993) Structure-based inhibitors of HIV-1 protease. Annu. Rev. Biochem. 62: 543-585

Wolff M, Seemann M, Tse Sum Bui B, Frapart Y, Tritsch D, Estrabot AG, Rodríguez-Concepción M, Boronat A, Marquet A and Rohmer M (2003) Isoprenoid biosynthesis via the methylerythritol phosphate pathway: the (*E*)-4-hydroxy-3-methylbut-2-enyl diphosphate reductase (LytB/IspH) from *Escherichia coli* is a [4Fe-4S] protein. FEBS Lett. 541: 115-120

Woods DD (1940) The relation of *p*-aminobenzoic acid to the mechanism of action of sulphanilamide. Br. J. Exp. Pathol. 21: 74-90

World Health Organization (2011) WHO model list of Essential Medicines. 17th Edition. (http://www.who.int/medicines/publications/essentialmedicines/en/index.html)

Ye Q, Liu J and Walsh CT (1990) *p*-Aminobenzoate synthesis in *Escherichia coli*. Purification and characterization of PabC as aminodeoxychorismate synthase and enzyme X as aminodeoxychorismate lyase. Proc. Natl. Acad. Sci. 87: 9391-9395

Yeh E and DeRisi JL (2011) Chemical rescue of malaria parasites lacking an apicoplast defines organelle function in blood-stage *Plasmodium falciparum*. PLoS Biol. 9: 1-10

Yun M, Wu Y, Li Z, Zhao Y, Waddell MB, Ferreira AM, Lee RE, Bashford D and White SW (2012) Catalysis and sulfa drug resistance in dihydropteroate synthase. Science 335: 1110-1114

Zhang H, Zhang H, Gao ZQ, Wang WJ, Liu GF, Xu JH, Su XD and Dong YH (2013) Structure of the type VI effector-immunity complex (Tae4-Tai4) provides novel insights into the inhibition mechanism of the effector by its immunity protein. J. Biol. Chem. 288: 5928-5939

Zhao L, Chang WC, Xiao Y, Liu HW and Liu P (2013) Methylerythritol phosphate pathway of isoprenoid biosynthesis. Annu. Rev. Biochem. 82: 497-530

Zürcher M and Diederich F (2008) Structure-based drug design: exploring the proper filling of apolar pockets at enzyme active sites. J. Org. Chem. 73: 4345-4361

APPENDIX 1

Representative experimental data from the purification of *Bc*IspF

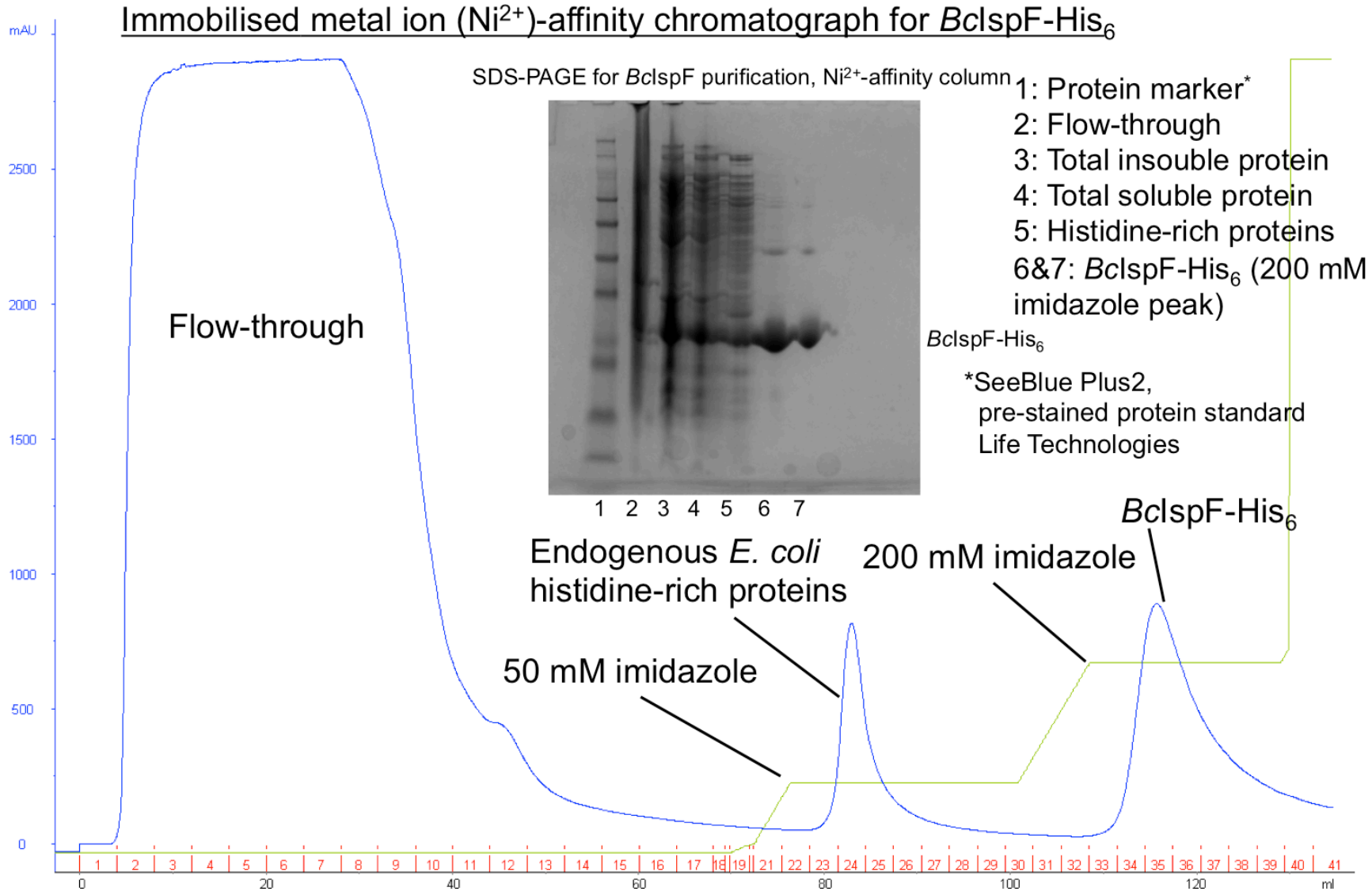
Immobilised metal ion (Ni^{2+})-affinity chromatograph for *Bc*lspF-His_6
mAU
2500
2000
1500
1000
500
0
Flow-through
SDS-PAGE for *Bc*lspF purification, Ni^{2+}-affinity column
1 2 3 4 5 6 7
1: Protein marker*
2: Flow-through
3: Total insouble protein
4: Total soluble protein
5: Histidine-rich proteins
6&7: *Bc*lspF-His_6 (200 mM imidazole peak)
*Bc*lspF-His_6
*SeeBlue Plus2, pre-stained protein standard Life Technologies
*Bc*lspF-His_6
Endogenous *E. coli* histidine-rich proteins
200 mM imidazole
50 mM imidazole
1 2 3 4 5 6 7 8 9 10 11 12 13 14 15 16 17 18 19 21 22 23 24 25 26 27 28 29 30 31 32 33 34 35 36 37 38 39 40 41
0 20 40 60 80 100 120 ml

Size-exclusion chromatograph for *Bc*IspF-His$_6$

Elution volume at peak maximum: 217 ml
Corresponding mass according
to column calibration: 52 kDa
Predicted mass (*ProtParam*): 57 kDa for trimer

Yield: 50 mg of *Bc*IspF from 2 L of LB$_{carb}$ culture

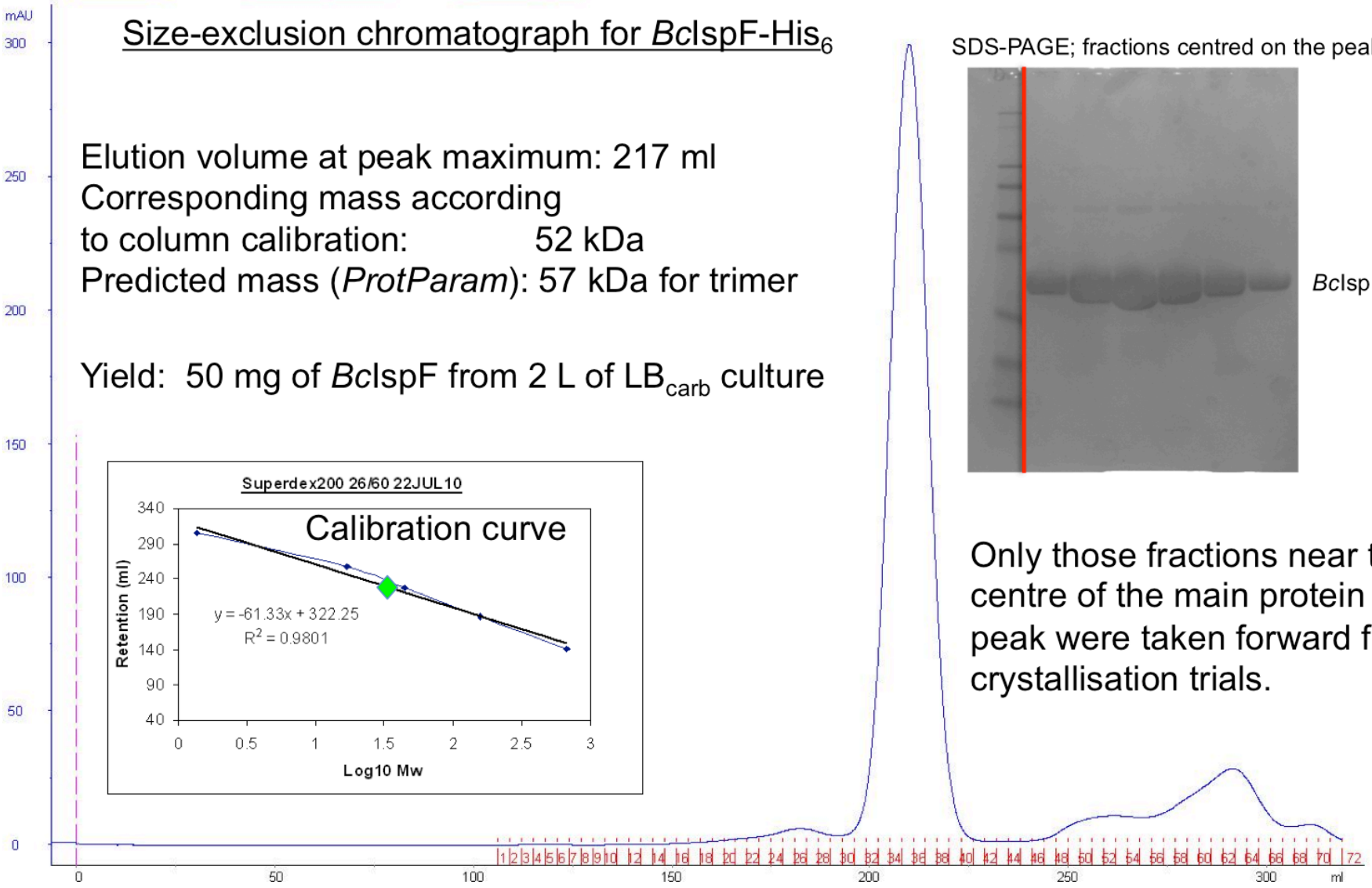

SDS-PAGE; fractions centred on the peak

*Bc*IspF-His$_6$

Only those fractions near the centre of the main protein peak were taken forward for crystallisation trials.

*Bc*IspF-His$_6$

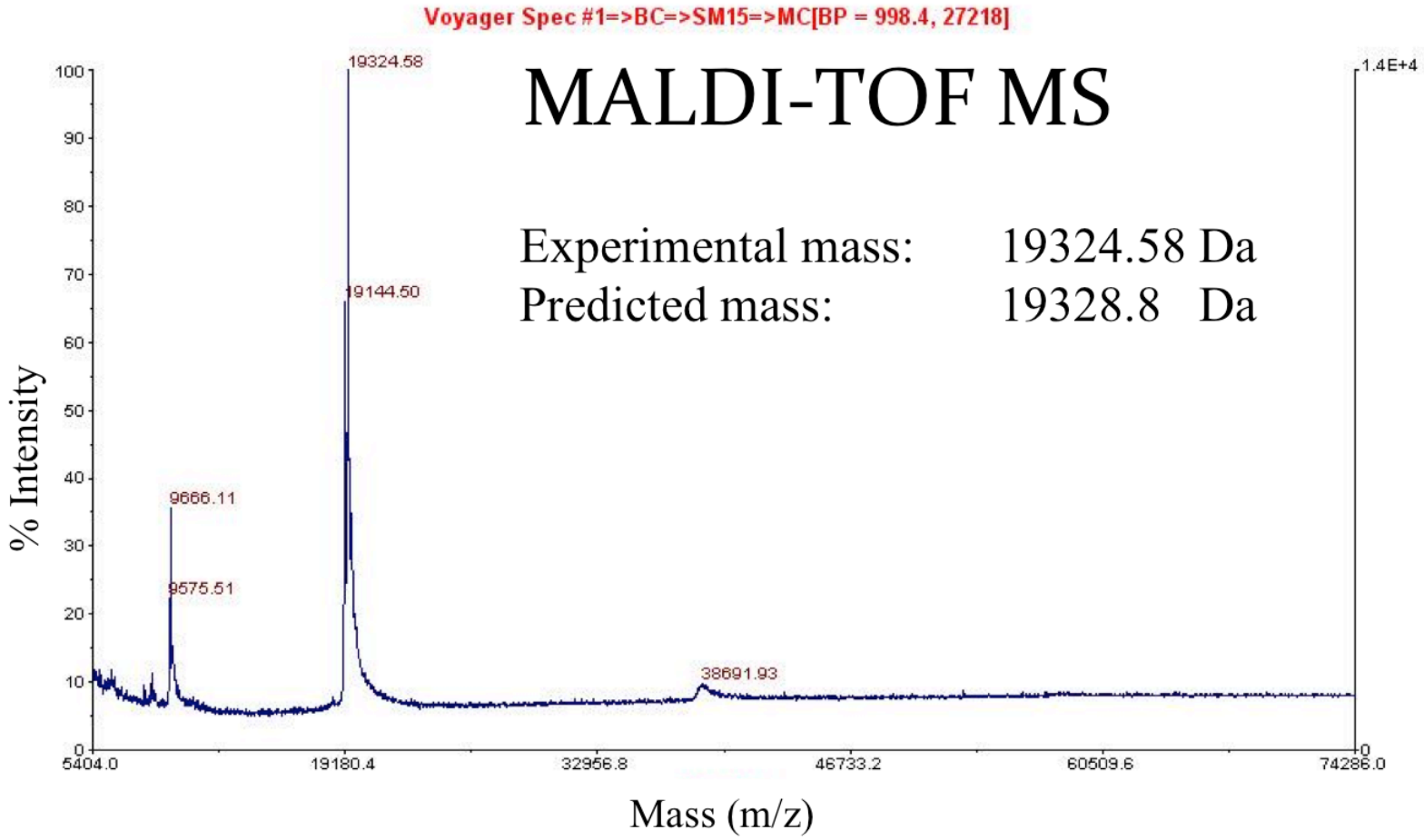
Voyager Spec #1=>BC=>SM15=>MC[BP = 998.4, 27218]
MALDI-TOF MS
Experimental mass: 19324.58 Da
Predicted mass: 19328.8 Da
19324.58
19144.50
9666.11
9575.51
38691.93
% Intensity
Mass (m/z)
1.4E+4
0
5404.0
19180.4
32956.8
46733.2
60509.6
74286.0

APPENDIX 2

Publications

OPEN ACCESS Freely available online

PLoS one

Pseudomonas aeruginosa 4-Amino-4-Deoxychorismate Lyase: Spatial Conservation of an Active Site Tyrosine and Classification of Two Types of Enzyme

Patrick E. F. O'Rourke, Thomas C. Eadsforth, Paul K. Fyfe, Sharon M. Shepherd, William N. Hunter*

Division of Biological Chemistry and Drug Discovery, College of Life Sciences, University of Dundee, Dundee, United Kingdom

Abstract

4-Amino-4-deoxychorismate lyase (PabC) catalyzes the formation of 4-aminobenzoate, and release of pyruvate, during folate biosynthesis. This is an essential activity for the growth of Gram-negative bacteria, including important pathogens such as *Pseudomonas aeruginosa*. A high-resolution (1.75 Å) crystal structure of PabC from *P. aeruginosa* has been determined, and sequence-structure comparisons with orthologous structures are reported. Residues around the pyridoxal 5′-phosphate cofactor are highly conserved adding support to aspects of a mechanism generic for enzymes carrying that cofactor. However, we suggest that PabC can be classified into two groups depending upon whether an active site and structurally conserved tyrosine is provided from the polypeptide that mainly forms an active site or from the partner subunit in the dimeric assembly. We considered that the conserved tyrosine might indicate a direct role in catalysis: that of providing a proton to reduce the olefin moiety of substrate as pyruvate is released. A threonine had previously been suggested to fulfill such a role prior to our observation of the structurally conserved tyrosine. We have been unable to elucidate an experimentally determined structure of PabC in complex with ligands to inform on mechanism and substrate specificity. Therefore we constructed a computational model of the catalytic intermediate docked into the enzyme active site. The model suggests that the conserved tyrosine helps to create a hydrophobic wall on one side of the active site that provides important interactions to bind the catalytic intermediate. However, this residue does not appear to participate in interactions with the C atom that undergoes an sp^2 to sp^3 conversion as pyruvate is produced. The model and our comparisons rather support the hypothesis that an active site threonine hydroxyl contributes a proton used in the reduction of the substrate methylene to pyruvate methyl in the final stage of the mechanism.

Citation: O'Rourke PEF, Eadsforth TC, Fyfe PK, Shepherd SM, Hunter WN (2011) *Pseudomonas aeruginosa* 4-Amino-4-Deoxychorismate Lyase: Spatial Conservation of an Active Site Tyrosine and Classification of Two Types of Enzyme. PLoS ONE 6(9): e24158. doi:10.1371/journal.pone.0024158

Editor: Andrew J. Roe, University of Glasgow, United Kingdom

Received May 25, 2011; **Accepted** August 1, 2011; **Published** September 15, 2011

Funding: This research has been funded by the Wellcome Trust (grant no. 082596 and 083481) and European Commission Seventh Framework Programme (FP7/2007-2013, AEROPATH grant no. 223461). The funders had no role in study design, data collection and analysis, decision to publish, or preparation of the manuscript.

Competing Interests: The authors have declared that no competing interests exist.

* E-mail: w.n.hunter@dundee.ac.uk

Introduction

Aminodeoxychorismate lyase catalyzes the formation of *para*-aminobenzoate (PABA) from 4-amino-4-deoxychorismate (Figure 1) as part of the biosynthetic route to folate [1][2]. The enzyme, encoded by the *pabC* gene, is labeled as PabC.

In *Escherichia coli* and many other bacteria, PABA is synthesized in two steps starting from chorismate [3]. The first step produces 4-amino-4-deoxychorismate [4] by transferring ammonia, derived from glutamine, to chorismate. This reaction is performed by PABA synthase, a heterodimer of proteins encoded by the *pabA* and *pabB* genes [5]. 4-amino-4-deoxychorismate is then converted to PABA with the loss of pyruvic acid (Figure 1). The pyridoxyl 5′-phosphate (PLP) - dependent PabC catalyzes this second step [2][3][6][7]. In the Gram-positive *Bacillus subtilis* a third chemical step is required for PABA biosynthesis. Chorismate is first converted to 2-amino-2-deoxyisochorismate before production of 4-amino-4-deoxychorismate, which is then converted to PABA and pyruvate by PabC [8].

PABA is required for the biosynthesis of folic acid and by extension also of essential metabolites such as thymidylate and methionine. In addition, PABA is required for biosynthesis of antibiotics such as candicidin [9] and certain *Streptomycetes* even possess additional copies of *pabC*, located in antibiotic production operons [10].

The inhibition of PabC would reduce PABA levels and so deplete the supply of folic acid available to the microorganism. Provided that the microbe cannot obtain sufficient PABA from the cellular environment or by other means these cells would be expected to cease growth and die. This is what is observed in *pabC* knockouts in *E. coli* [7], *Pseudomonas aeruginosa* [11], *Helicobacter pylori* [12] and *Acinetobacter baylyi* [13]. A few anti-microbial agents exert their effect through inhibition of folate biosynthesis. Sulphonamides for example deplete bacterial intracelluar folate levels by inhibiting PABA synthase and dihydropteroate synthetase [14]. Combining novel PabC inhibitors with sulphonamides or with other anti-folates such as the dihydrofolate reductase inhibitor trimethoprim, could produce a synergistic anti-microbial effect and new inhibitors of PabC would allow such a hypothesis to be tested.

X-ray crystal structures of PabC from *E. coli* [15], *Thermus thermophilus* [16] and *Legionella pneumophila* [Protein Data Bank

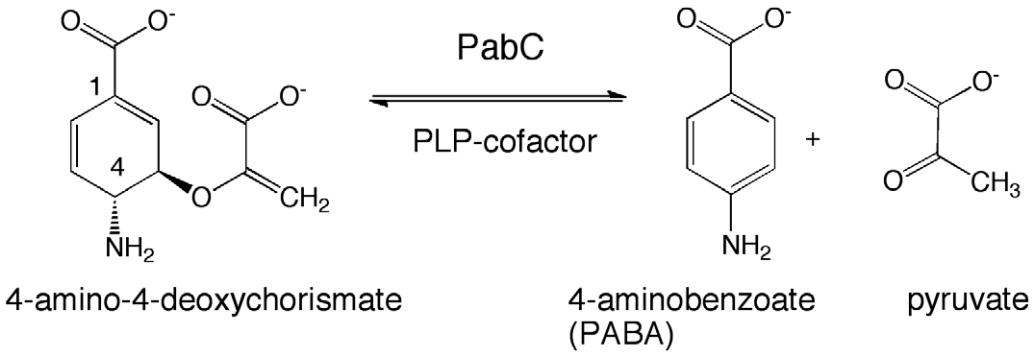

Figure 1. PabC catalyzes the conversion of 4-amino-4-deoxychorismate to 4-aminobenzoate and pyruvate.
doi:10.1371/journal.pone.0024158.g001

(PDB) code 3lul] have been determined. PabC displays a similar overall fold to branched-chain amino acid transferases and D-amino acid transferases [15][17][18]. These aminotransferases have been investigated to identify potential inhibitors for example in support of research for treatments of neurodegenerative disease [19][20][21][22]. Moreover, since PLP-dependent enzymes provide opportunities for the design of mechanism-based suicide inhibitors [17] this enzyme family appears an attractive one from the perspective of structure and mechanism-based drug discovery. The absence of the enzyme in humans and its essentiality in various microbes suggests that inhibition of PabC offers the possibility of new therapies targeting a range of microbial infections and structural studies provide useful data to assess the potential of this protein for such early stage drug discovery [23].

We have a particular interest in pathogens for which current treatments are unsatisfactory, for example Gram-negative bacteria such as *P. aeruginosa*, that are highly adaptable to their environment and which possess efficient and varied drug-resistance mechanisms. *P. aeruginosa* is often the cause of life-threatening infections in people with cystic fibrosis, burns victims and immunocompromised individuals [24][25]. We describe the construction of an efficient bacterial recombinant expression system, enzyme purification and crystallization protocols, and report the high-resolution crystal structure of PabC from *P. aeruginosa* (*Pa*PabC). Comparisons with previously determined PabC structures are presented, concentrating on active site cofactor interactions. Our structure-based comparisons identified the potential for a tyrosine to participate in catalysis and suggested that a re-evaluation of a published mechanism is warranted.

Materials and Methods

Cloning, protein purification and analytical ultracentrifugation

The *P. aeruginosa pabC* gene (locus tag: PA2964) was amplified from genomic DNA (American Type Culture Collection 47085, strain PAO1) by PCR using the following primers:

*Pa*PabC forward primer

5′-**CAT ATG** CTG GAC TGG GTC GAC-3′ (*Nde*I restriction site in bold)

*Pa*PabC reverse primer:

5′-**GGA TCC** TCA GAA ATC CAG GTC G-3′ (*Bam*HI restriction site in bold)

The PCR product was blunt-end ligated into a TOPO cloning vector (Invitrogen) then ligated into a modified pET15b expression vector (Novagen) that produces a hexahistidine-tag linked via a tobacco-etch virus (TEV) protease cleavage site. The resulting plasmid was heat-shock transformed into *E. coli* BL-21 (DE-3) GOLD cells (Novagen). Cultures were grown at 37°C in 2 L of Luria-Bertani medium supplemented with 100 μg mL^{-1} carbenicillin. Gene expression was induced, when the OD_{600} reached 0.6, by addition of 1 mM IPTG and growth continued for a further 16 hours at 18°C. Cells were harvested by centrifugation (3000× *g* at 4°C for 30 minutes), resuspended in 50 mM Tris-HCl, 200 mM NaCl, pH 7.5, and lysed by passage through a French pressure cell. Cell lysate was clarified by ultracentrifugation (40000× *g* at 4(C for 30(minutes) and the supernatant was passed through a 0.2 μm filter.

The lysate was loaded onto an immobilised metal ion affinity chromatography column (5 mL HisTrap HP, GE Healthcare) with the assistance of an FPLC system (Äkta Explorer, GE Healthcare). The hexahistidine-tagged protein was eluted from the column by a linear concentration gradient of imidazole and fractions were analysed by SDS-PAGE. Selected fractions were pooled and dialysed into 100 mM HEPES, 500 mM NaCl pH 7.5. Attempts to cleave the hexa-histidine tag by addition of TEV protease had produced large amounts of precipitate so it was decided to leave the purification tag in place. The protein was further purified by size exclusion gel chromatography (Superdex 200 26/60, GE Healthcare). This column had previously been calibrated with molecular weight standards, blue dextran (>2,000 kDa), thyroglobulin (669 kDa), ferritin (440 kDa), aldolase (158 kDa), conalbumin (75 kDa), ovalbumin (43 kDa), carbonic anhydrase (29.5 kDa), ribonuclease A (13.7 kDa) and aprotinin (6.5 kDa); (GE Healthcare; data not shown). Protein purity was assessed by SDS-PAGE, matrix assisted laser desorption/ionisation – time of flight mass spectrometry (MALDI-TOF MS) and electrospray ionisation mass spectrometry.

The protein concentration was determined spectrophotometrically using a theoretical extinction coefficient of 33,460 M^{-1} cm^{-1} (ProtParam, [26]).

Crystallization, X-ray data collection, structure solution and refinement

*Pa*PabC was crystallized at 20°C by the hanging drop vapour diffusion method. The enzyme was concentrated to 33 mg mL^{-1} in 100 mM HEPES, 500 mM NaCl pH 7.5. Stock solutions of PLP (100 mM in DMSO) and PABA (200 mM in deionized water) were prepared and added to the PabC solution to give final concentrations of 0.1 mM PLP and 10 mM PABA. The mixture was left to incubate for 3 hrs then crystallization drops were assembled by mixing 1 μL of the protein:ligand mixture with 1 μL of reservoir containing 10% (w/v) PEG 400, 1.8 M ammonium sulfate and 100 mM MES pH 6.5. Clumps of pale yellow,

orthorhombic blocks grew over one week and a fragment of approximate dimensions 0.3 mm×0.2 mm×0.1 mm was used for data collection. Addition of cryoprotectant (25% v/v glycerol) was required to allow crystals to be mounted in a gaseous nitrogen cryostream at −173°C for diffraction experiments. Crystals were initially characterized using a copper anode X-ray generator (Rigaku 007) and an image plate detector (RAXIS IV^{++}). The crystal was stored in liquid nitrogen for data collection at the European Synchrotron Radiation Facility (ESRF, Grenoble, France).

Diffraction data were collected on beamline ID29 at ESRF using a Quantum4 CCD detector. It proved beneficial to use the automated crystal annealing facility established on the station. Data were indexed and integrated using MOSFLM [27], and scaled with SCALA [28]. Crystallographic statistics are presented in Table 1. The search model for molecular replacement was prepared by generating a poly-alanine model of the *E. coli* PabC structure (PDB code 1et0, [15]) from which all waters and non-protein molecules had been removed. This model shares 35% sequence identity with *Pa*PabC. Molecular replacement calculations were performed using MOLREP [29].

Refinement was performed in REFMAC5 [30][31] and the model was inspected and manipulated in COOT [32]. Strict non-crystallographic symmetry restraints were employed in the early stages of the refinement and then removed. The presence of the PLP cofactor covalently bound to Lys140 was confirmed by calculating an omit electron density map (Figure 2). The N-terminal histidine tag was not visible in electron density maps. A number of ligands (tetraethylene glycol, 1,2-ethanediol, di(hydroxymethyl)ether, glycerol, chloride and sulfate ions) were assigned on the basis of the difference density and chemical environment, and refined satisfactorily. Both tetraethylene glycol and ethylene glycol are likely decomposition products of PEG400 used in crystallization, impurities or represent partially ordered molecules. MOLPROBITY [33] was used to assess model geometry, AREAIMOL [31] and the Protein Interfaces, Surfaces and Assemblies, EMBL server [http://www.ebi.ac.uk/msd-srv/prot_int/pistart.html; [34]] were used to calculate surface and interface areas. Figure 1 was prepared with CHEMDRAW (Adept Scientific), Figure 5 with ALINE [35] and the remainder using PyMOL [36] and ILLUSTRATOR (Adobe Systems Inc.).

Amino acid sequence alignments and analysis

A search of the UniProt database with the Enzyme Commission number for PabC (4-amino-4-deoxychorismate lyase; 4.1.3.38) identified 368 entries. These were clustered such that sequences

Table 1. Crystallographic statistics.

Space group	$P\,2_12_12_1$
Unit cell dimensions: *a*, *b*, *c* (Å)	40.8, 66.8, 202.7
Resolution range (Å)	30.00 - 1.75
Unique reflections	56255
Completeness (%)	98.9 (98.5)[a]
$<I/\sigma(I)>$	10.7 (2.5)
Multiplicity	3.7 (3.3)
R_{merge}[b]	7.8 (45.1)
No. of reflections	53372
R_{cryst}[c], R_{free}[d]	16.7, 21.5
Protein residues	538
Ligands	2× PLP, 3 Cl^-, 2 SO_4^{2-}, 2 glycerol, 3 di(hydroxyethyl)ether, 5 tetraethyleneglycol, 3 1,2-ethanediol & 474 waters
r.m.s. deviations from ideal geometry	
bond lengths (Å)	0.025
bond angles (°)	2.1
B values (Å^2)	
From Wilson Plot	18.4
Mean *B* values	Chain A, main chain atoms: 15.1
	Chain A, side chain atoms: 18.2
	Chain B, main chain atoms: 18.5
	Chain B, side chain atoms: 20.7
	Waters: 30.8
	PLP: Chain A 15.8 Chain B 21.5
	Other ligands 36.3
Ramachandran favoured/allowed (%)	93.7/99.4 (3 outliers: Arg90, Chains A, B Leu89, Chain B)

[a]Values in parentheses refer to the highest resolution shell (1.84−1.75 Å).
[b]$R_{merge} = \sum_{hkl}\sum_i |I_i(hkl) - <I(hkl)>| / \sum_{hkl}\sum_i I_i(hkl)$; where $I_i(hkl)$ is the intensity of the *i*th measurement of reflection *hkl* and $<I(hkl)>$ is the mean value of $I_i(hkl)$ for all *i* measurements.
[c]$R_{cryst} = \sum_{hkl}||F_o| - |F_c|| / \sum|F_o|$, where F_o is the observed structure factor and F_c is the calculated structure factor.
[d]R_{free} is the same as R_{cryst} except calculated with a subset, 5%, of data that are excluded from refinement calculations.
doi:10.1371/journal.pone.0024158.t001

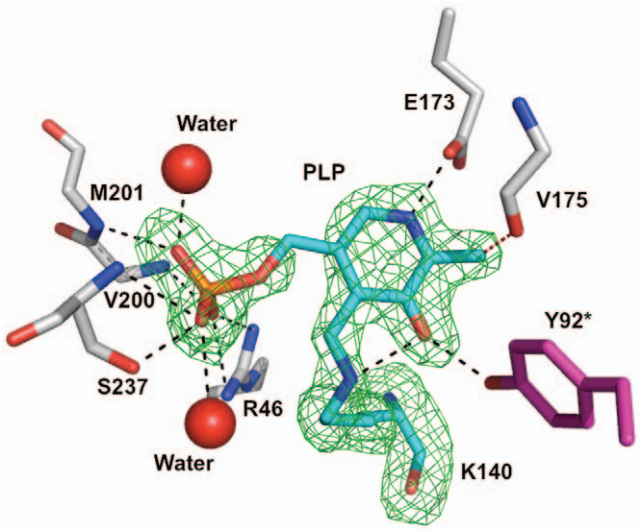

Figure 2. The omit map for PLP and Lys140 from subunit A. $|(F_o)-(F_c)|$ difference density contoured at 3σ (green chicken wire). Selected hydrogen bonding associations between the protein, two water molecules (red spheres) and PLP are depicted as dashed lines. A * marks Tyr92 as contributed from subunit B. The side chain of Glu173 displays two rotamers with only one shown.
doi:10.1371/journal.pone.0024158.g002

with a 90% or greater similarity to each other were grouped and a representative sequence identified. This reduced the list to 197 entries. Sequences consisting of more than 400 amino acids were removed and this further reduced the list to 181 entries. These were aligned using MUSCLE [37] and then inspected following pairwise alignment with *Pa*PabC. A conservative group of 129 putative PabC sequences was then identified following the removal of sequences that were fragmentary, labeled as other proteins or which displayed a sequence identity of less than or equal to 20%.

Molecular modeling of the catalytic intermediate

A model of the substrate, 4-amino 4-deoxychorismate, was prepared using PRODRG [38] and placed into the active site using the molecular graphics program COOT [32] with the position of the bound pyridoxyl 5′ phosphate as a guide to allow formation of the catalytic intermediate. The active site was prepared for docking of this ligand using ICM pro (MolSoft L.L.C; http://www.molsoft.com/index.html) with the centre of the ligand-binding site defined by a cavity that contained the residues within 5 Å of the 4-amino 4-deoxychorismate. The top ten docking poses, as scored by ICM Pro software gave similar orientations in the active site and one was selected for discussion and display.

Results and Discussion

Overall structure

Size exclusion gel filtration, carried out during protein purification, indicated a single species of approximate mass 50 kDa that is commensurate with a homodimeric species. In the crystal structure two polypeptide chains, labelled A and chain B together constitute the asymmetric unit in *Pa*PabC (Figure 3), and the crystals have an estimated bulk solvent content of 45%. The polypeptide chains form a dimer (Figure 3) and, as described below, such oligomerization is required to create the enzyme active site. The presence of a *Pa*PabC dimer is consistent with previous studies since all PabC structures solved to date are

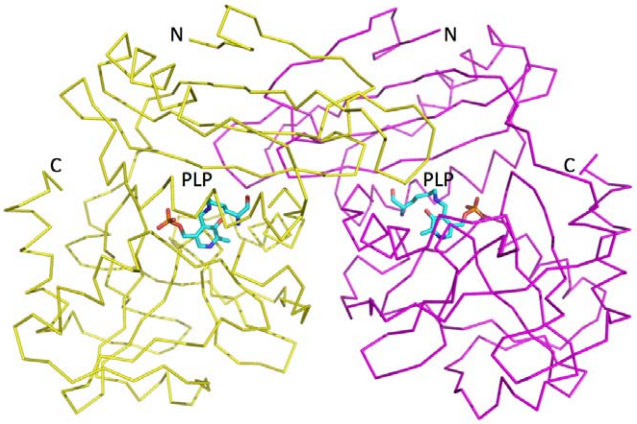

Figure 3. The *Pa*PabC dimer. Each subunit is depicted as a Cα trace (yellow and purple) with the PLP shown as stick model in a similar fashion to Figure 3. The N and C – terminal residue positions are labelled.
doi:10.1371/journal.pone.0024158.g003

dimeric or in the case of *T. thermophilus* PabC, a dimer-of-dimers is observed [16].

The *Pa*PabC subunits display a high degree of non-crystallographic symmetry. The rmsd following a least-squares fit of 270 Cα positions is 0.4 Å. It is therefore only necessary to detail one subunit and one active site.

The *Pa*PabC subunit is constructed from two domains (Figure 4). The N-terminal domain (domain I) is smaller than the C-terminal domain (domain II). Domain I comprises residues 1–107, which

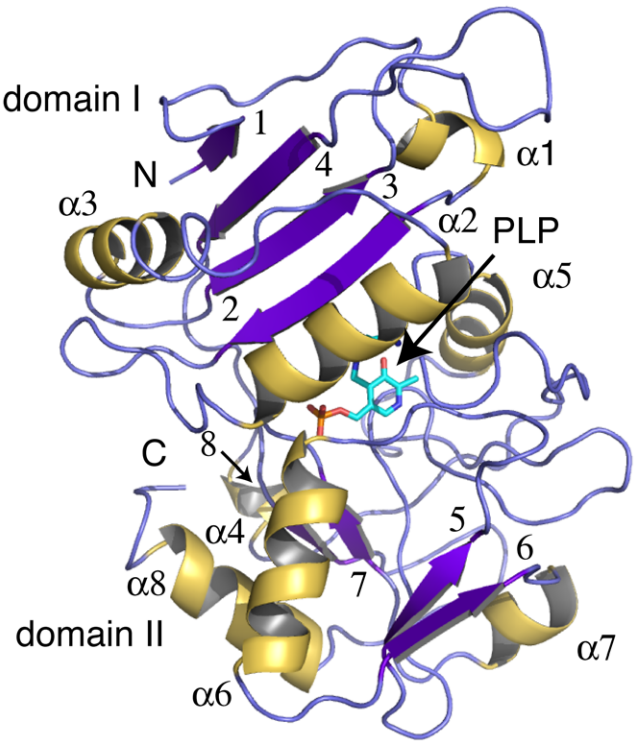

Figure 4. Ribbon diagram of the *Pa*PabC monomer (β-sheet is shown in purple, α-helix in yellow). Domain I is formed by α-helices 1–3 and the anti-parallel β-strands 1–4. Domain II is formed by α-helices 4–8 and β-strands 5–8.
doi:10.1371/journal.pone.0024158.g004

contains three α-helices (α1-3) and a four-stranded anti-parallel β-sheet in order β1-β4-β3-β2. Domain II comprises residues 112–271 that form five α-helices (α4–8), one short two-stranded parallel β-sheet (β5–β6) and one short two-stranded anti-parallel β-sheet (β7–β8). Residues 108–111 link the two domains. The PLP cofactor is covalently bound to Lys140 that is in domain II. The active site is formed in a cleft formed between the two domains (Figure 3).

Sixty residues from each subunit, provided by both domains, contribute to dimer formation. These residues participate in around 30 hydrogen-bonding associations and eight salt bridge interactions to stabilize the quaternary structure. Most of the residues that contribute to the dimer interface are found in two patches; residues Ala10 to Gly25 centred on α1 and residues Arg127 to Ala152 centered on α5.

The approximate dimensions of the dimer, which constitutes the asymmetric unit, are 80 Å×40 Å×40 Å and this displays a solvent accessible surface area of approximately 21,000 $Å^2$. The contact area between the two subunits occupies approximately 2,050 $Å^2$, about 15% of the surface of a subunit. These values are similar to those observed for other PabC proteins, for example the interface of the *E. coli* protein (PDB code 1et0) covers an area of 2,130 $Å^2$.

The structures of PabC from three organisms (*E. coli*, *L. pneumophila* and *T. thermophilus*) display a high degree of structural conservation with *Pa*PabC. Least-squares fitting of the Cα positions of single subunits results in RMSD values of between 1.27 and 1.95 Å, with a coverage in the range of 81 to 92% of the structures. The sequence identity shared with *Pa*PabC, falls in the range 26% to 35%.

The active site and mechanistic considerations

The active site of *Pa*PabC is positioned between the two domains of the monomer close to the dimer interface (Figure 3). Here, the PLP cofactor is covalently linked to Lys140, bound and oriented by interactions with key residues, a selection of which are depicted in Figure 2. The PLP phosphate accepts hydrogen bonds donated by a cluster of main chain amide groups from Val200, Met201 and Ser237, and the side chain of Arg46. The side chain of Arg46 is itself positioned by interactions with the side chain of Glu28, which in turn accepts a hydrogen bond from His43 ND1. Two well ordered water molecules mediate hydrogen bonding networks linking the phosphate group to Asn178 OD1 and Arg202 N on one side, the main chain O and N groups of Thr29 on the other. The cofactor ring is sandwiched between Val197 and the main chain of a tripeptide segment comprising Val175-Phe176-Ser177. A hydrogen bond between Asn236 ND2 and the carbonyl of Phe176 in conjunction with hydrogen bonds formed between the amide groups and the side chain of Glu161 helps to determine the conformation of the tripeptide that forms a tight turn, between β9 and β10, that covers part of the cofactor.

The PLP methyl group makes van der Waals interactions with Gln147 CG and is positioned 3.2 Å distant from the carbonyl oxygen of Val175. The geometry of this latter contact is compatible with the presence of a C-H•••O hydrogen bond [39]. The side chain of Gln147 is held in place by a hydrogen bond with Arg144 NE. The arginine side chain is itself positioned by hydrogen bonds formed with the carbonyl groups of Leu139 and His141. There are also three water molecules (data not shown), which form a complex network of hydrogen bonds linking the side chain of Arg144 to other sections of the enzyme. In addition the positive dipole from α6, the closest residue on this helix is Gly199, provides an attractive force to interact with the PLP phosphate. The side chain of Glu173 displays a degree of conformational freedom with two rotamers being observed. One rotamer places the side chain to accept a hydrogen bond donated from PLP N1 (Figure 2). The alternative rotamer places the carboxylate at a distance of 3.7 Å from N1 (data not shown). Tyr92 from the partner subunit forms a hydrogen bond to PLP O3. The cofactor is also likely to posses an intra-molecular hydrogen bond involving O3 and NZ of Lys140. The side chain of Phe27, Val197 and aliphatic components of Arg46 and Arg144 surround the side chain of Lys140.

No structures of PabC-ternary complexes have yet been published to inform on aspects of substrate recognition and enzyme activity. Given the importance of such complexes we judged it important to get such data and attempted to determine structures of *Pa*PabC in complex with a number of compounds, for example, the sample used for structure determination was crystallized in the presence of 10 mM PABA. However, we have been unable to identify electron density compatible with binding of any such ligand in the substrate-binding pocket. We judged therefore that the position of PLP and Lys140 NZ, together with the conservation of amino acid sequence and structures give an indication of where substrate binds and which residues are important for substrate recognition and catalytic function. Consideration of an amino acid sequence alignment and structural overlay of *Pa*PabC with three other structures in the PDB proved particularly informative. To this we added molecular modelling and docking of the covalent intermediate formed during catalysis.

The contributions of 24 residues, within about 5 Å of PLP, to binding the cofactor and organising the active site are described above and summarized in Figure 5. Seven of these residues are strictly conserved in PabC of *P. aeruginosa*, *E. coli*, *L. pneumophila* and *T. thermophilus* (Phe27, Thr29, His43, Arg46, Gly199, Lys140 and Arg202 in *Pa*PabC). With one exception these residues contribute to the active site using the chemical properties of their side chains. The exception is Gly199 where any alteration on Cα would result in a steric clash with the phosphate group of PLP. Another seven residues contribute to the active site primarily through the hydrogen bonding capacity of the main chain (Val175, Phe176, Ser177, Leu139, His141, Val200 and Met201). Phe176 is not conserved in any of the three other sequences but the remainder are conserved in at least one other orthologue. Ser237 interacts with the PLP phosphate using main chain and side chain groups. This residue is only different in the *E. coli* sequence where an alanine is observed and an additional water molecule binds nearby helping to satisfy hydrogen-bonding capacity (data not shown). A similar observation is made when considering *Pa*PabC Asn236. The residue is conserved in *Ec*PabC and *Lp*PabC but changed to glycine in *Tt*PabC where a water molecule is observed to replace the side chain (data not shown). Asn178 is strictly conserved in *Ec*PabC and *Lp*PabC but changed to serine in *Tt*PabC. The side chain here simply helps to form one side of the cofactor-binding site. Val197 is conserved in *Ec*PabC and conservatively substituted as leucine in the other two sequences. The residue at this position in the active site forms van der Waals interactions with the cofactor. In *Pa*PabC Arg144 NE donates hydrogen bonds to Gln147 OE1 and the carbonyl of His141; interactions that help to create one side of the cofactor-binding site and to fix the position of Val197. These residues and the interactions they form appear to be conserved in *Ec*PabC but not in *Lp*PabC or *Tt*PabC. Sequence and structure alignments (not shown) indicate that *Pa*PabC Arg144 is replaced by tyrosine in both *Lp*PabC and *Tt*PabC and *Pa*PabC Gln147 replaced by an alanine in *Lp*PabC and a tyrosine in *Tt*PabC. This is an intriguing observation to be discussed below.

There are three glutamates amongst the 24 residues discussed above, Glu28, Glu161 and Glu173. Glu28 helps to position Arg46 to bind the cofactor phosphate. Both residues are strictly

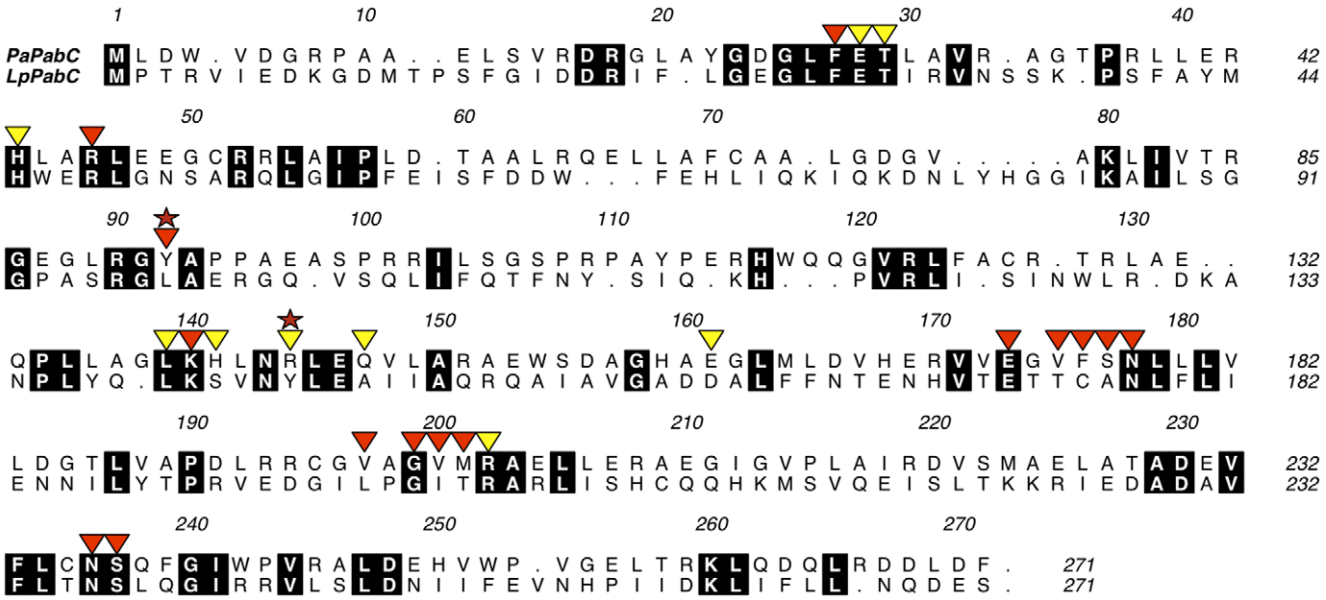

Figure 5. Structure-based alignment of *Pa*PabC and *Lp*PabC. Residues encased in black are strictly conserved. Red stars indicate the tyrosine residues at Position I (*Pa*PabC Y92) and Position II (*Lp*PabC Y144). Triangles mark residues that are discussed in the text. Red triangles identify Lys140 and residues that interact directly with the Lys140-PLP adduct; yellow triangles mark residues that contribute to the organization of the active site or that participate in solvent mediated interactions between the protein and the cofactor.
doi:10.1371/journal.pone.0024158.g005

conserved in *Lp*PabC. A conservative substitution of the glutamate to threonine occurs in both *Ec*Pabc and *Tt*PabC and the hydrogen bonding interactions to support the role of an arginine binding the cofactor are preserved. Glu161 helps to configure a tripeptide segment to cover part of the cofactor and this feature is conserved since a glutamate is present in the other structures or, as in *Lp*PabC an aspartate occupies this position. The carboxylate side chain of Glu173 can interact directly with the cofactor by accepting a hydrogen bond donated from N1. In a similar fashion to what is observed for Glu161, such interactions occur in the orthologues with the residue either strictly conserved, or as in *Tt*PabC, replaced by aspartate.

A catalytic mechanism, based on previous studies of PLP-dependent enzymes, was proposed for PabC prior to any structural data being available [10]. Following structure determination of *Ec*PabC, a model of substrate binding was prepared to inform an assessment of the mechanism [15]. The contribution of PLP was considered the same, that is, following covalent linkage the enzyme-cofactor adduct undergoes a nucleophilic attack by the substrate amino group to produce a reactive external aldimine. This species then undergoes α-proton elimination, at C4, to the ε-amino group of a lysine to yield a reaction intermediate. In *Ec*PabC Lys159 forms the covalent link to the cofactor and likely responsible for α-proton abstraction. Nakai *et al.*, [15] further

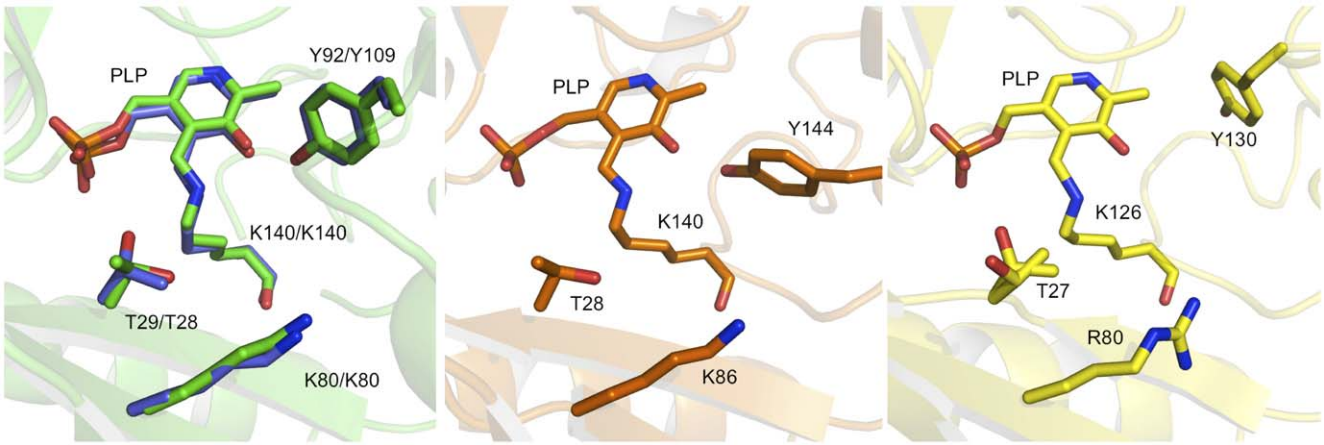

Figure 6. Structural conservation of tyrosine in the PabC active site. PLP is shown in the same manner as Figure 2. Left panel. A structural overlay of *Pa*PabC (green C atoms) and *Ec*PabC (blue C atoms). Here, Tyr92 and Tyr109, which represent position I, are contributed from the partner subunit. Centre panel. *Lp*PabC. Right panel. *Tt*PabC. Residue Thr27 displays two rotamers. In the *Lp*PabC and *Tt*PabC structures, Tyr144 and Tyr130 respectively represent position II and belong to the same subunit that forms the PLP-binding site.
doi:10.1371/journal.pone.0024158.g006

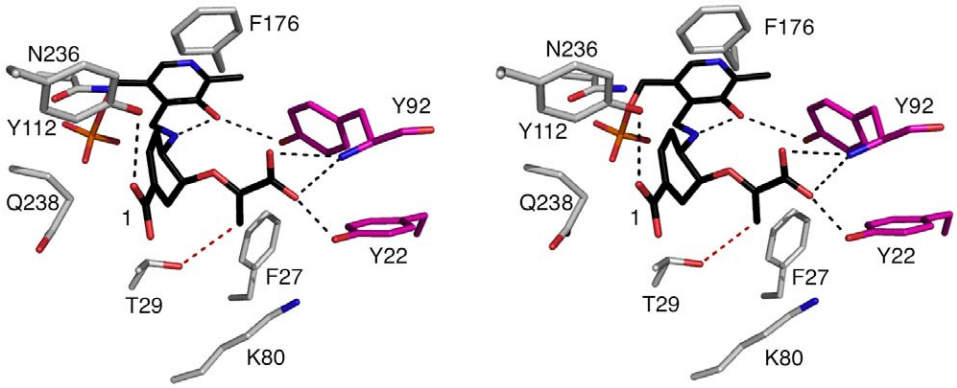

Figure 7. A stereoview of the catalytic intermediate docked into the active site of *Pa*PabC. The protein components are colored as in Figure 2. The C atoms of the modelled intermediate are black. Black dashed lines represent potential hydrogen bonding interactions, with a separation of 3.5 Å or less, and the red dashed line between Thr29 OG1 and the sp^2 hybridized C indicates the proximity of functional groups likely involved in catalysis.
doi:10.1371/journal.pone.0024158.g007

suggested that Thr28 of *Ec*PabC supplies a proton to reduce the olefin moiety of the substrate as pyruvate is released. To recover the Schiff-base form of the enzyme, PABA is released and PLP reacts with Lys159.

Three residues described as contributing to the mechanism of action in *Ec*PabC, Thr28, Lys97 and Lys159 [15], are strictly conserved in *Pa*PabC as Thr29, Lys80 and Lys140. They are also conserved in *Lp*PabC and *Tt*PabC with the conservative change of Lys80 to arginine in the thermophilic orthologue (Figure 5). Lys140 of *Pa*PabC is suitably placed to support α-proton abstraction and although Thr29 may engage in the proposed proton shuffling with both the olefin moiety of the substrate and Lys80 we noted an alternative residue that might fulfil this role. This residue may have been overlooked because Nakai *et al.*, [15] had access to only a single structure of PabC and alignments based on sequences alone would not identify a tyrosine that is conserved in three-dimensions.

In *Ec*PabC and *Pa*PabC tyrosine OH groups (Tyr109 and Tyr92 respectively), from the partner subunit, donate a hydrogen bond to PLP O3 (Figures 2, 6); an interaction that influences the electronic structure of the cofactor [15]. The sequence alignment of PabC orthologues suggests a degree of variation in the identity of the amino acid that occupies the position of this tyrosine (Figure 5). The structural overlays are striking since they clearly identify a conserved tyrosine in relation to the cofactor (Figure 6). In *Ec*PabC and *Pa*PabC, Tyr109 and Tyr92 respectively, are contributed from the partner subunit. We call this position I. However, in *Lp*PabC and *Tt*PabC, Tyr144 and Tyr130 respectively, are contributed from the same subunit, or position II.

We isolated 129 putative PabC sequences to investigate the distribution of tyrosine at these two positions seeking to address the hypothesis that if tyrosine is present at position I then it is likely absent from position II and *vice versa*. This hypothesis holds true for 125 out of the 129 sequences (data not shown). Two sequences, which share less than 30% sequence identity, have a tyrosine at both positions. Analyses of the sequences suggests that PabC can be classified into two groups depending on whether this active site tyrosine is provided by the same subunit which primarily forms the active site or from a partner subunit.

Furthermore the high degree of conservation of an active site tyrosine in three-dimensional structures of PabC suggests a functional role. One possibility is that this residue could act as a proton donor for the methylene to methyl reduction that completes the reaction. Such a reduction would have little influence on the cleavage of the C-O bond of the substrate since the driving force for that reaction would be production of a conjugated aromatic six-carbon ring system. Our model of the catalytic intermediate (Figure 7) was specifically created to investigate the potential role of this active site tyrosine and to re-evaluate the reduction process that completes the reaction.

The model suggests that Tyr112 donates a hydrogen bond to the C1 carboxylate whilst, with contributions from the partner subunit, the main chain amide of Tyr92 and hydroxyl group of Tyr22 donate hydrogen bonds to the other carboxylate of the intermediate (Figure 7). Tyr92 contributes to the positioning and electronic structure of the cofactor by virtue of the hydrogen bond involving the hydroxyl group with the PLP carbonyl (Figure 2). The bulk of the tyrosine side chain serves to create a hydrophobic wall on one side of the active site. Although placed to interact with the catalytic intermediate this residue does not appear to be involved in donating a proton to convert methylene to methyl as part of the catalytic cycle (Figure 7). Rather, Thr29, as first postulated by Nakai *et al.*, [15] appears to fulfil such a role with the hydroxyl group placed about 3.5 Å from the olefin (Figure 7). Lys80 NZ is around 4.3 Å distant from the sp^2 hybridized C and it is possible that an alternative rotamer could bring this functional group into play with respect to either providing a proton itself or in activating the Thr29 hydroxyl for proton donation. We note that Thr29 is strictly conserved in 123 out of the 129 PabC sequences and conservatively substituted by serine in another five sequences. The single sequence in which we could not identify conservation in terms of a threonine or serine corresponding to Thr29 is the putative PabC from *Pantoea vagans*. This is a poorly conserved sequence sharing approximately 30% identity.

To further investigate the structure-activity relationship of PabC, and to assess the potential of this enzyme as a target for structure-based drug discovery will require the powerful combination of steady-state kinetic analysis with site-directed mutagenesis studies, and to carry out screening of chemical libraries. It will be imperative to extend from our work and to elucidate a means whereby structural data on enzyme-ligand complexes can be obtained.

Acknowledgments

We thank our colleague Mark Agacan for discussions, staff at ESRF for access to facilities and excellent support. Coordinates and structure factors are deposited with the PDB under accession code 2y4r.

Author Contributions

Conceived and designed the experiments: PEFO TCE WNH. Performed the experiments: PEFO TCE PKF SMS. Analyzed the data: PEFO TCE PKF WNH. Contributed reagents/materials/analysis tools: SMS. Wrote the paper: PEFO TCE WNH.

References

1. Ye Q, Liu J, Walsh CT (1990) *p*-Aminobenzoate synthesis in *Escherichia coli*: Purification and characterization of PabB as aminodeoxychorismate synthase and enzyme X as aminodeoxychorismate lyase. Proc Natl Acad Sci U S A 87: 9391–9395.
2. Green JM, Nichols BP (1991) p-Aminobenzoate biosynthesis in *Escherichia coli*. J Biol Chem 266: 12971–12975.
3. Nichols BP, Seibold AM, Doktor SZ (1989) para-Aminobenzoate synthesis from chorismate occurs in two steps. J Biol Chem 264: 8597–8601.
4. Anderson KS, Kati WM, Ye Q, Liu J, Walsh CT, et al. (1991) Isolation and structure elucidation of the 4-amino-4-deoxychorismate intermediate in the PABA enzymatic pathway. J Am Chem Soc 113: 3198–3200.
5. Parsons JF, Jensen PY, Pachikara AS, Howard AJ, Eisenstein E, et al. (2002) Structure of *Escherichia coli* aminodeoxychorismate synthase: architectural conservation and diversity in chorismate-utilizing enzymes. Biochemistry 41: 2198–2208.
6. Slock J, Stahly DP, Han CY, Six EW, Crawford IP (1990) An apparent *Bacillus subtilis* folic acid biosynthetic operon containing pab, an amphibolic trpG gene, a third gene required for the synthesis of para-aminobenzoic acid, and the dihydropteroate synthase gene. J Bacteriol 172: 7211–7226.
7. Schadt HS, Schadt S, Oldach F, Sussmuth RD (2009) 2-Amino-2-deoxychorismate is a key intermediate in *Bacillus subtilis* p-aminobenzoic acid biosynthesis. J Am Chem Soc 10: 3481–3483.
8. Aparicio JF, Caffrey P, Gil JA, Zotchev SB (2003) Polyene antibiotic biosynthesis gene clusters. Appl Microbiol Biotechnol 61: 179–188.
9. Zhang Y, Bai L, Deng Z (2009) Functional characterization of the first two actinomycete 4-amino-4-deoxychorismate lyase genes. Microbiol 155: 2450–2459.
10. Green JM, Merkel WK, Nichols BP (1992) Characterization and sequence of Escherichia coli pabC, the gene encoding aminodeoxychorismate lyase, a pyridoxal phosphate-containing enzyme. J Bacteriol 174: 5317–5323.
11. Hoang TT, Karkhoff-Schweizer RR, Kutchma AJ, Schweizer HP (1998) A broad-host-range Flp-FRT recombination system for site-specific excision of chromosomally-located DNA sequences: application for isolation of unmarked *Pseudomonas aeruginosa* mutants. Gene 212: 77–86.
12. Salama NR, Shepherd B, Falkow S (2004) Global transposon mutagenesis and essential gene analysis of *Helicobacter pylori*. J Bacteriol 183: 7926–7935.
13. de Berardinis V, Vallenet D, Castelli V, Besnard M, Pinet A, et al. (2008) A complete collection of single-gene deletion mutants of *Acinetobacter baylyi* ADP1. Mol Syst Biol 4: 174.
14. Brown GM (1962) The biosynthesis of folic acid. II. Inhibition by sulfonamides. J Biol Chem 237: 536–540.
15. Nakai T, Mizutani H, Miyahara I, Hirotsu K, Takeda S, et al. (2000) Three-dimensional structure of 4-amino-4-deoxychorismate lyase from *Escherichia coli*. J Biochem 128: 29–38.
16. Padmanabhan B, Bessho Y, Ebihara A, Antonyuk SV, Ellis MJ, et al. (2009) Structure of putative 4-amino-4-deoxychorismate lyase from *Thermus thermophilus* HB8. Acta Crystallogr F 65: 1234–1239.
17. Eliot AC, Kirsch JF (2004) Pyridoxal phosphate enzymes: Mechanistic, structural, and evolutionary considerations. Annu Rev Biochem 73: 383–415.
18. Jhee K, Yoshimura T, Miles EW, Takeda S, Miyahara I, et al. (2000) Stereochemistry of the transamination reaction catalyzed by aminodeoxychorismate lyase from *Escherichia coli*: Close relationship between fold type and stereochemistry. J Biochem 128: 679–686.
19. Soper TS, Manning JM (1981) Different modes of action of inhibitors of bacterial D-amino acid transaminase. A target enzyme for the design of new antibacterial agents. J Biol Chem 256: 4263–4268.
20. Castell A, Mille C, Unge T (2010) Structural analysis of mycobacterial branched-chain aminotransferase: implications for inhibitor design. Acta Cryst D 66: 549–557.
21. Hu LY, Boxer PA, Kesten SR, Lei HJ, Wustrow DJ, et al. (2006) The design and synthesis of human branched-chain amino acid aminotransferase inhibitors for treatment of neurodegenerative diseases. Bioorg Med Chem Lett 16: 2337–2340.
22. Lepore BW, Liu D, Peng Y, Fu M, Yasuda C, et al. (2010) Chiral discrimination among aminotransferases: Inactivation by 4-amino-4,5-dihydrothiophenecarboxylic acid. Biochem 49: 3138–3147.
23. Hunter WN (2009) Structure-based ligand design and the promise held for antiprotozoan drug discovery. J Biol Chem 284: 11749–11753.
24. George AM, Jones PM, Middleton PG (2009) Cystic fibrosis infections: treatment strategies and prospects. FEMS Microbiol Lett 300: 153–164.
25. Kerr KG, Snelling AM (2009) *Pseudomonas aeruginosa*: a formidable and ever-present adversary. J Hosp Infect 73: 338–344.
26. Gasteiger E, Hoogland C, Gattiker A, Duvaud S, Wilkins MR, et al. (2005) Protein Identification and Analysis Tools on the ExPASy Server. In Walker JM, ed. The Proteomics Protocols Handbook. TotowaNJ: Humana Press Inc. pp 571–607.
27. Leslie AG (2006) The integration of macromolecular diffraction data. Acta Crystallogr D 62: 48–57.
28. Evans P (2006) Scaling and assessment of data quality. Acta Crystallogr D 62: 72–82.
29. Vagin A, Teplyakov A (1997) MOLREP: an automated program for molecular replacement. J Appl Crystallogr 30: 1022–1025.
30. Murshudov GN, Vagin AA, Dodson EJ (1997) Refinement of macromolecular structures by the maximum-likelihood method. Acta Crystallogr D 53: 240–255.
31. Collaborative Computational Project, Number 4 (1994) Acta Cryst D 50: 760–763.
32. Emsley P, Cowtan K (2004) *Coot*: model-building tools molecular graphics. Acta Crystallogr D 60: 2126–2132.
33. Davis IW, Leaver-Fay A, Chen VB, Block JN, Kapral GJ, et al. (2007) MolProbity: all-atom contacts and structure validation for proteins and nucleic acids. Nucleic Acids Res 35: W375–383.
34. Krissinel E, Henrick K (2007) Inference of macromolecular assemblies from crystalline state. J Mol Biol 372: 774–797.
35. Bond CS, Schuttelkopf AW (2009) ALINE: a WYSIWYG protein-sequence alignment editor for publication-quality alignments. Acta Cryst D65: 510–512.
36. DeLano WL The PyMOL Molecular Graphics System, Schrödinger, LLC.
37. Edgar RC (2004) MUSCLE: multiple sequence alignment with high accuracy and high throughput. Nucleic Acids Res 32: 1792–97.
38. Schüttelkopf AW, van Aalten DM (2004) PRODRG: a tool for high-throughput crystallography of protein-ligand complexes. Acta Crystallogr D 60: 1355–1363.
39. Leonard GA, McAuley-Hecht K, Brown T, Hunter WN (1995) Do C-H•••O hydrogen bonds contribute to the stability of nucleic acid base pairs? Acta Crystallogr D 51: 136–139.

Acta Crystallographica Section D
Biological Crystallography
ISSN 0907-4449

Structural basis for type VI secreted peptidoglycan DL-endopeptidase function, specificity and neutralization in *Serratia marcescens*

Velupillai Srikannathasan,[a] Grant English,[b] Nhat Khai Bui,[c]‡ Katharina Trunk,[b] Patrick E. F. O'Rourke,[a] Vincenzo A. Rao,[a] Waldemar Vollmer,[c] Sarah J. Coulthurst[b]* and William N. Hunter[a]*

[a]Division of Biological Chemistry and Drug Discovery, College of Life Sciences, University of Dundee, Dundee DD1 5EH, Scotland, [b]Division of Molecular Microbiology, College of Life Sciences, University of Dundee, Dundee DD1 5EH, Scotland, and [c]Centre for Bacterial Cell Biology, Institute for Cell and Molecular Biosciences, Newcastle University, Newcastle upon Tyne NE2 4HH, England

‡ Current address: Helmholtz Institute for Pharmaceutical Research Saarland, Department of Microbial Natural Products, Saarland University, 66123 Saarbrücken, Germany.

Correspondence e-mail: s.j.coulthurst@dundee.ac.uk, w.n.hunter@dundee.ac.uk

Received 16 July 2013
Accepted 13 August 2013

PDB References: Ssp1, 4bi3; Ssp1-C50A, 4bi4; Ssp1–Rap1a, 4bi8; Rap1a, 3zfi; Rap2a, 3zib

Some Gram-negative bacteria target their competitors by exploiting the type VI secretion system to extrude toxic effector proteins. To prevent self-harm, these bacteria also produce highly specific immunity proteins that neutralize these antagonistic effectors. Here, the peptidoglycan endopeptidase specificity of two type VI secretion-system-associated effectors from *Serratia marcescens* is characterized. These small secreted proteins, Ssp1 and Ssp2, cleave between γ-D-glutamic acid and L-*meso*-diaminopimelic acid with different specificities. Ssp2 degrades the acceptor part of cross-linked tetratetrapeptides. Ssp1 displays greater promiscuity and cleaves monomeric tripeptides, tetrapeptides and pentapeptides and dimeric tetratetra and tetrapenta muropeptides on both the acceptor and donor strands. Functional assays confirm the identity of a catalytic cysteine in these endopeptidases and crystal structures provide information on the structure–activity relationships of Ssp1 and, by comparison, of related effectors. Functional assays also reveal that neutralization of these effectors by their cognate immunity proteins, which are called resistance-associated proteins (Raps), contributes an essential role to cell fitness. The structures of two immunity proteins, Rap1a and Rap2a, responsible for the neutralization of Ssp1 and Ssp2-like endopeptidases, respectively, revealed two distinct folds, with that of Rap1a not having previously been observed. The structure of the Ssp1–Rap1a complex revealed a tightly bound heteromeric assembly with two effector molecules flanking a Rap1a dimer. A highly effective steric block of the Ssp1 active site forms the basis of effector neutralization. Comparisons with Ssp2–Rap2a orthologues suggest that the specificity of these immunity proteins for neutralizing effectors is fold-dependent and that in cases where the fold is conserved sequence differences contribute to the specificity of effector–immunity protein interactions.

1. Introduction

Specialized secretion systems are key to bacterial fitness, survival and pathogenesis. They perform a myriad of roles in the processes that influence growth, colonization, attack and defence as bacteria interact with each other and with eukaryotic organisms (Filloux, 2011; Gerlach & Hensel, 2007). The recently identified type VI secretion system (T6SS), which is present in about 25% of Gram-negative bacteria for which genome sequences are available (Boyer *et al.*, 2009), can be used to target bacterial and eukaryotic cells and is thus important for both inter-bacterial competition and pathogenesis (Burtnick *et al.*, 2011; de Pace *et al.*, 2010; Jani &

Cotter, 2010). Antibacterial T6SSs mediate the efficient killing of competitors by direct injection of toxic antagonistic effector proteins into target cells (Murdoch *et al.*, 2011; Hood *et al.*, 2010; MacIntyre *et al.*, 2010; Schwarz *et al.*, 2010).

T6SS gene clusters encode the core components of a secretion machine capable of membrane perforation. This is a multi-protein needle-like assembly, resembling the contractile bacteriophage tail, that delivers effectors across three envelope layers in a single step (Bönemann *et al.*, 2010; Cascales & Cambillau, 2012; Silverman *et al.*, 2012). The clusters also encode accessory and post-translational regulatory components. Some T6SS-secreted effector proteins are also encoded within these large gene clusters. In the case of antibacterial T6SSs, effectors are always encoded adjacent to specific cognate immunity proteins. Immunity proteins bear appropriate signals to direct their localization to the compartment in which the toxic effectors act; for example, a Sec signal sequence guides localization to the periplasm. The provision of a cognate immunity protein provides protection against attack from sister cells (Coulthurst, 2013).

Different catalytic activities are associated with T6SS effectors. These include actin cross-linking and ADP-ribosylation, which disrupt the cytoskeletons of mammalian and amoebal cells (Pukatzki *et al.*, 2007; Rosales-Reyes *et al.*, 2012), and phospholipases, which degrade phosphatidylethanolamine, the major component of the bacterial membrane (Russell *et al.*, 2013). The best-characterized effectors are peptidoglycan hydrolases, which exhibit potent antibacterial activity (Russell *et al.*, 2011, 2012). These enzymes degrade peptidoglycan, the heteropolymer that occupies the periplasmic space, imparts mechanical strength to the cell wall and helps to maintain the shape of Gram-negative bacteria.

Peptidoglycan hydrolases constitute a large enzyme family which displays a rich diversity in terms of structure, mechanism and specificity (Vollmer *et al.*, 2008). There are enzymes specific for every glycosidic and amide bond in peptidoglycan. Such diversity is exploited to regulate bacterial cell growth, division and daughter-cell separation and, of particular interest here, to provide bactericidal properties that can be exploited in niche competition. Several classes of peptidoglycan hydrolases have been identified as T6SS effector proteins. These are termed Tse proteins. Tse3 from *Pseudomonas aeruginosa* is a muramidase, cleaving the glycan backbone (Russell *et al.*, 2011), and the C-terminal domain of *Vibrio cholerae* VgrG-3 has been suggested to have lysozyme-like muramidase activity (Brooks *et al.*, 2013). A diverse group of T6SS-secreted peptidoglycan amidases which cleave peptide cross-links has been described (Russell *et al.*, 2012). Within this superfamily, four distantly related families with distinct cleavage specificities were defined. Family 1 (Tae1), which includes Tse1 from *P. aeruginosa*, hydrolyses peptide cross-links at the γ-D-glutamyl-*meso*-diaminopimelate DL-bond, representatives of families 2 and 3 (Tae2 and Tae3) hydrolyse DD-cross-links between D-*m*A_2pm (*meso*-diaminopimelate) and D-alanine, and a representative of family 4, Tae4 from *Salmonella enterica* serovar Typhimurium, also hydrolyses the γ-D-glutamyl-*m*A_2pm DL-bond. Structures of Tse1 from *P. aeruginosa* and of Tae4 from *Salmonella* Typhimurium and *Enterobacter cloacae* (Benz *et al.*, 2012; Chou *et al.*, 2012; Ding *et al.*, 2012; Zhang *et al.*, 2013) place these T6-secreted effectors in the NlpC/P60 family of endopeptidases, amidases and acyltransferases (named after the new lipoprotein C from *Escherichia coli* and a 60 kDa extracellular protein from *Listeria monocytogenes*; Anantharaman & Aravind, 2003). The opportunistic pathogen *Serratia marcescens* has recently been shown to utilize T6-dependent secretion of two family 4 amidases, Ssp1 and Ssp2, to mediate antibacterial activity (English *et al.*, 2012).

Bacteria that secrete potent peptidoglycan hydrolase effectors using the T6SS to attack competitors could generate a deleterious effect on their own population. To cope with this potential for friendly-fire damage, such bacteria also possess cognate immunity or resistance proteins located in the periplasm. These immunity proteins bind their cognate effectors with low nanomolar affinity to neutralize them in a highly specific manner (English *et al.*, 2012). Four distinct families of putative immunity proteins are associated with the four Tae amidase families (Tai1–Tai4; Russell *et al.*, 2012). In *S. marcescens*, the resistance-associated proteins Rap1a and Rap2a neutralize Ssp1 and Ssp2, respectively (English *et al.*, 2012). Additionally, two other Rap proteins, Rap1b and Rap2b, are encoded together with Ssp1 and Ssp2 in the same locus within the T6SS gene cluster. The structures of Rap1b and Rap2b revealed a novel α-helix fold and a dimeric assembly (English *et al.*, 2012), which was later observed in the Tai4 proteins from *E. cloacae* (*Ec*Tai4) and *Salmonella* Typhimurium (*S*TTai4; Zhang *et al.*, 2013). This fold is a template for some T6SS immunity proteins, called Tsi proteins, but not all. For example, analysis of the Tse1/Tsi1 effector/immunity protein combination found in *P. aeruginosa* revealed Tsi1 to be an all-β protein (Benz *et al.*, 2012; Ding *et al.*, 2012; Shang *et al.*, 2012), whereas Tsi2, the immunity protein associated with the cytoplasmic effector Tse2, in the same organism has a helical fold that is distinct again (Li *et al.*, 2012). That effector immunity defence systems based on distinct folds have evolved is perhaps to be expected, given the strong evolutionary pressure applied by multifarious secreted effectors. Indeed, such pressure may even have contributed to the acquisition of effector–immunity pairs encoded outside T6SS operons (for example, all three Tse/Tsi pairs in *P. aeruginosa*).

Here, we assess the peptidoglycan hydrolase specificity of Ssp1 and Ssp2 and the protective role of cognate immunity proteins. We define the specificity of the enzymes and confirm using site-directed mutagenesis that an *in vivo* cell-killing mechanism is directly attributable to their catalytic activity. We report crystallographic analyses of *S. marcescens* Ssp1, a disabled mutant (Ssp1-C50A), Rap1a, Rap2a and the heterotetrameric Ssp1–Rap1a complex. Our data provide information on the enzyme mechanism, aspects of substrate specificity, the structural classification of Ssp1 and Rap proteins, including the identification of a novel immunity protein fold, and the molecular details of how an effector

is neutralized by its cognate immunity protein, and suggest generic features related to function that allow the classification of these proteins into distinct groups. Finally, we consider diversity within the Tae4 family of effectors and their immunity proteins and how this may explain the presence of multiple homologues within the same organism.

2. Materials and methods

2.1. Recombinant protein production and effector–immunity protein complex formation

Recombinant Ssp1 and Ssp2 were expressed in *E. coli* BL21 (DE3), and Rap1a and Rap2a, minus their N-terminal periplasmic targeting sequences, were expressed in *E. coli* Rosetta-gami (DE3) and purified in high yield using established protocols (English *et al.*, 2012). The predicted catalytic cysteine of Ssp1 and Ssp2 (Cys50) was mutated to an alanine using the QuikChange II Site-Directed Mutagenesis Kit (Stratagene) and the altered proteins were purified as for the wild-type samples. For co-expression of the Ssp1–Rap1a and Ssp2–Rap2a complexes, full-length mature Rap1a (residues 25–127) and Rap2a (residues 25–131), without signal peptides, were cloned using *Nde*I and *Xho*I restriction sites at the second multiple-cloning site of the co-expression vector pACYCDuet-1 (Novagen), and full-length Ssp1 (residues 1–163) and Ssp2 (residues 1–158) were subsequently cloned using *Nco*I and *Bam*HI restriction sites at the first multiple-cloning site. This introduces an N-terminal His_6 tag into the expressed product. Both the Ssp1–Rap1a and Ssp2–Rap2a complexes were produced in *E. coli* Rosetta-gami (DE3) and were purified by immobilized metal-ion affinity chromatography (English *et al.*, 2012) and size-exclusion gel-filtration chromatography with a Superdex 75 10/300 GL column (GE Healthcare). The samples were concentrated to 13.5 mg ml^{-1} by centrifugation (10 000 molecular-weight cutoff, Amicon) and dialyzed into 10 m*M* sodium phosphate pH 6.4. A high level of purity of greater than 95% was confirmed by SDS–PAGE. Size-exclusion chromatography was also used to investigate the association of cognate Ssp-C50A mutant–Rap combinations, with the proteins being mixed in equimolar amounts prior to separation, as described by English *et al.* (2012).

2.2. Peptidoglycan-cleavage assay

Purified peptidoglycan sacculi (300 µg) from *E. coli* D456, consisting mainly of tetrapeptides with lower fractions of tripeptides and pentapeptides (Chou *et al.*, 2012), were incubated with either Ssp1 or Ssp2 (100 µg ml^{-1}) or, as a control, no enzyme in 300 µl 20 m*M* sodium phosphate pH 4.8 for 4 h at 310 K. The samples were incubated with 40 µg ml^{-1} of the muramidase Cellosyl (kindly provided by Höchst AG, Frankfurt, Germany) for 16 h at 310 K to convert the residual peptidoglycan and solubilized fragments into muropeptides. The sample was boiled for 10 min and insoluble material was removed by centrifugation. The muropeptides were reduced with sodium borohydride and analyzed by high-pressure liquid chromatography using established methods (Glauner, 1988; Chou *et al.*, 2012; Russell *et al.*, 2012). The profile/retention times were compared with previous samples for which mass-spectrometric analyses with fragmentation had been carried out and which had identified that the linear disaccharide hexapeptide elutes before the disaccharide dipeptide, whereas the branched disaccharide hexapeptide elutes after the disaccharide dipeptide.

2.3. Phenotypic assays to characterize the C50A mutants of Ssp1 and Ssp2

These assays were performed using the bacterial strains, plasmids and protocols described previously (English *et al.*, 2012). The QuikChange II Site-Directed Mutagenesis Kit (Stratagene) was used to generate C50A (Cys50 to Ala) mutants of Ssp1 and Ssp2 in the existing plasmids pSC152 and pSC138 (for periplasmic expression in *E. coli*) and pSC539 and pSC541 (for complementation of the cognate mutation in *S. marcescens*). Microscopic analysis, antibacterial co-culture (competition) assays and immunodetection of secreted Ssp2 were performed as described in the previous study. In brief, the format of the antibacterial co-culture assays was that the attacker and target strains were mixed in a 1:1 ratio, co-cultured on solid Luria–Bertani (LB) media for 7.5 h at 303 K and the surviving target cells (in this case a streptomycin-resistant version of the Δ*rap2a*, Δ*clpV* mutant) were enumerated by serial dilution and viable counts on streptomycin-containing media. ClpV is an ATPase that is essential for the type VI secretion system to function and so deletion provides an appropriate control. Statistical significance testing was performed using ANOVA followed by Dunnett's post-test (GraphPad Prism software). For the detection of Ssp1 and Ssp2 levels in solid-grown *E. coli* or *S. marcescens*, cells were removed from the surface of agar plates, resuspended in liquid media, boiled and the total cell extract was separated by SDS–PAGE followed by anti-Ssp1 or anti-Ssp2 immunoblotting as described previously (English *et al.*, 2012).

2.4. Bioinformatic analyses

Multiple Ssp/Tae4 homologues were identified from public databases as part of previous studies (English *et al.*, 2012; Russell *et al.*, 2012). Multiple sequence alignments were generated using *MUSCLE* (Edgar, 2004), and *Jalview* (Waterhouse *et al.*, 2009) was used to visualize the alignment and to calculate the resulting tree (using neighbour-joining construction and the BLOSUM62 distance matrix). Genomic analyses using publicly available databases (http://www.ncbi.nlm.nih.gov/ and http://www.sanger.ac.uk/resources) allowed the identification of adjacently encoded candidate immunity proteins, which were then used as bait to interrogate the *S. marcescens* Db11 genome and determine the Rap protein to which each was most closely related.

2.5. Crystallographic analyses

2.5.1. Crystal growth and data collection. For crystallization trials, Rap1a was dialyzed against 25 m*M* Tris–HCl,

Table 1
Crystallographic statistics.

Values in parentheses are for the highest resolution shell.

Structure/PDB code	Ssp1/4bi3	Ssp1-C50A/4bi4	Rap1a/3zfi	Rap2a/3zib	Ssp1–Rap1a/4bi8
Space group	$P2_12_12_1$	$P2_12_12_1$	$C222_1$	$P2_1$	$P322_1$
Wavelength (Å)	1.5418	1.5418	0.97950	0.96110	1.5418
Unit-cell parameters					
a (Å)	56.83	56.79	82.65	39.65	68.47
b (Å)	65.26	64.59	93.00	81.35	68.47
c (Å)	97.50	97.87	51.26	58.45	92.52
β (°)				91.54	90.00
Resolution range (Å)	48.75–1.85 (1.95–1.85)	48.93–2.21 (2.26–2.21)	46.50–1.98 (2.09–1.98)	40.67–1.90 (2.00–1.90)	49.92–2.00 (2.05–2.00)
No. of reflections	503341 (41592)	139598 (9390)	63106 (8849)	214423 (31351)	493039 (32290)
Unique reflections	31504 (4357)	18726 (1331)	14089 (2003)	29067 (4190)	17462 (1279)
Completeness (%)	99.4 (100.0)	99.9 (98.5)	99.9 (100.0)	99.4 (98.9)	99.9 (99.1)
$R_{\rm merge}$† (%)	7.4 (23.9)	7.5 (26.3)	6.6 (48.6)	9.7 (51.6)	10.9 (58.7)
Multiplicity	16.0 (9.5)	7.5 (7.1)	4.5 (4.4)	7.4 (7.5)	28.2 (25.2)
$\langle I/\sigma(I)\rangle$	33.7 (10.2)	23.0 (8.1)	13.4 (2.7)	15.3 (4.0)	40.9 (11.4)
Wilson *B* (Å^2)	10.7	18.1	31.5	21.7	18.8
$R_{\rm work}$‡/$R_{\rm free}$§ (%)	20.4/24.0	19.2/24.6	19.2/23.4	18.3/23.4	17.9/22.7
No. of residues	326	326	185	377	256
No. of waters	300	372	57	137	192
No. of ligands	3 K^+, 5 SO_4^{2-}	1 glycerol			
DPI¶ (Å)	0.13	0.21	0.15	0.15	0.16
R.m.s.d. bond lengths†† (Å)	0.006	0.008	0.018	0.019	0.006
R.m.s.d. angles†† (°)	0.967	1.301	1.925	1.745	1.020
Average *B* factors (Å^2)					
Chain *A*	12.7	17.7	34.3	19.7	15.6
Chain *B*	11.2	17.9	35.2	23.0	22.6
Chain *C*				22.4	
Chain *D*				18.9	
Waters	15.2	25.1	34.8	30.6	27.0
K^+	22.0				
SO_4^{2-}	12.5				
Glycerol		35.9			
Ramachandran plot analysis					
Favoured regions	97.1	97.0	97.0	99.0	96.4
Allowed regions	2.9	3.0	3.0	1.0	3.2
Outliers	0	0	0	0	0.4 [Lys125]

† $R_{\rm merge} = \sum_{hkl}\sum_i |I_i(hkl) - \langle I(hkl)\rangle| / \sum_{hkl}\sum_i I_i(hkl)$, where $I_i(hkl)$ is the intensity of the *i*th measurement of reflection *hkl* and $\langle I(hkl)\rangle$ is the mean value of $I_i(hkl)$ for all *i* measurements. ‡ $R_{\rm work} = \sum_{hkl} ||F_{\rm obs}| - |F_{\rm calc}|| / \sum_{hkl} |F_{\rm obs}|$, where $F_{\rm obs}$ is the observed structure factor and $F_{\rm calc}$ is the calculated structure factor. § $R_{\rm free}$ is the same as $R_{\rm cryst}$ except calculated with a subset (5%) of data that were excluded from the refinement calculations. ¶ Diffraction-component precision index (Cruickshank, 1999). †† Engh & Huber (1991).

150 m*M* sodium chloride pH 7.5 and all other samples were in 100 m*M* sodium phosphate pH 6.4. The sitting-drop vapour-diffusion method was used with 0.2 µl drops with a 1:1 ratio of protein solution to reservoir solution at 293 K. Several commercially available screens were used in 96-well plates with a Phoenix Liquid Handling System (Rigaku, Art Robbins Instruments) to scout out initial conditions, which were then optimized.

Crystals of Ssp1 were obtained by combining protein solution at a concentration of 10 mg ml^{-1} with reservoir solution consisting of 0.2 *M* potassium sulfate, 20% PEG 3350. Orthorhombic block crystals grew to a maximum dimension of approximately 350 µm over 5 d. The Ssp1-C50A mutant (10 mg ml^{-1}) gave isomorphous crystals (maximum dimension of 250 mm) in 2 d using reservoir solution consisting of 0.1 *M* sodium citrate pH 5.5, 20% PEG 3000. The Ssp1–Rap1a complex at 13.5 mg ml^{-1} formed clusters of plate-like crystals using a reservoir solution consisting of 12.5% PEG 1000, 12.5% PEG 3350, 12.5% MPD. These crystals attained a maximum size of 200 µm within 3 d. A single-crystal fragment was removed from the cluster for diffraction measurements. Monoclinic blocks of Rap2a were grown by combining a protein concentration of 13.5 mg ml^{-1} with a reservoir solution consisting of 25% PEG 1000, 0.1 *M* MES pH 6.5. These crystals attained a maximum dimension of 200 µm within 5 d. A slender orthorhombic crystal of Rap1a with approximate dimensions of 150 × 35 × 35 µm was observed after about one month using a reservoir solution consisting of 25% PEG 3350, 100 m*M* bis-tris pH 5.5. We were unable to obtain crystals of the Ssp2–Rap2a complex.

All crystals were soaked briefly in mother liquor adjusted to contain 20%(*v*/*v*) glycerol as a cryoprotectant prior to flash-cooling in liquid nitrogen and use in diffraction experiments. Data for Ssp1, the Ssp1-C50A mutant and the Ssp1–Rap1a complex were measured at 100 K using a Rigaku MicroMax-007 rotating-anode X-ray generator (Cu $K\alpha$) coupled to a Saturn 944 CCD detector and were processed using *XDS* (Kabsch, 2010) or *HKL*-3000 (Minor *et al.*, 2006). The Rap1a and Rap2a data were collected on beamlines I04 and I03 of the Diamond Light Source, respectively, and were indexed and integrated in *iMosflm* (Battye *et al.*, 2011). Data sets were analyzed and scaled with *POINTLESS* and *SCALA* (Evans, 2006) from the *CCP*4 program suite (Winn *et al.*, 2011).

The isomorphous Ssp1 and Ssp1-C50A crystals contained two polypeptides in the asymmetric unit with an estimated solvent content of 50% and a $V_{\rm M}$ of 2.46 Å^3 Da^{-1}. The Ssp1–Rap1a complex crystal presented a heterodimer in the asymmetric unit with an estimated solvent content of 40% and a $V_{\rm M}$ of 2.06 Å^3 Da^{-1}. Rap2a crystallized with four molecules in the asymmetric unit, an estimated solvent content of 40% and a $V_{\rm M}$ of 2.06 Å^3 Da^{-1}, whilst Rap1a displayed two molecules in the asymmetric unit with an estimated solvent content of 45% and a $V_{\rm M}$ of 2.06 Å^3 Da^{-1}.

2.5.2. Structure determination and refinement. The Ssp1 structure was solved targeting the single-wavelength anomalous scattering properties of sulfur (Micossi *et al.*, 2002). *Auto-Rickshaw*, the EMBL Hamburg automated structure-determination platform (Panjikar *et al.*, 2005), was used. The heavy-atom structure-factor contributions were estimated in *SHELXC* (Sheldrick, 2010; Sheldrick *et al.*, 2001) and the

maximum resolution for substructure determination and initial phase calculation was set to 2.30 Å. All 14 heavy atoms (sulfurs) were found using *SHELXD* (Schneider & Sheldrick, 2002). The correct hand for the substructure was determined using *ABS* (Hao, 2004) and *SHELXE* (Sheldrick, 2002) and the initial phases produced a CC (correlation coefficient) of 0.32. The initial phases were improved by density modification (Terwilliger, 2003) prior to phase extension to 1.85 Å resolution. The CC improved to 0.63, resulting in an electron-density map with excellent quality. Almost 80% of the model was constructed in *ARP*/*wARP* (Langer *et al.*, 2008). The initial model consisted of two polypeptides of 295 residues in total, with $R_{\rm work}$ and $R_{\rm free}$ values of 29.7 and 31.4%, respectively. Subsequent model building extended this to 326 residues, with the $R_{\rm work}$ and $R_{\rm free}$ values improving to 20.7 and 24.1%, respectively.

A molecule of Ssp1 was used to solve the structures of the Ssp1–Rap1a complex and the Ssp1-C50A mutant by molecular replacement (*autoMR*; Winn *et al.*, 2011). The structures of Rap1a and Rap2a were solved by molecular replacement (*Phaser*; McCoy *et al.*, 2007) using the structure of Rap1a from the Ssp1–Rap1a complex and Rap2b (PDB entry 4b6i; English *et al.*, 2012), respectively. In the latter case the sequence identity shared by the search model and the target structure is only about 20%.

All structures were refined in an iterative process combining *REFMAC*5 (Murshudov *et al.*, 2011) with electron-density and difference-density map inspections and model manipulations in *Coot* (Emsley *et al.*, 2010). For those structures with multiple copies in the asymmetric unit, tight NCS (noncrystallographic symmetry) restraints were imposed which were gradually released during refinement. Translation/libration/screw analysis (TLS) refinements were applied with the appropriate groups determined using the *TLSMD* server (Painter & Merritt, 2006). Water molecules, and in the case of the Ssp1 structure also potassium and sulfate ions, were added

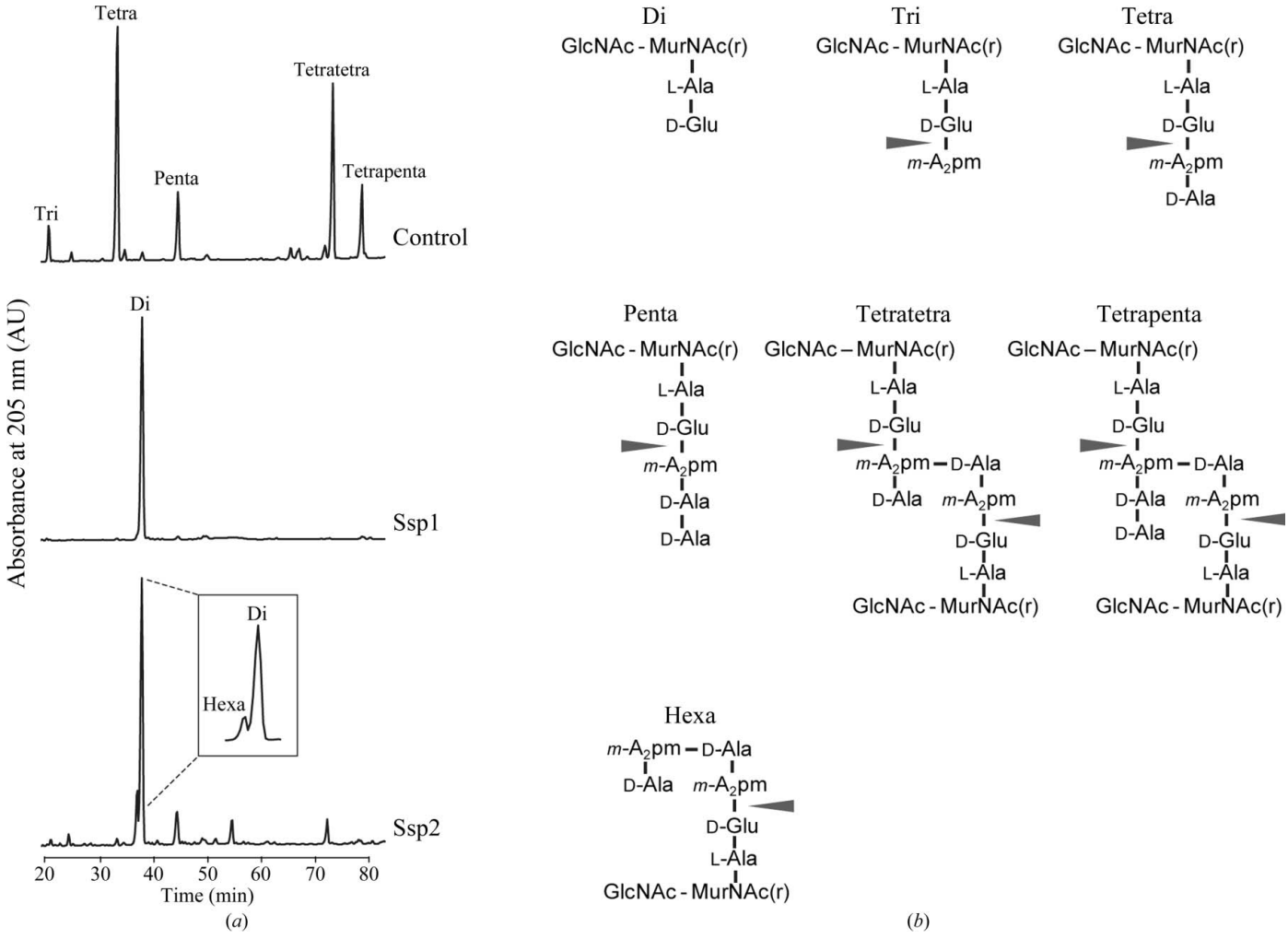

Figure 1
The specificity of Ssp1 and Ssp2. (*a*) Peptidoglycan from *E. coli* strain D456 was incubated with Ssp1, Ssp2 or no enzyme (control) followed by digestion with the muramidase Cellosyl and analysis of the resulting muropeptides by HPLC. Both Ssp1 and Ssp2 cleaved non-cross-linked (tri, tetra and penta) and cross-linked (tetratetra and tetrapenta) muropeptides between D-glutamate and *meso*-diaminopimelic acid (*m*-A_2pm), resulting in the disaccharide dipeptide (di) product. Ssp2 also produced a small amount of the disaccharide hexapeptide (hexa) product. (*b*) Proposed structures of the muropeptides separated in (*a*). The arrows indicate the cleavage sites of D-*i*Glu-*m*-A_2pm endopeptidases in peptidoglycan. GlcNAc, *N*-acetylglucosamine; MurNAc(r), *N*-acetylmuramitol; *m*-A_2pm, *meso*-diaminopimelic acid.

during the refinement process. Where appropriate, dual rotamer side-chain conformations were also included. Refinements were terminated when there were no significant changes in the R_{work} and R_{free} values and inspection of the difference density maps suggested that no further corrections or additions were justified.

MolProbity (Chen *et al.*, 2010) was used to investigate the model geometry. Secondary-structure and surface-interaction analyses were performed using *DSSP* (Kabsch & Sander, 1983) and *PISA* (Krissinel & Henrick, 2007), respectively. Figures were prepared using *ALINE* (Bond & Schüttelkopf, 2009) and *PyMOL* (Schrödinger). The *DALI* server was used to search the PDB for structural homologues, whilst superpositions were calculated using *DaliLite* (Holm & Park, 2000).

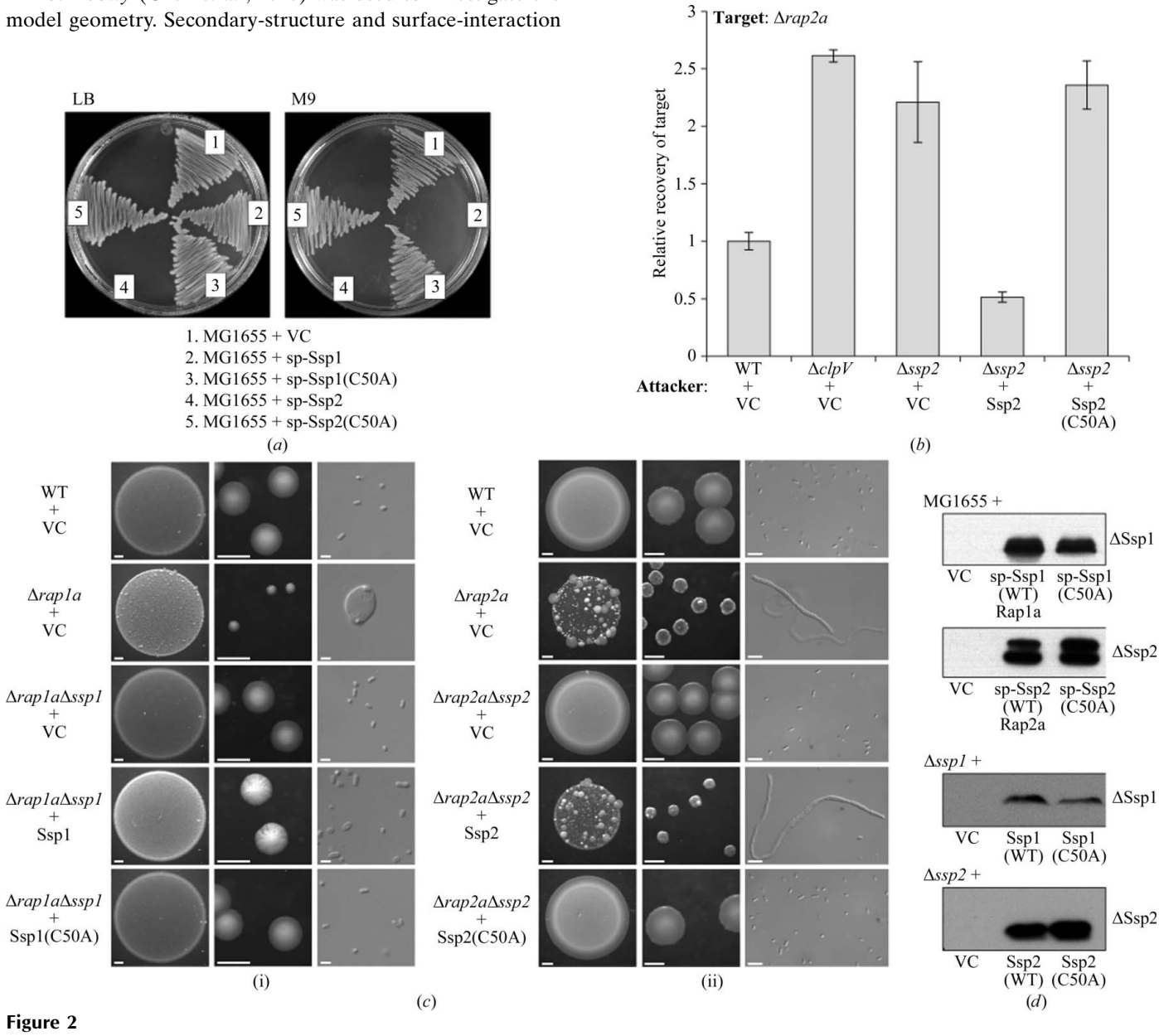

Figure 2
The Ssp1 and Ssp2 C50A mutants are inactive. (*a*) Growth of *E. coli* MG1655 transformed with plasmids expressing $OmpA_{sp}$-Ssp1 (sp-Ssp1; pSC152), $OmpA_{sp}$-Ssp1(C50A) [sp-Ssp1(C50A); pSC548], $OmpA_{sp}$-Ssp2 (sp-Ssp2; pSC138) or $OmpA_{sp}$-Ssp2(C50A) [sp-Ssp2(C50A); pSC549] from an arabinose-inducible promoter, or with the empty vector (VC, pBAD18-Kn), on LB or M9 medium containing 0.2% arabinose. (*b*) Recovery of a sensitive Δ*rap2a* mutant as the target strain following co-culture with the different attacking strains indicated, expressed relative to recovery of target when co-cultured with the wild-type strain. Attacking strains are wild-type *S. marcescens* Db10 (WT), mutant lacking ClpV (Δ*clpV*), mutant lacking Ssp2 (Δ*ssp2*), each carrying either the vector control plasmid (+VC; pSUPROM) or a plasmid expressing wild-type Ssp2 (+Ssp2; pSC541) or the C50A mutant of Ssp2 [+Ssp2(C50A); pSC1230]. (*c*) Phenotypes of wild-type *S. marcescens* Db10 and selected single and double mutants carrying plasmids expressing variants of Ssp1 or Ssp2 following growth on solid medium. For each strain, representative images of the morphology of a culture spot (left; scale bar 1 mm), single colonies (middle; scale bar 1 mm) and individual cells [right; scale bar 2 μm in (i) or 5 μm in (ii)] are shown. Plasmids direct the expression of wild-type Ssp1 (+Ssp1; pSC539), the C50A mutant of Ssp1 [+Ssp1(C50A); pSC1229], wild-type Ssp2 (+Ssp2; pSC541), the C50A mutant of Ssp2 [+Ssp2(C50A); pSC1230] or represent the vector control (+VC, pSUPROM). Growth was for 48 h on MM (i) or 24 h on LB (ii). (*d*) Immunoblot analysis of levels of Ssp1 or Ssp2 proteins from *E. coli* MG1655 (top two panels) or *S. marcescens* (bottom two panels) grown on solid medium. Strains and plasmids are as in (*a*)–(*c*), except that wild-type $OmpA_{sp}$-Ssp1 and $OmpA_{sp}$-Ssp2 were co-expressed with their cognate immunity proteins to allow the strains to grow [sp-Ssp1(WT)Rap1a; pSC160 or sp-Ssp2(WT)Rap2a; pSC144].

Relevant crystallographic statistics and geometric details of the refined models were extracted from the programs used in the analyses and are reported in Table 1.

3. Results and discussion

3.1. Activity of Ssp1 and Ssp2 and neutralization by cognate Rap partners

We previously identified *S. marcescens* Ssp1 and Ssp2 as periplasmic acting antibacterial T6SS effectors (English *et al.*, 2012) and noted their membership, on the basis of sequence similarity, of the family 4 amidases (Tae4 proteins) proposed by Russell *et al.* (2012). We aimed to experimentally determine the enzymatic activity of each protein. The incubation of peptidoglycan sacculi with purified Ssp1 or Ssp2, followed by muramidase digestion and high-pressure liquid-chromatography analysis, revealed the disaccharide dipeptide as the single major product. This indicates that both enzymes cleave the amide bond in peptidoglycan between isoglutamic acid and *meso*-diaminopimelic acid. Ssp1 quantitatively hydrolyzed monomeric tripeptides, tetrapeptides and pentapeptides, as well as dimeric tetratetrapeptides and tetrapentapeptides, on both the acceptor and the donor side (Fig. 1). In the cross-linked peptides, the ε-amino group of the *meso*-diaminopimelic acid residue at position 3 on the acceptor side is connected by an amide bond to the α-carboxylic group of D-alanine at position 4 on the donor side. Although Ssp2 was active against these muropeptides, the cleavage of monomeric pentapeptide and dimeric tetratetrapeptide was less efficient and the partially cleaved disaccharide hexapeptide product was detected (Fig. 1*a*). This behaviour is similar to the family 4 amidase Tae4 from *Salmonella* Typhimurium (*S*TTae4, also known as Tae4^{TM}; Russell *et al.*, 2012). Hence, Ssp2 and *S*TTae4 preferentially cleave tetrapeptides in the acceptor part of cross-linked peptides. This is distinct from *P. aeruginosa* Tse1, which preferentially cleaves pentapeptides in the donor part of cross-linked peptides (Chou *et al.*, 2012; Russell *et al.*, 2012). These data indicate that Ssp1 and Ssp2 are distinctive peptidoglycan DL-endopeptidases in terms of specificity, with the former being more promiscuous regarding the chemical structure that it is able to recognize and then cleave.

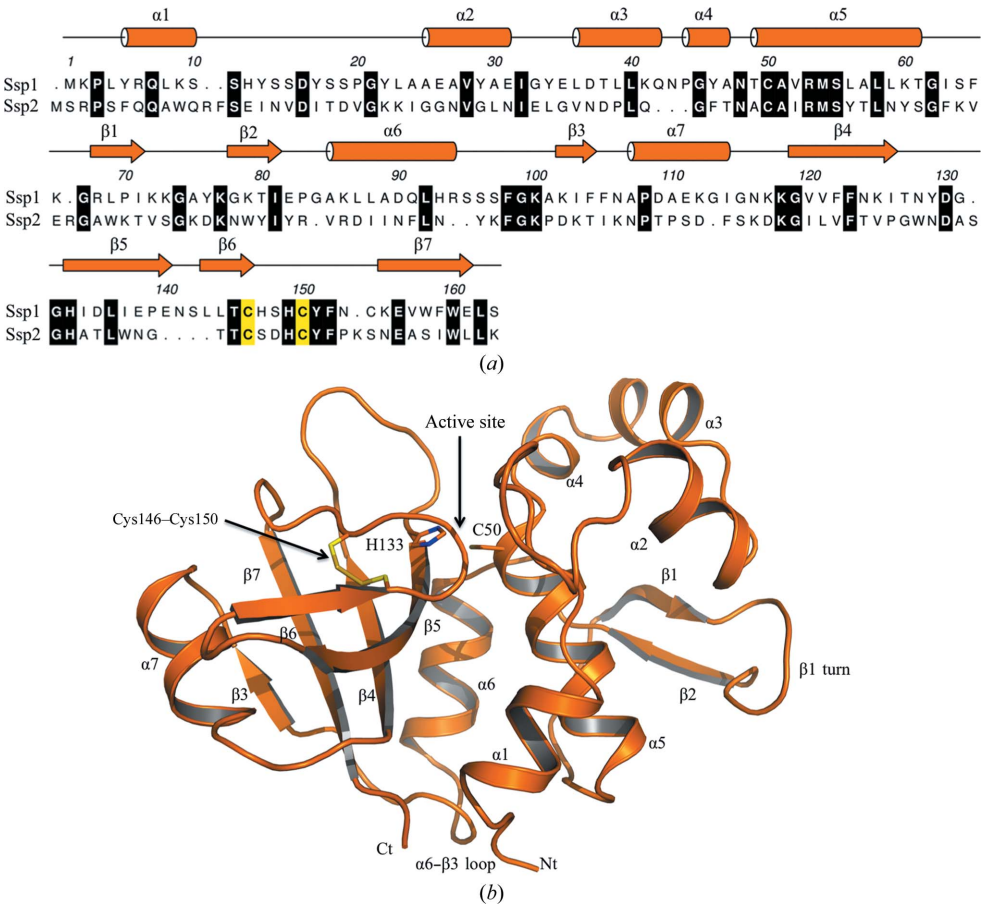

Figure 3
Primary, secondary and tertiary structure of Ssp1. (*a*) The amino-acid sequence of Ssp1 with assigned elements of secondary structure. Helices are depicted as cylinders and β-strands as arrows. An alignment of Ssp1 and Ssp2 is also shown with strictly conserved residues shown on a black background. Residues involved in disulfide-bond formation are coloured yellow. (*b*) Cartoon representation of Ssp1 with secondary-structure elements labelled. The disulfide bond is shown in stick representation with C-atom positions in yellow and S-atom positions in gold. His133 and Cys50 (sticks) mark the active site.

Established functional assays were utilized to examine the effect of mutating the catalytic cysteine (Cys50) of Ssp1 and Ssp2. Heterologous expression targeting Ssp1 and Ssp2 to the periplasm of *E. coli* MG1655 prevents growth on M9 minimal medium and, in the case of Ssp2, also on LB medium. As shown in Fig. 2(*a*), Ssp1-C50A and Ssp2-C50A were no longer toxic to *E. coli*. In *S. marcescens* itself, a mutant lacking the immunity protein, Δ*rap2a*, is susceptible to self-killing by Ssp2 injected by the wild-type strain. This is shown in two ways. Firstly, co-culture of a wild-type attacker strain with a Δ*rap2a* target strain results in the death of the latter. When the attacker lacks a functional T6SS (Δ*clpV*) or Ssp2 (Δ*ssp2* mutant), increased recovery of the target strain is observed. Complementation of the Δ*ssp2* mutant attacker by expression of wild-type Ssp2 from a plasmid restores the killing activity, with the recovery of the target reduced below the levels observed with the wild-type attacker. However, the expression of Ssp2-C50A was unable to complement the Δ*ssp2* mutant and restore the killing

activity (Fig. 2*b*). Secondly, a single Δ*rap2a* mutant exhibits fitness and morphological defects when grown on solid medium and these defects are alleviated when *ssp2* is also deleted in a Δ*rap2a*Δ*ssp2* mutant. Plasmid-mediated expression of Ssp2 in the Δ*rap2a*Δ*ssp2* mutant re-induced the fitness and morphological defects caused by self-killing; however, expression of the Ssp2-C50A mutant had no negative effect (Fig. 2*c*). Similarly, expression of Ssp1, but not Ssp1-C50A, in a Δ*rap1a*Δ*ssp1* mutant induced mild morphological defects (Fig. 2*c*). In each case, an equivalent level of stable expression of Ssp1-C50A and Ssp2-C50A compared with wild-type Ssp1 and Ssp2 was confirmed by immunoblotting (Fig. 2*d*).

3.2. Catalytic inactivation of Ssp1 and Ssp2 does not affect their secretion or immunity protein binding

It was necessary to confirm that the above observations were not affected by any influence of the catalytic C50A mutation on immunity protein binding or secretion of the effectors. Each of the Ssp C50A mutants was mixed with an equimolar amount of the cognate Rap protein, followed by size-exclusion chromatography analysis to monitor complex formation. In each case, a single species of apparent molecular weight ∼55 kDa was observed (Supplementary Fig. S1*a*[1]). This behaviour exactly matches that of the wild-type proteins (English *et al.*, 2012) and indicates that complexes consisting of two Ssp and two Rap polypeptides are formed. It was also demonstrated that the Ssp2-C50A mutant protein was secreted by the T6SS of *S. marcescens* as efficiently as the wild-type protein (Supplementary Fig. S1*b*). We conclude that mutation of the catalytic cysteine in Ssp1 and Ssp2 abolishes their bacteriolytic effect because the DL-endopeptidase activity is compromised. Furthermore, we can conclude that the Ssp–Rap interaction does not depend on the catalytic cysteine and that recognition of the Ssp effectors by the T6SS machinery is also independent of their enzymatic activity.

3.3. Structure of Ssp1

To gain a detailed insight into the structure and activity of the peptidoglycan endopeptidase effector Ssp1, we applied crystallographic methods. Isomorphous crystal structures of Ssp1 (at 1.85 Å resolution) and the active-site Ssp1-C50A mutant (at 2.2 Å resolution) reveal the overall enzyme structure and details of the active site. The protein is a monomer in solution but crystallized with two molecules in the asymmetric unit, each consisting of residues 1–163. The root-mean-square deviations (r.m.s.d.s) between least-squares superimposed C^{α} atoms gives an average of 0.3 Å when comparing the four polypeptides in the crystal structures. The copies in the asymmetric unit are therefore judged to be essentially identical and neither mutagenesis of the catalytic Cys50 nor crystal lattice packing interactions induces any major structural changes.

[1] Supplementary material has been deposited in the IUCr electronic archive (Reference: BE5242). Services for accessing this material are described at the back of the journal.

The primary, secondary and tertiary structure of Ssp1 (Fig. 3) classifies it into the NlpC/P60 cysteine peptidase superfamily (Anantharaman & Aravind, 2003). The overall dimensions of the bilobal structure are about 35 × 40 × 50 Å. An N-terminal subdomain comprises residues 1–95 and is formed by six α-helices (α1–α6) and, on the surface of the protein, a β-hairpin-like loop (β1, turn, β2). A short peptide segment links α6 to β3, which represents the start of the C-terminal subdomain. This subdomain is dominated by a four-stranded antiparallel β-sheet with order β3–β7–β4–β5, which is flanked on one side by α7 and β6 and on the other by α6. A disulfide bond is observed between Cys146 at the C-terminal end of β6 and Cys150 located on the loop linking β6 to β7. A cleft, the substrate-binding site, is created between the subdomains by residues in the α1–α2 and α4–α5 links, the C-terminal segment of β6 and the loop leading to β7. The disulfide linkage appears important to create one side of the active site and perhaps also contributes to the stability of the C-terminal subdomain fold.

The family 4 amidase effectors hydrolyze the amide bond between D-Glu and *m*A_2pm. They are similar to CHAP (cysteine, histidine-dependent amidohydrolases/peptidases) family members, a subset of the NlpC/P60 superfamily with a strictly conserved cysteine–histidine catalytic dyad (Fyfe *et al.*, 2008). In the case of Ssp1, Cys50 is located in the N-terminal subdomain and His133 in the C-terminal subdomain (Fig. 3*b*). Cys50 donates a hydrogen bond to a water molecule, which in turn interacts with His133, Asn48 and Tyr129 (Fig. 4). Asp135 accepts a hydrogen bond from His133 and appears to complete a catalytic triad reminiscent of that observed in typical cysteine peptidases. The mechanism of such cysteine-dependent proteases, especially papain, is well documented (Alphey & Hunter, 2006 and references therein). The Cys–His

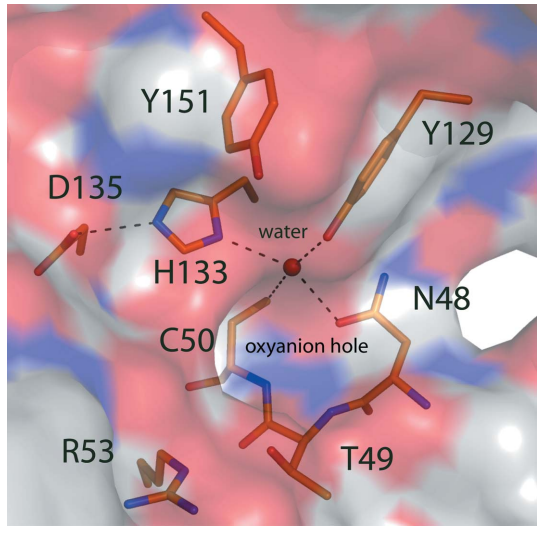

Figure 4
The Ssp1 catalytic centre. The protein is shown as a semi-transparent van der Waals surface coloured according to atom type (N, blue; O, red; S, yellow; C, white). A water (blue sphere) participates in four hydrogen-bonding interactions with Asn48, Cys50, Tyr129 and His133. Hydrogen bonds are shown as dashed lines and selected residues are presented as sticks with C-atom positions coloured orange, N blue, O red and S yellow.

catalytic dyad forms a thiolate–imidazolium pair that is oriented by a hydrogen bond between the histidine and an acidic residue. In this case the residues are Cys50, His133 and Asp135. The generation of a thiolate Cys50 following proton abstraction by His133 would support nucleophilic attack at the γ-D-glutamyl-*m*A_2pm amide bond to form an acyl thioester. Hydrolysis of the thioester, exploiting an activated water molecule, then releases the products. The main-chain amides of the catalytic cysteine and Thr49 create an oxyanion hole that may support thiolate attack on the amide linkage by stabilizing the tetrahedral intermediate formed prior to the formation of an acyl-enzyme complex. In this there are striking parallels to the reaction catalyzed by nicotinamidase (Fyfe *et al.*, 2009).

Ssp1 shares about 20% sequence identity with Ssp2, but we do not have a structure of Ssp2 for comparative purposes to address the observation of distinct substrate specificities. However, the closest structural relative of Ssp1 is the bacteriolytic effector Tae4 from *E. cloacae* and *S. typhimurium* (PDB entries 4hfk and 4hff, respectively; Zhang *et al.*, 2013), with *Z*-scores of 17 and 16 and r.m.s.d.s of 2.2 and 2.1 Å for the least-squares fit of 138 and 137 C^{α} positions, respectively. Ssp1 shares about 15% sequence identity with these proteins but, despite such a low sequence similarity, the r.m.s.d. values and overlay confirm that these structures share the same fold (Supplementary Fig. S2). On the basis that Ssp2 shares about 50% sequence identity with Tae4 and the same substrate specificity, we suggest that it provides a suitable surrogate structure for comparative purposes.

An overlay of the Ssp1 and Tae4 structures confirms similarities in the protein fold and the relative positions of residues linked to catalytic activity. However, the overlay also indicates noteworthy differences (Supplementary Figs. S2 and S3). The α1–α2 loop in Ssp1, consisting of about 15 amino acids, lines one side of the active site then extends away from the catalytic core. Adjacent to this loop is a turn carrying the Cys146 and Cys150 disulfide. The turn and the polypeptide that follows, which lead directly into β7, line the active site. In *Ec*Tae4, the disulfide is conserved (Cys137 and Cys141), as is the structure just after the turn. An eight-residue segment extends from the turn and curls over to narrow the active-site cleft. In *S*TTae4 the conserved residues Cys135 and Cys139 are in a reduced form, for reasons that are not made clear, and the polypeptide chain at the periphery of the active site is flexible and disordered, as shown by inflated thermal parameters and a lack of electron density. Alignment of the Ssp1 and Ssp2 amino-acid sequences (Fig. 3*a*) indicates that there is a truncation of four residues in the region of the disulfide-containing loop and this may reduce the size of the active-site cleft of Ssp2 compared with Ssp1. The alignment also suggests that Asp135 of Ssp1, assigned as a component of the catalytic triad, is not conserved and corresponds to Thr133 in Ssp2. In *S*TTae4 and *Ec*TAE4 a threonine is also present at this position (Supplementary Fig. S4). A superposition of Ssp1 and *Ec*TAE4 indicates a difference of Ser148 replaced by Asp139, with the carboxylic acid side chain positioned to fulfil the role of Asp135 of Ssp1 in the catalytic triad (Supplementary Fig. S3). The aspartate is conserved in Ssp2, *S*TTae4 and *Ec*TAE4 (Supplementary Fig. S4).

The peptidoglycan hydrolase assay data indicate that Ssp2 preferentially targets the acceptor component of the peptidoglycan tetratetra cross-link rather than donor part and in this it is similar to Tae4 (Russell *et al.*, 2012). Ssp1 cleaves the acceptor and donor stem of cross-linked and non-cross-linked peptidoglycan. The differences evident from structural comparisons suggest that a distinctive and more open substrate-binding surface in Ssp1 compared with those observed in Tae4 structures or implied in Ssp2 might explain the promiscuous endopeptidase activity of Ssp1.

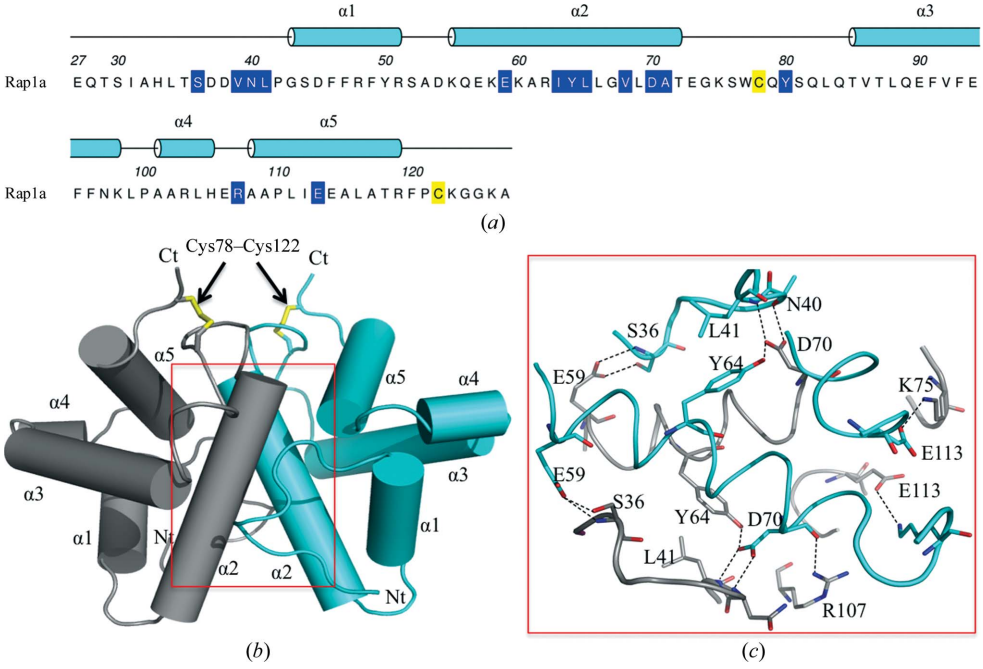

Figure 5
Primary, secondary and tertiary structure of Rap1a. (*a*) The sequence of mature Rap1a. The 26-residue N-terminal signal sequence is not shown. These residues represent the cleaved N-terminal signal sequence that was omitted from the analysis. The assigned α-helical secondary structure is shown and the helices are numbered. Residues involved in disulfide-bond formation are coloured yellow and residues that contribute to the dimer interface are shown on a blue background. (*b*) Cartoon representation of the Rap1a dimer with labelled helices; Nt and Ct mark the N- and C-terminal positions. The disulfides formed between Cys78 and Cys122 are shown as yellow sticks. (*c*) The residues and hydrogen bonds (dashed lines) at the dimer interface. C atoms are shown in grey and cyan to distinguish the subunits.

Structures of complexes with the appropriate ligands would be required to further investigate this point.

3.4. Structure of Rap1a

Next, we sought to reveal molecular details of the immunity proteins Rap1a and Rap2a, which neutralize Ssp1 and Ssp2 toxicity, respectively (English *et al.*, 2012). The structure of Rap1a was determined to about 2.0 Å resolution (Table 1) and the amino-acid sequence with assigned secondary structure is depicted in Fig. 5(*a*). A search for structural orthologues failed to identify anything of relevance in the PDB. We therefore conclude that the Rap1a fold has not been observed previously, making it a unique member of the T6SS immunity family of proteins. Several other candidate immunity proteins identified in other organisms share significant sequence identity with Rap1a (see below). Therefore, we propose that this group of proteins be referred to as the 'Tai4a' immunity proteins, to reflect the fact that whilst they are immunity proteins to Tae4 effectors, they are distinct from the main family of Tai4 proteins, which includes Rap1b, Rap2a and Rap2b.

The Rap1a subunit displays a compact globular structure constructed from five α-helices that assemble to form the highly stable symmetric dimer that constitutes the asymmetric unit (Fig. 5). This is consistent with the size-exclusion chromatography data, which identified that only a dimer was observed in solution (Supplementary Fig. S1). The NCS is highly conserved, with an r.m.s.d. of 0.6 Å for a least-squares overlay of 96 C^{α} positions. A disulfide bond is formed between Cys78 (in the α2–α3 loop) and Cys122 in the C-terminal region. This interaction appears to be crucial to stabilizing the subunit fold since it helps position α2, α3 and α5 close to each other and these segments of secondary structure provide the side chains that form the hydrophobic core of the subunit. During initial recombinant expression tests it was noted that soluble protein was only produced in *E. coli* Rosetta-gami (DE3) cells, a strain that promotes the formation of disulfide bonds in the cytoplasm and so mimics what might occur in the oxidative environment of the periplasm. This suggests that the covalent bond is necessary for correct folding to occur and for stability of the Rap1a fold and dimeric quaternary structure.

Interactions involving residues in α2 make the major contribution to dimer formation. Each subunit contributes a surface area of 1130 Å^2 to the dimer interface, which is 20% of the solvent-accessible surface area (ASA) of the subunit (5700 Å^2). Such a percentage of surface area is indicative of a stable association (Krissinel & Henrick, 2007). Eight residues from each subunit form a network of hydrogen bonds using both main-chain and side-chain functional groups (Ser36, Asn40, Leu41, Glu59, Tyr64, Asp70, Lys75, Arg107 and Glu113, Fig. 5*c*). There are also indirect hydrogen-bonding interactions *via* well ordered water molecules that link a number of side chains and main chains. Hydrophobic interactions that contribute to the stability of the dimer mainly involve the aliphatic side chains of Val39, Ile63, Leu66, Val68 and Ala71, but also Tyr80.

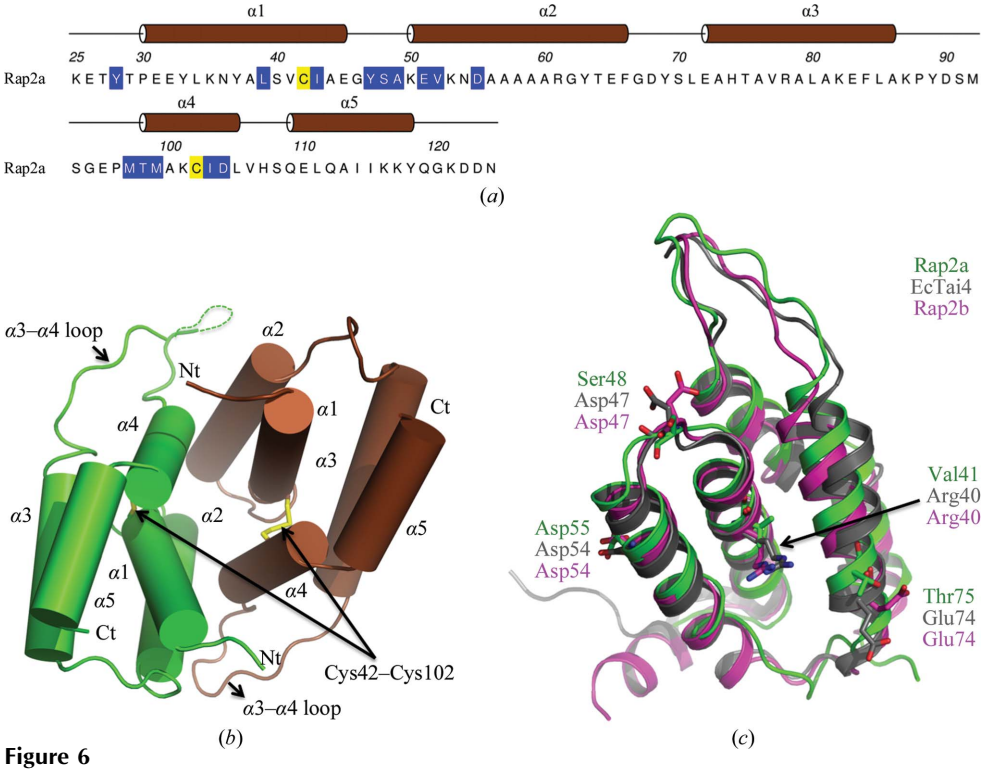

Figure 6
Primary, secondary and tertiary structure of Rap2a. (*a*) The amino-acid sequence with assigned secondary structure and helices numbered. Residues involved in disulfide-bond formation are coloured yellow and residues involved in subunit–subunit interactions are shown on a blue background. (*b*) Cartoon representation of the Rap1a dimer with subunits coloured brown and green. The disulfides and the N- and C-termini are labelled. (*c*) Cartoon representation of Rap2b (pink) and *Ec*Tai4 (grey) superimposed on Rap2a (green). Asp54 and Asp47 are involved in the hydrogen-bond network in the interface in *Ec*Tai4 and are absolutely conserved in Rap2b; in Rap2a, Asp47 is replaced by Ser48. Arg40 and Glu74 (replaced by Val41 and Thr75, respectively, in Rap2a) have been shown to play a major role in binding to *Ec*Tae4; both of these residues are also conserved in Rap2b but not in Rap2a.

3.5. Structure of Rap2a

Rap2a, like Rap1a, is predicted to be localized in the periplasm and could only be produced in soluble recombinant form using the *E. coli* Rosetta-gami (DE3) strain. It is also a stable dimer in solution as shown by size-exclusion chromatography (English *et al.*, 2012). The structure was determined at 1.9 Å resolution with four molecules, arranged as two dimers, in the asymmetric unit. These four molecules, subunits *A*–*B* and *C*–*D*, are similar

overall, with r.m.s.d.s between superimposed C^{α} atoms ranging from 0.6 Å (subunits *A* and *B*, residues Thr27–Gln123) to 0.7 Å (subunits *C*, residues 27–127, and *D*, residues 27–126). Minor deviations from NCS are observed in a five-residue loop between α2 and α3 (Gly67–Leu71) and indicate some conformational freedom in this part of the molecule. The ASA of a Rap2a subunit averages at approximately 6110 $Å^2$; the range is from 6140 $Å^2$ for subunit *C* to 6090 $Å^2$ for subunit *D*. Dimer formation occludes an area that is approximately 20% of the ASA, which is indicative of a stable association (Krissinel & Henrick, 2007).

The Rap2a subunit displays a compact globular structure of five α-helices with an extended loop linking α3 to α4 (Figs. 6*a* and 6*b*). A disulfide bond between Cys42 and Cys102 links α1 to α4 and interactions of other side-chain groups on these elements of secondary structure help to create the helical bundle fold and in particular to align α2. Together, α1, α2, the α2–α3 loop and α4 form the dimer interface, giving rise to a twofold NCS axis, and a combination of hydrogen-bonding, salt-bridge and van der Waals interactions serve to stabilize the association. Main-chain hydrogen-bonding contributions come from the amides of Ser48, Ala49, Met97, Thr98 and Met99 on both chains. Side-chain contributions come from the hydroxyl groups of Tyr28 and Tyr47 and the carboxylates of Glu51, Asp55 and Asp104. Several solvent-mediated contacts also serve to link functional groups on partner subunits (not shown). The side chains of Leu39, Ile43, Tyr47, Val52, Met99 and Ile103 are involved in van der Waals interactions with the partner subunit to stabilize the dimer.

Despite a low level of sequence conservation, the structural similarity of five T6SS immunity proteins (Rap1b, Rap2a, Rap2b, *Ec*Tai4 and *S*TTai4) indicates an orthologous subset. This structurally defined set is consistent with the designation of a 'Tai4' family of immunity proteins cognate to the Tae4 effectors (Russell *et al.*, 2012). Pairwise comparisons indicate a range of sequence identities from 15 to 35%, and matching between 93 and 124 C^{α} positions gives an r.m.s.d. range of 1.2–1.7 Å indicative of close structural similarity. The structural overlay is exemplified by superposition of Rap2a, Rap2b and *Ec*Tai4 (Fig. 6*c*). Of note is the conservation of an extended or protruding loop structure which is highly variable in terms of amino-acid sequence (see Fig. 7 in English *et al.*, 2012). Parts of the *Ec*Tai4 subunit involved in interaction with an effector, identified by the positions of Val41 and Thr75 in Rap2a, are also well conserved in terms of overall structure (Fig. 6*c*).

This subset of immunity proteins also display similar dimer structures and the Cys42–Cys102 disulfide bond in Rap2a is conserved in Rap1b and Rab2b. The covalent interaction appears to be important for the creation of the subunit fold

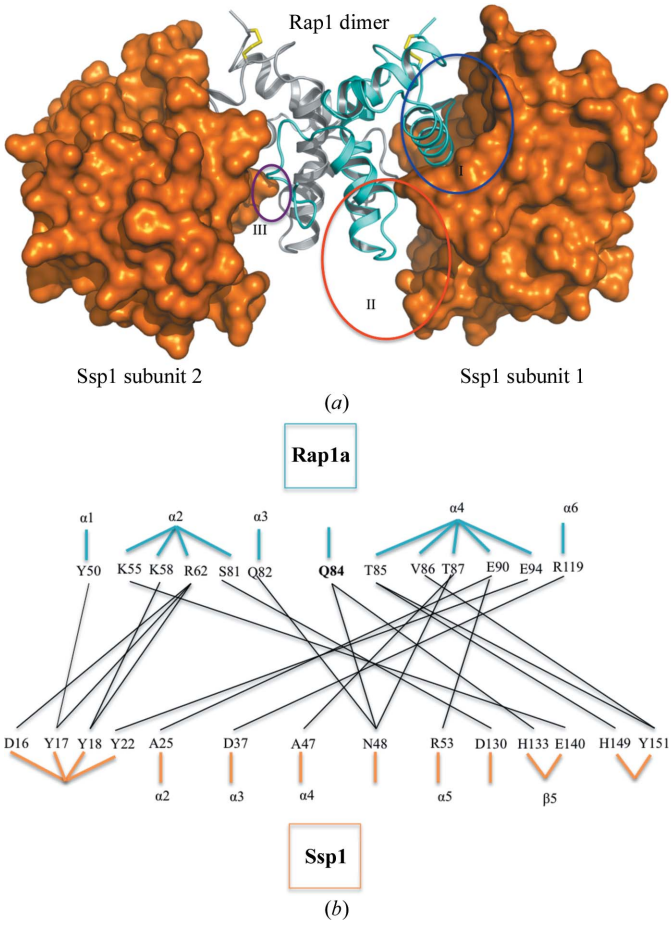

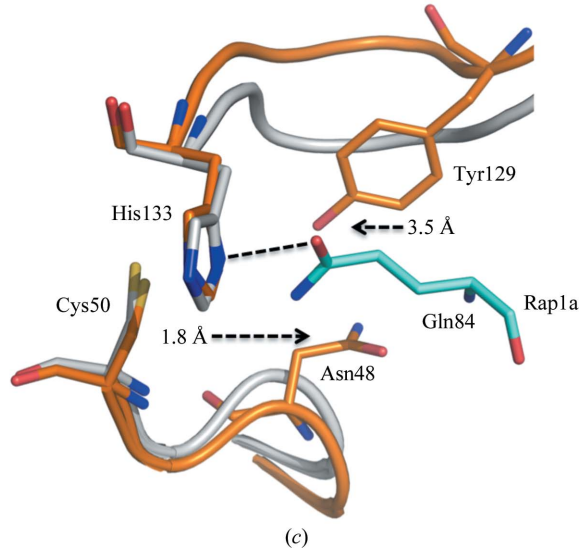

Figure 7
The Ssp1–Rap1a heterotetramer complex. (*a*) Ssp1 is shown as an orange van der Waals surface and the Rap1a subunits are shown as cyan and grey ribbons. The disulfide bonds in Rap1a are presented as yellow sticks. Blue, red and purple circles mark the three distinct areas (I–III) of interaction between the effector and immunity proteins. (*b*) Schematic diagram showing the hydrogen-bonding and salt-bridge interaction network involved in complex formation. Black lines mark interacting residues. Residue positions in the protein structures are given by labelling the appropriate secondary structure. The exceptions are Gln84 in Rap1a, which occurs just prior to α3 in this structure, and Asn48 and Asp130 in Ssp1, which are between α4 and α5 and at the C-terminal segment of β4, respectively. (*c*) Gln84 directly interacts with the catalytic His133 and blocks the active site. Grey, apo Ssp1; dark orange, Ssp1 from the Ssp1–Rap1a complex; cyan, Rap1a from the Ssp1–Rap1a complex. Broken arrows indicate the adjustments of Asn48 and Tyr129 when comparing free and complexed Ssp1.

and the stable quaternary structure. In the structures of *Ec*Tai4 and *S*TTai4 there are conserved cysteines that match the disulfide-forming residues in the Rap proteins; however, they are in a reduced form. In *S*TTai4, for example, the distance between the SG atoms of Cys48 and Cys108 is 3.6 Å and the electron density unambiguously defines reduced cysteine residues. This difference in the redox states may simply reflect distinct experimental conditions.

3.6. Inhibition of Ssp1 by Rap1a

We next sought to delineate the molecular basis of how the *S. marcescens* Rap proteins neutralize their cognate Ssp amidase/endopeptidase effectors and what features engendered the exquisite specificity noted in the effector–resistance protein combinations. We previously proposed that the complexes exist as Ssp_2–Rap_2 heterotetramers based on biochemical analyses (English *et al.*, 2012), a conclusion that was subsequently confirmed by the structures of related Tae4–Tai4 complexes (Zhang *et al.*, 2013). The similarities of Ssp2 and Rap2a to Tae4 and Tai4 in terms of peptidoglycan hydrolase activity, sequence and structure suggested that the mode of effector inhibition is similar and this will be discussed below. In contrast, Ssp1 displays differences in activity and structure from Tae4 and is biologically distinct from Ssp2. In addition, the structure of Rap1a presents a new fold distinct from the Tai4 proteins; hence, it was important to elucidate the structure of an Ssp1–Rap1a complex.

Following purification using a co-expression strategy, we determined the structure of the Ssp1–Rap1a complex at about 2.0 Å resolution. There are two molecules in the asymmetric unit (one Ssp1 and one Rap1a) and a crystallographic twofold axis given by the symmetry operation $x - y, -y, -z + 2/3$ generates a heterotetramer (Fig. 7*a*). The overall dimensions of this heteromeric assembly are about $90 \times 50 \times 50$ Å and its molecular weight is approximately 60 kDa, consistent with that observed by size-exclusion chromatography during purification of the complex (Supplementary Fig. S1). The model contains residues 1–163 of Ssp1 and residues 30–123 of Rap1a. The solvent-accessible surface area of Ssp1 is 5840 Å^2 and about 16% of this (960 Å^2) is occluded when the complex with Rap1a is formed.

Rap1a interacts with Ssp1 using residues in $\alpha1$, $\alpha3$, $\alpha4$, $\alpha5$ and the $\alpha4$–$\alpha5$ loop (Fig. 7). In particular, the $\alpha4$–$\alpha5$ loop and $\alpha4$ of Rap1a are directly positioned to block the Ssp1 active site. An extensive network of hydrogen bonds, van der Waals forces and water-mediated hydrogen bonds are present at the Ssp1–Rap1a interface. These interactions occur primarily in two areas (areas I and II in Fig. 7*a*). A total of 13 Ssp1 residues (Asp16, Tyr17, Ser18, Tyr22, Ala25, Asp37, Ala47, Asn48, Arg53, Asp130, His133, His149 and Tyr151) and 12 Rap1a residues (Tyr50, Lys58, Arg62, Ser81, Gln82, Gln84, Thr85, Val86, Thr87, Glu90, Glu94 and Arg119) contribute to the network of interactions and the details are presented in a schematic form in Fig. 7(*b*). Gln84 of Rap1a forms a hydrogen bond to the N^{δ} atom of the catalytic His133 of Ssp1 and is a clear marker of the steric block provided by the immunity protein (Figs. 7*b* and 7*c*). Arg119, Arg66, Lys59, Glu94 and Glu94 of Rap1a form salt-bridge interactions with Asp37, Asp16, Glu140, Arg53 and Arg53 of Ssp1, respectively. Tyr50 in $\alpha1$ of Rap1a interacts with Tyr17 from Ssp1 through a hydrogen bond and π-stacking. A small interface (100 Å^2) is created where Asp36 from Rap1a and His149 from Ssp1 interact (area III in Fig. 7).

An overlay (not shown) of the two Rap1a structures, alone and in complex with Ssp1, gives an r.m.s.d. of 0.4 Å for 94 C^{α} atoms, indicating a high similarity in overall structure with no major conformational differences. Rap1a therefore appears to be a highly stable pre-formed binding partner for Ssp1 when in the correct redox state. There is, however, a localized effect following complex formation. In Rap1a, the segment linking $\alpha2$ and $\alpha3$, residues 74–84, shows high average *B* factors (temperature factors; 76.4 Å^2) compared with the overall average *B* factor (31.5 Å^2) and relatively diffuse electron density. This region contributes to Ssp1–Rap1a complex formation and becomes well ordered, with an average *B* factor of 15.6 Å^2 compared with the overall *B* factor of 22.6 Å^2 for the Rap1a component of the complex. The overall structure of Ssp1 is also well retained between the free and complexed states, with an r.m.s.d. of 0.8 Å for the least-squares fit of 162 C^{α} atoms. There are localized adjustments which appear to support complex formation. In the $\alpha1$–$\alpha2$ loop of Ssp1, Tyr17 is relocated by about 7 Å to interact with Tyr50 and Arg62 of Rap1a. In addition, Asn48 and Tyr129 of Ssp1 move 1.8 and 3.5 Å outwards and away from the catalytic centre (Fig. 7*c*).

The Tae4–Tai4 complex from *E. cloacae* also forms a heterotetrameric assembly, with the Tai4 dimer forming the central segment and a Tae4 effector at either end (Zhang *et al.*, 2013). The complex is stabilized by extensive noncovalent interactions formed between the effector and both Tai4 subunits. The protruding loop (Fig. 6*c*) of one Tai4 subunit binds in the active site of the effector and helices $\alpha2$ and $\alpha3$ of the other subunit are positioned to interact with residues in the N-terminal subdomain. This Tae4–Tai4 complex is likely to be a good model for the Ssp2–Rap2a complex. The close structural relationship, in terms of fold, for both the effector and the immunity proteins (see, for example, Fig. 6) would suggest that Rap2a would interact with Ssp2 in a similar fashion and that the selectivity of immunity proteins with the Rap2a fold for or against other enzymes would be determined by variation in the side chains. Such differences are likely to involve residues in the loops linking $\alpha2$ to $\alpha3$ and $\alpha3$ to $\alpha4$ in the immunity proteins, which interact with the $\alpha3$–$\alpha4$ section, the $\beta4$–$\beta5$ loop and the N-terminal section of $\beta7$ in some Tae4 proteins. These parts of the proteins are poorly conserved in terms of sequence identity (Supplementary Figs. S4 and S5).

However, the complex assembly that leads to inhibition is completely distinct between Ssp1 and the other Tae4 systems. Rap1a, which has a completely different fold to the conventional Tai4 proteins, does not possess a protruding loop, but in the complex a helix is positioned to block the effector active site and the interactions that stabilize the complex involve residues in the C-terminal subdomain of the effector rather than the N-terminal subdomain (Supplementary Fig. S6).

3.7. Co-evolved diversity within the Tae4/Ssp and Tai4/Rap families

Finally, we considered the question of why *S. marcescens* has two Tae4 homologues (Ssp1 and Ssp2) and four Rap-family proteins rather than just one amidase effector–immunity combination. Ssp1 and Ssp2 are not redundant since they elicit different biological consequences in a target cell. For example, as shown here and previously (Fig. 2; English *et al.*, 2012), an immunity mutant suffering Ssp2-mediated killing is highly unfit and displays striking cell filamentation, whereas an immunity mutant suffering Ssp1-mediated killing is less disabled and shows round enlarged cells. The difference between the Ssp1-mediated and Ssp2-mediated effects may be related to the apparent modulation of substrate preference observed in the *in vitro* enzyme assays, perhaps reflecting differences in the extent or pattern of cell-wall damage (Fig. 1).

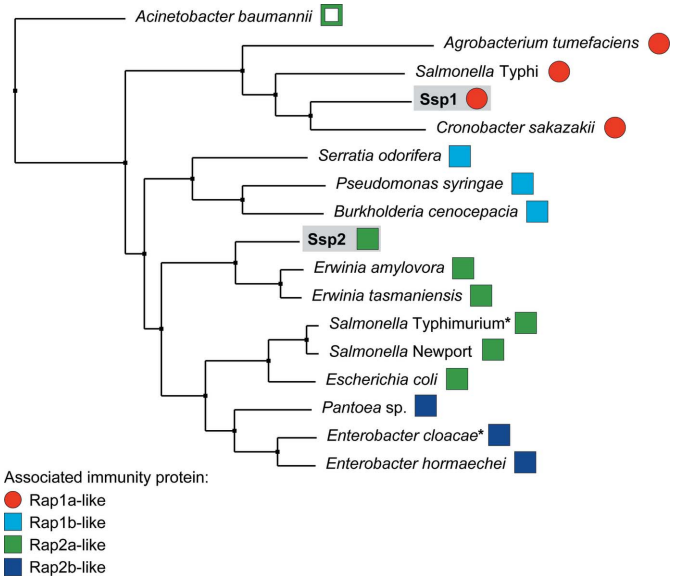

Figure 8
Subgroups of Tae4 family proteins and their associated immunity proteins. Neighbour-joining tree calculated from a multiple sequence alignment of Ssp1, Ssp2 and other Tae4 homologues from different bacterial species (a full alignment is shown in Supplementary Fig. S6). For each Tae4 protein, the adjacently encoded candidate immunity protein was identified by genomic analysis and the *S. marcescens* Rap protein to which it was most closely related was determined. Tae4 homologues with associated immunity proteins similar to Rap1a (Tai4a) are shown by red circles, whereas those with immunity proteins of the Rap1b/Rap2a/Rap2b (Tai4) type are shown by squares (in light blue, green or dark blue for most similarity to Rap1, Rap2a or Rap2b, respectively). Apart from Ssp1 and Ssp2 from *S. marcescens*, the Tae4 homologues are labelled by organism and their identities are as follows (UniProt or genomic identifiers): *Acinetobacter baumannii*, B0VVE3_ACIBS; *Agrobacterium tumefaciens*, Atu4347; *Burkholderia cenocepacia*, Bcen_4030; *Cronobacter sakazakii*, ESA_03935; *Enterobacter cloacae*, ECL_01542; *Enterobacter hormaechei*, F5RYK9_9ENTR; *Erwinia amylovora*, EAMY_3018; *Erwinia tasmaniensis*, ETA_06210; *Escherichia coli*, ECEG_03250; *Pantoea* sp., S7A_11480; *Pseudomonas syringae*, Psyr_4040; *Salmonella enterica* serovar Newport, SNSL254_A0303; *S. enterica* serovar Typhimurium, STM0277; *S. enterica* serovar Typhi, STY0307; *Serratia odorifera*, D4E4R6_SEROD. Asterisks indicate the Tae4–Tai4 homologues for which structures have previously been reported (Zhang *et al.*, 2013) and the open square indicates that this candidate immunity protein showed only weak similarity to Rap2a. Details of the Tae4 homologues and associated immunity proteins are given in Supplementary Table S1.

This study has unexpectedly revealed that the cognate immunity protein for Ssp1, Rap1a, has a distinct structure compared with the other Rap and Tai4 proteins studied to date (Fig. 5).

A comparison of the amino-acid sequences of Ssp1, Ssp2 and Tae4 homologues showed that Ssp1 and several other Tae4 homologues form a distinct grouping (Fig. 8). This is consistent with several structural differences being observed in Ssp1 compared with *Ec*Tae4 (Supplementary Fig. S2). When the adjacently encoded known or putative immunity protein was identified for all of these effectors and compared with the four *S. marcescens* Rap proteins, a pattern became evident. The Ssp1-like proteins all co-occur with immunity proteins of the Rap1a type. The other Tae4 homologues are less separated from each other, but there is a clustering of Tae4 proteins sharing related immunity proteins. So, for example, the three Tae4 proteins whose immunity proteins are most closely related to Rap1b all cluster together (Fig. 8) and the Tae4 homologues most similar to Ssp2 all have associated Rap2a-like immunity proteins (Fig. 8). Hence, effector and immunity proteins appear to have co-evolved within the Tae4 and Tai4 family. In particular, the Ssp1-like proteins appear to form a subgroup distinct enough to utilize a structurally unrelated immunity protein ('Tai4a'), exemplified by Rap1a. The reason for this divergence is unclear, although it is consistent with the distinct biological phenotypes associated with the two effectors. Having both Ssp1 and Ssp2 is likely to confer an evolutionary advantage on the secreting organism, perhaps with each being more efficient against different target species or under different growth conditions than the other. Additionally, having Ssp1 may allow attack on a close relative with Ssp2/Rap2a and *vice versa*, maximizing the ability to distinguish 'self' from competitors.

This analysis strongly suggests that Rap1b and Rap2b are not 'inactive' immunity proteins; rather, they are likely to provide protection against incoming Tae4 proteins from other T6SS-elaborating bacterial species. Rap1b is most closely related to immunity proteins associated with Tae4 proteins (Fig. 8) and thus would be expected to bind an effector of this type and not Ssp1- or Ssp2-like Tae4 proteins. Similarly, Rap2b may neutralize Tae4 proteins related to *Ec*Tae4 (Fig. 8). This idea would also predict that neither Rap1b nor Rap2b would bind Ssp1 or Ssp2, and indeed we have shown previously that they do not (English *et al.*, 2012). Other bacteria can also be observed to possess 'extra' Tai4 proteins compared with their Tae4 complement (this study and Russell *et al.*, 2012). For example, *Cronobacter sakazakii* has 'orphan' Rap1a, Rap2a-like and Rap2b-like proteins (ESA_03939, ESA_03933 and ESA_03932) in addition to its Ssp1–Rap1a pairing. Thus, one could envisage an 'arms race' in which attackers can gain an advantage by acquiring a Tae4 protein of a different subgroup whilst targets can counter by acquiring an immunity protein of the matching type.

4. Concluding remarks

Our structural and activity data, and comparisons with related systems, reveal that the T6SS family 4 endopeptidase effectors

are likely to share the same enzyme mechanism but fall into two functional categories in terms of overall structure and substrate processing. One displays narrow specificity and one is more promiscuous. Some of the immunity proteins encoded within the T6SS gene clusters, those cognate to Tae4/family 4 effectors, can be placed in two protein-fold families which we suggest be termed (i) Tai4, as described previously and including Rap2a, *Ec*Tai4 and *S*TTai4, and (ii) Tai4a, including Rap1a and described for the first time here. Although distinct in terms of structure, the two families are built upon similar underlying principles, namely stable dimeric small α-helical bundles. These T6SS-associated immunity proteins and indeed the effectors in *S. marcescens* appear to rely on the formation of disulfide linkages for folding and activity.

Although the mode of effector inhibition is conserved in the two families, namely a steric block of the active site within a heterotetrameric complex, our study reveals that a very different structure can be used to accomplish effector neutralization. The inhibitory action of immunity proteins is therefore highly specific for effector proteins, even though some effectors have closely related enzyme activities. The type VI-associated endopeptidase effectors are highly basic proteins, as exemplified by Ssp1 and Ssp2, with predicted pI values of 9.1 and 9.3, respectively. These enzymes act on peptidoglycan and process a substrate in the vicinity of two acidic carboxylates, the D-Glu residues. The immunity proteins are acidic; the pI values for the four Rap proteins fall in the range 5.1–6.3 after omitting the signal peptides. Such complementarity of charge contributes to the high-affinity interactions that support complex formation, despite distinctive structures and variation in sequence, and may generate long-range electrostatic attraction to assist correct binding.

The exact mechanism by which the effector proteins are secreted using the T6SS is not yet known. One model suggests a needle comprising a channel formed by haemolysin-coregulated protein (Hcp) oligomers with an internal diameter reported as about 40 Å (Mougous *et al.*, 2006). How this value was estimated is not detailed. We would suggest that from measurements across the pore and taking van der Waals radii into consideration, 40 Å might be a generous estimate of the pore size. We analyzed the globular dimensions of the family 4 endopeptidase effectors and the largest, by a small margin, is Ssp1, with approximate dimensions of $35 \times 40 \times 50$ Å, taking into consideration the van der Waals radii. Such effector proteins, when folded, are therefore comparable in size with or smaller than the pore of the Hcp oligomer. Some effectors may be translocated out of the cell in an intact folded and functional state (Benz *et al.*, 2012) and some may be only partially folded when they are the substrate for the T6SS (Chou *et al.*, 2012). It is possible that Ssp1, Ssp2 and related effectors may utilize disulfide bonds to 'lock' their final structure once translocated away from the reducing environment of the cytoplasm, either in the extracellular environment or within the periplasm of a target cell. In this sense, the T6SS may have evolved to exploit redox status in the periplasm both for arming effector warheads when engaged in attack or for generating a protective armour when in defensive mode.

This work was supported by the Wellcome Trust (grants 082596, 094090, 100476 and a PhD studentship), the European Commission (the Aeropath project), a Biotechnology and Biological Sciences Research Council–Pfizer studentship, the Royal Society of Edinburgh (Research Fellowship to SJC), the Medical Research Council (grant MR/K000111X/1) and the European Commission DIVINOCELL project (WV). We thank Panjikar Santosh for assistance and useful discussions.

References

Alphey, M. S. & Hunter, W. N. (2006). *Acta Cryst.* F**62**, 504–508.
Anantharaman, V. & Aravind, L. (2003). *Genome Biol.* **4**, R11.
Battye, T. G. G., Kontogiannis, L., Johnson, O., Powell, H. R. & Leslie, A. G. W. (2011). *Acta Cryst.* D**67**, 271–281.
Benz, J., Sendlmeier, C., Barends, T. R. & Meinhart, A. (2012). *PLoS One*, **5**, e40453.
Bond, C. S. & Schüttelkopf, A. W. (2009). *Acta Cryst.* D**65**, 510–512.
Bönemann, G., Pietrosiuk, A. & Mogk, A. (2010). *Mol. Microbiol.* **76**, 815–821.
Boyer, F., Fichant, G., Berthod, J., Vandenbrouck, Y. & Attree, I. (2009). *BMC Genomics*, **10**, 104.
Brooks, T. M., Unterweger, D., Bachmann, V., Kostiuk, B. & Pukatzki, S. (2013). *J. Biol. Chem.* **288**, 7618–7625.
Burtnick, M. N., Brett, P. J., Harding, S. V., Ngugi, S. A., Ribot, W. J., Chantratita, N., Scorpio, A., Milne, T. S., Dean, R. E., Fritz, D. L., Peacock, S. J., Prior, J. L., Atkins, T. P. & Deshazer, D. (2011). *Infect. Immun.* **79**, 1512–1525.
Cascales, E. & Cambillau, C. (2012). *Philos. Trans. R. Soc. Lond. B Biol. Sci.* **367**, 1102–1111.
Chen, V. B., Arendall, W. B., Headd, J. J., Keedy, D. A., Immormino, R. M., Kapral, G. J., Murray, L. W., Richardson, J. S. & Richardson, D. C. (2010). *Acta Cryst.* D**66**, 12–21.
Chou, S., Bui, N. K., Russell, A. B., Lexa, K. W., Gardiner, T. E., LeRoux, M., Vollmer, W. & Mougous, J. D. (2012). *Cell Rep.* **1**, 656–664.
Coulthurst, S. J. (2013). *Res. Microbiol.* **164**, 640–654.
Cruickshank, D. W. J. (1999). *Acta Cryst.* D**55**, 583–601.
Ding, J., Wang, W., Feng, H., Zhang, Y. & Wang, D.-C. (2012). *J. Biol. Chem.* **287**, 26911–26920.
Edgar, R. C. (2004). *Nucleic Acids Res.* **32**, 1792–1797.
Emsley, P., Lohkamp, B., Scott, W. G. & Cowtan, K. (2010). *Acta Cryst.* D**66**, 486–501.
Engh, R. A. & Huber, R. (1991). *Acta Cryst.* A**47**, 392–400.
English, G., Trunk, K., Rao, V. A., Srikannathasan, V., Hunter, W. N. & Coulthurst, S. J. (2012). *Mol. Microbiol.* **86**, 921–936.
Evans, P. (2006). *Acta Cryst.* D**62**, 72–82.
Filloux, A. (2011). *Front. Microbiol.* **2**, 155.
Fyfe, P. K., Oza, S. L., Fairlamb, A. H. & Hunter, W. N. (2008). *J. Biol. Chem.* **283**, 17672–17680.
Fyfe, P. K., Rao, V. A., Zemla, A., Cameron, S. & Hunter, W. N. (2009). *Angew. Chem. Int. Ed. Engl.* **48**, 9176–9179.
Gerlach, R. G. & Hensel, M. (2007). *Int. J. Med. Microbiol.* **297**, 401–415.
Glauner, B. (1988). *Anal. Biochem.* **172**, 451–464.
Hao, Q. (2004). *J. Appl. Cryst.* **37**, 498–499.
Holm, L. & Park, J. (2000). *Bioinformatics*, **16**, 566–567.
Hood, R. D. *et al.* (2010). *Cell Host Microbe*, **7**, 25–37.
Jani, A. J. & Cotter, P. A. (2010). *Cell Host Microbe*, **8**, 2–6.
Kabsch, W. (2010). *Acta Cryst.* D**66**, 125–132.
Kabsch, W. & Sander, C. (1983). *Biopolymers*, **22**, 2577–2637.
Krissinel, E. & Henrick, K. (2007). *J. Mol. Biol.* **372**, 774–797.
Langer, G., Cohen, S. X., Lamzin, V. S. & Perrakis, A. (2008). *Nature Protoc.* **3**, 1171–1179.

Li, M., Le Trong, I., Carl, M. A., Larson, E. T., Chou, S., De Leon, J. A., Dove, S. L., Stenkamp, R. E. & Mougous, J. D. (2012). *PLoS Pathog.* **8**, e1002613.
MacIntyre, D. L., Miyata, S. T., Kitaoka, M. & Pukatzki, S. (2010). *Proc. Natl Acad. Sci. USA*, **107**, 19520–19524.
McCoy, A. J., Grosse-Kunstleve, R. W., Adams, P. D., Winn, M. D., Storoni, L. C. & Read, R. J. (2007). *J. Appl. Cryst.* **40**, 658–674.
Micossi, E., Hunter, W. N. & Leonard, G. A. (2002). *Acta Cryst.* D**58**, 21–28.
Minor, W., Cymborowski, M., Otwinowski, Z. & Chruszcz, M. (2006). *Acta Cryst.* D**62**, 859–866.
Mougous, J. D., Cuff, M. E., Raunser, S., Shen, A., Zhou, M., Gifford, C. A., Goodman, A. L., Joachimiak, G., Ordoñez, C. L., Lory, S., Walz, T., Joachimiak, A. & Mekalanos, J. J. (2006). *Science*, **312**, 1526–1530.
Murdoch, S. L., Trunk, K., English, G., Fritsch, M. J., Pourkarimi, E. & Coulthurst, S. J. (2011). *J. Bacteriol.* **193**, 6057–6069.
Murshudov, G. N., Skubák, P., Lebedev, A. A., Pannu, N. S., Steiner, R. A., Nicholls, R. A., Winn, M. D., Long, F. & Vagin, A. A. (2011). *Acta Cryst.* D**67**, 355–367.
Pace, F. de, Nakazato, G., Pacheco, A., de Paiva, J. B., Sperandio, V. & da Silveira, W. D. (2010). *Infect. Immun.* **78**, 4990–4998.
Painter, J. & Merritt, E. A. (2006). *J. Appl. Cryst.* **39**, 109–111.
Panjikar, S., Parthasarathy, V., Lamzin, V. S., Weiss, M. S. & Tucker, P. A. (2005). *Acta Cryst.* D**61**, 449–457.
Pukatzki, S., Ma, A. T., Revel, A. T., Sturtevant, D. & Mekalanos, J. J. (2007). *Proc. Natl Acad. Sci. USA*, **104**, 15508–15513.
Rosales-Reyes, R., Skeldon, A. M., Aubert, D. F. & Valvano, M. A. (2012). *Cell. Microbiol.* **14**, 255–273.
Russell, A. B., Hood, R. D., Biu, N. K., LeRoux, M., Vollmer, W. & Mougous, J. D. (2011). *Nature (London)*, **109**, 19804–19809.
Russell, A. B., LeRoux, M., Hathazi, K., Agnello, D. M., Ishikawa, T., Wiggins, P. A., Wai, S. N. & Mougous, J. D. (2013). *Nature (London)*, **496**, 508–512.
Russell, A. B., Singh, P., Brittnacher, M., Bui, N. K., Hood, R. D., Carl, M. A., Agnello, D. M., Schwarz, S., Goodlett, D. R., Vollmer, W. & Mougous, J. D. (2012). *Cell Host Microbe*, **11**, 538–549.
Schneider, T. R. & Sheldrick, G. M. (2002). *Acta Cryst.* D**58**, 1772–1779.
Schwarz, S., Hood, R. D. & Mougous, J. D. (2010). *Trends Microbiol.* **18**, 531–537.
Shang, G., Liu, X., Lu, D., Zhang, J., Li, N., Zhu, C., Liu, S., Yu, Q., Zhao, Y., Zhang, H., Hu, J., Cang, H., Xu, S. & Gu, L. (2012). *Biochem. J.* **448**, 201–211.
Sheldrick, G. M. (2002). *Z. Kristallogr.* **217**, 644–650.
Sheldrick, G. M. (2010). *Acta Cryst.* D**66**, 479–485.
Sheldrick, G. M., Hauptman, H. A., Weeks, C. M., Miller, R. & Usón, I. (2001). *International Tables for Macromolecular Crystallography*, Vol. *F*, edited by M. G. Rossmann & E. Arnold, pp. 333–345. Dordrecht: Kluwer Academic Publishers.
Silverman, J. M., Brunet, Y. R., Cascales, E. & Mougous, J. D. (2012). *Annu. Rev. Microbiol.* **66**, 453–472.
Terwilliger, T. C. (2003). *Acta Cryst.* D**59**, 38–44.
Vollmer, W., Joris, B., Charlier, P. & Foster, S. (2008). *FEMS Microbiol. Rev.* **32**, 259–286.
Waterhouse, A. M., Procter, J. B., Martin, D. M., Clamp, M. & Barton, G. J. (2009). *Bioinformatics*, **25**, 1189–1191.
Winn, M. D. *et al.* (2011). *Acta Cryst.* D**67**, 235–242.
Zhang, H., Zhang, H., Gao, Z.-Q., Wang, W.-J., Liu, G.-F., Xu, J.-H., Su, X.-D. & Dong, Y.-H. (2013). *J. Biol. Chem.* **288**, 5928–5939.

Supplementary Material

Structural basis for Type VI secretion peptidoglycan DL-endopeptidase function, specificity and neutralization in *Serratia marcescens*.

Velupillai Srikannathasan, Grant English, Nhat Khai Bui, Katharina Trunk, Patrick E. F. O'Rourke, Vincenzo A. Rao, Waldemar Vollmer, Sarah J. Coulthurst* and William N. Hunter*

Supplementary Table S1. Ssp/Tae4 family proteins and corresponding adjacently-encoded immunity proteins.

Organism	Ssp/Tae4 protein		Adjacent Immunity Protein		
	UNIPROT identifier or name	Genomic identifier	UNIPROT identifier or name	Genomic identifier	Closest Rap
Agrobacterium tumefaciens C58	Q7CUP8_AGRT5	Atu4347	A9CGG9_AGRT5	Atu4346	Rap1a (SMA2260)
Burkholderia cenocepacia AU1054	Q1BN86_BURCA	Bcen_4030	Q1BN87_BURCA	Bcen_4029	Rap1b (SMA2262)
Cronobacter sakazakii ATCC BAA-894	A7MQ14_CROS8	ESA_03935	A7MQ15_CROS8[1]	ESA_03936	Rap1a (SMA2260)
Enterobacter cloacae ATCC 13047	D5C6F6_ENTCC	ECL_01542	D5C6F7_ENTCC	ECL_01543	Rap2b (SMA2266)
Enterobacter hormaechei ATCC 49162	F5RYK9_9ENTR		F5RYK8_9ENTR		Rap2b (SMA2266)
Erwinia amylovora CFBP1430	D4I0Q7_ERWAC	EAMY_3018	D4I0Q6_ERWAC	EAMY_3017	Rap2a (SMA2265)
Erwinia tasmaniensis Et1/99	B2VH84_ERWT9	ETA_06210	B2VJE3_ERWT9	ETA_06220	Rap2a (SMA2265)
Escherichia coli B354	D6J6Z7_ECOLX	ECEG_03250	D6J6Z8_ECOLX	ECEG_03251	Rap2a (SMA2265)
Pantoea sp. Sc1	H8DNR2_9ENTR	S7A_11480	H8DNR1_9ENTR	S7A_11475	Rap2b (SMA2266)
Pseudomonas syringae pv. *syringae* B728a	Q4ZP52_PSEU2	Psyr_4040	Q4ZP51_PSEU2	Psyr_4041	Rap1b (SMA2262)
Salmonella Newport SL254	B4SV53_SALNS	SNSL254_A0303	B4SV54_SALN	SNSL254_A0304	Rap2a (SMA2265)
Salmonella Typhi CT18	Q8Z963_SALTI	STY0307	Q8Z964_SALTI	STY0306	Rap1a[2] (SMA2260)
Salmonella Typhimurium LT2	Q93IS4_SALTY	STM0277	Q8ZRL5_SALTY	STM0278	Rap2a (SMA2265)
Serratia odorifera DSM 4582	D4E4R6_SEROD		D4E4R5_SEROD		Rap1b (SMA2262)
Acinetobacter baumannii SDF	B0VVE3_ACIBS	p2ABSDF0033	B0VVE4_ACIBS	p2ABSDF0034	(Rap2a)[3] (SMA2265)
Serratia marcescens Db10	Ssp1	SMA2261	Rap1a	SMA2260	
Serratia marcescens Db10	Ssp2	SMA2264	Rap2a	SMA2265	

[1] Note that this is not the same protein as the one identified as a Tai4 protein in this organism by Russell *et al.*, 2012; that protein, ESA_03932, is an orphan Tai4 protein of the Rap2b type not immediately adjacent to Tae4

[2] STY0306 (SciQ) is approximately twice the size of other Rap proteins, resembling a fusion of two adjacent Rap1a proteins

[3] p2ABSDF0034 is shows only very weak sequence similarity with Rap2a

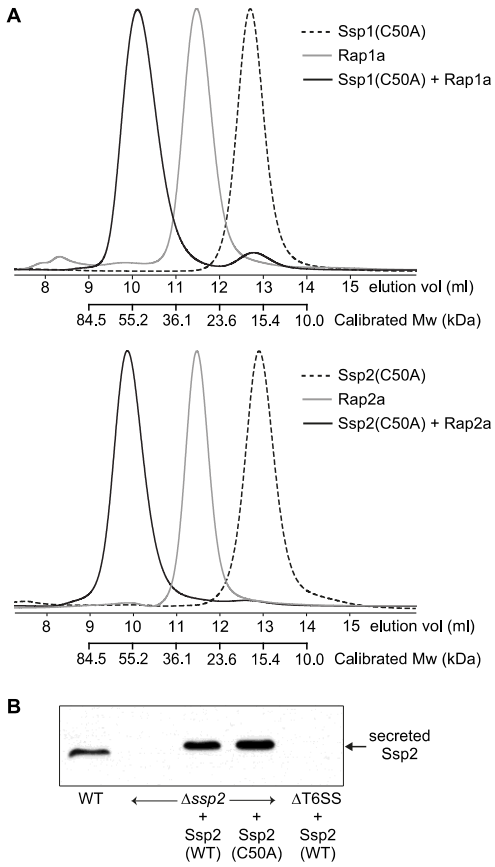

Supplementary Figure S1. Immunity protein binding and secretion is not impaired in Ssp1 and Ssp2 C50A mutants. (A) Size exclusion chromatography analysis of complex formation between Ssp1 (C50A) and Rap1a, top, or Ssp2 (C50A) and Rap2a, bottom. 10 nmol of the protein indicated, or of each protein in the case of the mixtures, was separated on a calibrated Superdex 75 10/300 GL column. (B) Immunoblot detection of Ssp2 in the secreted fraction of the strains indicated: wild type *S. marcescens* Db10 [WT]; mutant lacking Ssp2 [Δ*ssp2*]; Δ*ssp2* mutant carrying plasmids expressing wild type Ssp2 [+Ssp2(WT); pSC541] or the C50A mutant of Ssp2 [+Ssp2(C50A); pSC1230]; and a Type VI secretion system mutant [ΔT6SS] expressing wild type Ssp2.

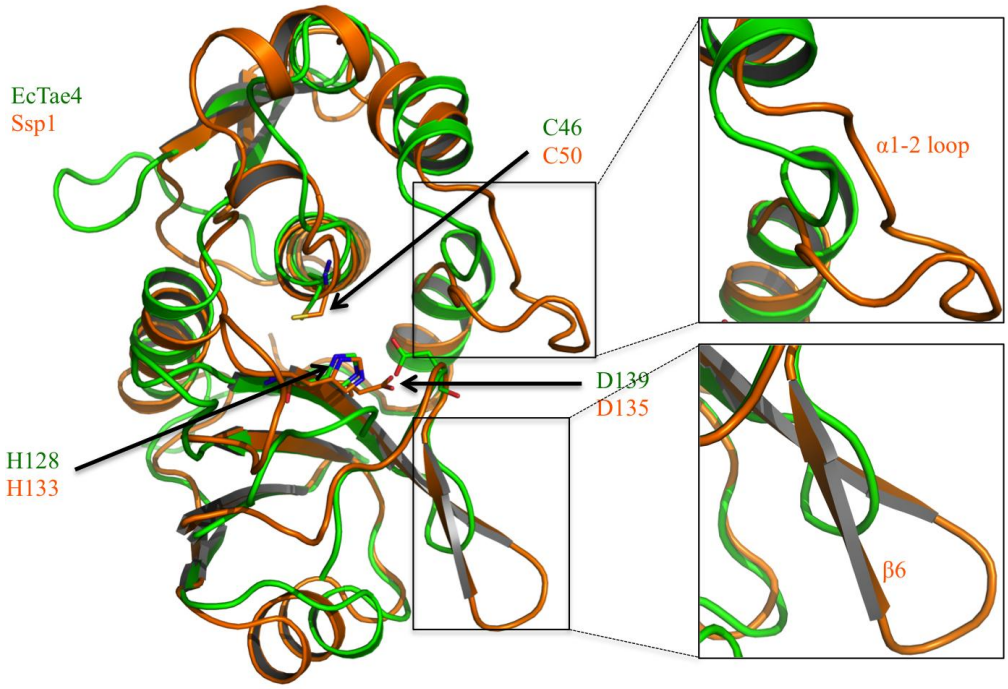

Supplementary Figure S2. Superimposition of Ssp1 (orange ribbon) and *Ec*Tae4 (green ribbon). The catalytic triads (histidine, cysteine and aspartate) are shown as sticks and divergent regions are shown in the boxes.

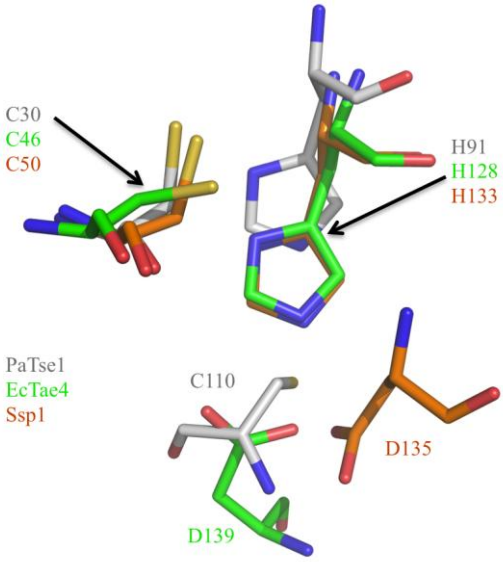

Supplementary Figure S3. Superimposition of the catalytic residues of Ssp1, *Pa*Tse1 and *Ec*Tae4. The color code is N blue, O red, S yellow then C positions for Ssp1 orange, *Pa*Tse1 grey and *Ec*Tae4 green.

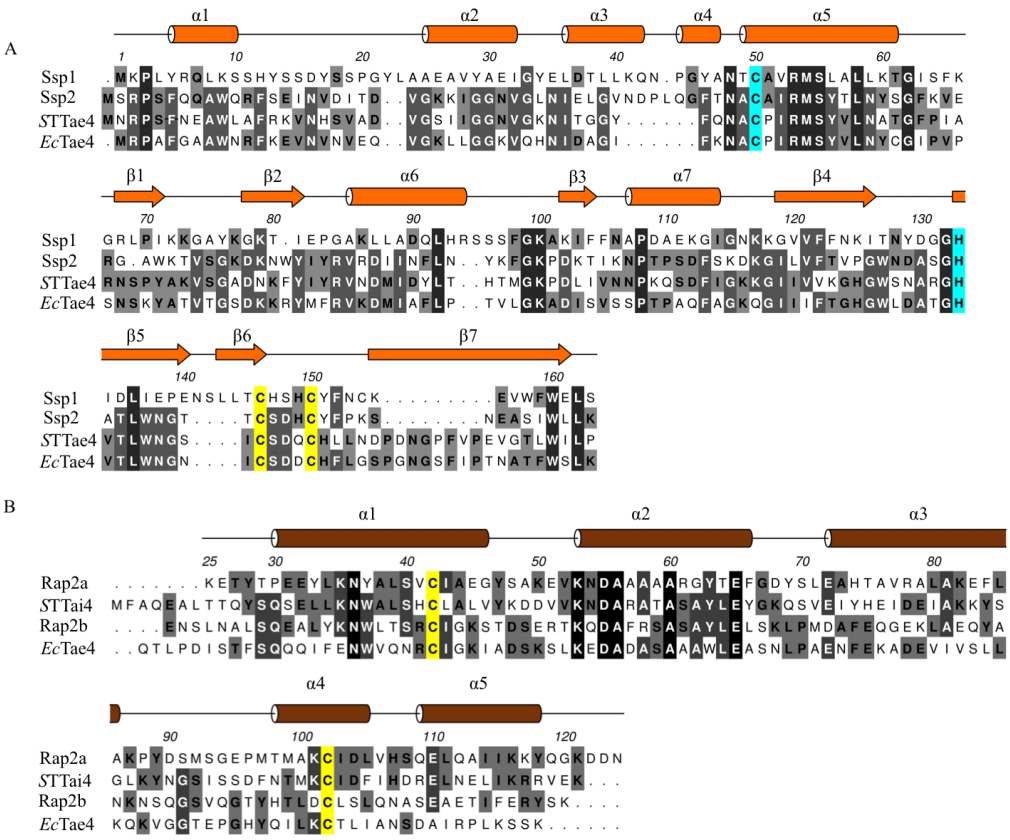

Supplementary Figure S4. Sequence alignment of Ssp1 and selected homologues. A. Structure-based sequence alignment highlights the conserved secondary-structure content (orange cylinders and sheets) in this group of four endopeptidase effectors. Residues involved in disulfide bond formation are coloured yellow. The catalytic histidine and cysteine residues are marked in cyan. The alignment was generated using ClustalW and the figure was prepared using *ALINE* (Bond & Schüttelkopf, 2009). B. An alignment of *S. marcescens* Rap2a with Tai4 from *E. cloacae* and *S.* Typhimurium. Sequence numbering and secondary structure has been drawn based on the Rap2a crystal structure (without signal peptide - brown). Strictly conserved residues in all four sequences are encased in black, conserved in two or three in shades of grey with the conserved cysteines involved in disulfide bond formation highlighted in yellow.

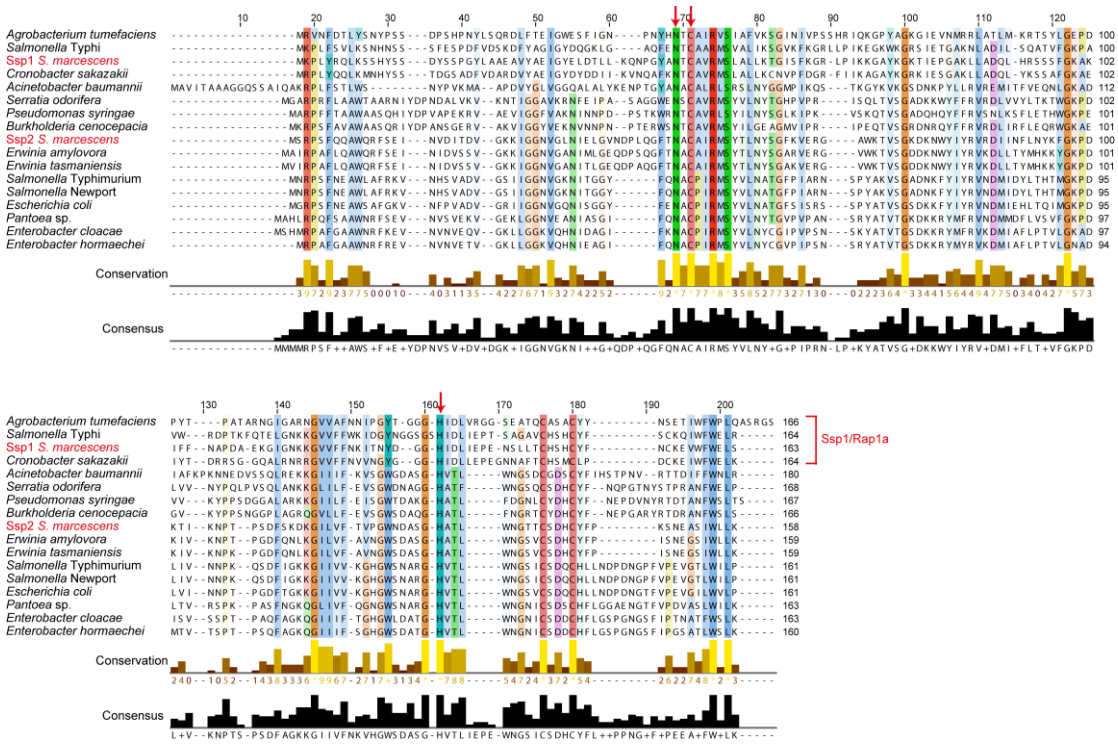

Supplementary Figure S5. Multiple sequence alignment of Ssp1 and Ssp2 with other Tae4 proteins. Alignment was generated using MUSCLE (Edgar, 2004) and visualised using Jalview (Waterhouse *et al.*, 2009). Red arrows show the amino acid residues forming the catalytic triad. The Ssp1-like proteins associated with Rap1a-type immunity proteins are also indicated. The Tae4 homologues are labelled by organism and their identities are as follows (UNIPROT identifier, genomic identifier): *Acinetobacter baumannii* (B0VVE3_ACIBS, p2ABSDF0033), *Agrobacterium tumefaciens* (Q7CUP8_AGRT5, Atu4347), *Burkholderia cenocepacia* (Q1BN86_BURCA, Bcen_4030), *Cronobacter sakazakii* (A7MQ14_CROS8, ESA_03935), *Enterobacter cloacae* (D5C6F6_ENTCC, ECL_01542), *Enterobacter hormaechei* (F5RYK9_9ENTR), *Erwinia amylovora* (D4I0Q7_ERWAC, EAMY_3018), *Erwinia tasmaniensis* (B2VH84_ERWT9, ETA_06210), *Escherichia coli* (D6J6Z7_ECOLX, ECEG_03250), *Pantoea* sp. (H8DNR2_9ENTR, S7A_11480), *Pseudomonas syringae* (Q4ZP52_PSEU2, Psyr_4040), *Salmonella enterica* serovar Newport (B4SV53_SALNS, SNSL254_A0303), *Salmonella enterica* serovar Typhimurium (Q93IS4_SALTY, STM0277) *Salmonella enterica* serovar Typhi (Q8Z963_SALTI, STY0307), *Serratia odorifera* (D4E4R6_SEROD). See also Supplementary Table S1.

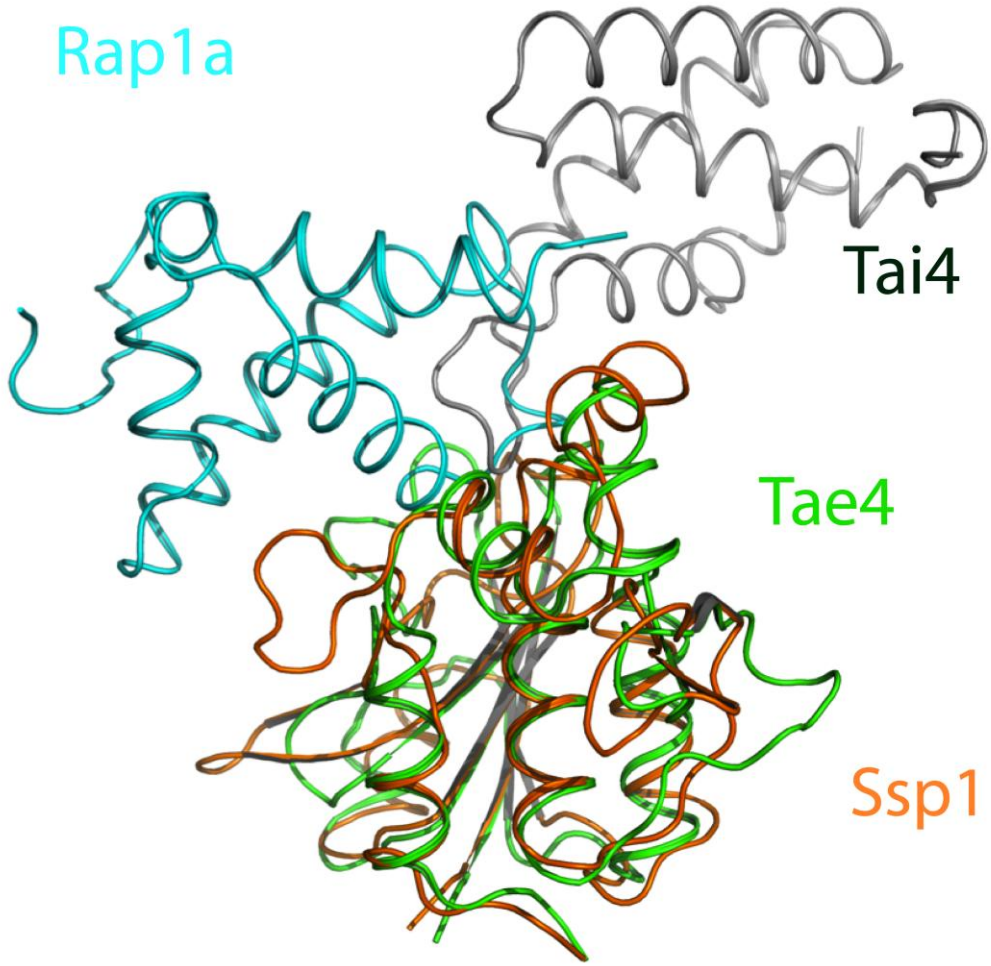

Supplementary Figure S6. Distinct placement of the immunity proteins inhibits different peptidoglycan endopeptidases. Four polypeptides are shown in ribbon style; Ssp1 is colored orange, *Ec*Tae4 is green, one subunit of *Ec*Tai4 is grey and one subunit of Rap1a is cyan. A least-squares overly of Ssp1 and Tae4 was carried out and this then highlights the different positions that the immunity proteins occupy when they bind and inhibit their cognate effector.